

 Open access • Report • DOI:10.2172/1557591

A Deterministic and Probabilistic Framework for Forecasting of Time-Series Damage States and Associated End-of-Life of a Pressurizer Water Reactor Surge Line under Design-Basis and Grid-Load-Following Loading Conditions — [Source link](#)

Subhasish Mohanty, Jae Phil Park, Daniel Franken, Joseph Listwan ...+2 more authors

Published on: 01 Sep 2018

Topics: Pressurizer and Load following power plant

Related papers:

- [Mathematical modeling of a pressurizer in a pressurized water reactor for control design](#)
- [An Interval Approach to Nonlinear Controller Design for Load-Following Operation of a Small Modular Pressurized Water Reactor](#)
- [Dynamic modelling, simulation, and control design of a pressurized water-type nuclear power plant](#)
- [Efficient global sensitivity analysis of structural vibration for a nuclear reactor system subject to nonstationary loading](#)
- [An Optimal Nonlinear Dynamic Inversion Based Controller Design for Load-Following PWR](#)

Share this paper:    

View more about this paper here: <https://typeset.io/papers/a-deterministic-and-probabilistic-framework-for-forecasting-274382mmac>

A Deterministic and Probabilistic Framework for Forecasting of Time-Series Damage States and Associated End-of-Life of a Pressurizer Water Reactor Surge Line under Design-Basis and Grid-Load-Following Loading Conditions

Argonne National Laboratory

About Argonne National Laboratory

Argonne is a U.S. Department of Energy laboratory managed by UChicago Argonne, LLC under contract DE-AC02-06CH11357. The Laboratory's main facility is outside Chicago, at 9700 South Cass Avenue, Argonne, Illinois 60439. For information about Argonne and its pioneering science and technology programs, see www.anl.gov.

DOCUMENT AVAILABILITY

Online Access: U.S. Department of Energy (DOE) reports produced after 1991 and a growing number of pre-1991 documents are available free via DOE's SciTech Connect (<http://www.osti.gov/scitech/>)

Reports not in digital format may be purchased by the public from the National Technical Information Service (NTIS):

U.S. Department of Commerce
National Technical Information Service
5301 Shawnee Rd
Alexandria, VA 22312
www.ntis.gov
Phone: (800) 553-NTIS (6847) or (703) 605-6000
Fax: (703) 605-6900
Email: **orders@ntis.gov**

Reports not in digital format are available to DOE and DOE contractors from the Office of Scientific and Technical Information (OSTI):

U.S. Department of Energy
Office of Scientific and Technical Information
P.O. Box 62
Oak Ridge, TN 37831-0062
www.osti.gov
Phone: (865) 576-8401
Fax: (865) 576-5728
Email: **reports@osti.gov**

Disclaimer

This report was prepared as an account of work sponsored by an agency of the United States Government. Neither the United States Government nor any agency thereof, nor UChicago Argonne, LLC, nor any of their employees or officers, makes any warranty, express or implied, or assumes any legal liability or responsibility for the accuracy, completeness, or usefulness of any information, apparatus, product, or process disclosed, or represents that its use would not infringe privately owned rights. Reference herein to any specific commercial product, process, or service by trade name, trademark, manufacturer, or otherwise, does not necessarily constitute or imply its endorsement, recommendation, or favoring by the United States Government or any agency thereof. The views and opinions of document authors expressed herein do not necessarily state or reflect those of the United States Government or any agency thereof, Argonne National Laboratory, or UChicago Argonne, LLC.

A Deterministic and Probabilistic Framework for Forecasting of Time-Series Damage States and Associated End-of-Life of a Pressurizer Water Reactor Surge Line under Design-Basis and Grid-Load-Following Loading Conditions

**Subhasish Mohanty¹, Jae Phil Park², Daniel Franken³, Joseph Listwan¹,
Saurin Majumdar¹, and Ken Natesan¹**

¹Argonne National Laboratory

²2018 summer intern at Argonne National Laboratory from Pusan National University at Busan

³2018 DOE-NEUP summer intern at Argonne National Laboratory from Kansas State University at Manhattan

September 2018

This page intentionally left blank

ABSTRACT

This report presents an update on the environmental fatigue research that is being conducted at Argonne National Laboratory in support of the Department of Energy's Light Water Reactor Sustainability (LWRS) program. The present semi-annual report covers the period between May 2018 and September 2018. In this report, we present the work performed to further improve the capability for structural integrity prediction. Part of this work focused on validating a computational fluid dynamics model for modeling thermal stratification. We also present finite element (FE) model based thermal-mechanical stress analysis of a pressurized water reactor (PWR) surge line under grid-load-following loading condition. In addition, we present work related to end-of-life prediction of a PWR surge line based on ASME code and NUREG-6909 deterministic approaches under design-basis and grid-load-following conditions.

Our research in this report period also majorly involved with the development of a strategy for probabilistic fatigue life estimation. First, we applied a Weibull probabilistic modeling approach based on end-of-life fatigue data (traditional S~N data under in-air and PWR water conditions) to estimate the probabilistic life for a given strain amplitude. Second, we developed a data analytics based Markov-Chain-Monte-Carlo (MCMC) model for probabilistic modeling of time-series fatigue damage states and the associated probabilistic end-of-life of a component. Unlike the Weibull type approach, the MCMC type may not require a large number of fatigue tests for estimating the end-of-life for given loading and environmental conditions. We demonstrated the use of this framework through symmetric fatigue tests (stress- or strain-controlled tests either under in-air or PWR-water conditions) obtained from our earlier experiments. The MCMC model can use base time-series data either obtained from a model or fatigue experiment. Since experimental data are typically more accurate than model-calculated data, we used experiment-based time-series data to demonstrate the MCMC framework. However, when performing a complex experiment is not possible (due to time and costs involved), a model-based approach can be used to generate the time-series data. Similar model-based data are presented in our earlier report (e.g. for cyclic hardening damage states of a PWR surge line under constant amplitude and design-basis loading [1]). However, for the MCMC work in this report, we used experiment-based time-series damage states obtained from fatigue experiments under design-basis and grid-load-following loading conditions. The experimental loading inputs were based on thermal-mechanical FE model results of a typical PWR surge line. Then, we used the experimental time-series damage state data for forecasting the probabilistic time-series damage states and end-of-life of the PWR surge line. Based on this MCMC modeling strategy, and with the assumed loading, environment and thermal-mechanical boundary conditions, we have estimated that a 316SS-pure base metal PWR surge line would survive at least 159 years with zero failure probability.

This page intentionally left blank

TABLE OF CONTENTS

<i>A Deterministic and Probabilistic Framework for Forecasting of Time-Series Damage States and Associated End-of-Life of a Pressurizer Water Reactor Surge Line under Design-Basis and/or Grid-Load-Following Loading Conditions</i>	<i>ii</i>
ABSTRACT	<i>i</i>
Table of Contents	<i>iii</i>
List of Figures	<i>vi</i>
List of TABLES	<i>xii</i>
Abbreviations	<i>xiii</i>
Acknowledgments	<i>xiv</i>
1 Organization of This Report	<i>1</i>
2 Computational Fluid Dynamics Modeling of an Experimental Thermal-Stratification Flow Case 2	
2.1 Experimental Conditions	<i>3</i>
2.2 Computational Models	<i>3</i>
2.2.1 Material properties	<i>3</i>
2.2.2 Fluid models	<i>6</i>
2.2.3 Mesh and Boundary Conditions.....	<i>8</i>
2.3 CFD Model Results	<i>9</i>
2.3.1 Mesh Dependency	<i>9</i>
2.3.2 Model Dependency	<i>10</i>
3 Thermal-Mechanical Stress Analysis of PWR Surge Line under Grid-Load-Following Loading Cycles	<i>17</i>
3.1 3D Finite Element Model	<i>17</i>
3.2 Thermal Boundary Conditions	<i>19</i>
3.3 Heat Transfer Analysis Results	<i>21</i>
3.4 Thermal-Mechanical Stress Analysis Results	<i>23</i>
3.4.1 Elastic stress analysis results	<i>23</i>
3.4.2 Elastic-plastic stress analysis results	<i>31</i>
4 Similitude Fatigue Tests for PWR Surge Line under Pseudo Strain-Controlled Design-Basis and Grid-Load-Following Loading Cycles	<i>41</i>
4.1 Different Test Cases and Test Methodology	<i>41</i>
4.2 Grid-Load-Following In-air Fatigue Test (ET-F50)	<i>46</i>
4.3 Grid-Load-Following PWR-Water Fatigue Test (EN-F51)	<i>51</i>
4.4 Design-Basis PWR-Water Fatigue Test (EN-F53)	<i>53</i>

5	<i>Deterministic End-of-Life Estimation Using ASME and NURGE-6909 Based Approaches.</i>	57
5.1	Article KD-3 of ASME Code Procedure for In-Air Fatigue Evaluation.....	57
5.2	NUREG-6909 Procedure for PWR-Water Environment Fatigue Evaluation	61
5.3	Results for Fatigue Lives of PWR Surge Line.....	62
5.3.1	In-air and PWR-water environment fatigue lives under design-basis loading case.....	63
5.3.2	In-air and PWR-water environment fatigue lives under grid-load-following loading.....	67
5.4	Issues with ASME Code In-Air Life Estimation Approach and Suggested Way Forward	71
6	<i>End-of-Life Fatigue Data Based Probabilistic Modeling Using Weibull and Bootstrap Techniques</i>	73
6.1	Introduction	73
6.2	Weibull Modeling of End-of-Life Fatigue Data from the Literature	73
6.3	End-of-life Fatigue Modeling Based on Weibull Distribution	75
6.4	Model Estimation Uncertainty Quantification Using Bootstrapping Method.....	81
6.5	Empirical vs. Weibull CDF for End-of-Life Fatigue Data.....	85
7	<i>Time-Series Fatigue Damage States and Probabilistic Fatigue Life Prediction Using Markov-Chain-Monte-Carlo (MCMC) Techniques: Symmetric Loading Cases</i>	87
7.1	Introduction	87
7.2	The Hypothesis.....	88
7.3	Theoretical Background of MCMC Method.....	88
7.3.1	Use of ordinary Monte Carlo method.....	88
7.3.2	Use of Markov-Chain Method	89
7.4	Prediction of Time-Series Fatigue Damage States and Their Scatter	89
7.4.1	MCMC prediction of time-series ratcheting strain for stress-controlled loading conditions.....	91
7.4.2	MCMC prediction of time-series maximum stress for strain/stroke-controlled loading conditions	97
7.5	Prediction of Lifetime CDFs Based on MCMC Predicted Time-Series Damage States	109
7.5.1	In-air condition probabilistic fatigue life.....	109
7.5.2	PWR-water condition probabilistic fatigue life.....	115
8	<i>Time-Series Fatigue Damage States and Probabilistic Fatigue Life Prediction Using Markov-Chain-Monte-Carlo (MCMC) Techniques: Un-Symmetric Loading Cases</i>	119
8.1	MCMC model results for simplified design-basis loading case (ET-F47).....	122
8.2	MCMC model results for detailed design-basis loading case (ET-F48)	123
8.3	MCMC model results for grid-load-following loading case (EN-F51).....	124
8.4	MCMC model results for design-basis loading case (EN-F53)	125
9	<i>Summary and Future Study</i>	126
9.1	Summary	126

9.2 Future Work.....	126
<i>References.....</i>	<i>128</i>

LIST OF FIGURES

Figure 2. 1 Schematic of a thermal stratification experimental setup [15].....	3
Figure 2. 2 Expansion coefficient of water with temperature.....	4
Figure 2. 3 Viscosity of water with temperature.....	5
Figure 2. 4 Thermal conductivity of water with temperature.	5
Figure 2. 5 Heat capacity of water with temperature.....	6
Figure 2. 6 Fluid domain mesh.	8
Figure 2. 7 LES simulation results versus experimental results for higher density mesh	9
Figure 2. 8 Spalart-Allmaras simulation versus experimental results	10
Figure 2. 9 k- ω SST simulation versus experimental results.....	11
Figure 2. 10 k- ϵ RNG simulation versus experimental results.	11
Figure 2. 11 LES simulation results versus experimental results.	12
Figure 2. 12 Velocity contour of LES case.....	13
Figure 2. 13 LES simulation cross-section results.....	13
Figure 2. 14 k- ϵ RNG simulation cross-section results.	14
Figure 2. 15 k- ω SST simulation cross-section results.	14
Figure 2. 16 Spalart-Allmaras simulation cross-section results.....	15
Figure 2. 17 Temperature comparison of different models at 39 s.	15
Figure 3. 1 3D solid model of surge line that connects the hot leg and pressurizer [3].....	18
Figure 3. 2 3D finite element model of surge line for heat transfer and thermal-mechanical stress analysis [3].....	18
Figure 3. 3 Load following time versus rated power for a typical EDF reactor[19-20]	20
Figure 3. 4 Rated power versus temperature data used for estimating the temperature boundary condition during grid-load-following power operation	20
Figure 3. 5 Combined (heat-up, power operation, and cool-down) temperature boundary conditions applied to heat transfer analysis model of SL under a grid-load-following loading cycle: (a) full cycle, (b) during heat-up, and (c) during cool-down.....	21
Figure 3. 6 Simulated temperature history of full grid-load-following loading cycle (heat-up, power operation, and cool-down) at typical FE nodes near pressurizer end, mid-section, and HL end of SL.	22
Figure 3. 7 Magnified version of Figure 3.6 during power operation.	22
Figure 3. 8 The elastic FE simulated time-dependent Tresca stress ($\sigma_{max.prin.} - \sigma_{min.prin.}$), Von-Mises stress (σ_{Mises}) and stress component along the vertical direction (σ_{33}) at the centroid of a typical element near pressurizer end: (a) under full cycle, (b) during power operation (c) during heat-up, and (d) during cool-down.....	24
Figure 3. 9 The elastic FE simulated time-dependent maximum principal stress ($\sigma_{max.prin.}$) and minimum principal stress ($\sigma_{min.prin.}$) at the centroid of a typical element near pressurizer end: (a) under full cycle, (b) during heat-up, and (d) during cool-down.	25
Figure 3. 10 The elastic FE simulated time-dependent Von-Mises stress rate ($\dot{\sigma}_{Mises}$) at the centroid of a typical element near pressurizer end: (a) under full cycle, (b) during heat-up, and (c) during cool-down.....	26
Figure 3. 11 The elastic FE simulated time-dependent total strain (ϵ_{33}^{to}), thermal strain (ϵ_{33}^{θ}), and mechanical strain (ϵ_{33}^{me}) components along the vertical direction and at the centroid of a	

typical element near pressurizer end: (a) under full cycle, (b) during power operation (c) during heat-up, and (d) during cool-down. 27

Figure 3. 12 The elastic FE simulated time-dependent maximum principal strain ($\epsilon_{max.prin.}$) and minimum principal strain ($\epsilon_{min.prin.}$) at the centroid of a typical element near pressurizer end: (a) under full cycle, (b) during heat-up, and (c) during cool-down. 28

Figure 3. 13 The elastic FE simulated time-dependent along the vertical direction mechanical strain rate ($\dot{\epsilon}_{33}^{me}$) at the centroid of a typical element near pressurizer end: (a) under full cycle, (b) during heat-up, and (c) during cool-down. 29

Figure 3. 14 The elastic FE simulated hysteresis curves ($\epsilon_{33}^{to} \sim \sigma_{33}$ and $\epsilon_{33}^{me} \sim \sigma_{33}$) at the centroid of a typical element near pressurizer end and comparison with tensile test strain~stress curve for 300 °C. 30

Figure 3. 15 The elastic FE simulated hysteresis curves ($\epsilon_{33}^{to} \sim \sigma_{Mises}$, $\epsilon_{33}^{me} \sim \sigma_{Mises}$, and $\epsilon_{33}^{me} \sim \sigma_{Tresca}$) at the centroid of a typical element near pressurizer end and comparison with tensile test strain~stress curve for 300 °C. 30

Figure 3. 16 The elastic-plastic FE simulated time-dependent Tresca stress ($\sigma_{max.prin.} - \sigma_{min.prin.}$), Von Mises stress (σ_{Mises}), and stress component along the vertical direction (σ_{33}) at the centroid of a typical element near pressurizer end: (a) under full cycle, (b) during power operation (c) during heat-up, and (d) during cool-down. 33

Figure 3. 17 The elastic-plastic FE simulated time-dependent maximum principal stress ($\sigma_{max.prin.}$) and minimum principal stress ($\sigma_{min.prin.}$) at the centroid of a typical element near pressurizer end: (a) under full cycle, (b) during heat-up, and (d) during cool-down... 34

Figure 3. 18 The elastic-plastic FE simulated time-dependent Von-Mises stress rate ($\dot{\sigma}_{Mises}$) at the centroid of a typical element near pressurizer end: (a) under full cycle, (b) during heat-up, and (c) during cool-down. 35

Figure 3. 19 The elastic-plastic FE simulated time-dependent total strain (ϵ_{33}^{to}), thermal strain (ϵ_{33}^{θ}), and mechanical strain (ϵ_{33}^{me}) components along the vertical direction and at the centroid of a typical element near pressurizer end: (a) under full cycle, (b) during power operation, (c) during heat-up, and (d) during cool-down. 36

Figure 3. 20 The elastic-plastic FE simulated time-dependent plastic strain magnitude (ϵ_{mag}^{pl}) and plastic strain component along the vertical direction (ϵ_{33}^{pl}) at the centroid of a typical element near pressurizer end: (a) under full cycle, (b) during heat-up, and (c) during cool-down. 37

Figure 3. 21 The elastic-plastic FE simulated time-dependent maximum principal strain ($\epsilon_{max.prin.}$) and minimum principal strain ($\epsilon_{min.prin.}$) at the centroid of a typical element near pressurizer end: (a) under full cycle, (b) during heat-up, and (c) during cool-down... 38

Figure 3. 22 The elastic-plastic FE simulated time-dependent mechanical strain rate ($\dot{\epsilon}_{33}^{me}$) along the vertical direction at the centroid of a typical element near pressurizer end: (a) under full cycle, (b) during heat-up, and (c) during cool-down. 39

Figure 3. 23 The elastic-plastic FE simulated hysteresis curves ($\epsilon_{33}^{to} \sim \sigma_{33}$ and $\epsilon_{33}^{me} \sim \sigma_{33}$) at the centroid of a typical element near pressurizer end and comparison with tensile test strain~stress curve for 300 °C. 40

Figure 3. 24 The elastic-plastic FE simulated hysteresis curves ($\epsilon_{33}^{to} \sim \sigma_{Mises}$, $\epsilon_{33}^{me} \sim \sigma_{Mises}$, and $\epsilon_{33}^{me} \sim \sigma_{Tresca}$) at the centroid of a typical element near pressurizer end and comparison with tensile test strain~stress curve for 300 °C. 40

Figure 4. 1 Schematic showing the highlighted location (in red circle) of the 316 SS base metal specimens (ET-F50, EN-F51, and EN-F53) with respect to heat affected zone (HAZ) in 508 LAS-316 SS dissimilar metal weld (DMW). 43

Figure 4. 2 Strain versus stroke data from first cycle of ET-F13 fatigue test used for generating the stroke inputs for ET-F49 fatigue test. 43

Figure 4. 3 Applied stroke input and the desired gauge area strain for a single cycle for ET-F49 fatigue test. 44

Figure 4. 4 Applied stroke rate and the desired gauge area strain rate for a single cycle for ET-F49 fatigue test. 44

Figure 4. 5 Normalized applied strokes versus observed gauge area strains for 1000 fatigue cycles for ET-F49 fatigue test. 45

Figure 4. 6 Strain versus stroke data from first cycle of ET-F49 fatigue test used for generating the stroke inputs for ET-F50, EN-F51, and EN-F53 fatigue tests. 45

Figure 4. 7 Applied stroke input and the desired gauge area strain for a single cycle for ET-F50 fatigue test. 46

Figure 4. 8 Applied stroke rate and the desired gauge area strain rate for a single cycle in ET-F50 fatigue test. 47

Figure 4. 9 Normalized applied strokes versus observed gauge area strains for 1000 fatigue cycles in ET-F50 fatigue test. 47

Figure 4. 10 Observed stress up to 30,088 fatigue cycles for ET-F50 fatigue test. 48

Figure 4. 11 First 5-cycle grid-load-following condition applied stroke input for ET-F50 fatigue test. 48

Figure 4. 12 First 5-cycle observed strains for ET-F50 fatigue test. 49

Figure 4. 13 First 5-cycle observed strain rates for ET-F50 fatigue test. 49

Figure 4. 14 First 5-cycle observed stress for ET-F50 fatigue test. 50

Figure 4. 15 First 5-cycle observed strain versus observed stress hysteresis loops for ET-F50 fatigue test. 50

Figure 4. 16 Observed stress for the entire fatigue life for EN-F51 fatigue test. 51

Figure 4. 17 First 5-cycle observed stress for EN-F51 fatigue test. 52

Figure 4. 18 First 5-cycle applied stroke versus observed stress hysteresis loops for EN-F51 fatigue test. 52

Figure 4. 19 Applied stroke input and the desired gauge area strain for single-cycle design-basis type loading in EN-F53 fatigue test. 53

Figure 4. 20 Applied stroke rate and the desired gauge area strain rate for single-cycle design-basis type loading in EN-F53 fatigue test. 54

Figure 4. 21 Observed stress for the entire life for EN-F53 fatigue test. 54

Figure 4. 22 First 5-cycle design-basis loading condition applied stroke input for EN-F53 fatigue test. 55

Figure 4. 23 First 5-cycle observed stress for EN-F53 fatigue test. 55

Figure 4. 24 First 5-cycle applied stroke versus observed stress (hysteresis loop) for EN-F53 fatigue test. 56

Figure 5. 1 ASME design fatigue curve (2010 code version) for austenitic stainless steel at room temperature [24, 29].	61
Figure 5. 2 Elastic FE simulated maximum shear stress ($=\frac{1}{2}(\sigma_1 - \sigma_3)$) histories under design-basis loading case.	64
Figure 5. 3 Elastic-plastic FE simulated maximum shear stress ($=\frac{1}{2}(\sigma_1 - \sigma_3)$) histories under design-basis loading case.	64
Figure 5. 4 Elastic FE simulated maximum shear strain ($=\frac{1}{2}(\varepsilon_1 - \varepsilon_3)$) histories under design-basis loading case.	65
Figure 5. 5 Elastic-plastic FE simulated maximum shear strain ($=\frac{1}{2}(\varepsilon_1 - \varepsilon_3)$) histories under design-basis loading case.	65
Figure 5. 6 Elastic FE simulated maximum shear strain rate ($=\frac{1}{2}(\dot{\varepsilon}_1 - \dot{\varepsilon}_3)$) histories under design-basis loading case.	66
Figure 5. 7 Elastic-plastic FE simulated maximum shear strain ($=\frac{1}{2}(\dot{\varepsilon}_1 - \dot{\varepsilon}_3)$) histories under design-basis loading case.	66
Figure 5. 8 Elastic FE simulated maximum shear stress ($=\frac{1}{2}(\sigma_1 - \sigma_3)$) histories under grid-load-following loading case.	68
Figure 5. 9 Elastic-plastic FE simulated maximum shear stress ($=\frac{1}{2}(\sigma_1 - \sigma_3)$) histories under grid-load-following loading case.	68
Figure 5. 10 Elastic FE simulated maximum shear strain ($=\frac{1}{2}(\varepsilon_1 - \varepsilon_3)$) histories under grid-load-following loading case.	69
Figure 5. 11 Elastic-plastic FE simulated maximum shear strain ($=\frac{1}{2}(\varepsilon_1 - \varepsilon_3)$) histories under grid-load-following loading case.	69
Figure 5. 12 Elastic FE simulated maximum shear strain rate ($=\frac{1}{2}(\dot{\varepsilon}_1 - \dot{\varepsilon}_3)$) histories under grid-load-following loading case.	70
Figure 5. 13 Elastic-plastic FE simulated maximum shear strain ($=\frac{1}{2}(\dot{\varepsilon}_1 - \dot{\varepsilon}_3)$) histories under grid-load-following loading case.	70
Figure 6. 1 Digitized in-air strain versus life data as obtained from [39]	74
Figure 6. 2 Digitized PWR-water strain versus life data as obtained from [39].	75
Figure 6. 3 Functional fitting result of Eq. 6.3 with only exact data.	76
Figure 6. 4 MLE result of Eq. 6.6 with sample data of high-temperature air fatigue life.	80
Figure 6. 5 MLE result of Eq. 6.7 with sample data of PWR water fatigue life.	80
Figure 6. 6 Estimates from sample set (red lines) and bootstrap sample sets (blue circles) for high-temperature air.	82
Figure 6. 7 Estimates from sample set (red lines) and bootstrap sample sets (blue circles) for PWR water.	83
Figure 6. 8 Result of bootstrapping for MLE of Eq. 6.6, for high-temperature air.	84
Figure 6. 9 Result of bootstrapping for MLE of Eq. 6.7 for PWR water.	84

Figure 6. 10 Estimated Weibull CDF for high-temperature air with sample set (black lines), bootstrap sample set (grey lines), and empirical CDFs from raw data when the given ϵ_a is 0.2 or 0.6%. 86

Figure 6. 11 Estimated Weibull CDF for PWR water with sample set (black lines), bootstrap sample set (grey lines), and empirical CDFs from raw data when the given ϵ_a is 0.3 or 0.6%. 86

Figure 7. 1 Cyclic age versus ratcheting strain data, which were used as base data for MCMC modeling of ET-F43 test case. 92

Figure 7. 2 Histogram of ratcheting strain rate for ET-F43 data. 93

Figure 7. 3 Time-series state profile of ET-F43 data. 93

Figure 7. 4 Time-series state profile (red line) and 1,000 MCMC state profiles (light red lines) of ET-F43 data. 94

Figure 7. 5 Original ratcheting strain profile (black line), estimated 1,000 MCMC ratcheting strain profiles (grey line), and failure strain limits used for CDF calculation (red line) in ET-F43 test case. 94

Figure 7. 6 Cyclic age versus ratcheting strain data, which were used as base data for MCMC modeling of ET-F44. 95

Figure 7. 7 Histogram of ratcheting strain rate for EN-F44 data. 96

Figure 7. 8 Time-series state profile (red line) and 1,000 MCMC state profiles (light red lines) of EN-F44 data. 96

Figure 7. 9 Original ratcheting strain profile (black line), estimated 1,000 MCMC ratcheting strain profiles (grey line), and failure strain limits used for CDF calculation (red line) of EN-F44. 97

Figure 7. 10 Cyclic age versus maximum stress data, which were used as base data for MCMC modeling of ET-F44 loading and environment case. 98

Figure 7. 11 Histogram of maximum stress rate for ET-F06 data in hardening stage. 99

Figure 7. 12 Histogram of maximum stress rate for ET-F06 data in softening stage. 99

Figure 7. 13 Time-series state profile (red line) and 1,000 MCMC state profiles (light red lines) of ET-F06 data in hardening stage. 100

Figure 7. 14 Time-series state profile (red line) and 1,000 MCMC state profiles (light red lines) of ET-F06 data in softening stage. 100

Figure 7. 15 Original maximum stress profile (black line) and estimated 1,000 MCMC maximum stress profiles (grey line) for ET-F06 data. 101

Figure 7. 16 Cyclic age versus maximum stress data, which are used as base data for MCMC modeling of ET-F13 loading and environment case. 102

Figure 7. 17 Histogram of maximum stress rate for ET-F13 data in hardening stage. 102

Figure 7. 18 Histogram of maximum stress rate for ET-F13 data in softening stage. 103

Figure 7. 19 Time-series state profile (red line) and 1,000 MCMC state profiles (light red lines) of ET-F13 data in hardening stage. 103

Figure 7. 20 Time-series state profile (red line) and 1,000 MCMC state profiles (light red lines) of ET-F13 data in softening stage. 104

Figure 7. 21 Original maximum stress profile (black line) and converted 1,000 MCMC maximum stress profiles (grey line) for ET-F13 data. 104

Figure 7. 22 Cyclic age versus maximum stress data, which are used as base data for MCMC modeling of EN-F14 loading and environment case. 106

Figure 7. 23 Histogram of maximum stress rate for EN-F14 data in hardening stage.	106
Figure 7. 24 Histogram of maximum stress rate for EN-F14 data in softening stage.	107
Figure 7. 25 Time-series state profile (red line) and 1,000 MCMC state profiles (light red lines) of EN-F14 data in hardening stage.	107
Figure 7. 26 Time-series state profile (red line) and 1,000 MCMC state profiles (light red lines) of EN-F14 data during softening stage.	108
Figure 7. 27 Original maximum stress profile (black line) and predicted 1,000 MCMC maximum stress profiles (grey line) for EN-F14 data.	108
Figure 7. 28 CDF of Weibull-based fatigue life model for high-temperature air, strain amplitude of 0.5%, and strain control: best-fit sample set (black lines) and bootstrap confidence bound sample set (grey lines).	111
Figure 7. 29 Empirical CDF estimated from MCMC time-series ratcheting strain for ET-F43 test case.	112
Figure 7. 30 Empirical CDF estimated from MCMC estimated time-series ratcheting strain for ET-F06 test case.	112
Figure 7. 31 Empirical CDF estimated from MCMC estimated time-series ratcheting strain for ET-F13 test case.	113
Figure 7. 32 CDF of Weibull-based fatigue life model for high-temperature air, strain amplitude of 0.5%, and strain control: best-fit sample set (black lines) and bootstrap confidence bound sample set (grey lines).	116
Figure 7. 33 Empirical CDF estimated from MCMC-estimated time-series ratcheting strain for EN-F44 test case.	116
Figure 7. 34 Empirical CDF estimated from MCMC-estimated time-series ratcheting strain for EN-F14 test case.	117

LIST OF TABLES

Table 2. 1 Mesh Characteristics.....	10
Table 4. 1 Summary of different test cases and associated test parameters	42
Table 5. 1 Material properties for 316 SS at 300 °C.....	63
Table 5. 2 Fatigue lives under design-basis loading.....	67
Table 5. 3 Fatigue lives under grid-load-following loading	71
Table 7. 1 Symmetric (R= -1) type fatigue loading cases and associated environment for MCMC method evaluation.....	90
Table 7. 2 Summary of estimated life distributions for high temperature in-air condition.	114
Table 7. 3 Summary of estimated life distributions for PWR water condition.....	118
Table 8. 1 Summary of estimated life distributions for high-temperature in-air condition.	121

ABBREVIATIONS

3D	Three Dimensional
ANL	Argonne National Laboratory
ASME	American Society of Mechanical Engineers
CFD	Computational Fluid Dynamics
FE	Finite Element
HL	Hot Leg
HPC	High Performance Computing
HT	Heat Transfer
LWRS	Light Water Reactor Sustainability
MCMC	Markov-Chain-Monte-Carlo
PWR	Pressurized Water Reactor
SL	Surge Line
SS	Stainless Steel

ACKNOWLEDGMENTS

This research was supported through the U.S. Department of Energy's Light Water Reactor Sustainability program under the work package of environmental fatigue study, program manager Dr. Keith Leonard.

This page intentionally left blank

1 Organization of This Report

This report is organized in to following sections:

Section 1: Organization of this report

Section 2: Computational Fluid Dynamics Modeling of an Experimental Thermal-Stratification Flow Case

Section 3: Thermal-Mechanical Stress Analysis of PWR Surge Line under Grid-Load-Following Loading Cycles

Section 4: Similitude Fatigue Tests for PWR Surge Line under Pseudo Strain-Controlled Design-Basis and Grid-Load-Following Loading Cycles

Section 5: Deterministic End-of-Life Estimation Using ASME and NURGE-6909 Based Approaches

Section 6: End-of-Life Fatigue Data Based Probabilistic Modeling Using Weibull and Bootstrap Techniques

Section 7: Time-Series Fatigue Damage States and Probabilistic Fatigue Life Prediction Using Markov-Chain-Monte-Carlo (MCMC) Techniques: Symmetric Loading Cases

Section 8: Time-Series Fatigue Damage States and Probabilistic Fatigue Life Prediction Using Markov-Chain-Monte-Carlo (MCMC) Techniques: Un-Symmetric Loading Cases

Section 9: Summary and Future Study

2 Computational Fluid Dynamics Modeling of an Experimental Thermal-Stratification Flow Case

Thermal stratification is the process of a single fluid existing at two largely different temperatures in close proximity and at a low flow rate. The difference in temperatures in the fluid leads to different densities. The hotter fluid will be less dense and, therefore, experience more buoyancy force and will rise to the top. The colder fluid will be denser and will fall to the bottom. Since the fluid transfers heat to the piping, the pipe holding the fluid also experiences the effects of thermal stratification. A pipe experiencing thermal stratification will expand at the top and constrict at the bottom. The expansion and contraction of the pipe can lead to significant movement and stresses on the pipe.

In 1988, the Nuclear Regulatory Committee (NRC) reported in a bulletin that at the Farley Nuclear Power Plant (NPP) water was found to be leaking through the wall of an emergency core cooling pipe. It was discovered that thermal stratification in the piping led to cracks in the pipe wall, which led to the leaks [2]. Additionally, in 1988 the Trojan NPP reported unexpected movement and plastic deformation of the pressurizer surge line, also due to thermal stratification [3]. Since the discovery of the impact of thermal stratification on surge lines, rules and practices have been put into place to reduce the impact of stratification. While the rules and practices help prevent thermal stresses, they cannot completely eliminate thermal stresses, which over the life of a reactor may become significant. In the Argonne report on CFD analysis of thermal-mechanical stresses under transient conditions, the authors show that the stresses incurred during thermal stratification related transient cases can be significant [4].

As design life of NPPs is being extended, it is important to investigate the long-term effects that thermal stratification has on the safety of pressurizer surge lines and other similar components subjected to thermal stratification. Thermal stratification has been studied and reported extensively in the literature [4-15]. One common approach to studying this and related phenomena is to use a finite element code. By using a finite element code, the need for time-consuming and cost-prohibitive scaled experiments can be avoided; however, it is beneficial to be able to benchmark computational results with experimental results. In our earlier work [3], we extensively discussed the computational fluid dynamics (CFD) model of the thermal stratification in a PWR surge line and related stress analysis results under different transient conditions. However, the discussed CFD models in this work [3] were not benchmarked with respect to experimental data. Since there already exists reliable experimental data, the authors decided to create a computational model so that calculated results could be compared to experimental results. In the present work, we used a commercially available CFD code, called Abaqus CFD, to replicate an experimental setup developed by Rezende et al. [16]. Abaqus is a popular structural mechanics code that also has CFD capabilities. The goal of our work was to validate that Abaqus CFD can be used to accurately solve fluid flows, which then can be used to calculate structural loads. The reported work discusses the CFD model benchmarking results with respect to a transient thermal-stratification loading condition. Eventually the aim is to extend the discussed CFD modeling approach for thermal stratification and associated heat transfer modeling under full fuel cycle thermal loading. Note that the results discussed in subsequent sections of this report are related to full fuel-cycle thermal loading but not based on the output of the discussed CDF model results. Future work is needed to model the thermal stratification and heat transfer analysis under the full fuel cycle and use the associated results for thermal-mechanical stress analysis and associated fatigue life estimation. Nonetheless, we present the details of the CFD benchmarking results under an experimental transient condition.

2.1 Experimental Conditions

Experimental results gathered by Rezende et al. [16] were used as reference to compare thermal stratification results from an experiment to Abaqus CFD model calculations. In their paper Rezende et al. also created a computational model with the commercially available code Ansys CFX. The basic layout and configuration of the experimental setup can be seen in Figure 2.1. The system was composed of 0.1223-m diameter piping, which fed into a large reservoir. Water filled the system and then was pressurized to 2.11 MPa gauge. The water was then heated until it reached the desired temperature of 219.2°C, at which point the water was no longer heated. Cold water was then injected from the bottom piping at rate of 0.76 kg/s and temperature of 31.7°C. Note that in the original literature uncertainties were given for each parameter value. As the cold water entered the pipe, the less dense hot water remained stratified above the cold water. The water exiting the pipe left through 11 small holes that had been placed at the end of the horizontal section of pipe. Additionally, the entire setup was wrapped with two inches of stone wool insulation.

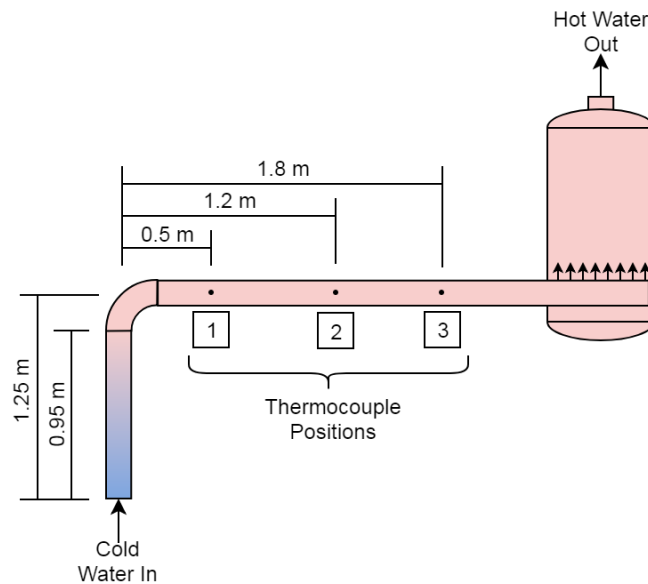


Figure 2. 1 Schematic of a thermal stratification experimental setup [16].

2.2 Computational Models

2.2.1 Material properties

Accurate CFD simulation results require correct values of the relevant material properties. Four material properties are required to adequately model water in a CFD simulation, properties such as density, viscosity, specific heat capacity, and thermal conductivity. The properties previously mentioned were taken from the IAPWS-IF97 database for a pressure of 2.11 MPa. Abaqus does not allow the input of temperature-dependent density values; instead, it relies on the use of the Boussinesq approximation to account for changes in density with temperature. Temperature-dependent expansion coefficients were

calculated with the densities given in the IAPWS-IF97 database. The reference temperature used in this calculation was taken to be 4°C. The equation for deriving the expansion coefficient is given below:

$$(\rho - \rho_0)g \approx -\rho_0\beta(\theta - \theta_0)g \tag{2.1}$$

The expansion coefficient values with temperature are displayed in Figure 2.2. Plots of the viscosity and thermal conductivity are shown in Figures 2.3 and 2.4, respectively. The water heat capacity properties are shown in Figure 2.5. In addition to the water properties, the solid properties of 316 stainless steel (SS) pipe must also be included. For the stainless steel pipe, the temperature-dependent properties of specific heat capacity and thermal conductivity were used and can be found in Ref. [4]. Additionally, the density of the pipe metal was taken to be a constant value of 8238 kg/m³.

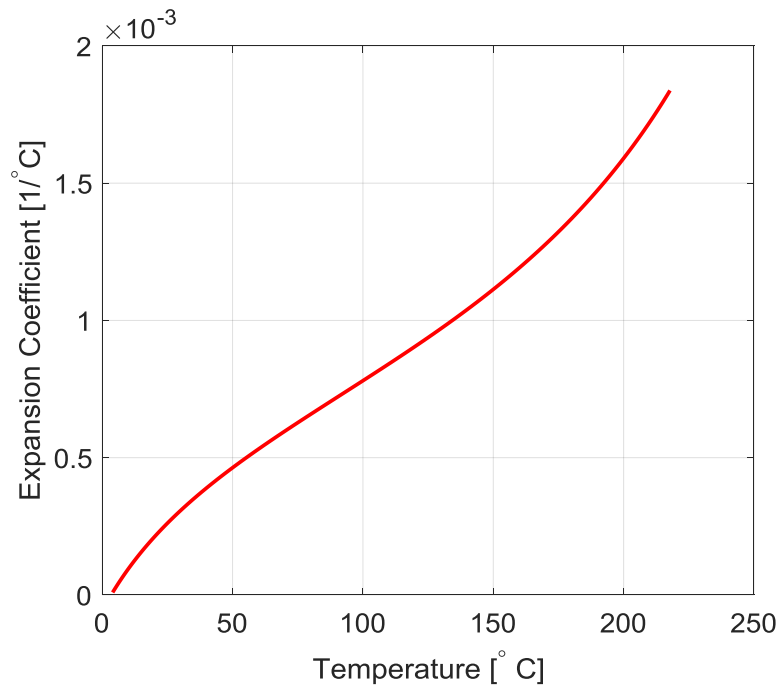


Figure 2. 2 Expansion coefficient of water with temperature.

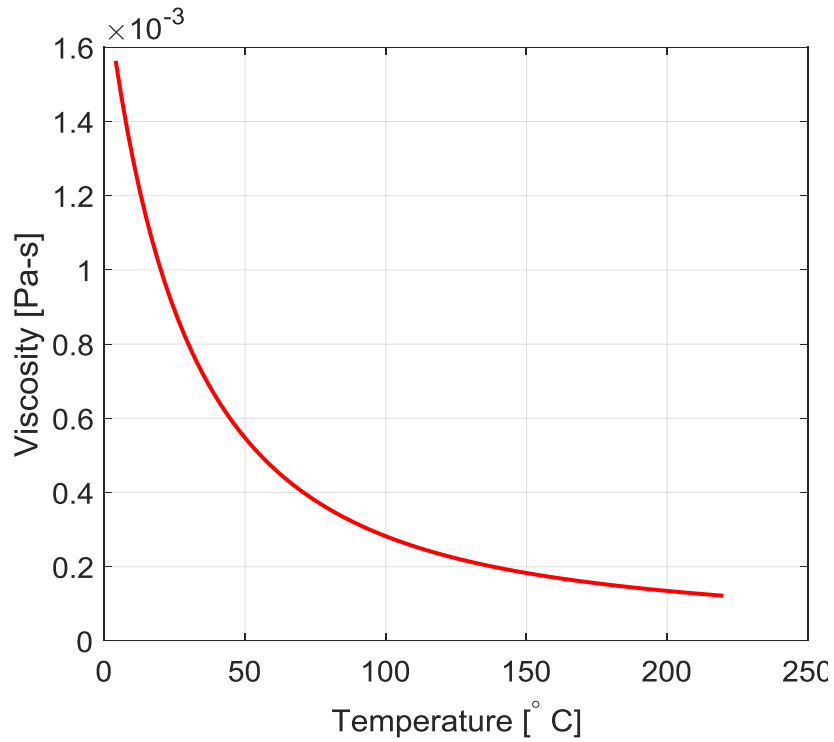


Figure 2. 3 Viscosity of water with temperature.

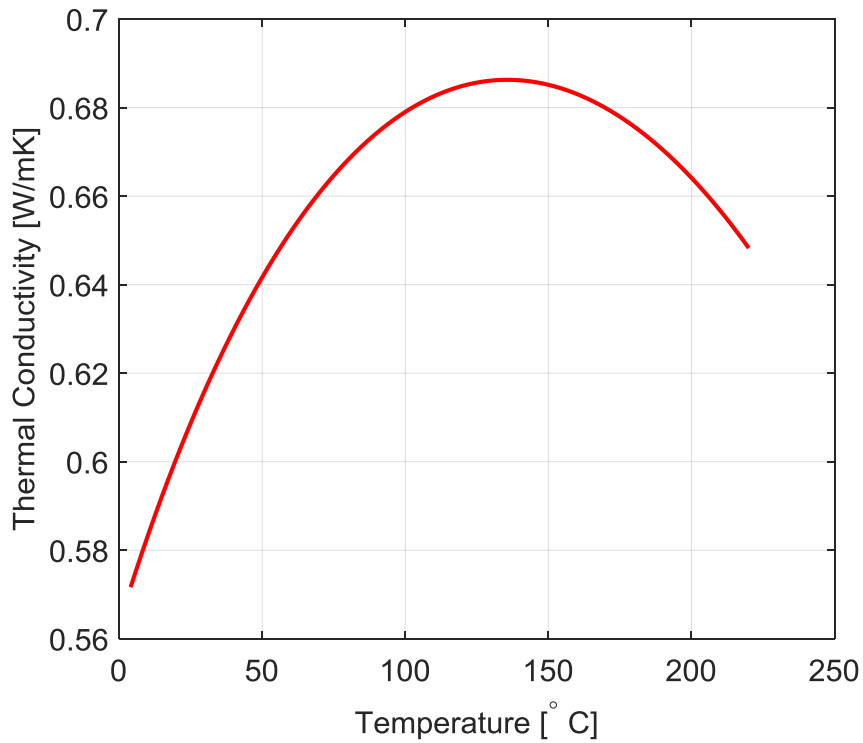


Figure 2. 4 Thermal conductivity of water with temperature.

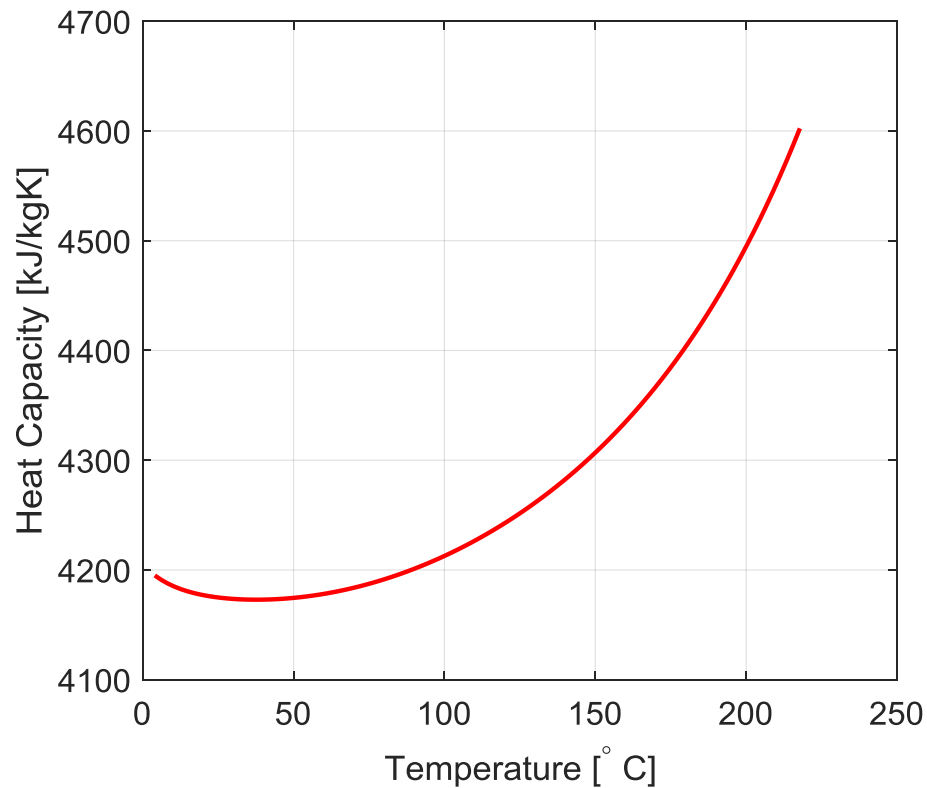


Figure 2. 5 Heat capacity of water with temperature.

2.2.2 Fluid models

For this study the following four ABAQUS based CFD turbulence models [16] were used: large-eddy simulation (LES), k- ϵ Reynolds-averaged Navier-Stokes (RNG), Spalart-Allmaras, and k- ω shear stress transport (SST). The goal was to see which models most accurately capture the thermal stratification effects and, at the same time, do so with computational economy. The LES model resolves the smallest length scales using low-pass filtering while numerically solving the larger scales. LES is generally a good method for solving medium-to-low Reynolds number flows but can become computationally expensive with finer meshes and more turbulent flows. The remaining methods are all RANS models, which incorporate time-averaging to give approximate turbulent flow solutions. The k- ϵ RNG is a two-equation method that is similar to k- ϵ but uses renormalization group methods to renormalize the unsteady Navier-Stokes equations. The renormalization allows the method to better account for effects of the smaller length scales. The equations describing this model are given below:

$$\frac{d}{dt} \int_V \rho k dV + \int_S \rho k (\mathbf{v} - \mathbf{v}_m) \cdot \mathbf{n} dS = \int_S \frac{\mu + \mu_T}{\sigma_k} \nabla k \cdot \mathbf{n} dS + \int_V \tau_{ij} S_{ij} + G_b dV - \int_V \rho \epsilon dV \quad (2.2)$$

$$\begin{aligned}
 \frac{d}{dt} \int_V \rho \epsilon \, dV + \int_S \rho \epsilon (\mathbf{v} - \mathbf{v}_m) \cdot \mathbf{n} \, dS \\
 = \int_S \frac{\mu + \mu_T}{\sigma_\epsilon} \nabla \epsilon \cdot \mathbf{n} \, dS + \int_V C_{\epsilon 1} \frac{\epsilon}{k} \tau_{ij} S_{ij} + C_{\epsilon 3} G_b \, dV - \int_V C_{\epsilon 2} \frac{\rho \epsilon^2}{k} \, dV
 \end{aligned}
 \tag{2.3}$$

Spalart-Allmaras is a one-equation method that is used to solve the transport equation for the turbulent kinematic viscosity. The equation for this model is as follows:

$$\begin{aligned}
 \frac{d}{dt} \int_V \rho \tilde{\nu} \, dV + \int_S \rho \tilde{\nu} (\mathbf{v} - \mathbf{v}_m) \cdot \mathbf{n} \, dS \\
 = \int_V \rho c_{b1} \tilde{S} \tilde{\nu} \, dV - \int_V \rho c_{w1} \left(\frac{\tilde{\nu}}{d} \right)^2 \, dV + \int_V \frac{\rho(1 + c_{b2})}{\sigma} \nabla \{(\mathbf{v} + \tilde{\nu}) \nabla \tilde{\nu}\} \, dV \\
 - \int_V \frac{\rho c_{b2}}{\sigma} \cdot (\mathbf{v} + \tilde{\nu}) \nabla \cdot \nabla \tilde{\nu} \, dV
 \end{aligned}
 \tag{2.4}$$

The SST is a two-equation eddy viscosity model. This method involves use of the k- ϵ model with the k- ω model in an attempt to maximize accuracy. The method can be thought of as using a k- ω type method for near wall treatment of the boundary layer, while using a k- ϵ type model near the free stream. The two equations for this model are as follows:

$$\begin{aligned}
 \frac{d}{dt} \int_V \rho k \, dV + \int_S \rho k (\mathbf{v} - \mathbf{v}_m) \cdot \mathbf{n} \, dS \\
 = \int_S (\mu + \sigma_k \mu_T) \nabla k \cdot \mathbf{n} \, dS + \int_V \tau_{ij} S_{ij} + G_b \, dV - \int_V \beta^* \rho \omega k \, dV
 \end{aligned}
 \tag{2.5}$$

$$\begin{aligned}
 \frac{d}{dt} \int_V \rho \omega \, dV + \int_S \rho \omega (\mathbf{v} - \mathbf{v}_m) \cdot \mathbf{n} \, dS \\
 = \int_S (\mu + \sigma_\omega \mu_T) \nabla \omega \cdot \mathbf{n} \, dS + \int_V \tau_{ij} S_{ij} + C_{\omega 3} G_b \, dV - \int_V \beta \rho \omega^2 \, dV \\
 + \int_V 2(1 - F_1) \rho \sigma_{\omega 2} \frac{1}{\omega} \nabla k \cdot \nabla \omega \, dV
 \end{aligned}
 \tag{2.6}$$

Further information about any of the models is available in Abaqus documentation or most other CFD reference material [17].

2.2.3 Mesh and Boundary Conditions

Dimensions from Rezende's et al. experiment [16] were used to develop the mesh. It should be noted that not all of the necessary dimensions were made available to completely match the experimental setup. The missing dimensions included the bend radius of the pipe and the diameter for the holes. Estimations of those values were used to develop the model. Furthermore, thermocouples were placed at different locations inside of the pipe. These details are not available and are thus not included in the discussed CFD models. The computational domain is composed of a fluid and solid domain. The construction of the two domains allowed for the heat transfer between the water and steel pipe. It should be noted that the reservoir tank was not included in the simulation as it was seen to be too computationally expensive given the computational hardware and software resource available.

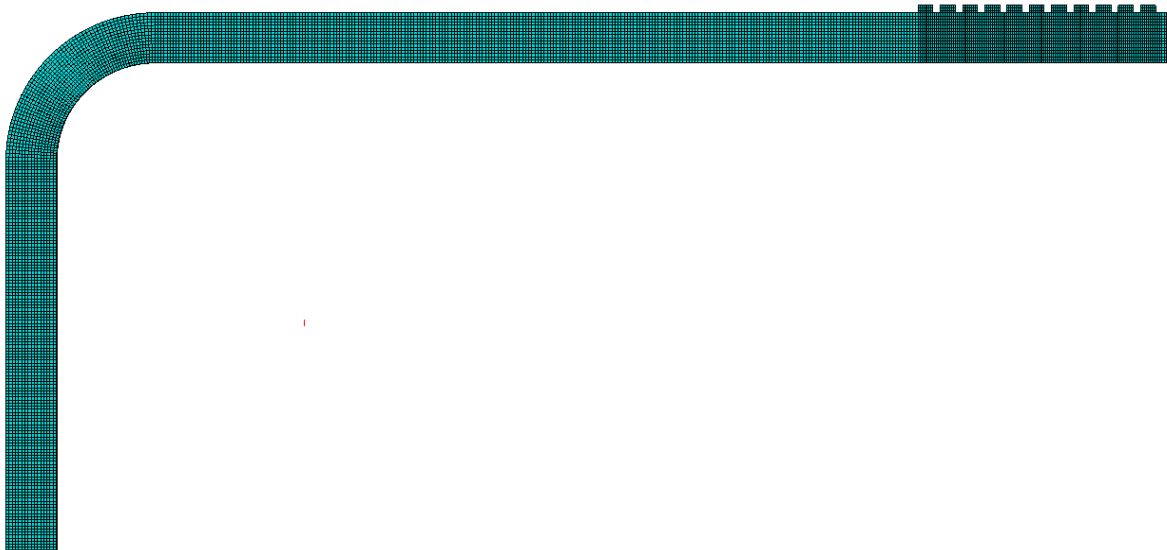


Figure 2.6 Fluid domain mesh.

Both the fluid and solid domain were cut in half by placing a vertical symmetry boundary in the middle of the pipe. Additionally, an inlet boundary was applied, which fixed the inlet mass flow rate at 0.76 kg/s and temperature at 31.7°C. A reference pressure point was placed at the middle of the bend in the pipe and set to a value of 2.11 MPa. The outlet pressure condition on the 11 holes was set to a value equal to the difference in static pressure from the reference point. The outside pipe wall was set to an adiabatic boundary condition. The fluid domain mesh contained 55218 elements and 66404 nodes, while the solid domain mesh contained 58348 elements and 75745 nodes. The mesh had an average aspect ratio of 1.37 with a worst aspect ratio of 4.77. The meshes were made to be structured hexagonal to reduce the computational cost. A cross-section view of the mesh can be seen in Figure 2.6. An adaptive time-step method was used in conjunction with a Courant–Friedrichs–Lewy (CFL) number. A fixed CFL number of 1.4 was used to adaptively change the time-step to maintain the CFL number.

2.3 CFD Model Results

To compare the Abaqus CFD results with the experimental results, three reference temperature measurement points were compared, as seen in Figure 2.1. In the experiment a multitude of thermocouple locations were used, but for this analysis, only the thermocouples in the middle of each monitoring location were considered. All simulations were completed using an 8-core Intel Xeon E5-2630 V3 processor with 16 GB of RAM.

2.3.1 Mesh Dependency

To check for mesh dependency, three meshes were used with the same model. The different mesh characteristics for the fluid domain can be seen in Table 2.1. The LES model was used to check for mesh dependency. Three measurement points from the experiment were used as locations for temperature reference. The temperatures from each mesh were compared to check for mesh dependency. A plot of the comparison is given in Figure 2.7. Mesh 1 had a solution time of 4 hours and 8 minutes, mesh 2 had a solution time of 17 hours and 32 minutes, while mesh 3 had a solution time of 29 hours and 54 minutes. While mesh 3 was the most accurate, it was seen as too expensive computational for the remaining runs. Mesh 2 showed similar results to mesh 3 without the slight temperature variations seen in mesh 1. Figure 2.7 shows very little variation in temperatures with time, indicating that mesh 2 is adequate to complete our computations and check for model dependency.

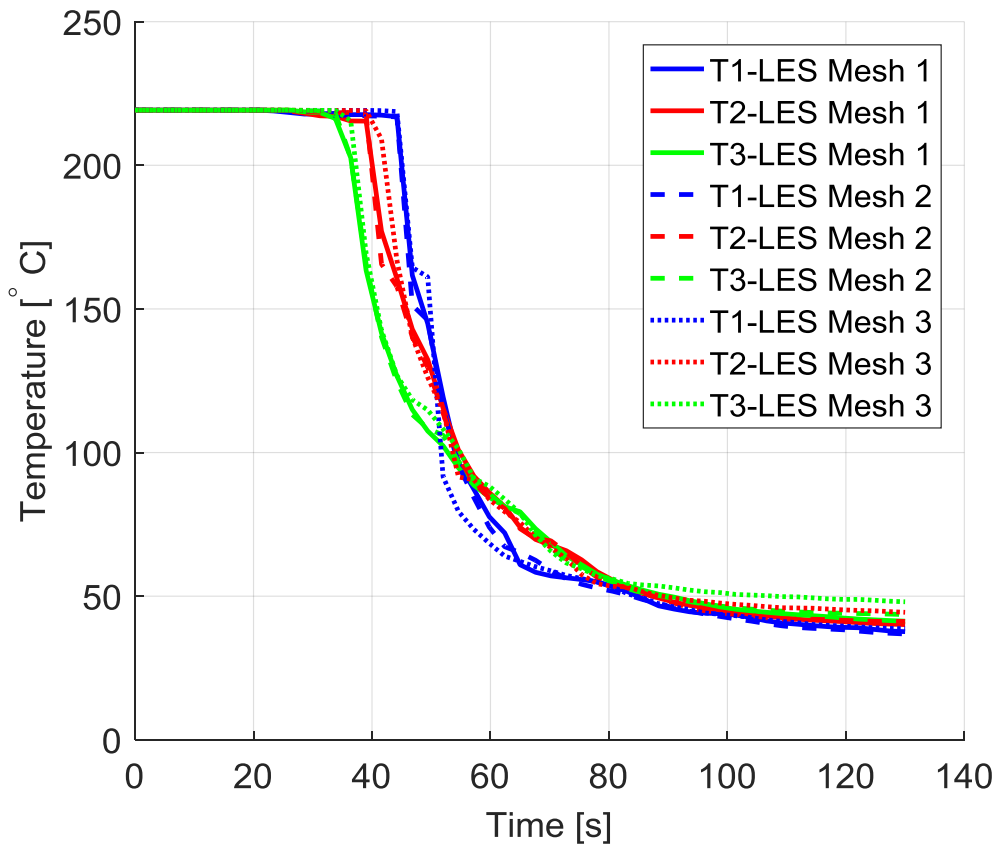


Figure 2.7 LES simulation results versus experimental results for higher density mesh

Table 2. 1 Mesh Characteristics

Mesh	Elements	Nodes
1	54970	71811
2	113566	142149
3	261756	304960

2.3.2 Model Dependency

To check for model dependency, four turbulence models were used. To measure the accuracy of the results, a side-by-side comparison of the experimental results is presented with the numerical results. The mesh used had an average y^+ value of 20.

The first presented turbulence model is the Spalart-Allmaras. The results from this model (Figure 2.8) show the basic general trend of the experimental results but fail to capture the time at which the initial temperature change begins. After around 80 seconds into the simulation, the results begin to closely resemble those of the experiment; however, prior to that there appears to be a bigger difference.

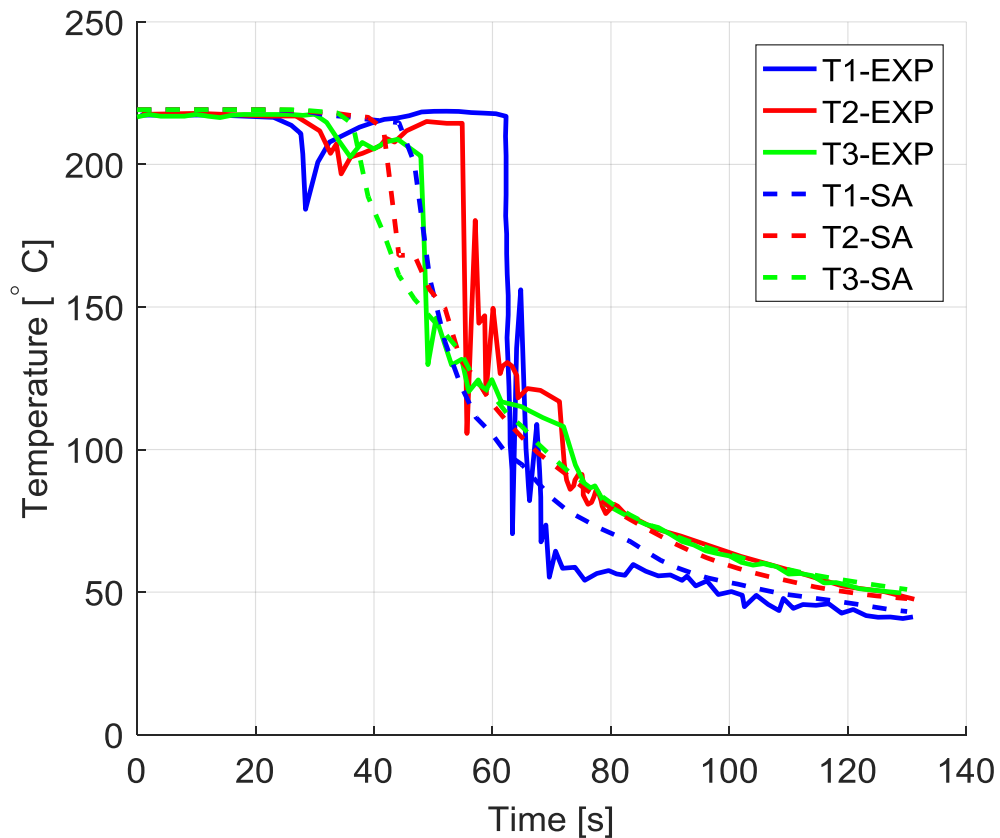


Figure 2. 8 Spalart-Allmaras simulation versus experimental results

The $k-\omega$ SST model results are given in Figure 2.9. They are the least accurate when compared to the results for the other models.

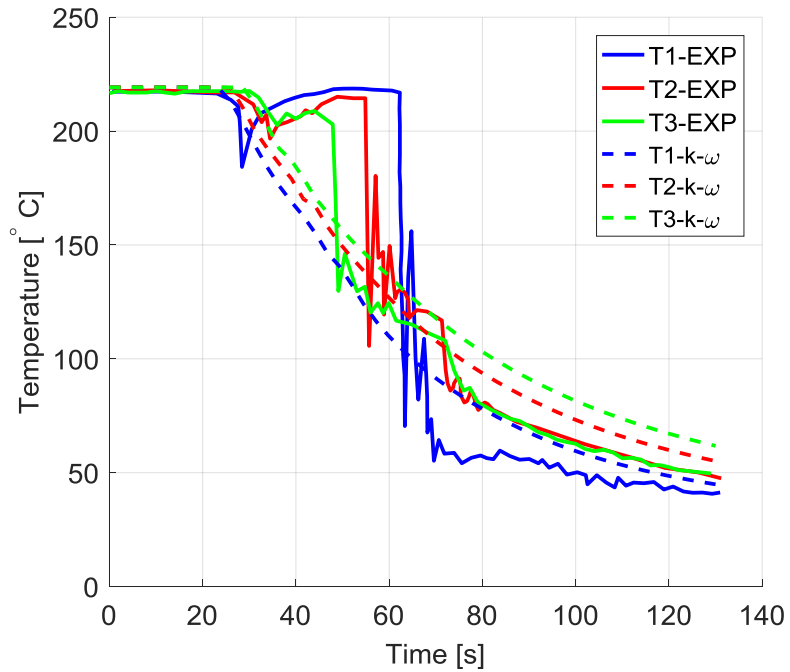


Figure 2. 9 $k-\omega$ SST simulation versus experimental results.

The $k-\epsilon$ RNG model has similar results (Figure 2.10) to the Spalart-Allmaras case, where the simulation results eventually converge to the experimental results.

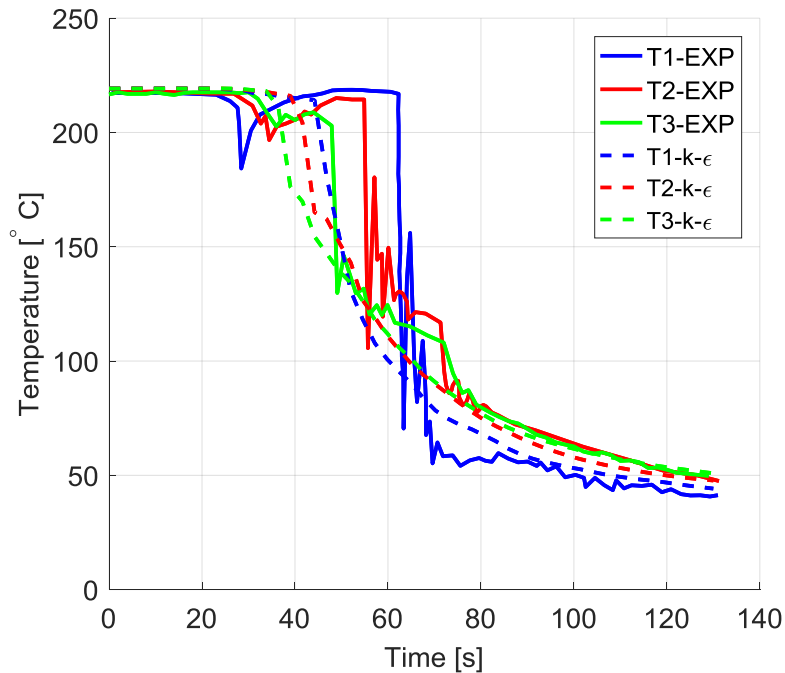


Figure 2. 10 $k-\epsilon$ RNG simulation versus experimental results.

The LES results are shown in Figure 2.11. They better predict the slope of the experiment, but do not accurately acquire the time at which temperature change occurs.

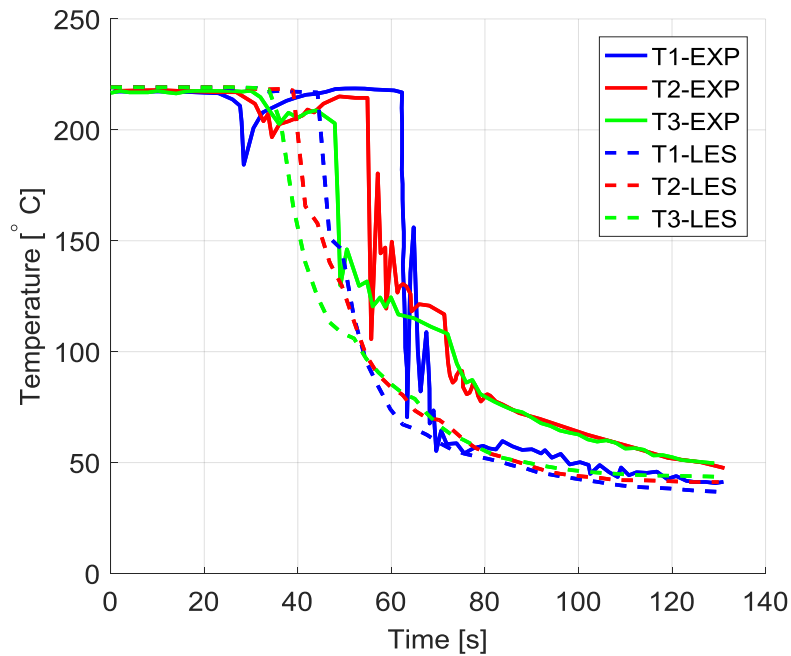


Figure 2. 11 LES simulation results versus experimental results.

Given the above comparisons, it appears that the LES model most accurately captures the trend seen in the experiment. The associated magnitude of the velocity is shown in Figure 2.12, which indicates that as the cold water enters the horizontal section of piping, it quickly moves down to the end of the pipe. A cross-section view of the velocity and temperature distributions with time (from different models) can be seen in Figures 2.13-2.17. Additionally, evident in Figures 2.13-2.17 is that after the cold water hits the wall below the holes, the cold water returns in the direction of the inlet. It is clear from these data that each model varies to some degree. The $k-\omega$ case is much different from all the other models and appears to show the most diffusion. A comparison of these models side by side is provided in Figure 2.17.

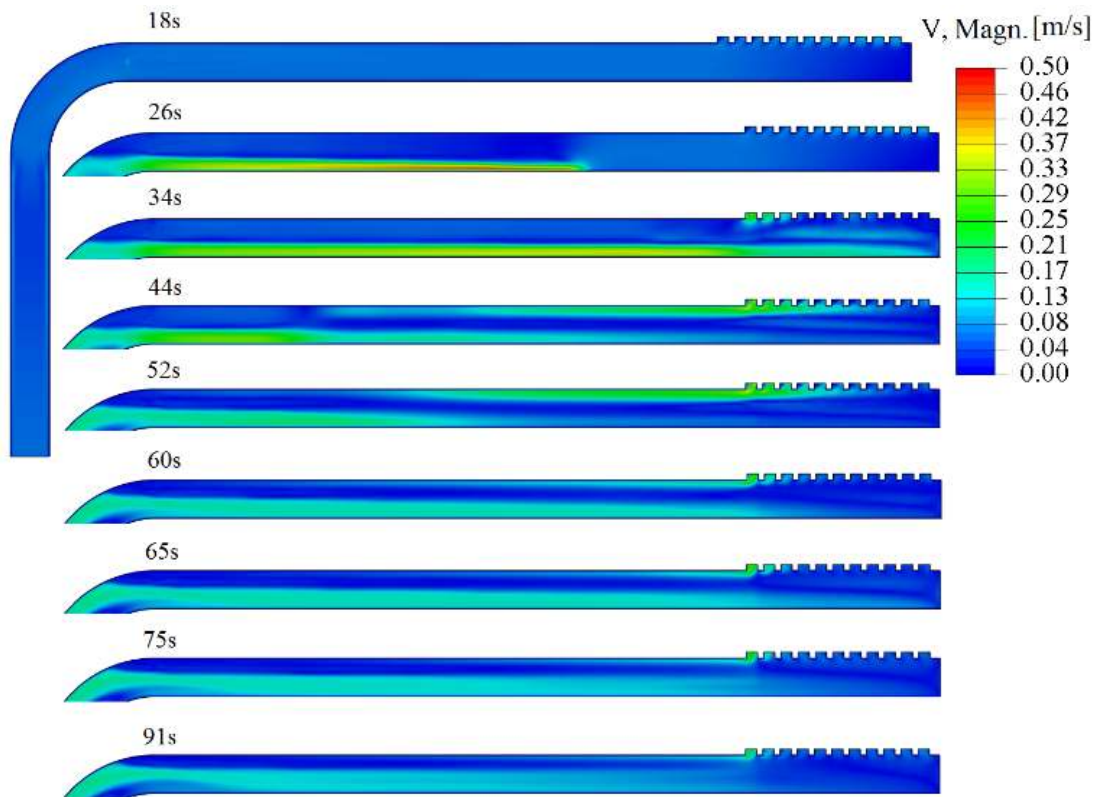


Figure 2. 12 Velocity contour of LES case.

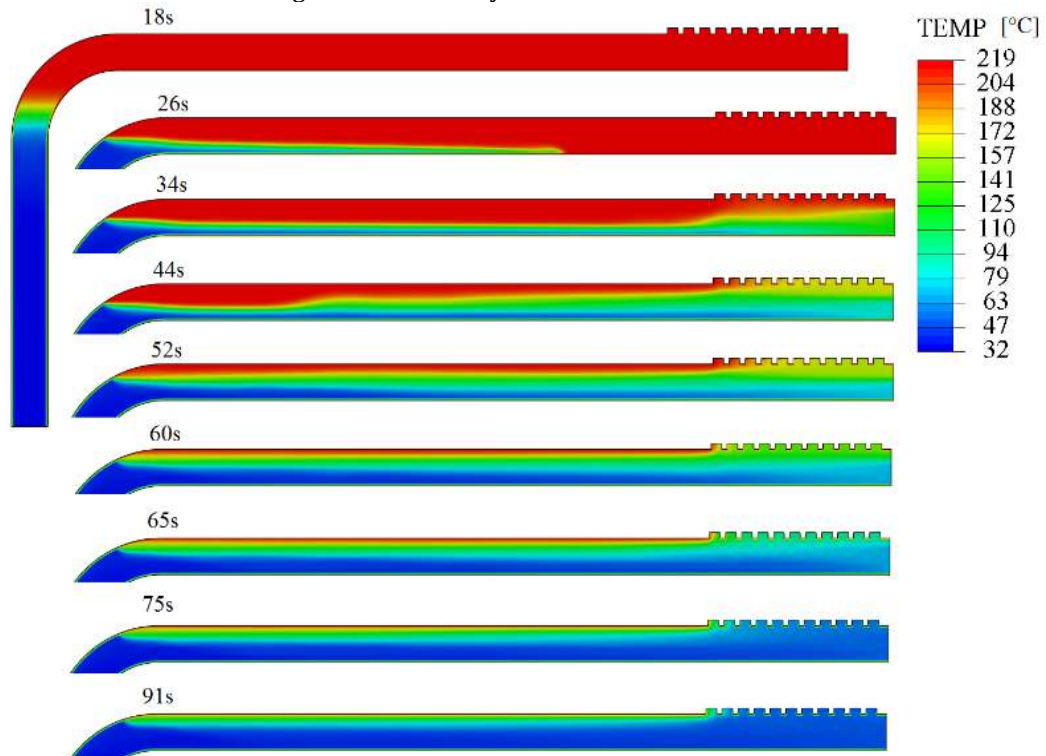


Figure 2. 13 LES simulation cross-section results.

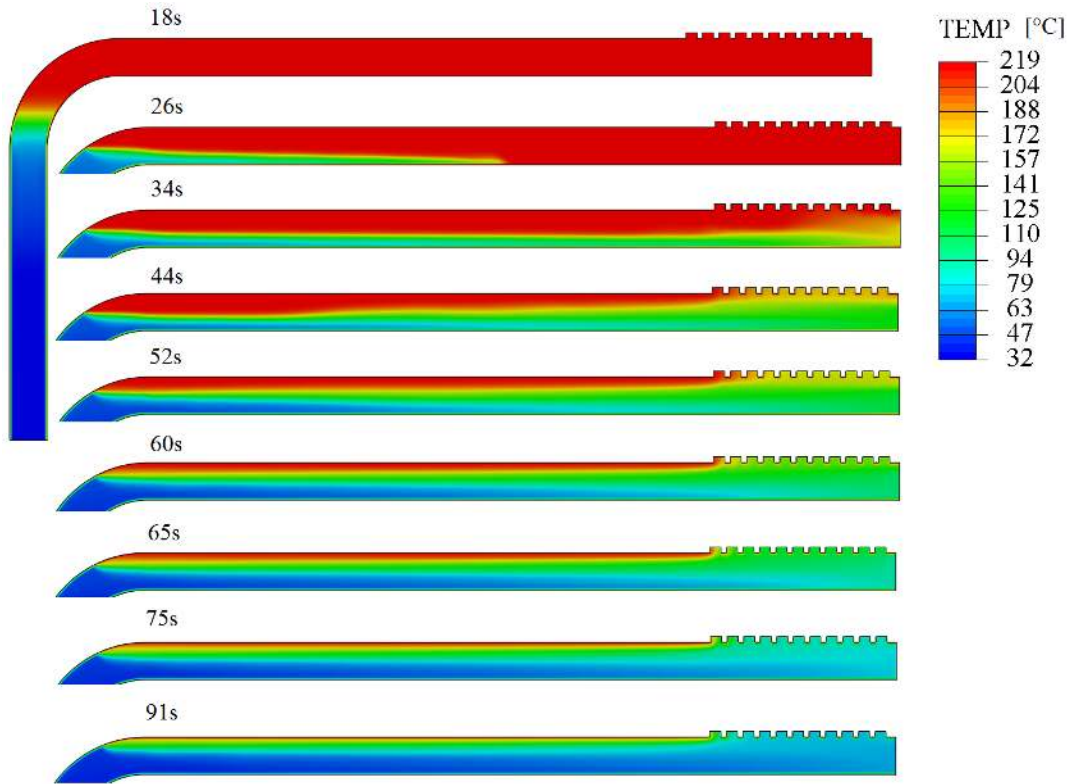


Figure 2.14 k- ϵ RNG simulation cross-section results.

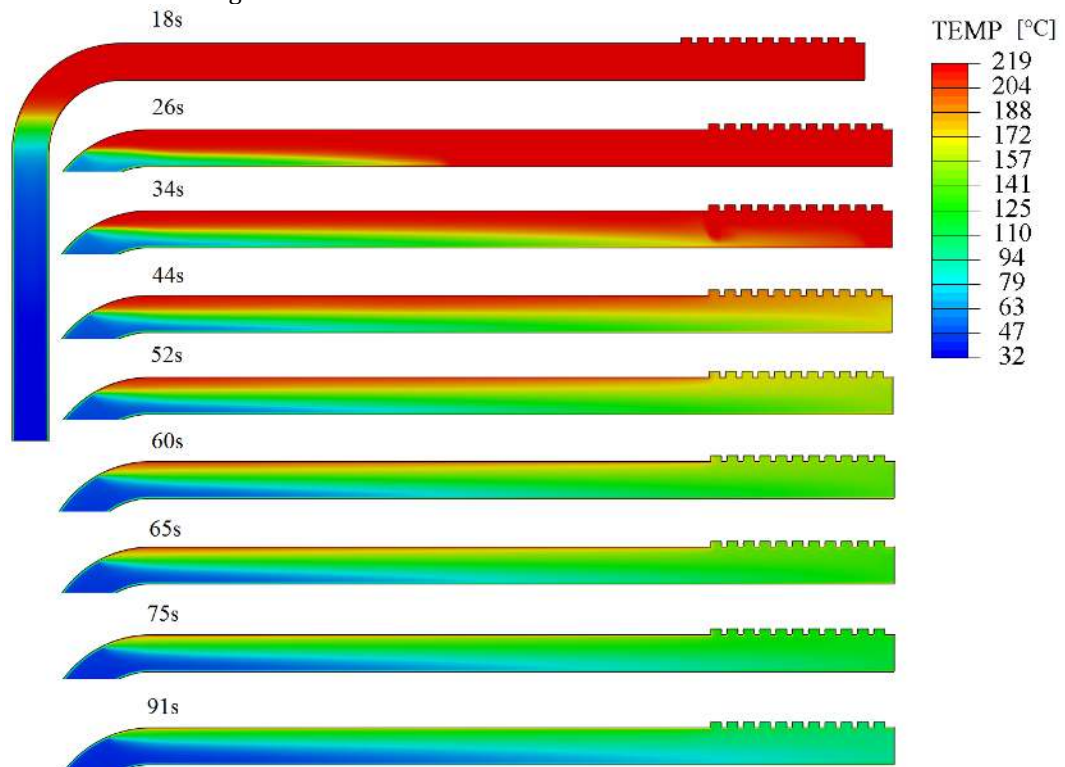


Figure 2.15 k- ω SST simulation cross-section results.

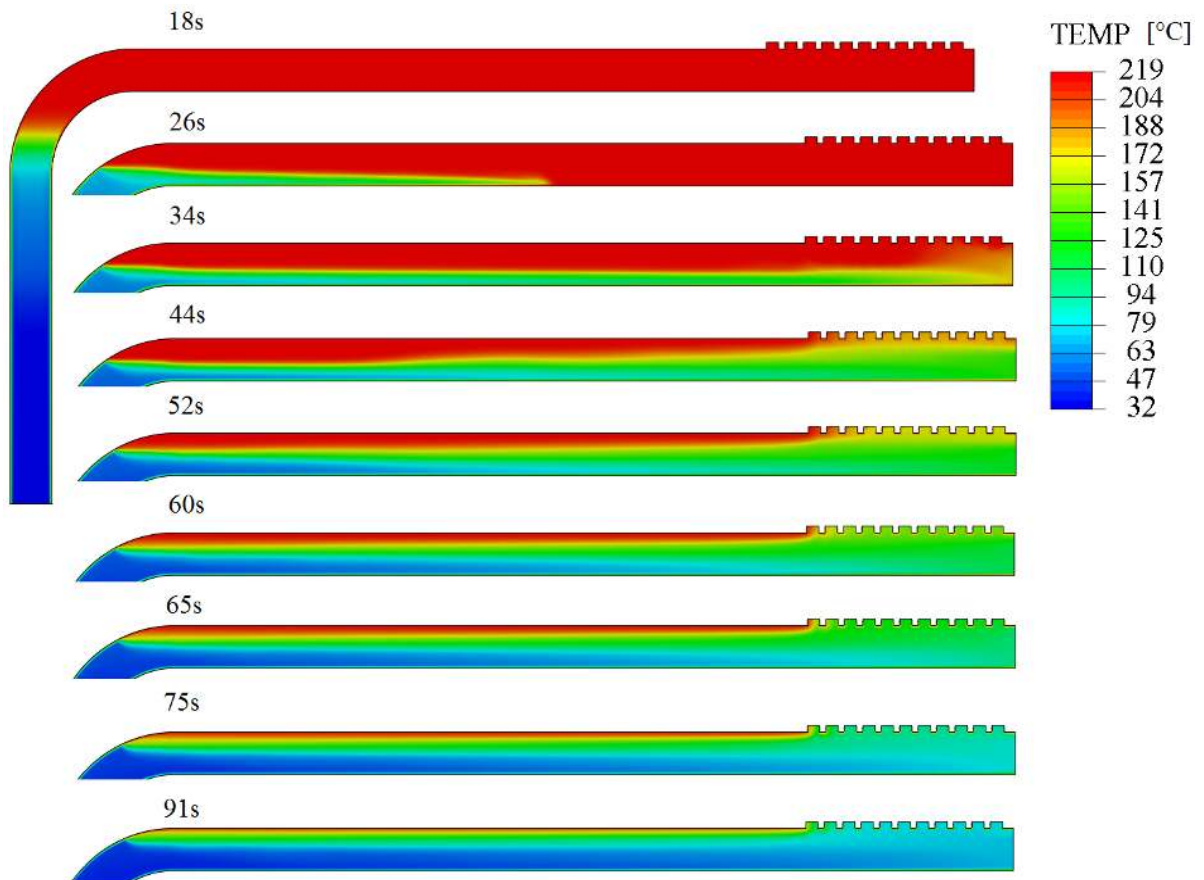


Figure 2. 16 Spalart-Allmaras simulation cross-section results.

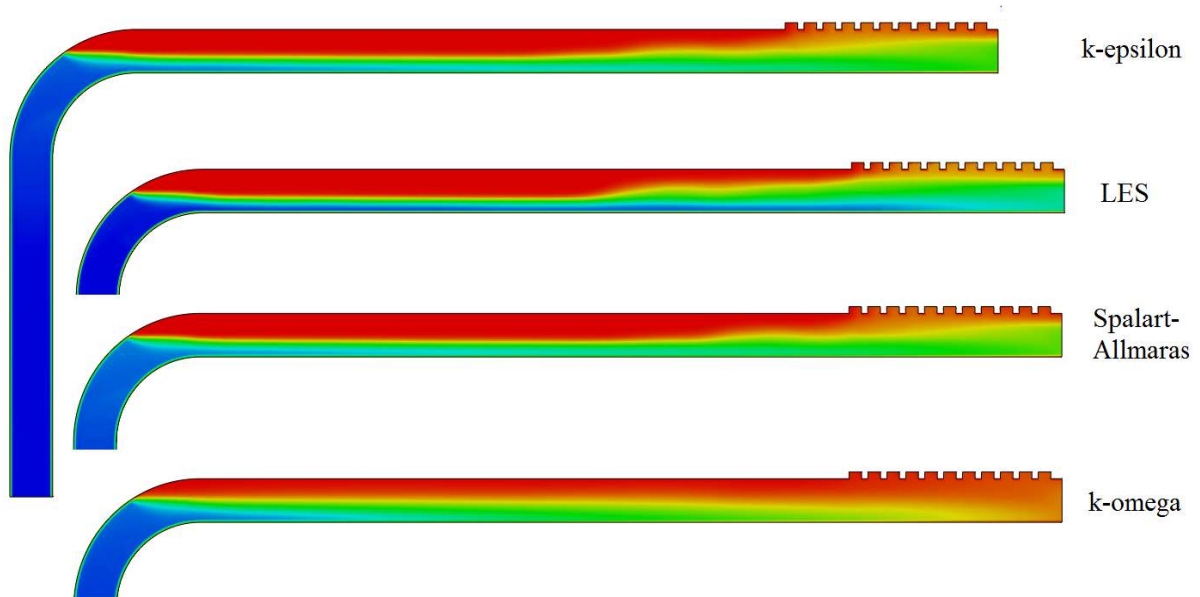


Figure 2. 17 Temperature comparison of different models at 39 s.

In summary, while CFD codes on thermal stratification in surge lines of PWRs have been investigated thoroughly in the literature, there is still a need to benchmark computational results with experimental results. Experimental results performed by Rezende et al. [15] were compared with computational results generated by the commercially available CFD code Abaqus CFD. Results from an analysis of mesh sensitivity and model dependency were presented. The mesh sensitivity study indicated that mesh 2 was accurate enough to provide good results without being too computationally expensive. The mesh sensitivity study showed that each model was in fair agreement, except for the $k-\omega$ SST case. As expected, the LES model provided the best results, which most closely matched the experimental results, but at a higher computational cost. The $k-\epsilon$ RNG model also provided good results with a lower computational cost. This finding is along the line of our earlier reported work [3]. The numerical results show the general qualitative features of the experimental results, but do not capture the time at which initial temperature change occurs. This might be due to other experimental artifacts.

3 Thermal-Mechanical Stress Analysis of PWR Surge Line under Grid-Load-Following Loading Cycles

Earlier we reported [1] the thermal-mechanical stress analysis of a PWR surge line (SL) under design-basis type loading. In this section, we discuss the thermal-mechanical stress analysis under grid-load-following loading conditions. Below we summarize the details of the finite element (FE) model and calculated results with it.

3.1 3D Finite Element Model

We have used the ABAQUS software for the development of a 3D FE model of a typical PWR SL pipe. Figure 3.1 shows the corresponding solid model of the SL and its connection locations with respect to the pressurizer and hot leg (HL). For computational economy, we only considered the central SL pipe. To achieve the most conservative stress analysis results for the structural analysis model, we assumed fixed displacement boundary conditions, both at the pressurizer and HL end of the SL pipe. For the heat transfer analysis, the thermal boundary conditions are discussed below. For the structural analysis, we used eight-noded linear brick element C3D8, and for the heat transfer analysis, we used eight-noded linear brick element DC3D8. Figure 3.2 shows an example hexahedral mesh for the SL pipe. The structural analyses were performed for elastic and elastic-plastic material properties. To compare the structural analysis results with isothermal fatigue test (at 300 °C) results, we used the isothermal material properties at 300 °C. The associated material properties can be found in Table 5.1 and in our earlier publication [4]. For the heat transfer analysis, we used the temperature-dependent material properties that can be found in [4].

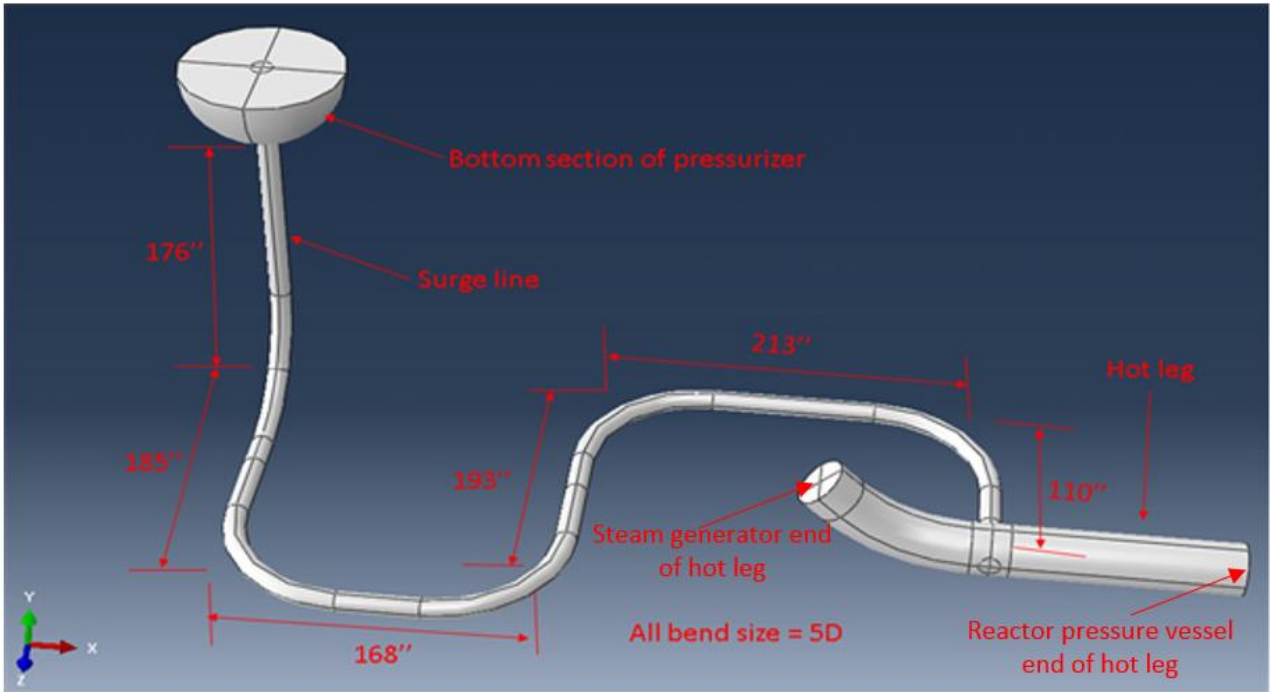


Figure 3. 1 3D solid model of surge line that connects the hot leg and pressurizer [4]

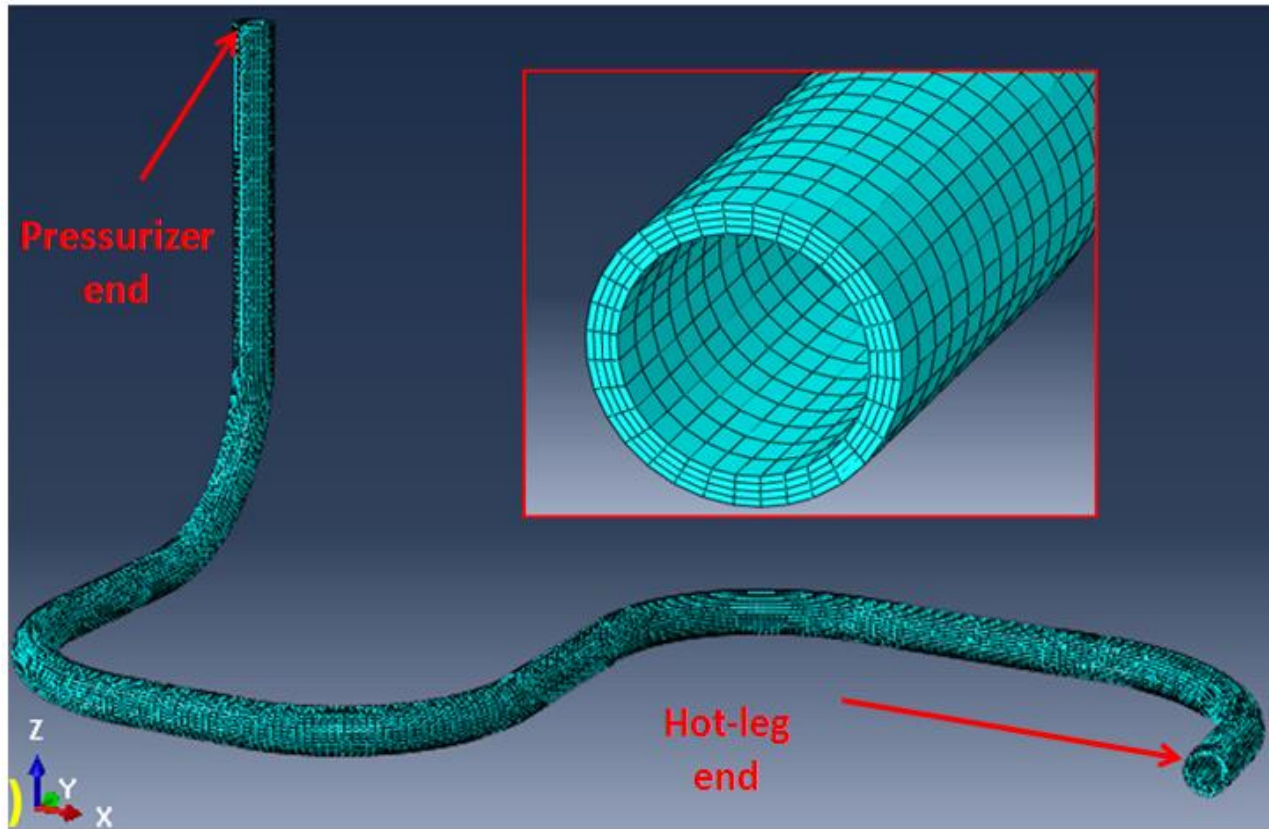


Figure 3. 2 3D finite element model of surge line for heat transfer and thermal-mechanical stress analysis [4]

3.2 Thermal Boundary Conditions

For the heat transfer analysis, we require input for the temperature boundary conditions (BC) at both ends of the SL pipe as well as the inside and outside surfaces of the SL pipe. Ideally, these input boundary conditions can be estimated from the output of SL fluid flow thermal-hydraulics or computational fluid dynamics (CFD) model results. In section 2 we discussed the results from preliminary CFD models. The purpose was to select appropriate CFD modeling techniques for thermal stratification modeling in an SL pipe. We validated our CFD modeling strategy in section 2 for a transient experimental loading case. In our earlier publication [4], we had discussed the CFD results for the SL pipe shown in Figure 3.2 for different transient cases. However, the full fuel cycle CFD model of the SL pipe is still under development. Instead, for the heat transfer analysis model discussed in this report, we applied simplified thermal boundary conditions by assuming the temperature histories at both ends of the SL pipe and its inside and outside surfaces. The full-cycle temperature BCs were obtained by combining the separately obtained temperature BCs during a typical four-loop type PWR heat-up, power operation, and cool-down. To determine the temperature BC during heat-up and cool-down operations, we followed the heating and cooling rate of a coolant loop as given in an EPRI document [18]. For example, the EPRI document shows that during a typical heat-up operation, the coolant loop has to be heated at a rate of 10 °F/hr HU from 80 °F to 160 °F, then 23 °F/hr HU to 183 °F. Next, the temperature was held at 183 °F for 10.5 hours, then increased at 33 °F/hr to 330 °F, then held at 330 °F for 2.3 hours. Finally, the temperature was increased at 33 °F/hr to 550 °F (287.8 °C), which is the hot standby temperature. For this case, a similar heating rate for the HL is followed with starting temperature of 80 °F (26.67 °C) up to the hot standby temperature of 550 °F (287.8 °C). The full-power operation maximum temperature for the HL and pressurizer is considered equal to 619.52 °F (326.4 °F) and 657.06 °F (347.3 °C), respectively. For the discussed loading cycle, a heating rate of 33 °F/hr was applied to heat up the HL temperature from hot standby to full power. During cool-down, a cooling rate of 33 °F/hr was followed to reduce the HL temperature from the full-power to hot-standby condition with a temperature of 550 °F (287.8 °C).

In our previous reported work [1] for design-basis loading condition models, we considered a flat HL temperature during full power operation. By contrast, in the present work for grid-load-following loading case, we considered a fluctuating temperature for the HL, which was estimated from the reactor operation time versus rated power fluctuation data given in a literature [19-22]. These data (Figure 3.3) were obtained in a typical EDF reactor. As shown in Figure 3.4, we plotted the associated reactor operation time versus HL temperature during the power operation. The grid-load-following power operation was followed by cool-down of the HL at a rate of 75 °F/hr from 550 °F (287.8 °C) to 250 °F (121.1 °C), then 46 °F/hr to 175 °F (79.4 °C). The temperature was held at 175 °F (79.4 °C) for 12 hours, then cooled down at 26 °F/hr to 120 °F (48.9 °C), then 6.8 °F/hr to 80 °F (26.67 °C). The temperature history of the pressurizer was estimated by back calculating the temperature for the saturation pressure history given in the EPRI document [18]. The maximum temperature of the pressurizer was considered equal to 657.06 °F (347.3 °C) at the saturation pressure of 2252.4 psi (15.53 MPa). The estimated HL and pressurizer temperature histories were applied to the HL and pressurizer end of the SL pipe. In addition, the inside wall of the SL pipe was subjected to the average of the HL and pressurizer temperature, whereas the outside wall of the SL pipe was subjected to adiabatic temperature boundary conditions. Figure 3.5 shows the corresponding temperature histories used as temperature boundary conditions during the heat transfer analysis.

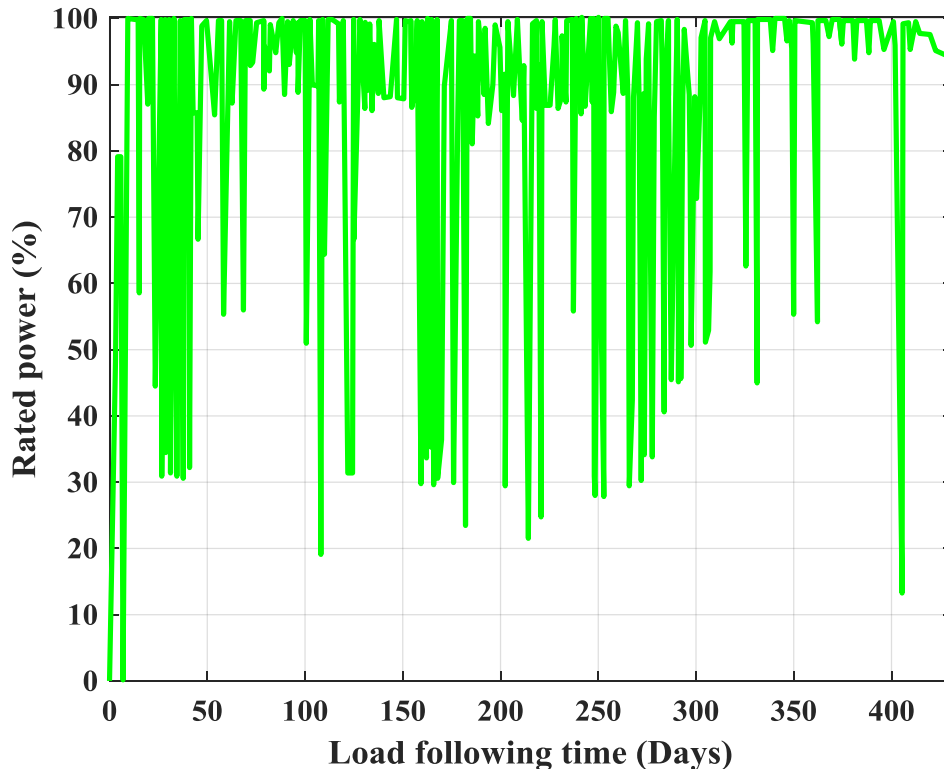


Figure 3. 3 Load following time versus rated power for a typical EDF reactor[19-20]

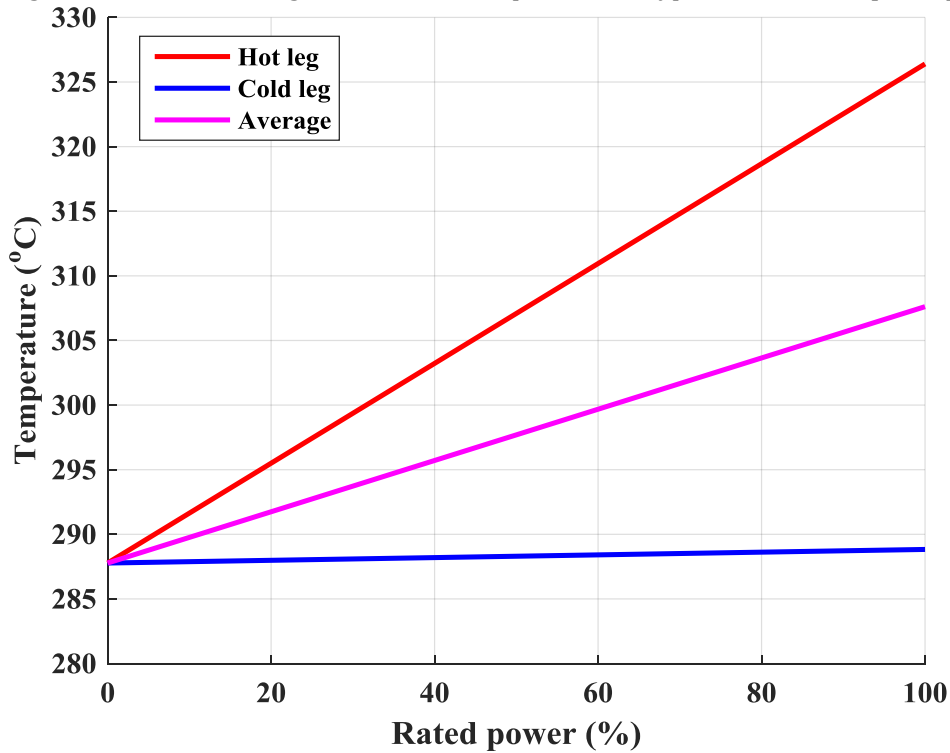


Figure 3. 4 Rated power versus temperature data used for estimating the temperature boundary condition during grid-load-following power operation

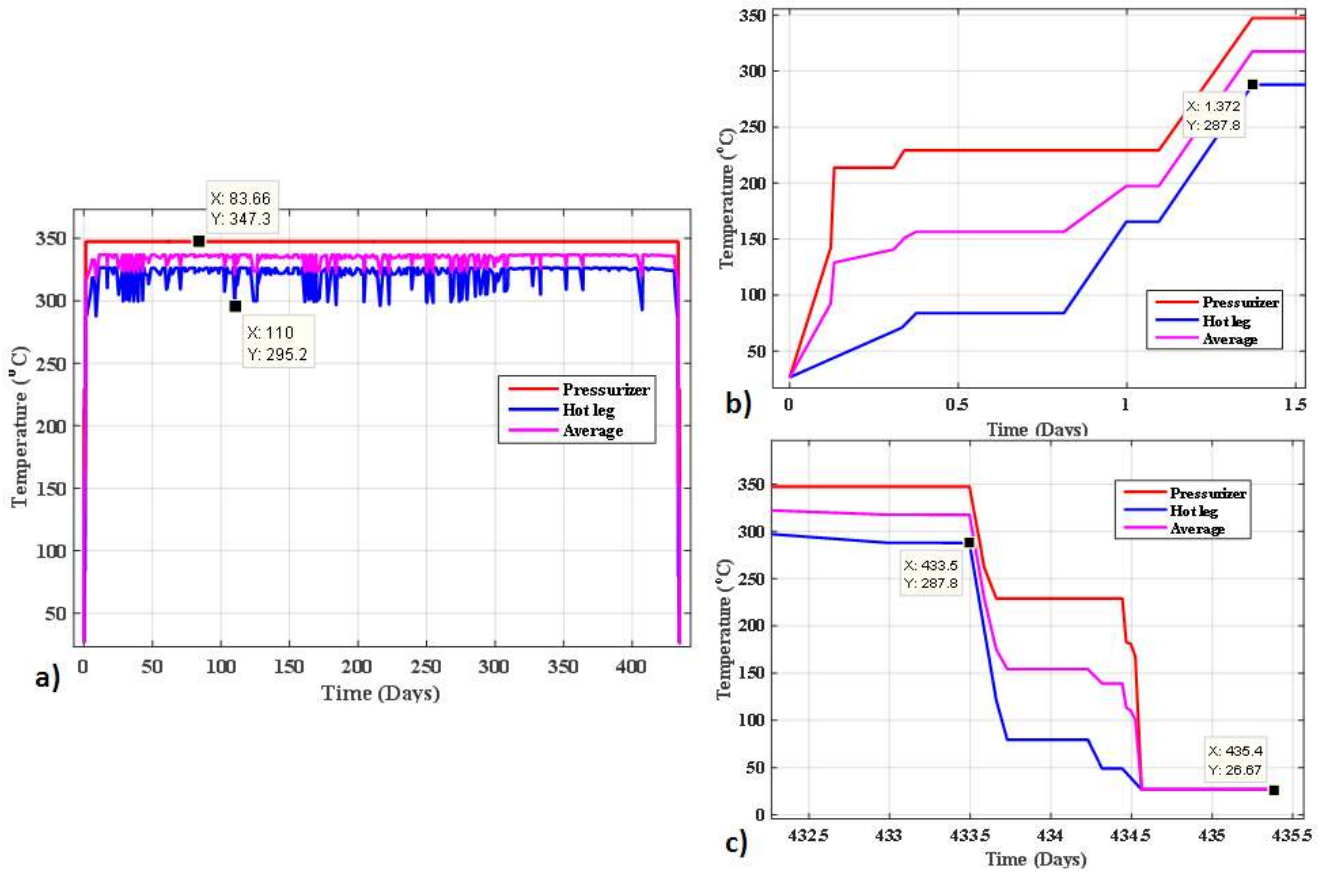


Figure 3.5 Combined (heat-up, power operation, and cool-down) temperature boundary conditions applied to heat transfer analysis model of SL under a grid-load-following loading cycle: (a) full cycle, (b) during heat-up, and (c) during cool-down.

3.3 Heat Transfer Analysis Results

A heat transfer analyses for grid-load-following loading cycles was performed with the SL FE model shown in Figure 3.2. This analysis used the temperature boundary conditions shown in Figure 3.5 to estimate the nodal temperatures that can be passed to the subsequent structural analysis FE models. Figure 3.6 shows the simulated temperature history at typical nodes near the pressurizer end, mid-section, and HL end of the SL. Figure 3.7 is a magnified version of Figure 3.6 showing temperature fluctuations during power operation. This figure shows that the HL end temperature varies from 295.2 °C to 326.3 °C. In the subsequent discussion of the FE based thermal-mechanical results and the corresponding experimental results, we will examine how this temperature variation affects the resulting stress, strain, and overall fatigue life.

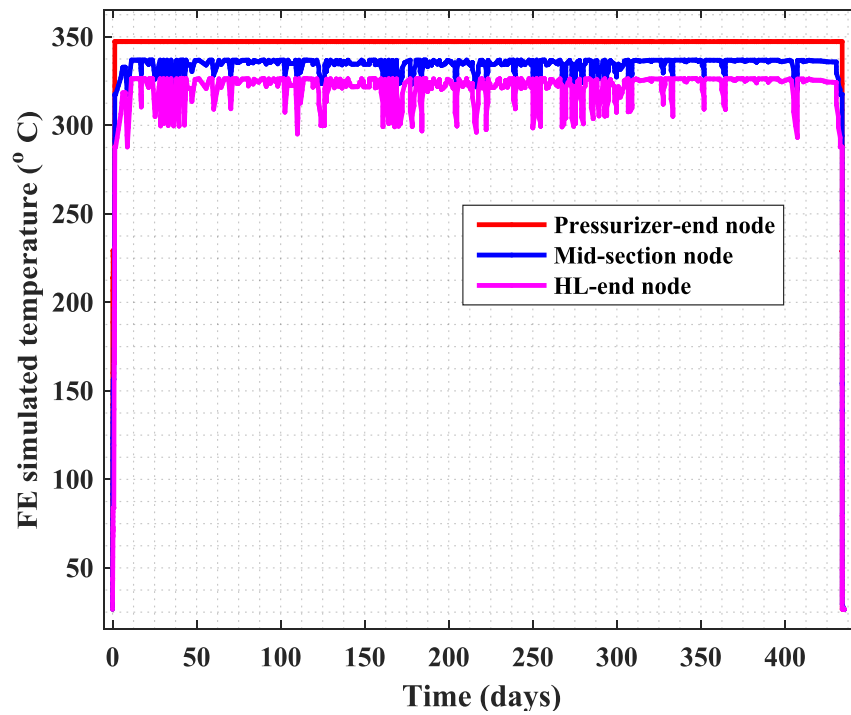


Figure 3. 6 Simulated temperature history of full grid-load-following loading cycle (heat-up, power operation, and cool-down) at typical FE nodes near pressurizer end, mid-section, and HL end of SL.

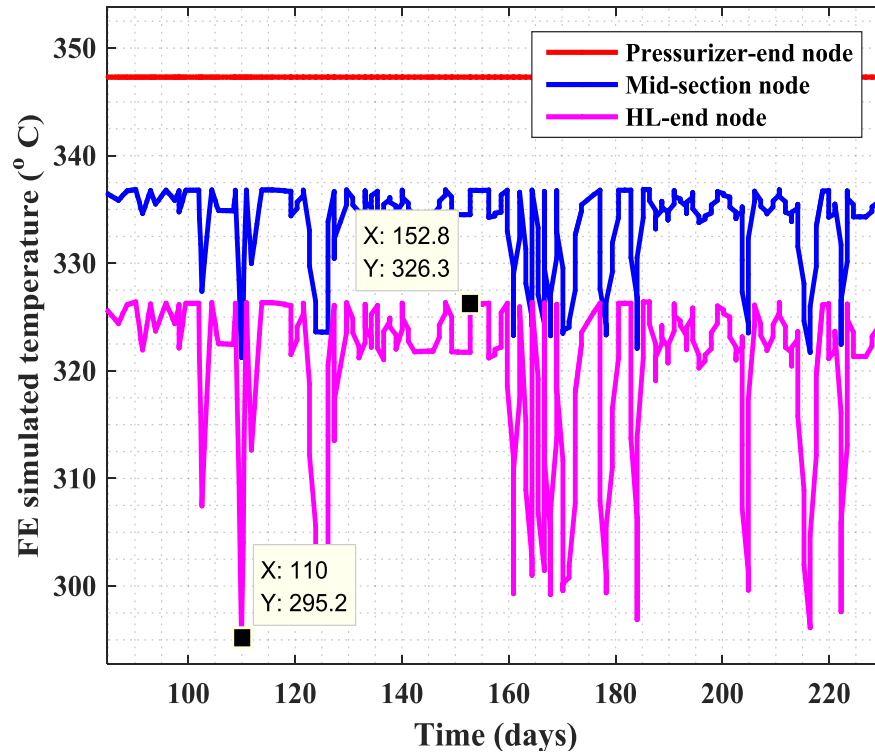


Figure 3. 7 Magnified version of Figure 3.6 during power operation.

3.4 Thermal-Mechanical Stress Analysis Results

Structural analyses were performed by using the nodal temperatures estimated from the above heat transfer simulation. Both elastic and elastic-plastic analyses were performed to show the importance of performing elastic-plastic analysis compared to the elastic analysis. In general, the elastic-analysis results are widely used for fatigue evaluation. We also used these results for end-of-life prediction based on ASME code and NUREG-6909 (discussed in section 5). The structural analyses results for both elastic and elastic-plastic models are discussed below.

3.4.1 Elastic stress analysis results

An elastic analysis was performed to simulate the time-dependent stress-strain in SL pipe subjected to the grid-load-following thermal loading shown in Figure 3.5. For this elastic analysis case, Figure 3.8 shows the elastic FE simulated time-dependent Tresca stress ($\sigma_{\max.prin.} - \sigma_{\min.prin.}$), Von Mises stress (σ_{Mises}), and the stress component along the vertical direction (σ_{33}) at the centroid of a typical element near the pressurizer end. Figure 3.9 shows the corresponding time-dependent maximum principal stress ($\sigma_{\max.prin.}$) and minimum principal stress ($\sigma_{\min.prin.}$). Figure 3.8 shows that the maximum Von Mises stress is 918 MPa, where the corresponding Von Mises stress amplitude is $918/2 = 459$ MPa. For the fatigue life estimation, the ASME code suggests use of the stress amplitude based on the principal stress components. With the Figure 3.9 results and ASME code criteria, the maximum stress amplitude (which is the equivalent of shear stress amplitude) is equal to

$$(1/2) \times (\sigma_{Max.prin} - \sigma_{Min.prin}) = (1/2) \times (341 - (-705)) = 523 \text{ MPa}$$

From both methods of stress amplitude calculation, the amplitude calculation based on the principal stress component is more conservative and is thus used for further fatigue evaluation (discussed in section 5). This choice is consistent with the ASME code suggestion. Figure 3.10 shows the time-dependent Von-Mises stress rate ($\dot{\sigma}_{Mises}$) history, with a maximum stress rate of approximately 0.1803 MPa/s. This type of rate information will help to select the appropriate stress rate while conducting a stress-controlled fatigue evaluation test.

Figure 3.11 shows the elastic FE simulated calculations for time-dependent total strain (ϵ_{33}^{to}), thermal strain (ϵ_{33}^{θ}), and mechanical strain (ϵ_{33}^{me}) components along the vertical direction and at the centroid of a typical element near the pressurizer end. The curves show that the total, thermal, and mechanical strains return to their starting values at the end of the loading cycle. Thermal strain returns to its starting value because of the linear calculation of the thermal strain in the FE model. The return of the total and mechanical strains to their original values is because of the linear elastic FE analysis. However, this behavior may not be the case for realistic elastic-plastic FE model results (as shown in section 3.4.2). Figure 3.12 shows the simulated time-dependent maximum principal strain ($\epsilon_{\max.prin.}$) and minimum principal strain ($\epsilon_{\min.prin.}$). Figure 3.13 shows the elastic FE simulated along the vertical direction for mechanical strain rates ($\dot{\epsilon}_{33}^{me}$), with a maximum possible strain rate of 7.12×10^{-5} %/s. Figure 3.14 shows the hysteresis curves $\epsilon_{33}^{to} \sim \sigma_{33}$ and $\epsilon_{33}^{me} \sim \sigma_{33}$ and their comparison with the tensile test strain~stress curve for 300 °C. Figure 3.15 shows the hysteresis curves $\epsilon_{33}^{to} \sim \sigma_{Mises}$, $\epsilon_{33}^{me} \sim \sigma_{Mises}$, and

$\epsilon_{33}^{ms} \sim \sigma_{Tresca}$ and comparison with the tensile test strain~stress curve for 300 °C. Figures 3.14 and 3.15 clearly show that the simulated strain versus stress curves are in no way comparable to the tensile test strain~stress curve. Although elastic stress analysis results are mandated for ASME code-based estimation of in-air condition fatigue and NUREG-6909 based estimation of PWR environment fatigue life (results discussed in section 5), the results in Figures 3.14 and 3.15 show why it is important to perform the elastic-plastic stress analysis.

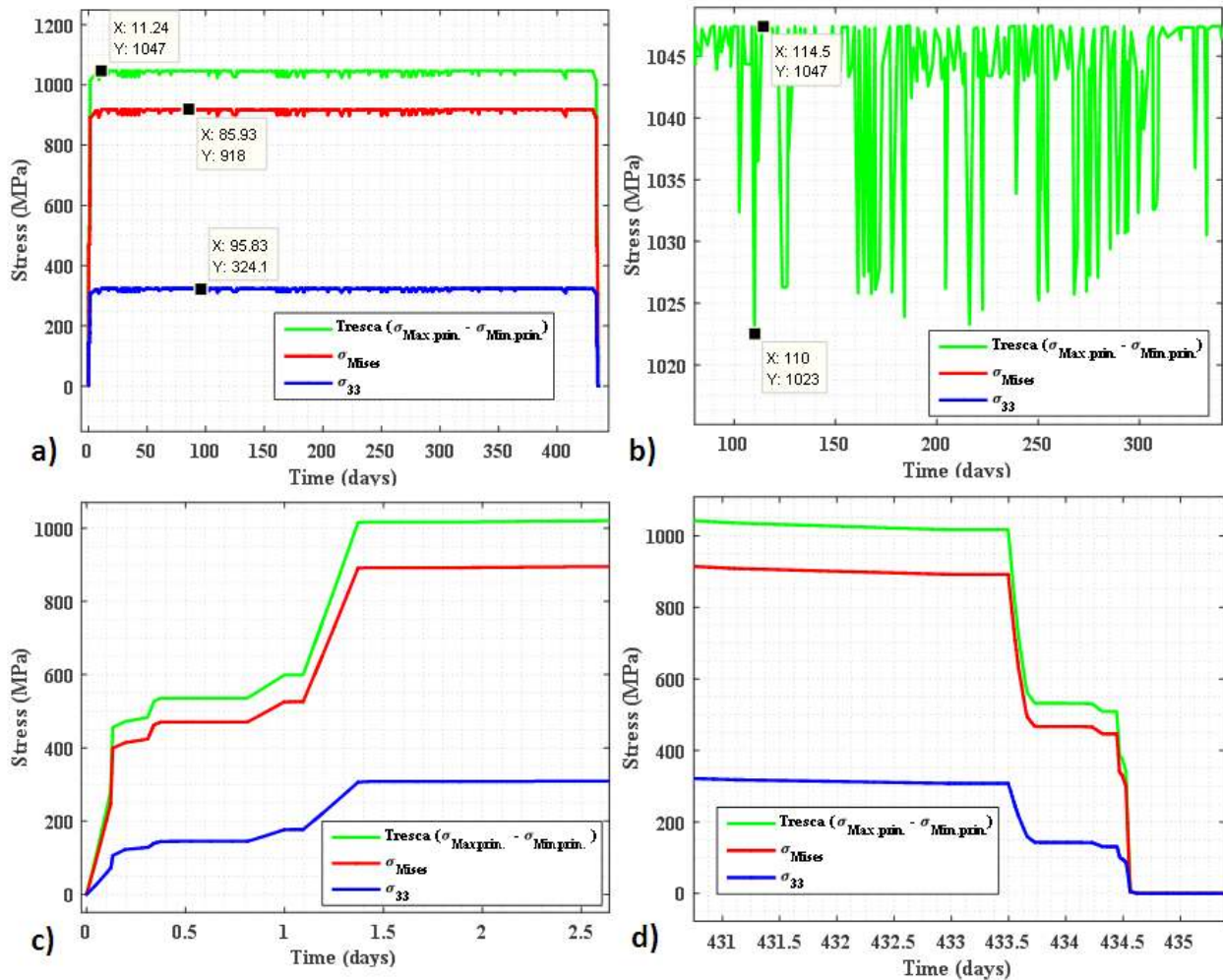


Figure 3.8 The elastic FE simulated time-dependent Tresca stress ($\sigma_{max.prin.} - \sigma_{min.prin.}$), Von-Mises stress (σ_{Mises}) and stress component along the vertical direction (σ_{33}) at the centroid of a typical element near pressurizer end: (a) under full cycle, (b) during power operation (c) during heat-up, and (d) during cool-down.

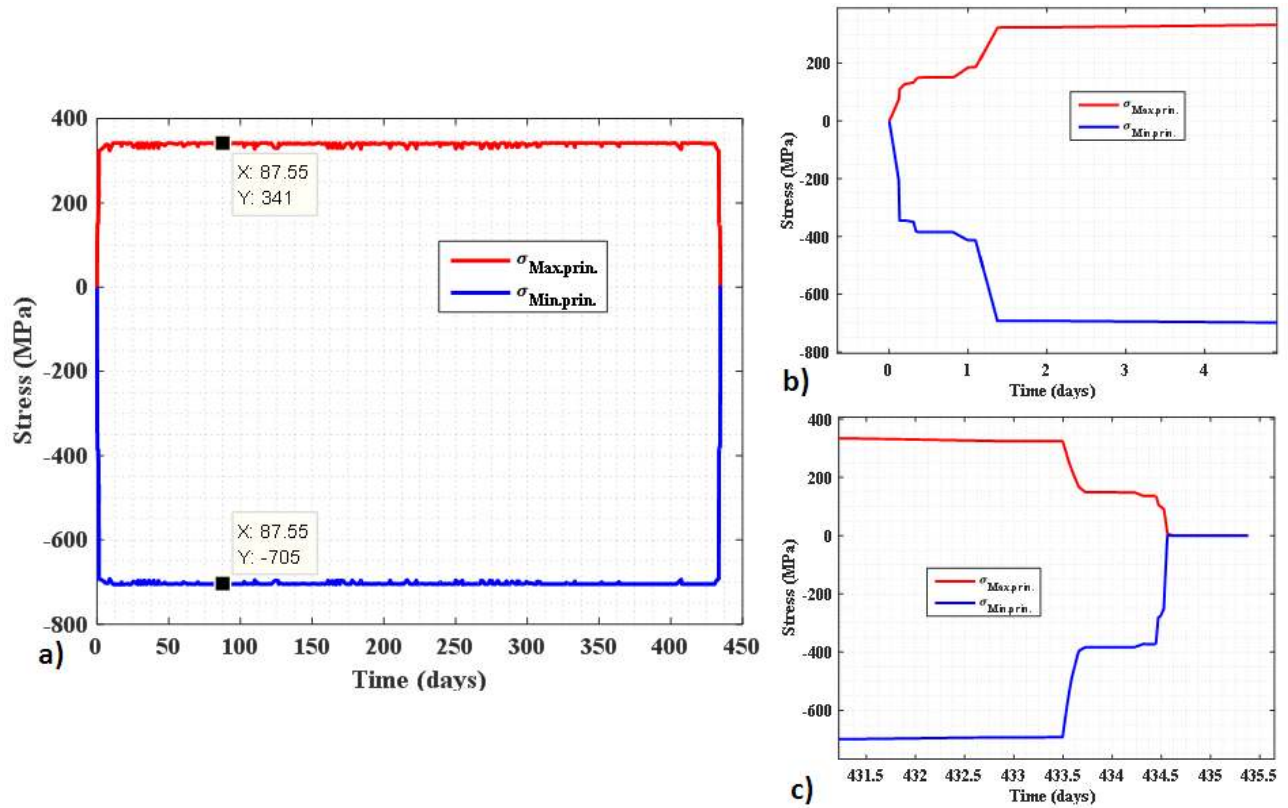


Figure 3.9 The elastic FE simulated time-dependent maximum principal stress ($\sigma_{\max.prin.}$) and minimum principal stress ($\sigma_{\min.prin.}$) at the centroid of a typical element near pressurizer end: (a) under full cycle, (b) during heat-up, and (d) during cool-down.

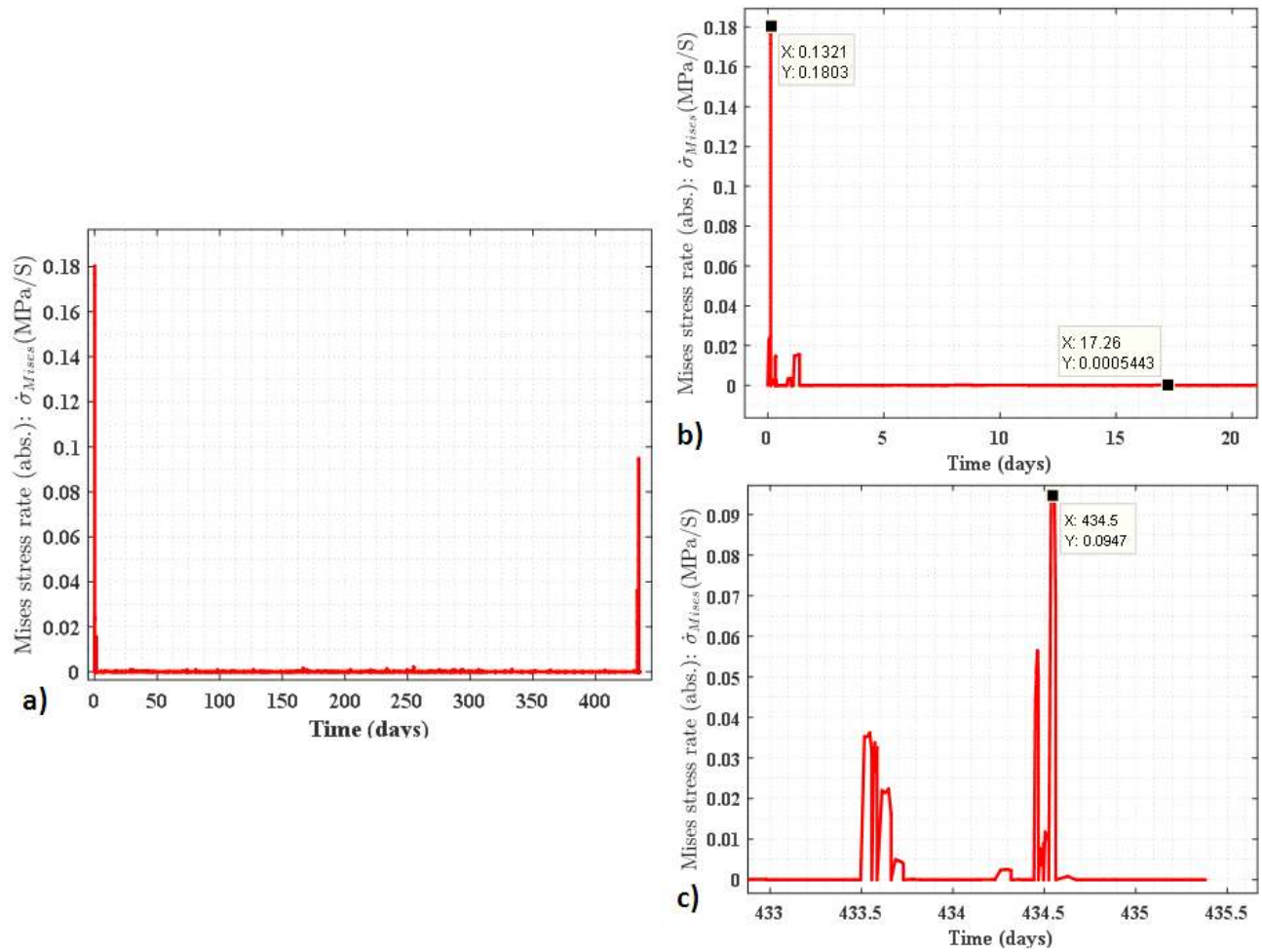


Figure 3.10 The elastic FE simulated time-dependent Von-Mises stress rate ($\dot{\sigma}_{Mises}$) at the centroid of a typical element near pressurizer end: (a) under full cycle, (b) during heat-up, and (c) during cool-down.

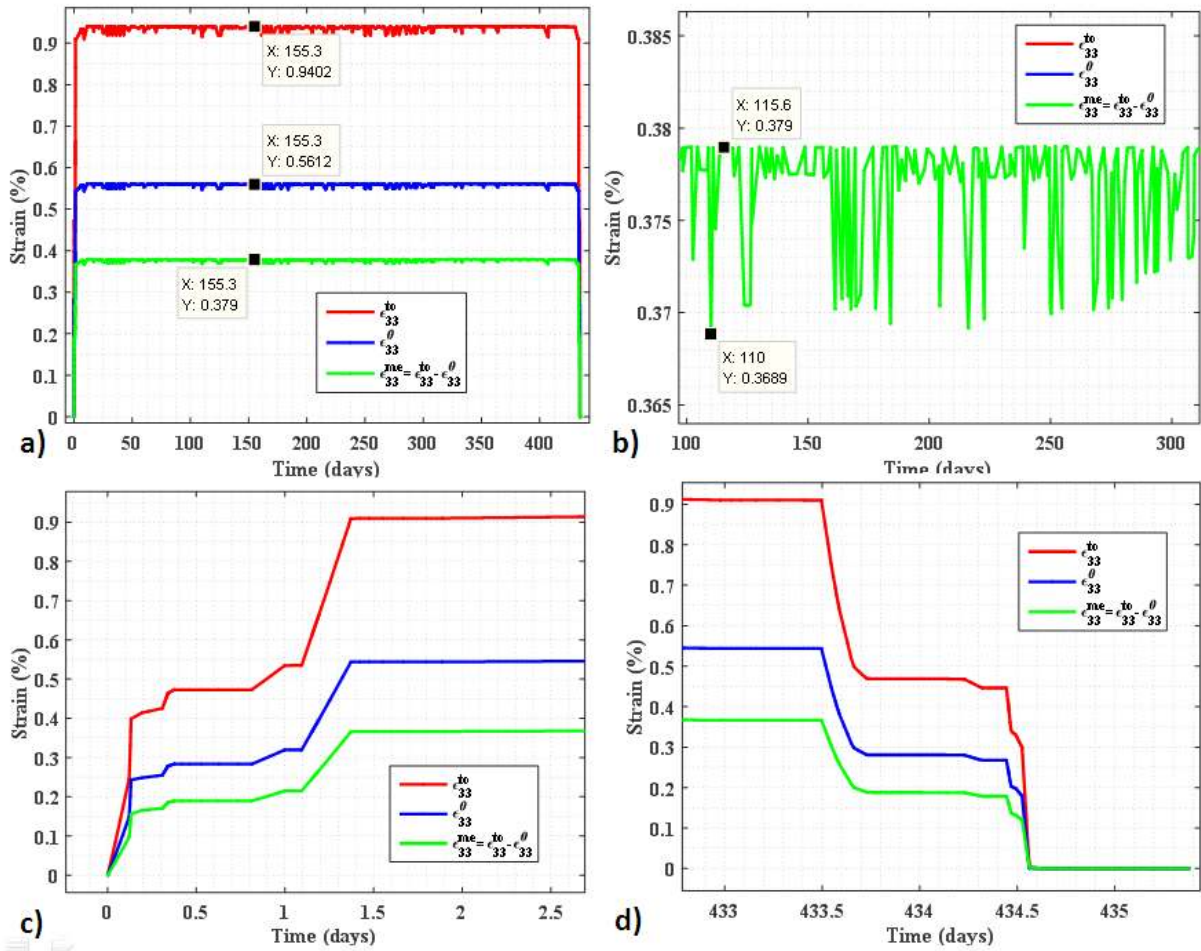


Figure 3.11 The elastic FE simulated time-dependent total strain (ϵ_{33}^{to}), thermal strain (ϵ_{33}^{θ}), and mechanical strain (ϵ_{33}^{me}) components along the vertical direction and at the centroid of a typical element near pressurizer end: (a) under full cycle, (b) during power operation (c) during heat-up, and (d) during cool-down.

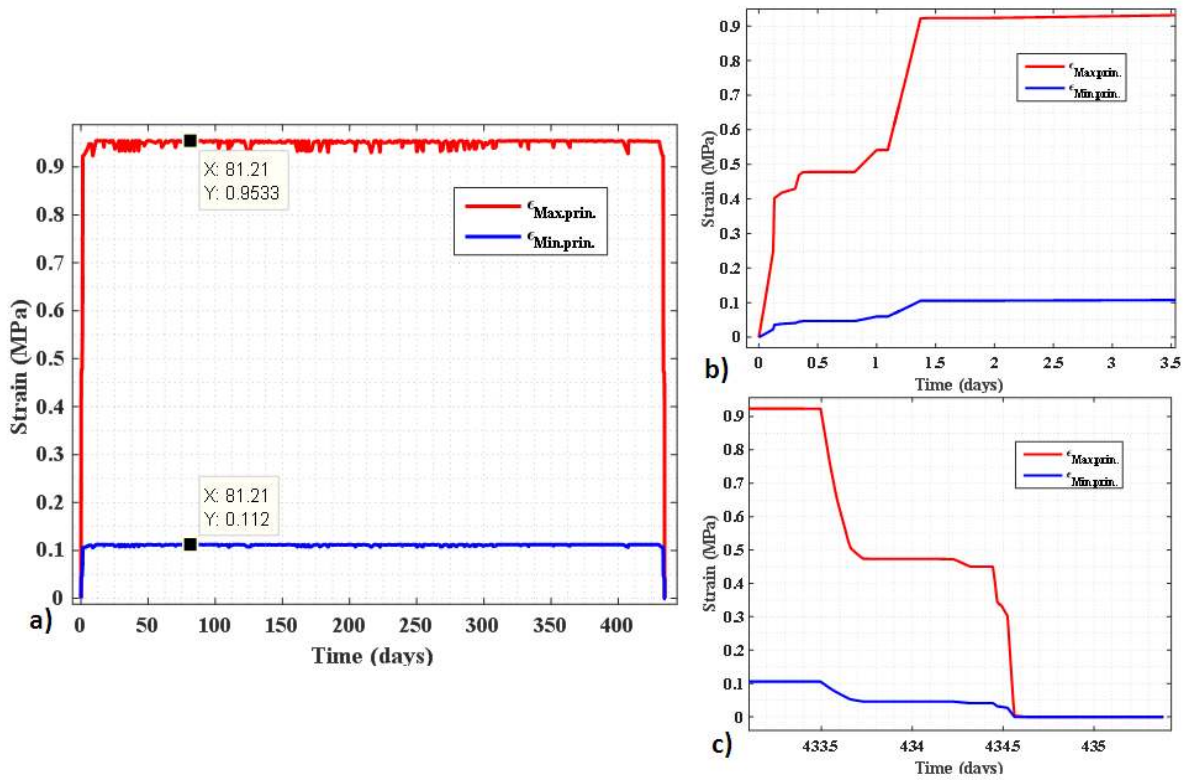


Figure 3.12 The elastic FE simulated time-dependent maximum principal strain ($\epsilon_{max.prin.}$) and minimum principal strain ($\epsilon_{min.prin.}$) at the centroid of a typical element near pressurizer end: (a) under full cycle, (b) during heat-up, and (c) during cool-down.

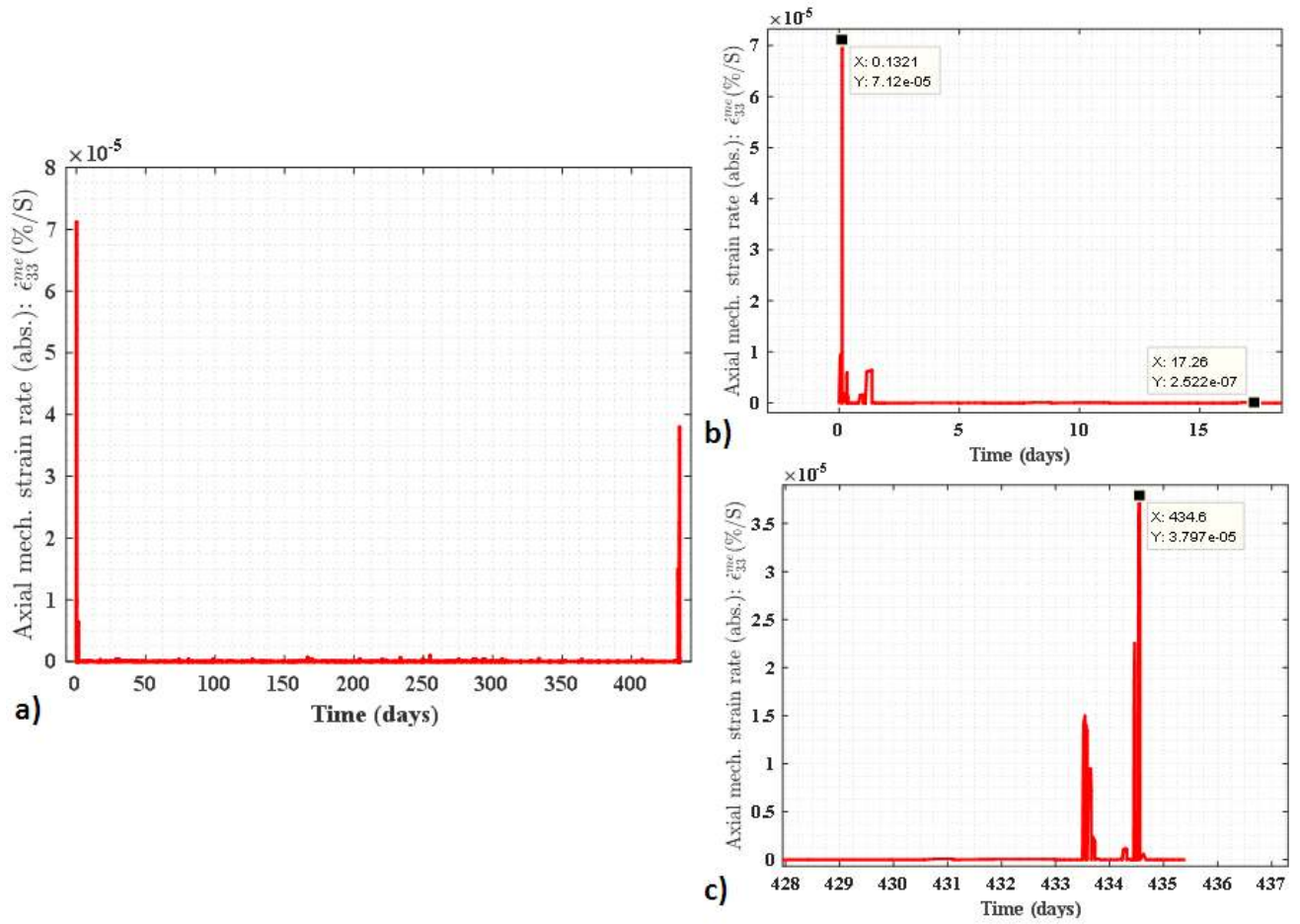


Figure 3.13 The elastic FE simulated time-dependent along the vertical direction mechanical strain rate ($\dot{\epsilon}_{33}^{me}$) at the centroid of a typical element near pressurizer end: (a) under full cycle, (b) during heat-up, and (c) during cool-down.

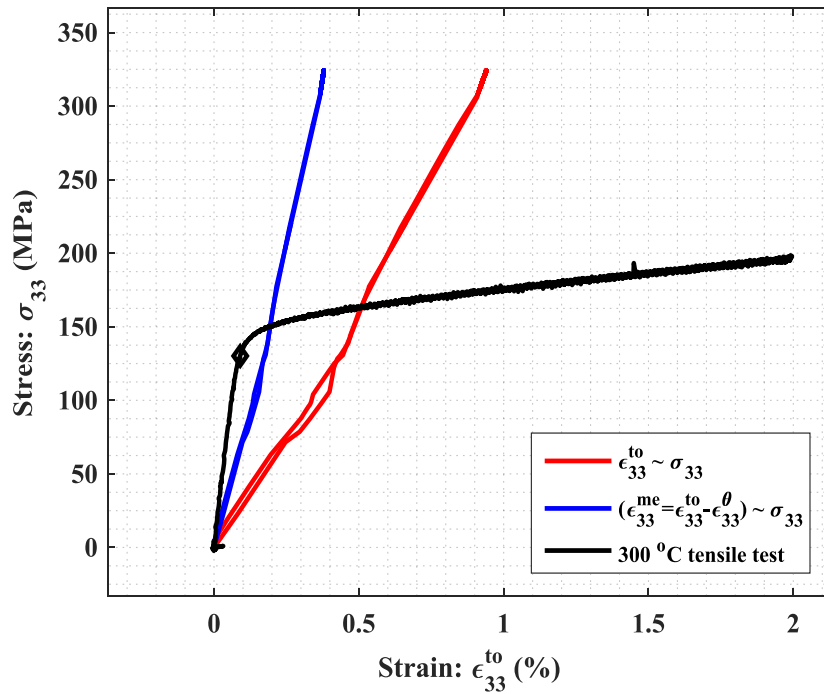


Figure 3. 14 The elastic FE simulated hysteresis curves ($\epsilon_{33}^{to} \sim \sigma_{33}$ and $\epsilon_{33}^{me} \sim \sigma_{33}$) at the centroid of a typical element near pressurizer end and comparison with tensile test strain~stress curve for 300 °C.

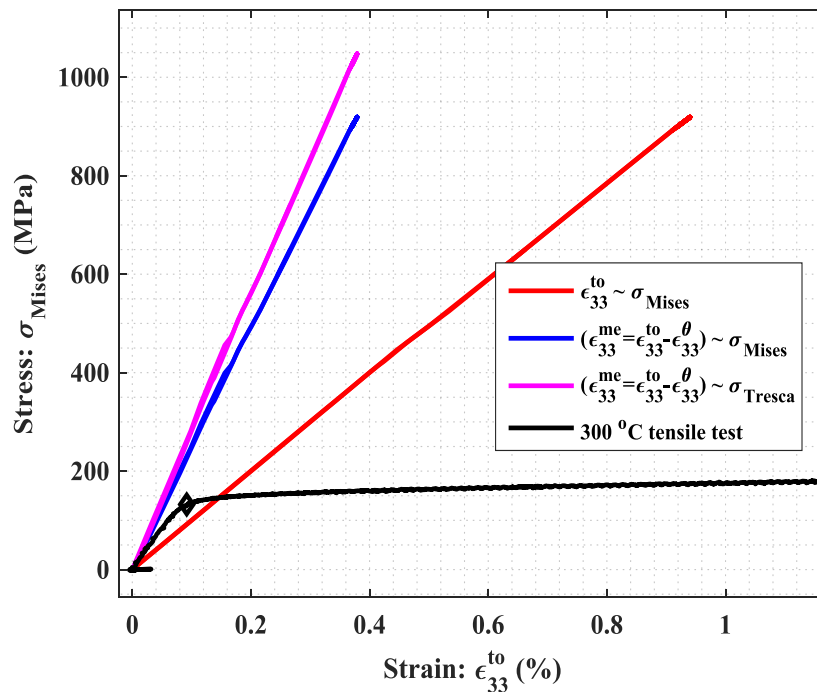


Figure 3. 15 The elastic FE simulated hysteresis curves ($\epsilon_{33}^{to} \sim \sigma_{Mises}$, $\epsilon_{33}^{me} \sim \sigma_{Mises}$, and $\epsilon_{33}^{me} \sim \sigma_{Tresca}$) at the centroid of a typical element near pressurizer end and comparison with tensile test strain~stress curve for 300 °C.

3.4.2 Elastic-plastic stress analysis results

In addition to elastic analysis, an elastic-plastic FE analysis of SL pipe was performed for the grid-load-following case. The objective was to estimate more realistic stress/strain profiles of the SL pipe, which can be used for fatigue experiments (discussed in section 4). Figure 3.16 shows the elastic-plastic FE simulated time-dependent Tresca stress ($\sigma_{\max.\text{prin.}} - \sigma_{\min.\text{prin.}}$), Von Mises stress (σ_{Mises}) and stress component along the vertical direction (σ_{33}) at the centroid of a typical element near the pressurizer end. Figure 3.17 shows the time-dependent maximum principal stress ($\sigma_{\max.\text{prin.}}$) and minimum principal stress ($\sigma_{\min.\text{prin.}}$). Figure 3.16 shows that the maximum Von Mises stress is approximately 167.3 MPa, and the maximum Tresca stress ($\sigma_{\max.\text{prin.}} - \sigma_{\min.\text{prin.}}$) is approximately 181 MPa. This Tresca stress amplitude is in good agreement with the experimentally observed stress amplitudes. For example, for a uniaxial fatigue test (ET-F50), the stress amplitude had a maximum of 192.2 MPa and minimum of -179.4 MPa (Figure 4.21 in section 4). The maximum shear stress amplitude for the simulation case can be calculated (based on the results shown in Figure 3.17) from the following:

$$(1/2) \times (\sigma_{\max.\text{prin.}} - \sigma_{\min.\text{prin.}}) = (1/2) \times (138 - (-42.3)) = 90.15 \text{ MPa}$$

Similar to be elastic analysis case, if we perform the elastic-plastic analysis based on shear stress $[(1/2) \times (\sigma_{\max.\text{prin.}} - \sigma_{\min.\text{prin.}})]$, it may over predict the fatigue life if a similar ASME code type fatigue evaluation approach is followed. Rather, if elastic-plastic analysis results are used for fatigue life estimation along with ASME code type approaches, it is suggested to use the Tresca stress, which is the difference between the maximum and minimum principal stress (i.e., $\sigma_{\max.\text{prin.}} - \sigma_{\min.\text{prin.}}$). The related results are discussed in section 5.

Based on the simulated Von-Mises stress (Figure 3.16), we estimated the Von-Mises stress rates ($\dot{\sigma}_{Mises}$). The resulting time-dependent stress rates are shown in Figure 3.18, which indicates that during the cool-down operation the maximum stress rate occurs, with a value of 0.02385 MPa/s. These types of results may be useful for planning a stress-controlled fatigue test.

Figure 3.19 shows the FE simulated time-dependent total strain ($\epsilon_{33}^{\text{to}}$), thermal strain ($\epsilon_{33}^{\text{th}}$), and mechanical strain ($\epsilon_{33}^{\text{me}}$) components along the vertical direction and at the centroid of a typical element near the pressurizer end. Figure 3.20 shows the time-dependent plastic strain magnitude ($\epsilon_{\text{mag}}^{\text{pl}}$) and plastic strain component along the vertical direction ($\epsilon_{33}^{\text{pl}}$). Figure 3.19 shows that, similar to the elastic analysis results, the thermal strain returns to its starting value at the end of the loading cycle. This occurs because of the linear calculation of the thermal strain in the FE model. However, unlike the elastic analysis, the total and mechanical strains do not return to their starting values at the end of the simulation. This occurs because of the nonlinear elastic-plastic FE analysis, which simulates the non-recoverable plastic deformation and associated accumulated plastic strain. Nevertheless, the elastic-plastic analysis results are more realistic since the FE model uses the full elastic-plastic stress-strain curve as the material property rather than just the elastic portion of the stress-strain curve. The non-recoverable plastic deformation is also evident in Figure 3.20. As shown, at the end of the first cycle the accumulated equivalent plastic strain magnitude ($\epsilon_{\text{mag}}^{\text{pl}}$) is approximately 0.1587%. Usually, in a stress-controlled loading condition (similar to a thermal cyclic loading condition, as in the present case), the accumulated plastic strain could grow further (leading to strain ratcheting) or could stabilize due to stress hardening and/or a mean stress shifting effect. Conducting a stress-controlled test is highly

complex (particularly if the material is subjected to elastic-plastic material behavior [23]). This type of plastic strain accumulation may not be observed in a strain-controlled fatigue test, although strain-controlled testing methods are widely followed for fatigue evaluation of metallic components. We also, for simplicity, performed a stroke-controlled or equivalent pseudo strain-controlled fatigue test based on the estimated mechanical strain shown in Figure 3.19. These results will be discussed in Section 4. Figure 3.19 indicates that the maximum mechanical strain is 0.642% at the full-power condition. The corresponding maximum mechanical strain from the elastic analysis is 0.379% (Figure 3.21). Based on the time-dependent mechanical strain in the vertical direction (Figure 3.19), we estimated the corresponding mechanical strain rate ($\dot{\epsilon}_{33}^{me}$). Figure 3.22 shows the time-dependent strain rates, with a maximum value of $14 \times 10^{-5}\%/s$, during the heat-up operation.

Figures 3.23 and 3.24 show the hysteresis curves either with respect to the component stress (σ_{33}), or the Von Mises stress (σ_{Mises}) and or the Tresca stress ($\sigma_{max.prin.} - \sigma_{min.prin.}$). In addition, these curves are either with respect to the total strain component (ϵ_{33}^{to}) or the mechanical strain component (ϵ_{33}^{me}). Comparing Figures 3.23 with 3.24 shows that the hysteresis curve with respect to the Von Mises stress better matches the experimental stress-strain curve (unlike the elastic case, where both figures are comparable to the tensile test curve for 300 °C). The comparison matches up to the first stress reversal. After that, the tensile test curve should not be compared since it does not capture the stress reversal behavior, as in the case of fatigue loading. Comparing the hysteresis curves $\epsilon_{33}^{to} \sim \sigma_{Mises}$ and $\epsilon_{33}^{me} \sim \sigma_{Mises}$ with the tensile test curve, we determined that the hysteresis curve with respect to mechanical strain (ϵ_{33}^{me}) better matches the tensile stress-strain curve compared to the hysteresis curve with respect to total strain (ϵ_{33}^{to}). Hence, the mechanical strain component should be used as the strain input for the isothermal fatigue test. The FE model-determined mechanical strain will be more representative compared to the total strain component because we used (which is also general practice) material properties from the FE model based on the mechanical stress-strain curves (obtained under 300 °C isothermal test conditions). Also evident from Figure 3.16, owing to grid-load-following rated power fluctuations, the maximum Tresca stress ($\sigma_{max.prin.} - \sigma_{min.prin.}$) varies from 157 to 181 MPa. The corresponding mechanical strain (ϵ_{33}^{me}) varies from 0.632 to 0.642%. Depending on the experimental control condition (e.g., stress versus strain control) and environment condition (in-air versus PWR water), the resulting fatigue lives of test specimen may vary due to stress/strain variations. For example due to stress and/or strain fluctuations, the oxide layer (under PWR environment) may break apart, leading to lower fatigue lives. The related test case results are discussed in section 4.

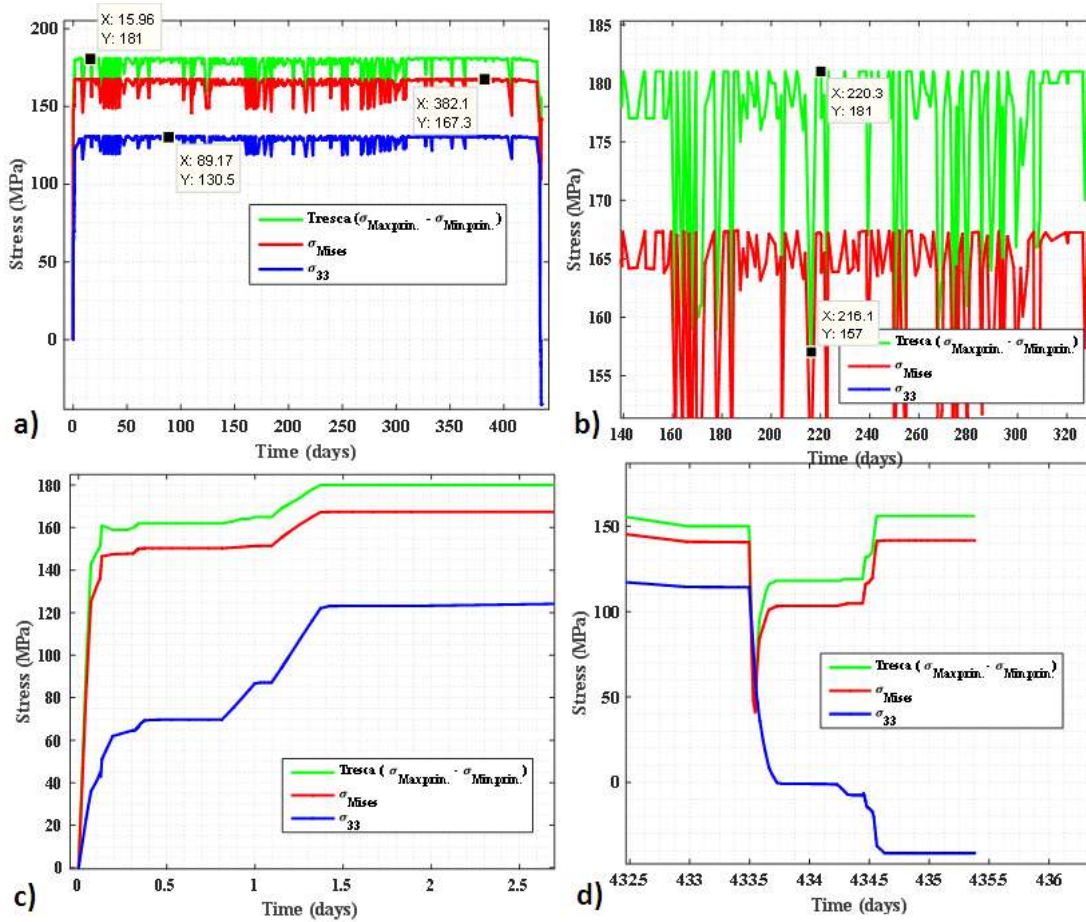


Figure 3.16 The elastic-plastic FE simulated time-dependent Tresca stress ($\sigma_{\max.prin.} - \sigma_{\min.prin.}$), Von Mises stress (σ_{Mises}), and stress component along the vertical direction (σ_{33}) at the centroid of a typical element near pressurizer end: (a) under full cycle, (b) during power operation (c) during heat-up, and (d) during cool-down.

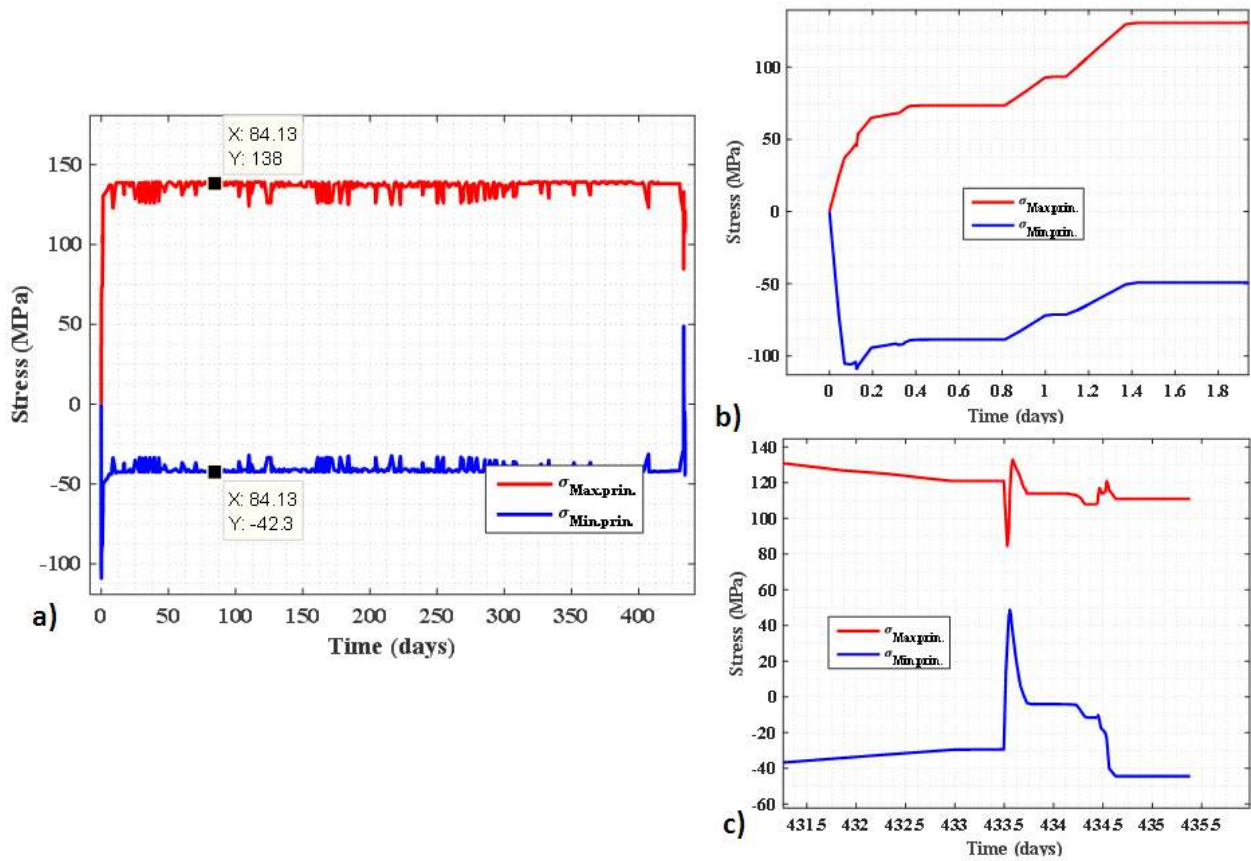


Figure 3. 17 The elastic-plastic FE simulated time-dependent maximum principal stress ($\sigma_{\max.prin.}$) and minimum principal stress ($\sigma_{\min.prin.}$) at the centroid of a typical element near pressurizer end: (a) under full cycle, (b) during heat-up, and (d) during cool-down.

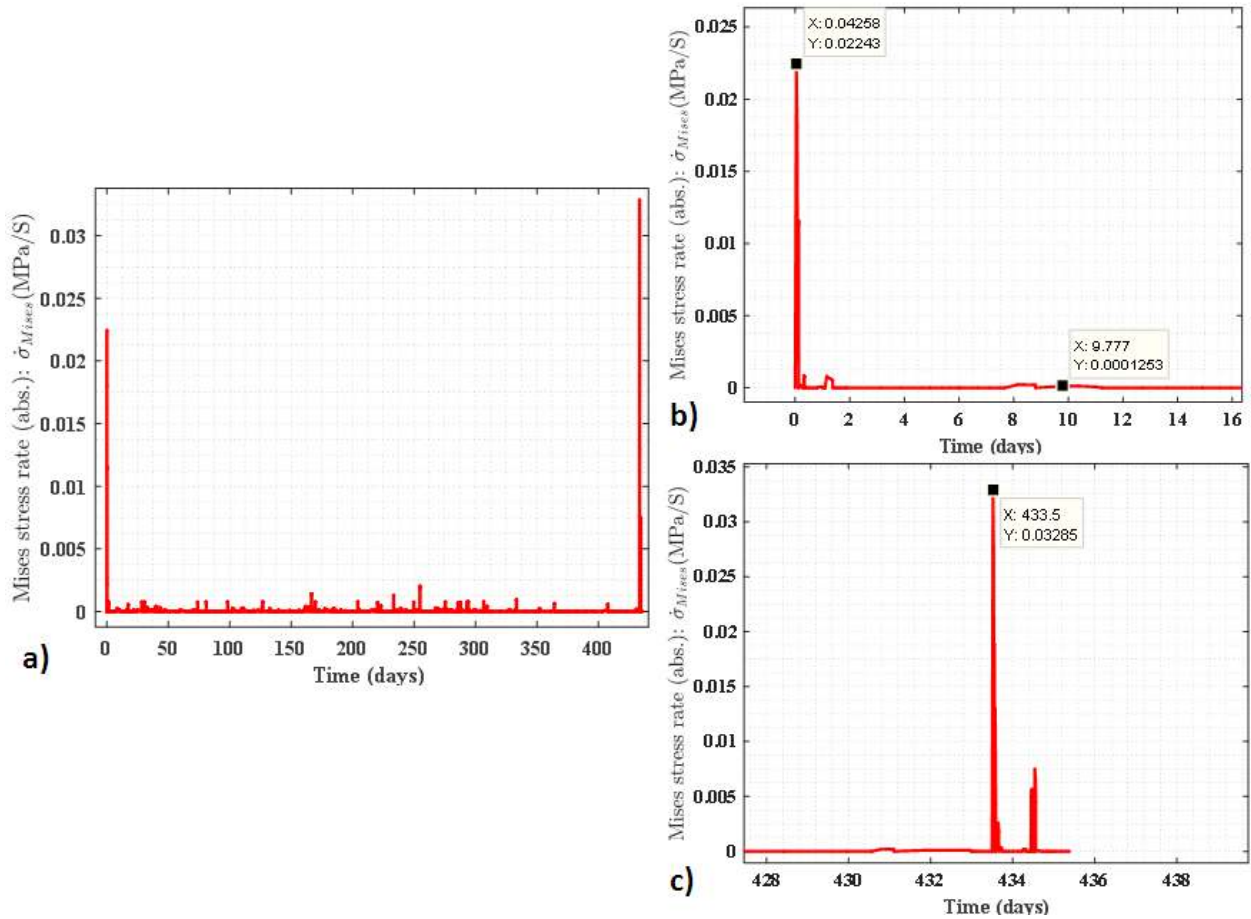


Figure 3.18 The elastic-plastic FE simulated time-dependent Von-Mises stress rate ($\dot{\sigma}_{Mises}$) at the centroid of a typical element near pressurizer end: (a) under full cycle, (b) during heat-up, and (c) during cool-down.

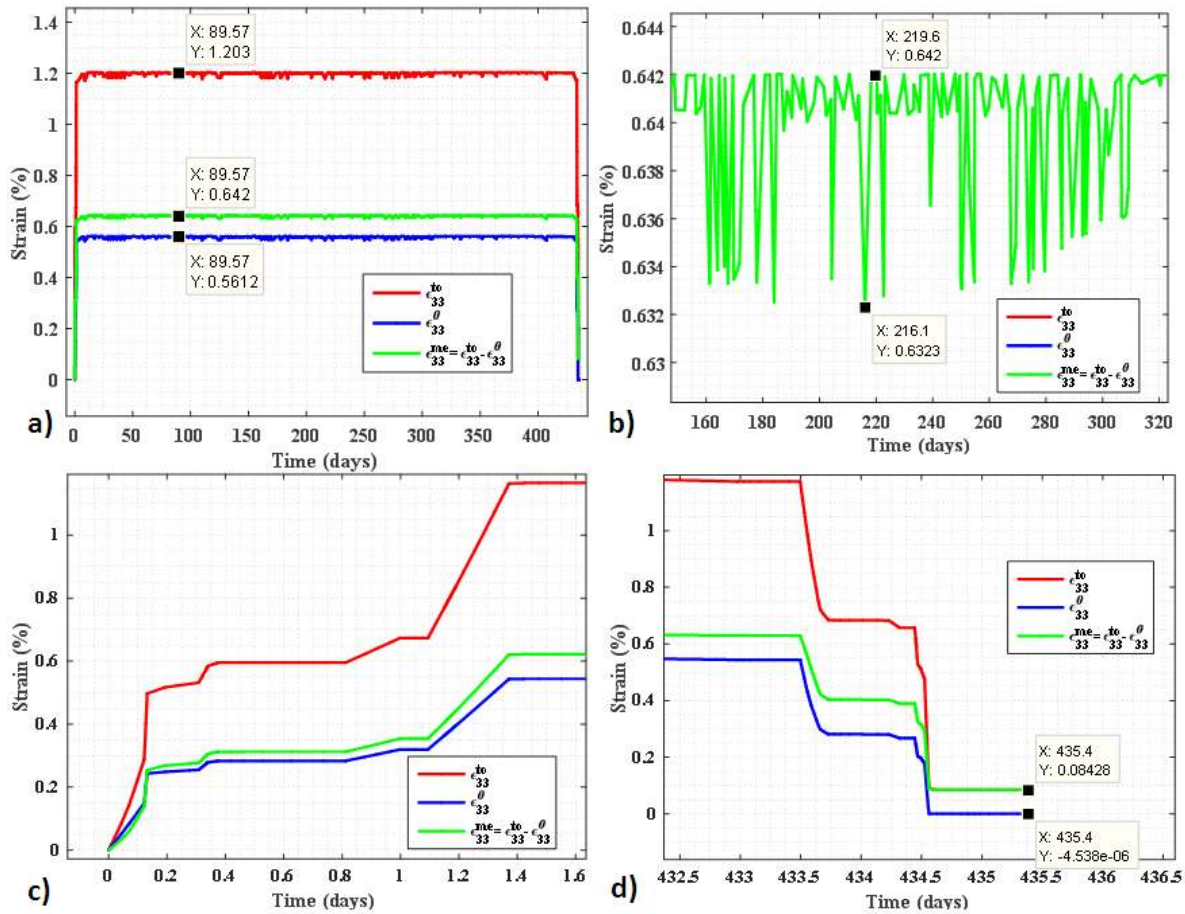


Figure 3.19 The elastic-plastic FE simulated time-dependent total strain (ϵ_{33}^{to}), thermal strain (ϵ_{33}^{θ}), and mechanical strain (ϵ_{33}^{me}) components along the vertical direction and at the centroid of a typical element near pressurizer end: (a) under full cycle, (b) during power operation, (c) during heat-up, and (d) during cool-down.

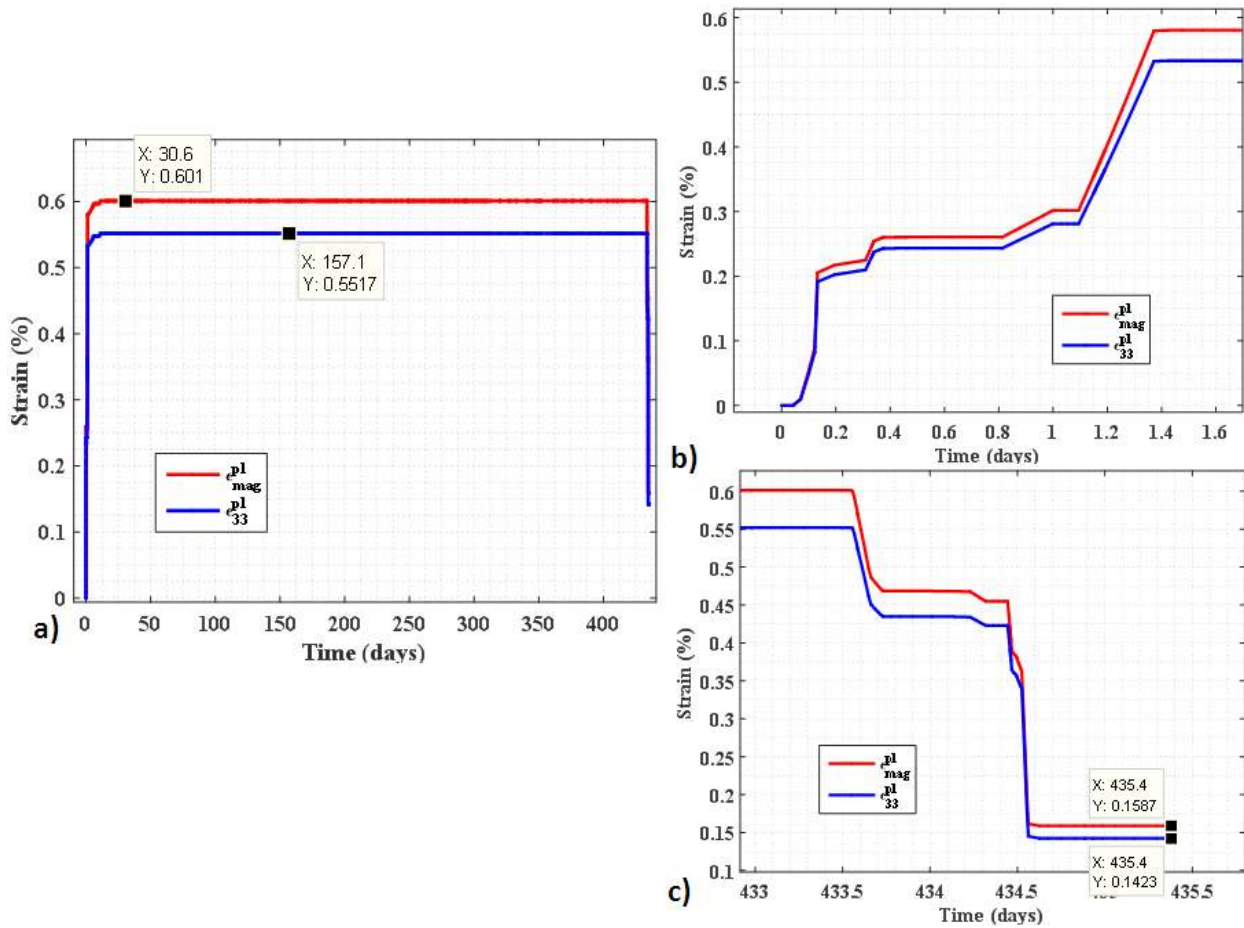


Figure 3. 20 The elastic-plastic FE simulated time-dependent plastic strain magnitude (ϵ_{mag}^{pl}) and plastic strain component along the vertical direction (ϵ_{33}^{pl}) at the centroid of a typical element near pressurizer end: (a) under full cycle, (b) during heat-up, and (c) during cool-down.

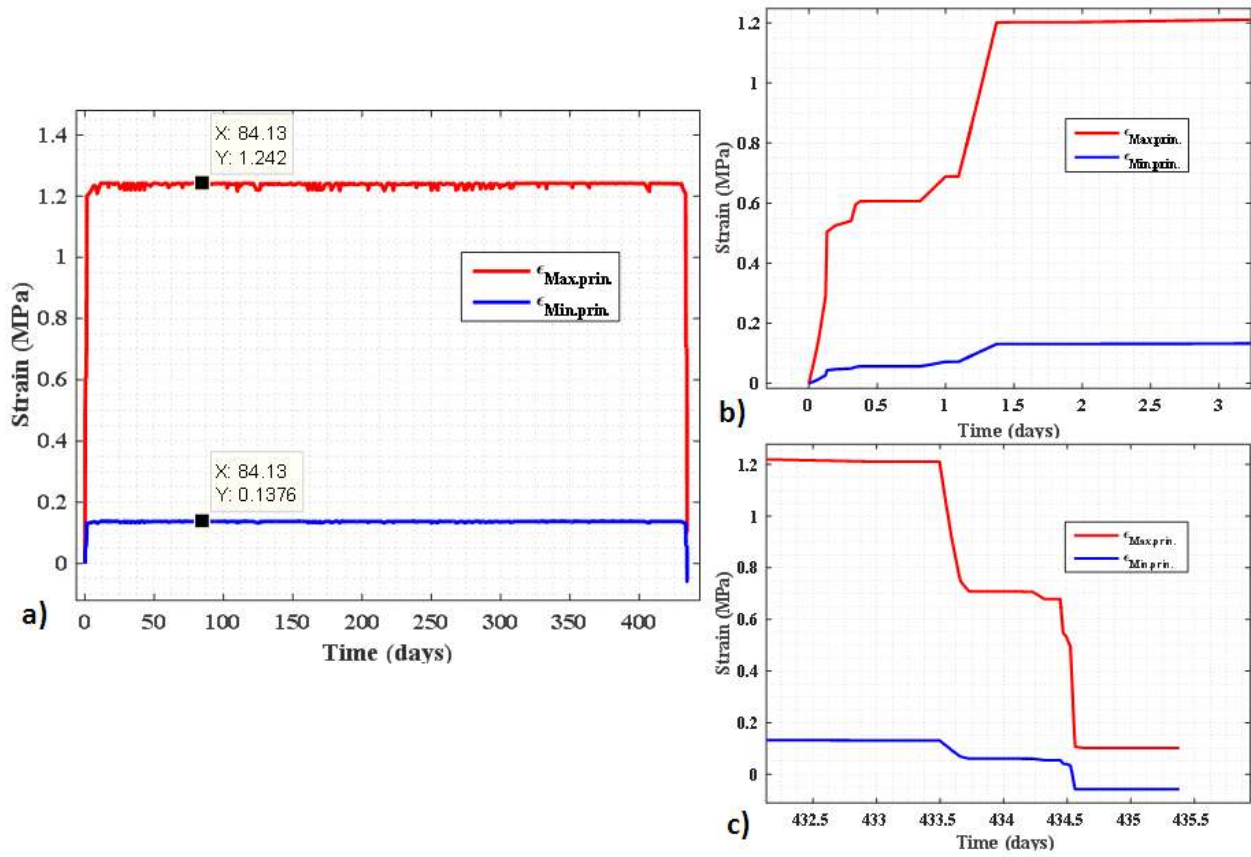


Figure 3. 21 The elastic-plastic FE simulated time-dependent maximum principal strain ($\epsilon_{max.prin.}$) and minimum principal strain ($\epsilon_{min.prin.}$) at the centroid of a typical element near pressurizer end: (a) under full cycle, (b) during heat-up, and (c) during cool-down.

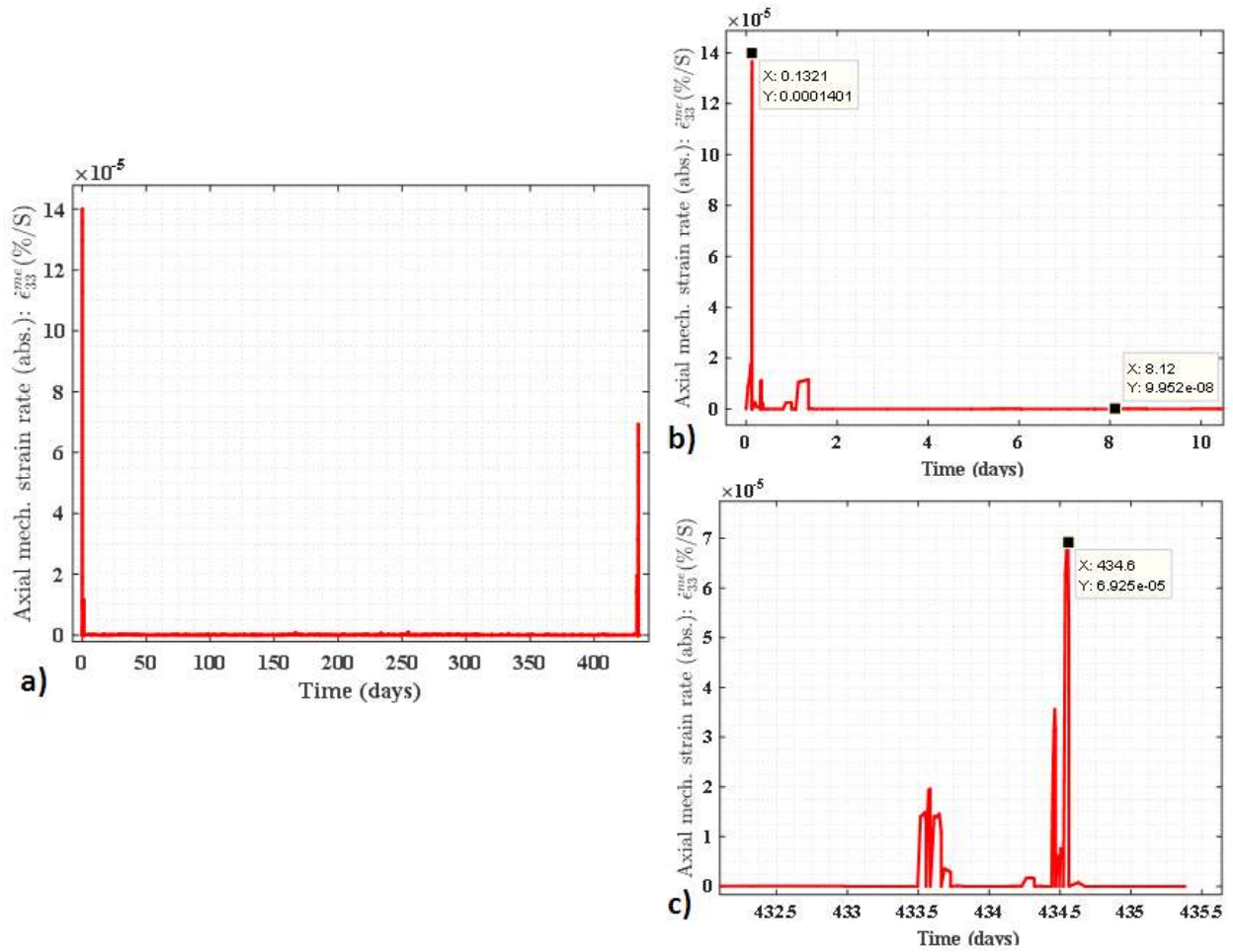


Figure 3.22 The elastic-plastic FE simulated time-dependent mechanical strain rate ($\dot{\epsilon}_{33}^{me}$) along the vertical direction at the centroid of a typical element near pressurizer end: (a) under full cycle, (b) during heat-up, and (c) during cool-down.

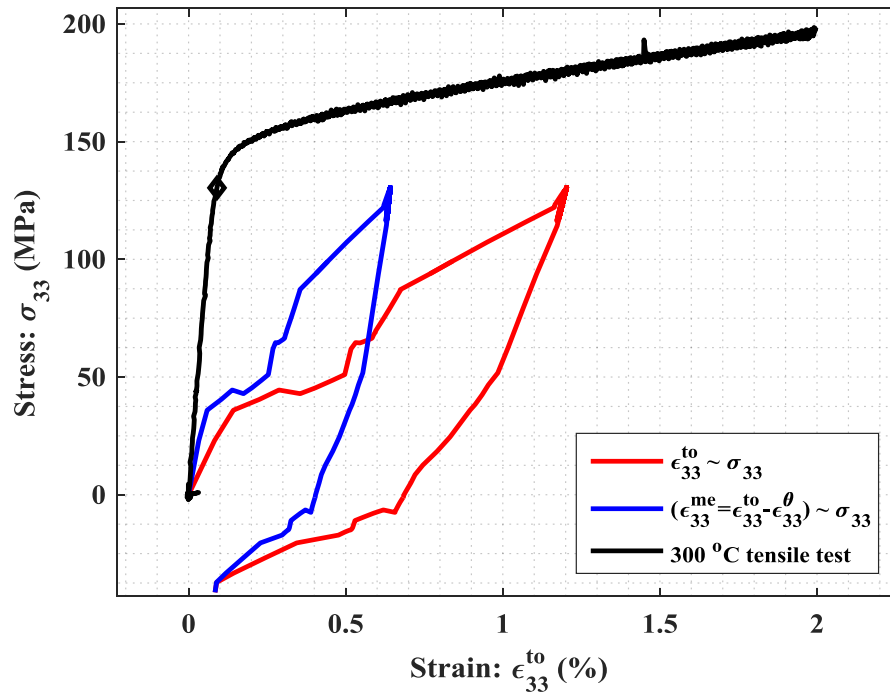


Figure 3.23 The elastic-plastic FE simulated hysteresis curves ($\epsilon_{33}^{to} \sim \sigma_{33}$ and $\epsilon_{33}^{me} \sim \sigma_{33}$) at the centroid of a typical element near pressurizer end and comparison with tensile test strain~stress curve for 300 °C.

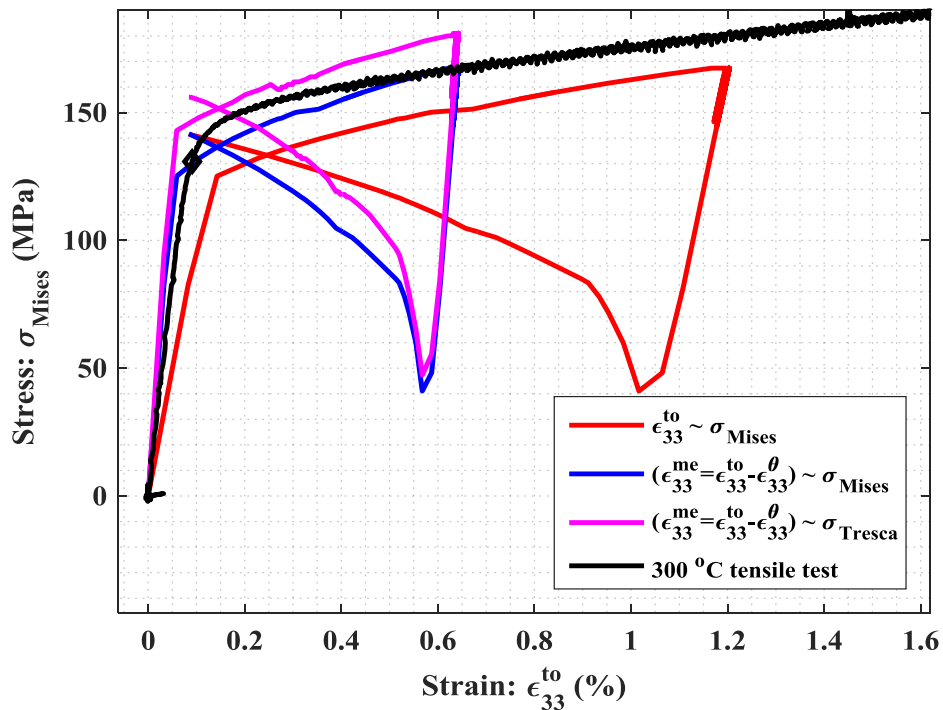


Figure 3.24 The elastic-plastic FE simulated hysteresis curves ($\epsilon_{33}^{to} \sim \sigma_{Mises}$, $\epsilon_{33}^{me} \sim \sigma_{Mises}$, and $\epsilon_{33}^{me} \sim \sigma_{Tresca}$) at the centroid of a typical element near pressurizer end and comparison with tensile test strain~stress curve for 300 °C.

4 Similitude Fatigue Tests for PWR Surge Line under Pseudo Strain-Controlled Design-Basis and Grid-Load-Following Loading Cycles

In the previous section, we presented finite element (FE) model results for 316 SS SL pipe under grid-load-following loading. The respective FE model results under the design-basis loading condition were reported in our earlier work [1]. Based on FE model results we predicted the number of cycles to fatigue failure using ASME code [24, 25] based approaches for predicting in-air fatigue lives and NUREG-6909 [26] based approaches for predicting PWR-water environment lives. To check the accuracy of the predicted fatigue lives under design-basis and grid-load-following loading, we conducted multiple fatigue tests during FY 2018. Some of the experimental results obtained under in-air and design-basis loading conditions were reported in our earlier work [1]. In this section we present additional experimental results conducted both under in-air and PWR-water loading conditions. In addition to the validation of the predicted fatigue lives, we also used the test data for time-series probabilistic modeling. These results are discussed in the later part of this report. The major aim of the testing was to investigate PWR-water environment fatigue with desired strain amplitudes and strain rates. That proved challenging because we could not control the strains since an extensometer couldn't be placed inside a small tube-type autoclave used for the PWR-water environment fatigue tests. Below we discuss the different test cases, as well as the methodology developed to conduct the required pseudo strain-controlled fatigue tests.

4.1 Different Test Cases and Test Methodology

Recently, we conducted four fatigue tests either in air or in PWR-water environment. The test parameters are summarized in Table 4.1. Out of the four 316 SS test specimens, the ET-F49 specimen was fabricated directly from 316SS base metal plate, whereas the other three specimens (ET-F50, EN-F51, and EN-F53) were fabricated from the heat affected zone (HAZ) of a 508 LAS-316 SS dissimilar metal weld (DMW) plate. We believe that the HAZ zone effect on the test specimens would not be much since the locations of the specimens were not exactly adjacent to the weld zones. Figure 4.1 shows the locations of the 316SS base metal specimens in the HAZ zone, highlighted in red circle. As mentioned above, the primary aim of the experimental activities is to conduct fatigue tests under desired loading conditions. For example we wanted to conduct the PWR environment fatigue tests under strain-controlled conditions, which would be more appropriate to compare the predicted fatigue lives based on ASME code and NUREG-6909 approaches, which are, in turn, based on design curves derived from strain-controlled fatigue tests (S-N curves). However, since we could not place an extensometer inside a tube type autoclave (used for the PWR-water tests at Argonne), it was a challenge to control the gauge area strain of specimens while also controlling other test variables such as stress or frame crosshead stroke. In the test cases, we used a stroke-controlled approach, since it would resemble more closely the displacement control type strain-control approach. Although the stroke-control approach is much better than the stress-control approach, controlling the stroke may not also allow obtaining the desired gauge area strain amplitudes and straining rates. This is due to the highly nonlinear behavior of cyclic hardening/softening (associated with strain increase or decrease) if other parameters (other than strain) are used for controlling the test. To avoid this issue, we developed a test strategy based on the test

results of two initial fatigue tests. First, based on the results of an earlier stroke-controlled test (ET-F13 test [27] conducted with constant stroke amplitude and constant stroke rate) we estimated the initial mapping parameters between observed strain and applied stroke input.

Table 4. 1 Summary of different test cases and associated test parameters

Test-ID	Loading type	Environment	Control condition	Metal type and surface finish	Intended strain amplitude (and strain rate)
ET-F49	Constant amplitude (R=-1 type loading)	In-air	Frame cross-head stroke control	316SS pure base metal, polished up to 0.3 μm	Amplitude = ± 0.65 % Rate = 0.1%/s
ET-F50	Grid-load-following	In-air	Frame cross-head stroke control	316SS base metal taken from HAZ of DMW, polished up to 0.3 μm	Amplitude = Max =0.642 % Min = 0.084 % Rate = 0.1%/s
EN-F51	Grid-load-following	PWR-water	Frame cross-head stroke control	316SS base metal taken from HAZ of DMW, polished up to 0.3 μm	Amplitude = Max =0.642 % Min = 0.084 % Rate = 0.1%/s
EN-F51	Design-basis loading	PWR-water	Frame cross-head stroke control	316SS base metal taken from HAZ of DMW, used machine fabricated as it is form without additional polishing	Amplitude = Max =0.642 % Min = 0.084 % Rate = 0.1%/s

The ET-F13 strain versus applied stroke input for the first cycle is shown in Figure 4.2. Using the estimated mapping parameters, we created test input for the desired strain amplitude ($\pm 0.65\%$) and strain rate (0.1%/s) in the ET-F49 in-air fatigue test. Figure 4.3 shows a comparison of the actual applied stroke amplitude and the corresponding intended strain amplitudes over a single cycle. This stroke cycle was repeated up to the final failure of the test specimen. Figure 4.4 shows the applied variable stroke rates and the corresponding intended constant strain rate. Figure 4.5 shows the normalized applied strokes versus observed gauge area strains for 1000 fatigue cycles. Note that this test was conducted under the in-air condition. This allows us to measure the gauge area strains, which can be used for checking the accuracy of the proposed pseudo strain control fatigue tests. Figure 4.5 shows that the strain amplitude dropped to 67.5% of its first cycle value, despite the above discussed attempt to control the strain. This drop is possibly due to ET-F13 strain rates, which were much different compared to the

intended strain rate of 0.1%/s. To further improve the strain control testing, we used the ET-F49 applied strokes and the corresponding observed strains to develop a second-level mapping model between observed strains and applied strokes. Based on these mapping parameters, the test inputs were estimated for the next conducted tests (grid-load-following fatigue tests ET-F50 and EN-F51 and design-basis fatigue test EN-F53). The resulting test results are discussed below. Figure 4.6 shows the strain versus stroke data from first cycle for ET-F49.

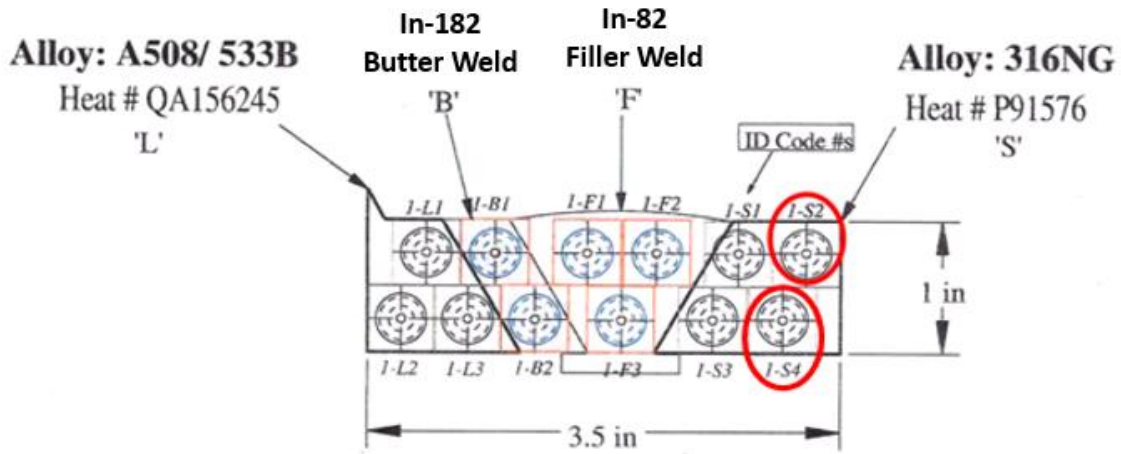


Figure 4. 1 Schematic showing the highlighted location (in red circle) of the 316 SS base metal specimens (ET-F50, EN-F51, and EN-F53) with respect to heat affected zone (HAZ) in 508 LAS-316 SS dissimilar metal weld (DMW).

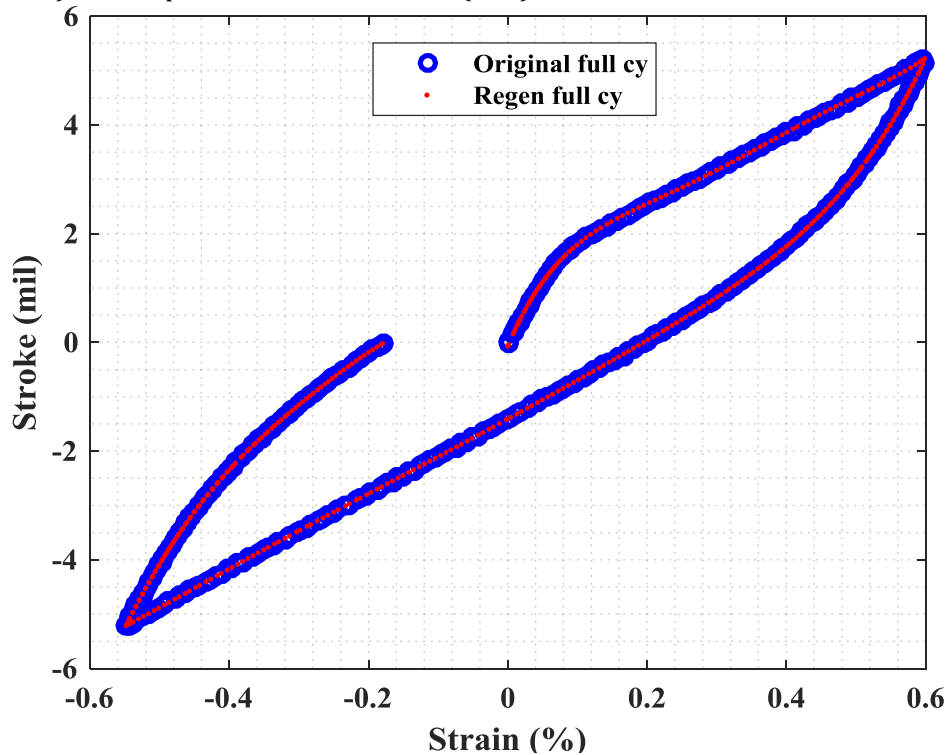


Figure 4. 2 Strain versus stroke data from first cycle of ET-F13 fatigue test used for generating the stroke inputs for ET-F49 fatigue test.

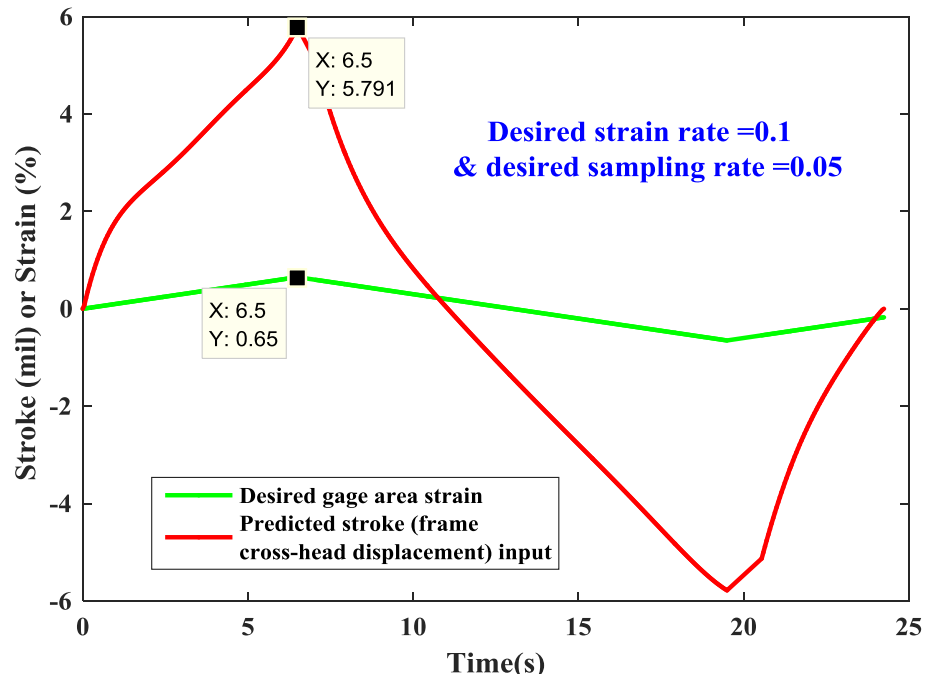


Figure 4. 3 Applied stroke input and the desired gauge area strain for a single cycle for ET-F49 fatigue test.

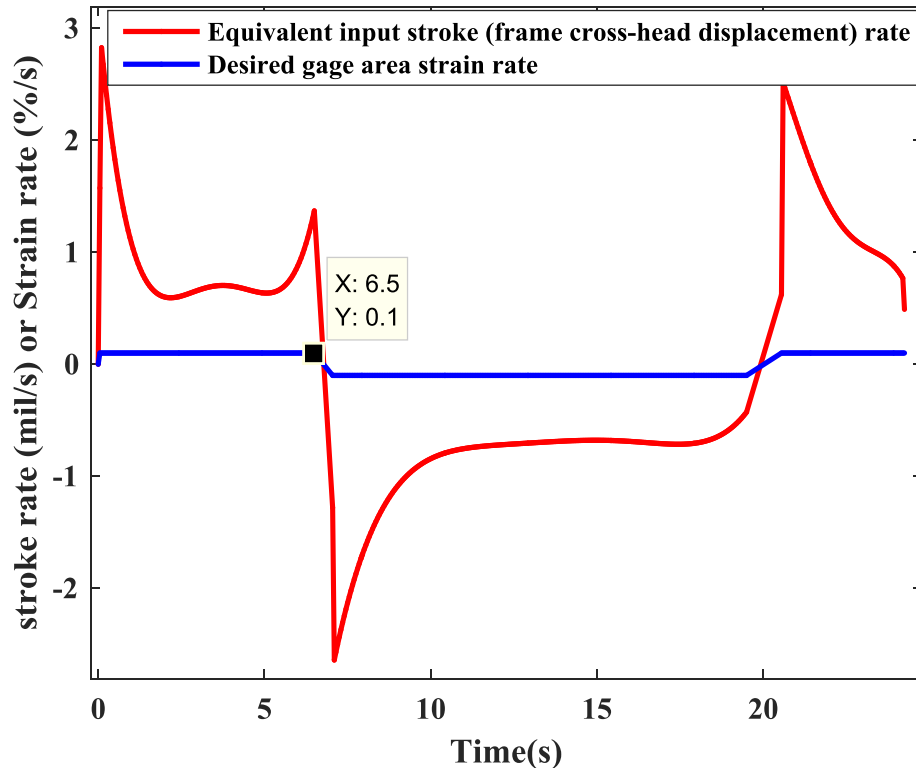


Figure 4. 4 Applied stroke rate and the desired gauge area strain rate for a single cycle for ET-F49 fatigue test.

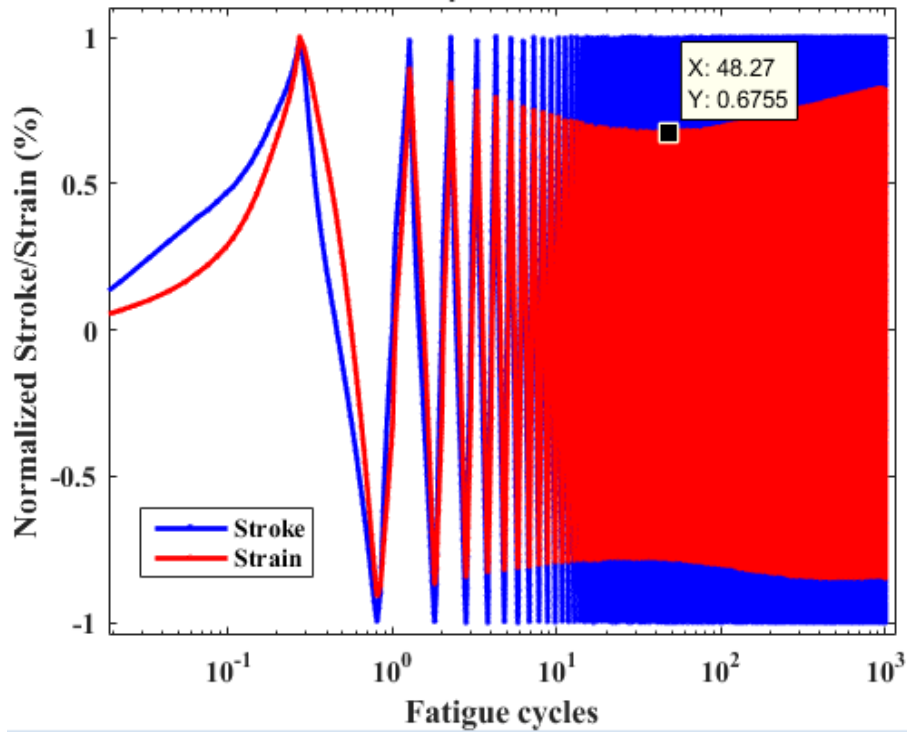


Figure 4.5 Normalized applied strokes versus observed gauge area strains for 1000 fatigue cycles for ET-F49 fatigue test.

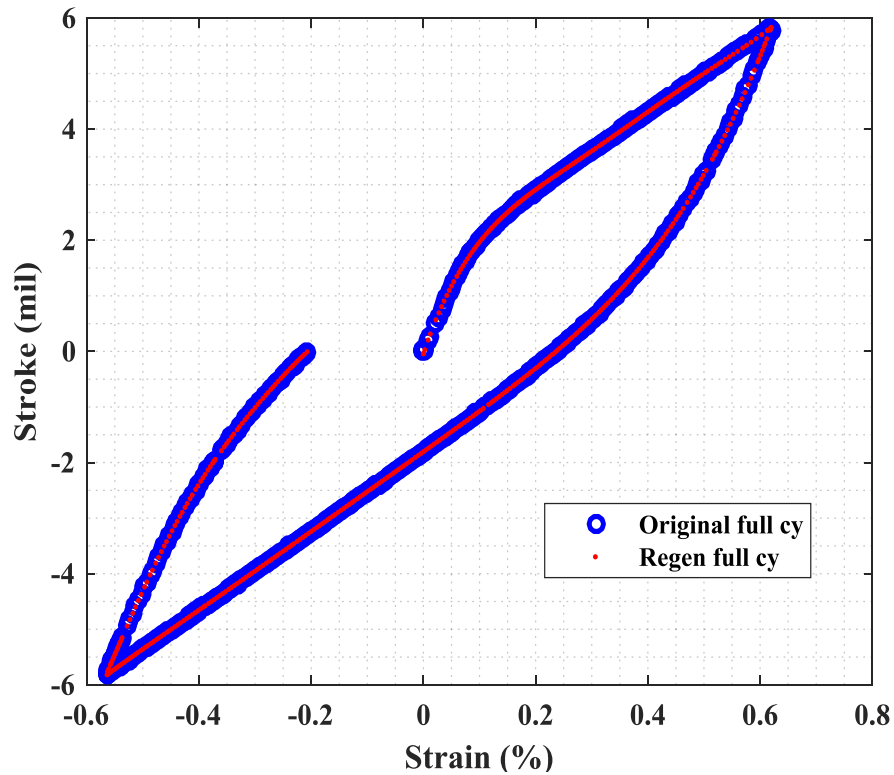


Figure 4.6 Strain versus stroke data from first cycle of ET-F49 fatigue test used for generating the stroke inputs for ET-F50, EN-F51, and EN-F53 fatigue tests.

4.2 Grid-Load-Following In-air Fatigue Test (ET-F50)

Based on the mapping parameters from ET-F49, we generated the stroke input for the grid-load-following fatigue test, ET-F50. Note that the stroke inputs correspond to the mechanical strains simulated through the elastic-plastic FE models discussed in section 3. Figure 4.7 shows the applied stroke input and the desired gauge area strain for a single cycle. Figure 4.8 shows the applied stroke rate and the desired gauge area strain rate for a single cycle. Figure 4.9 shows the normalized applied strokes versus observed gauge area strains for 1000 fatigue cycles. This figure shows that unlike the ET-F49 case the effect of cyclic strain hardening is not so severe: the strain amplitude drops only by 5% from its first cycle value. Figure 4.10 shows the corresponding observed stress up to 30,088 fatigue cycles. Note that, the test was stopped due to an unknown reason, possibly a software bug in the INSTRON test control software, which has issues if a large amount of data is collected. Figure 4.11 shows the applied stroke input for the first 5 cycles of the grid-load-following condition for ET-F50. Figures 4.12 and 4.13 show the strain amplitudes and strain rates, respectively. Figure 4.13 shows that the maximum strain rates are roughly maintained at the intended strain rate of 0.1%/s. Figure 4.12 shows that the maximum strain amplitude almost remains flat with approximate value of 0.617%. Note that the FE simulation of the intended maximum strain amplitude was 0.642%. The intended strain amplitude could not be achieved possible due to the usual experimental artifacts (e.g., control command versus actual actuator output), material microstructure variability, etc. Nonetheless, the observed results are promising for conducting a pseudo strain control test, while not actually controlling the strain. Figure 4.14 shows the first 5-cycle observed stress, and Figure 4.15 shows the corresponding first 5-cycle observed strain versus stress (hysteresis loop) for ET-F50.

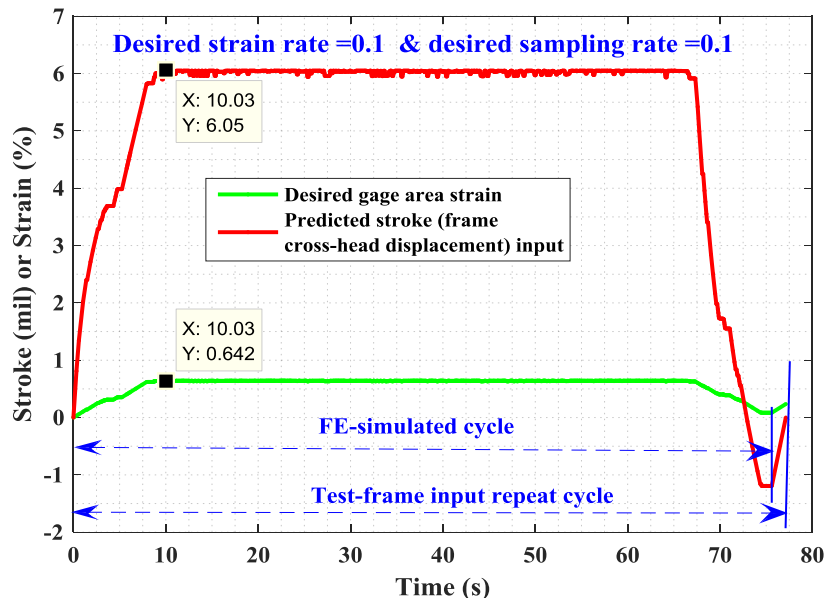


Figure 4. 7 Applied stroke input and the desired gauge area strain for a single cycle for ET-F50 fatigue test.

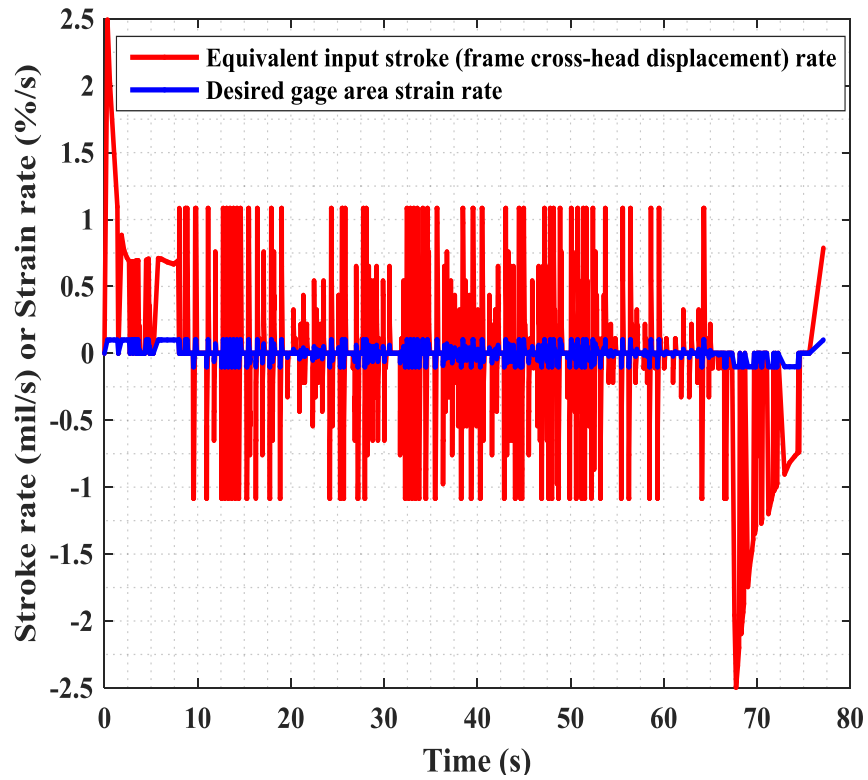


Figure 4. 8 Applied stroke rate and the desired gauge area strain rate for a single cycle in ET-F50 fatigue test.
Total cycle no. = 1000

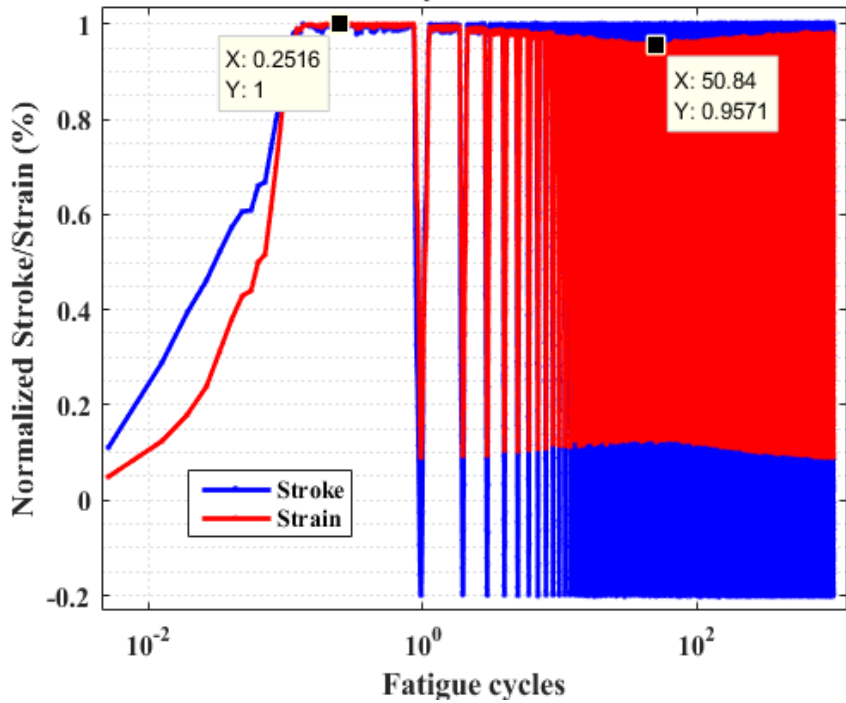


Figure 4. 9 Normalized applied strokes versus observed gauge area strains for 1000 fatigue cycles in ET-F50 fatigue test.

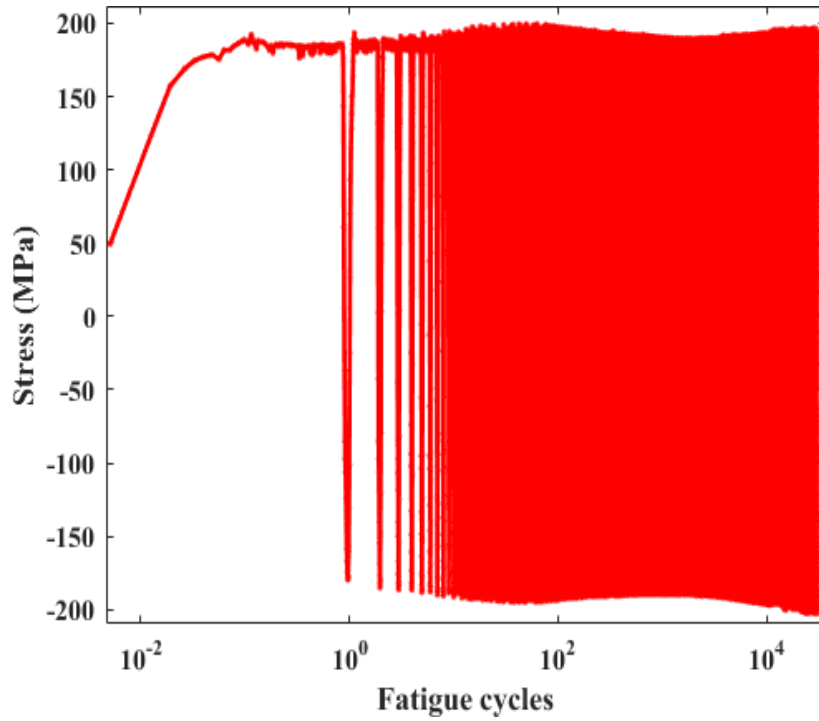


Figure 4.10 Observed stress up to 30,088 fatigue cycles for ET-F50 fatigue test.

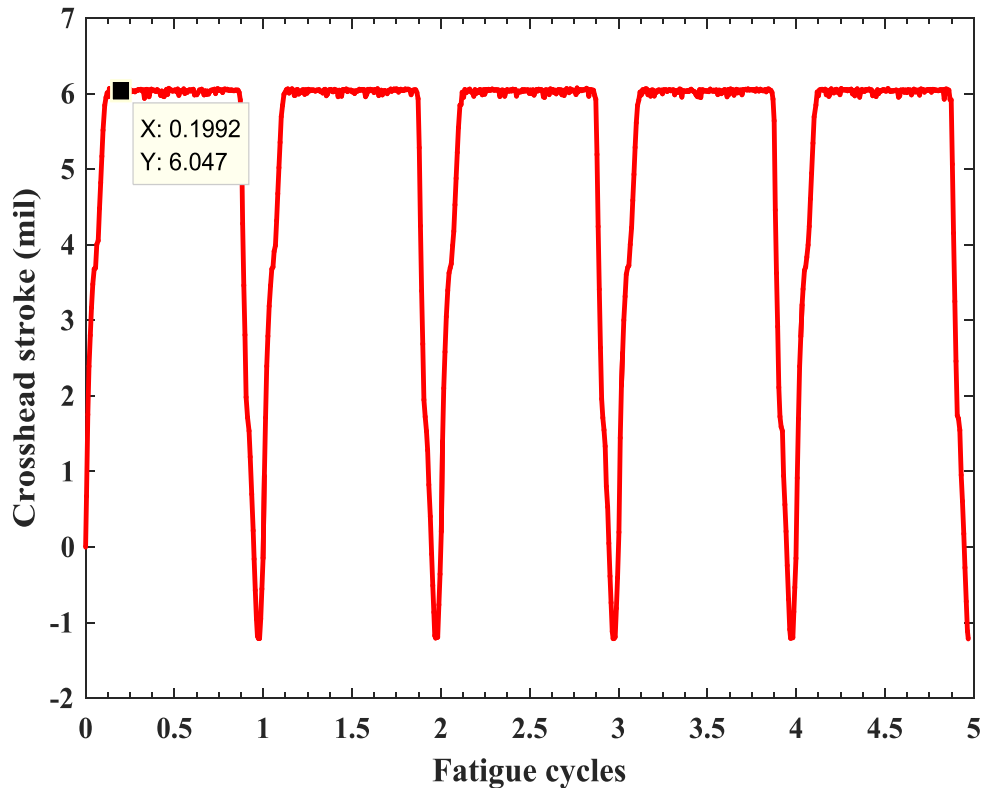


Figure 4.11 First 5-cycle grid-load-following condition applied stroke input for ET-F50 fatigue test

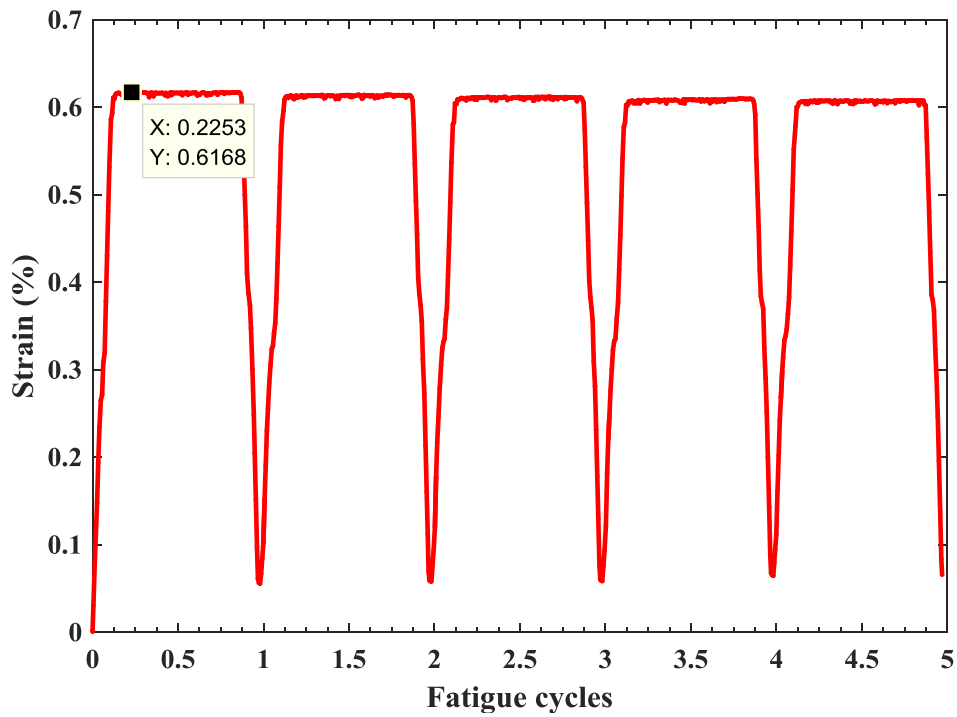


Figure 4. 12 First 5-cycle observed strains for ET-F50 fatigue test.

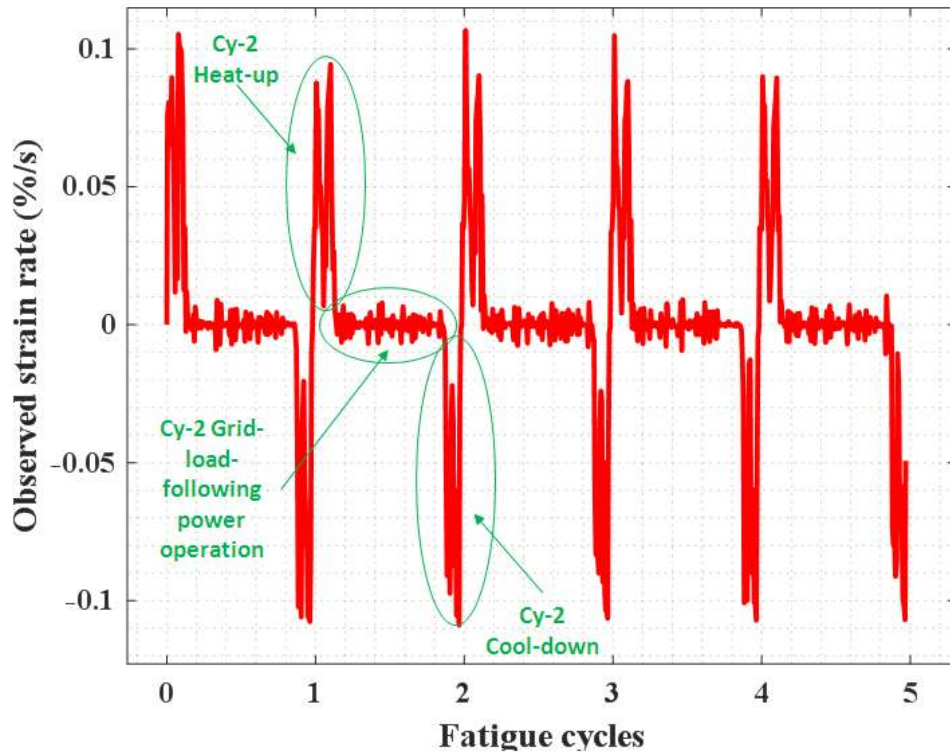


Figure 4. 13 First 5-cycle observed strain rates for ET-F50 fatigue test.

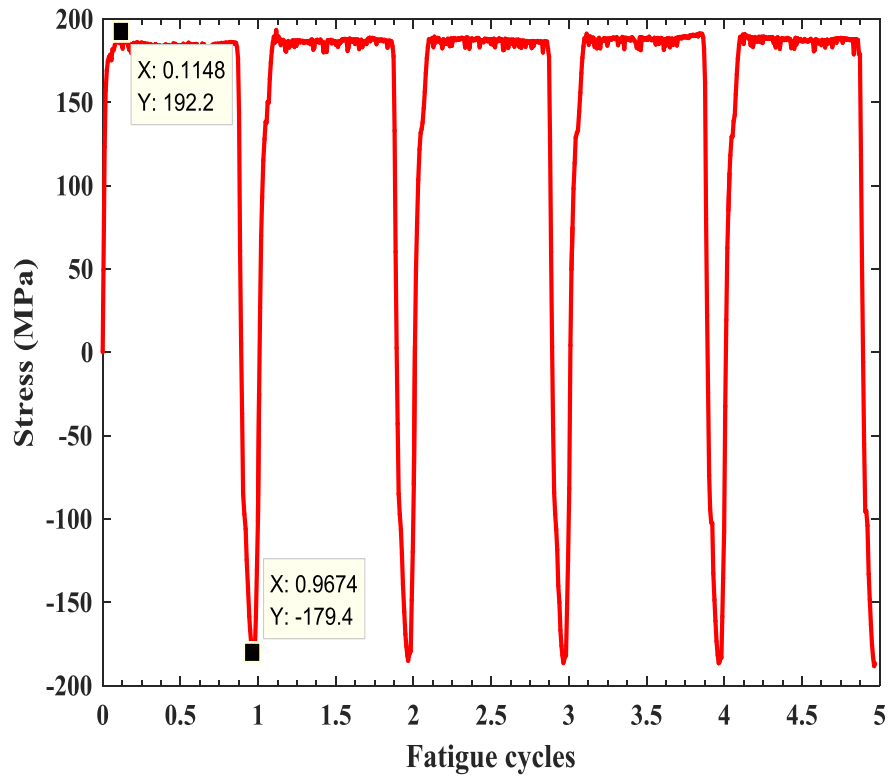


Figure 4. 14 First 5-cycle observed stress for ET-F50 fatigue test.

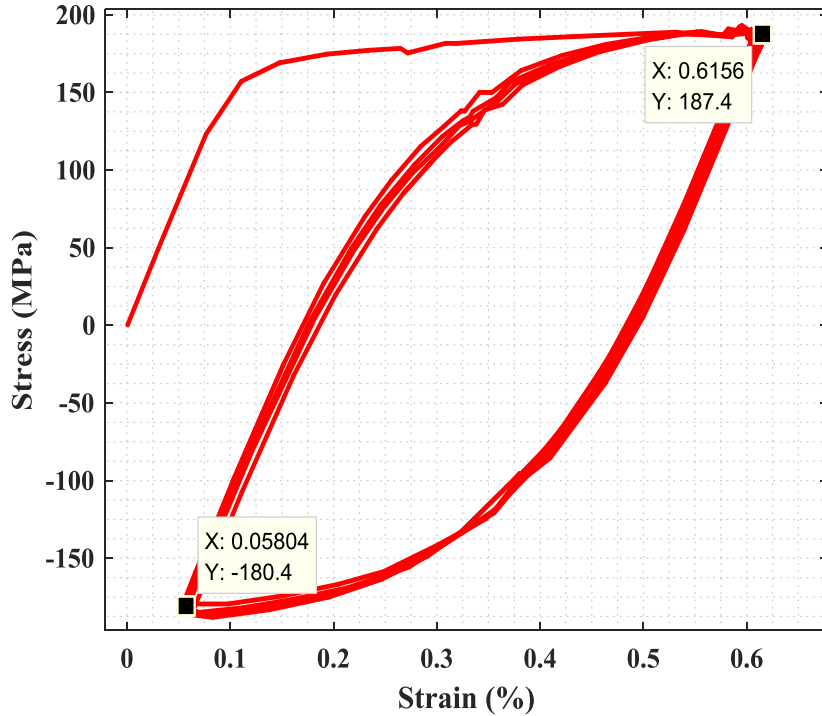


Figure 4. 15 First 5-cycle observed strain versus observed stress hysteresis loops for ET-F50 fatigue test.

4.3 Grid-Load-Following PWR-Water Fatigue Test (EN-F51)

Based on the same stroke input (see Figures 4.7 and 4.8) as ET-F50, we conducted a parallel fatigue test, EN-F51. Unlike ET-F50, which was conducted under the in-air condition, EN-F51 was conducted under the PWR primary water environment. The life of the specimen was approximately 9,999 cycles. Figure 4.16 shows the observed stress for the entire fatigue life of EN-F51. Figures 4.17 and 4.18 show the corresponding first 5-cycle observed stress and applied stroke versus observed stress hysteresis loops, respectively.

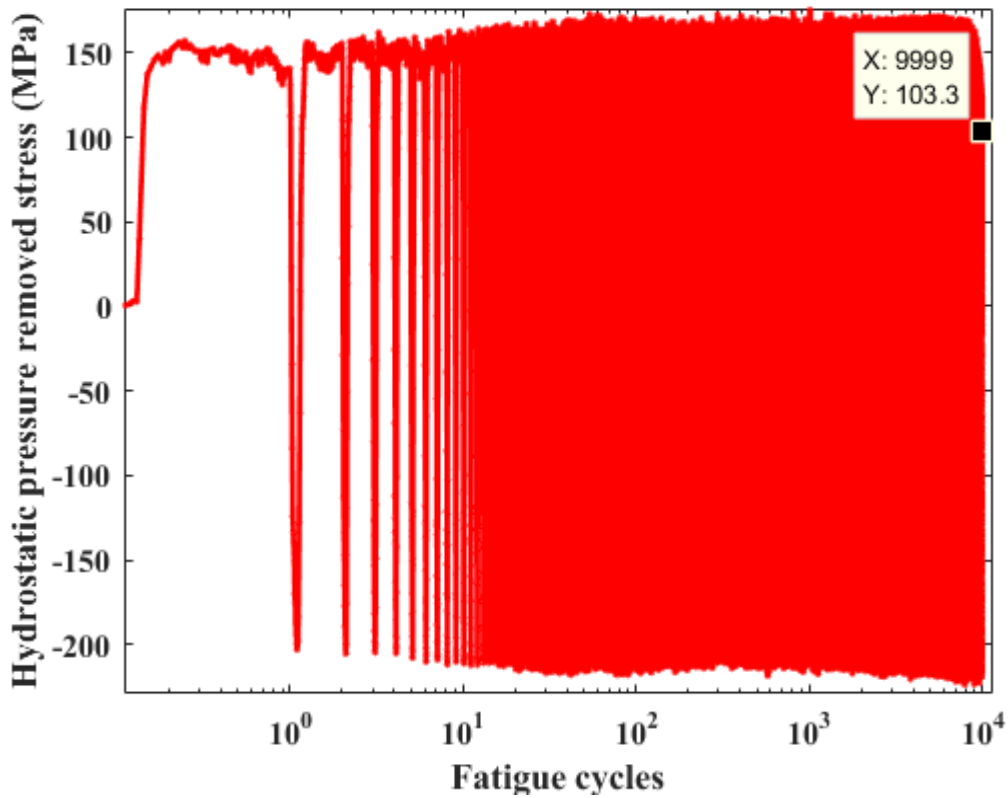


Figure 4. 16 Observed stress for the entire fatigue life for EN-F51 fatigue test.

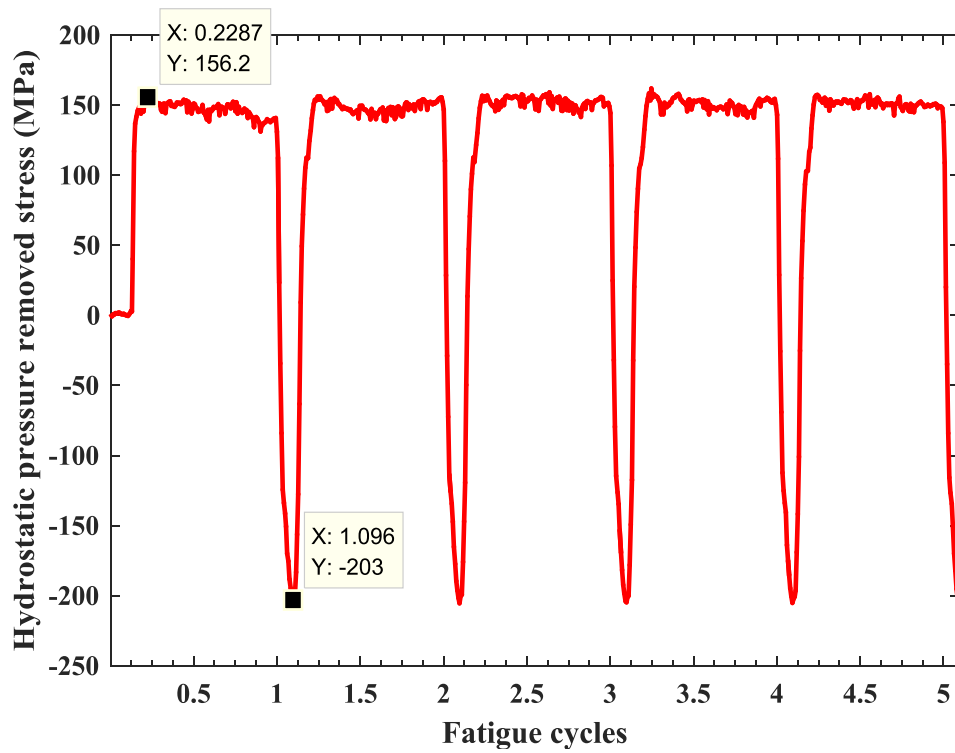


Figure 4. 17 First 5-cycle observed stress for EN-F51 fatigue test.

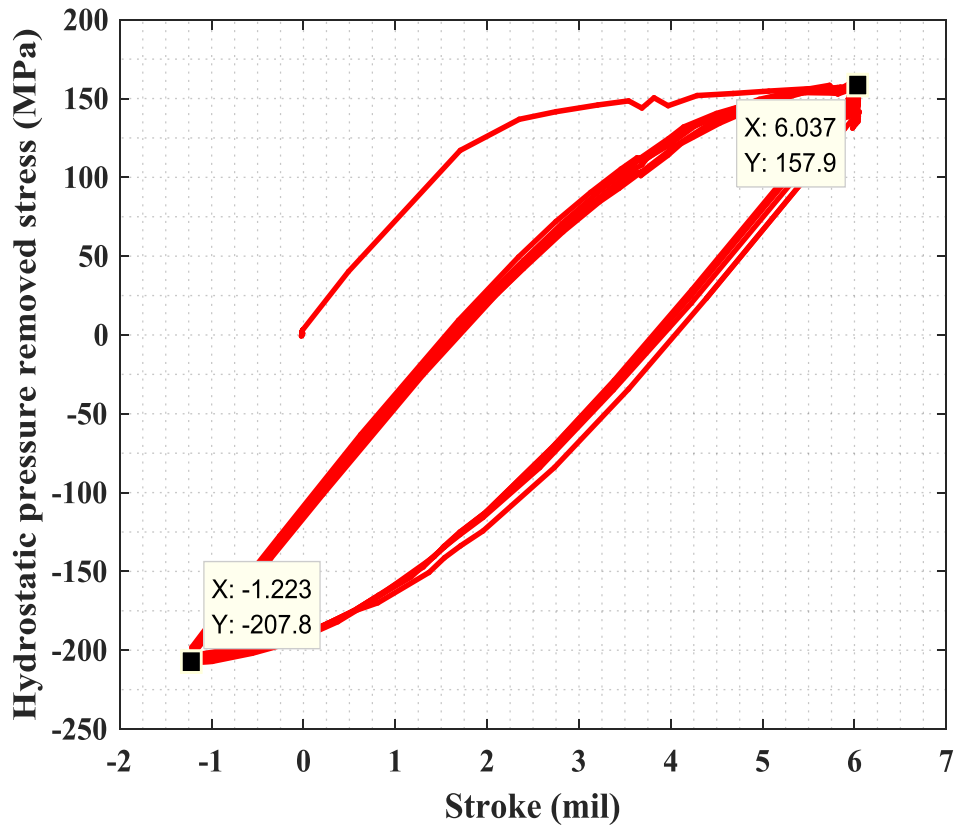


Figure 4. 18 First 5-cycle applied stroke versus observed stress hysteresis loops for EN-F51 fatigue test.

4.4 Design-Basis PWR-Water Fatigue Test (EN-F53)

Based on the mapping parameters discussed in section 4.1 (see Figure 4.6), we conducted another PWR-water environment fatigue test, EN-F53. The test was conducted to simulate the design-basis loading case discussed in our earlier work [1]. In our earlier work [1], we reported results from fatigue tests that were conducted under in-air condition design-basis loading, but the gauge area strain amplitudes were directly controlled. Similar to the grid-load-following loading case (EN-F51), the intended strain inputs for EN-F53 were based on the elastic-plastic FE results simulated under the design-basis loading condition. The details of the FE model can also be found in our earlier work [1]. Figure 4.19 shows the applied stroke input and the desired gauge area strain for EN-F53. Figure 4.20 shows a comparison of applied stroke rate and the desired gauge area strain rate for a single cycle. Figure 4.21 shows the observed stress for the entire fatigue life. Figures 4.22 and 4.23, respectively, show the first 5-cycle applied stroke inputs and observed stress. Figure 4.24 shows the first 5-cycle applied stroke versus observed stress hysteresis loops. The observed fatigue life for the EN-F53 specimen was 7,810 fatigue cycles.

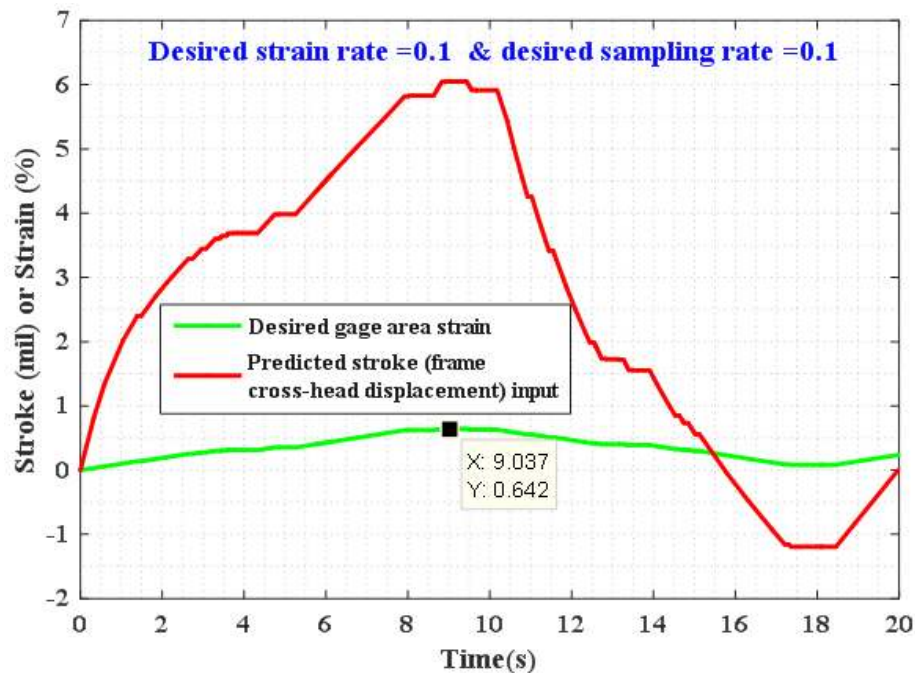


Figure 4. 19 Applied stroke input and the desired gauge area strain for single-cycle design-basis type loading in EN-F53 fatigue test.

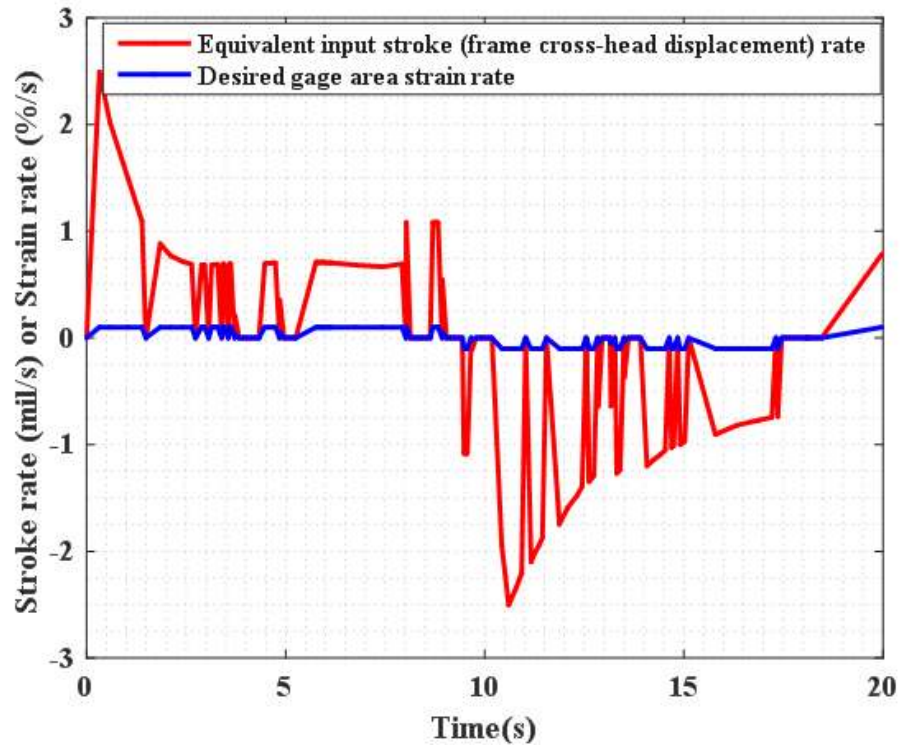


Figure 4. 20 Applied stroke rate and the desired gauge area strain rate for single-cycle design-basis type loading in EN-F53 fatigue test.

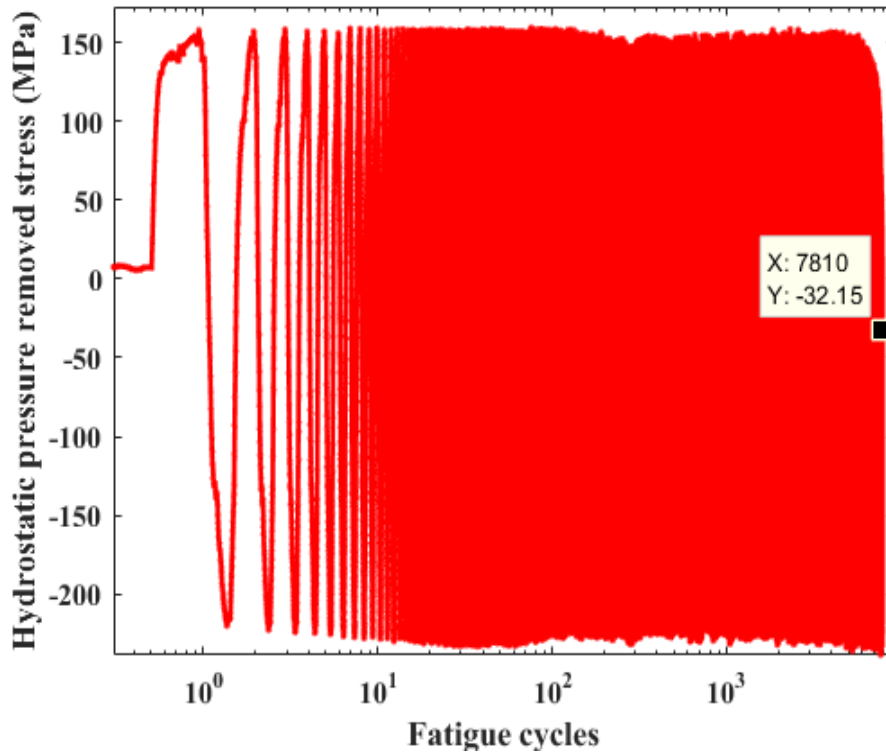


Figure 4. 21 Observed stress for the entire life for EN-F53 fatigue test.

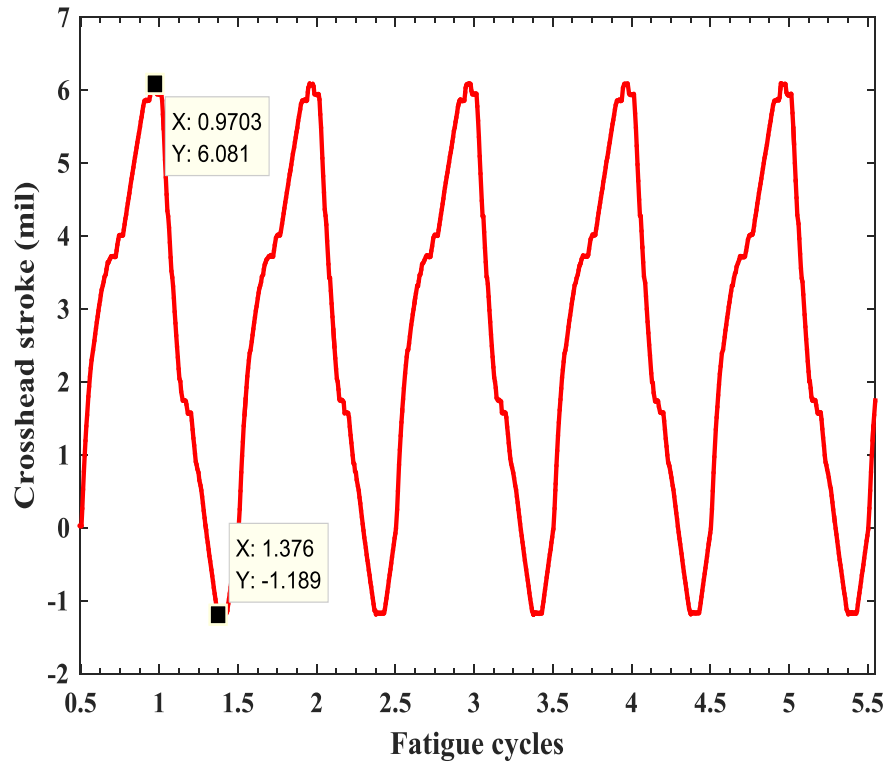


Figure 4. 22 First 5-cycle design-basis loading condition applied stroke input for EN-F53 fatigue test.

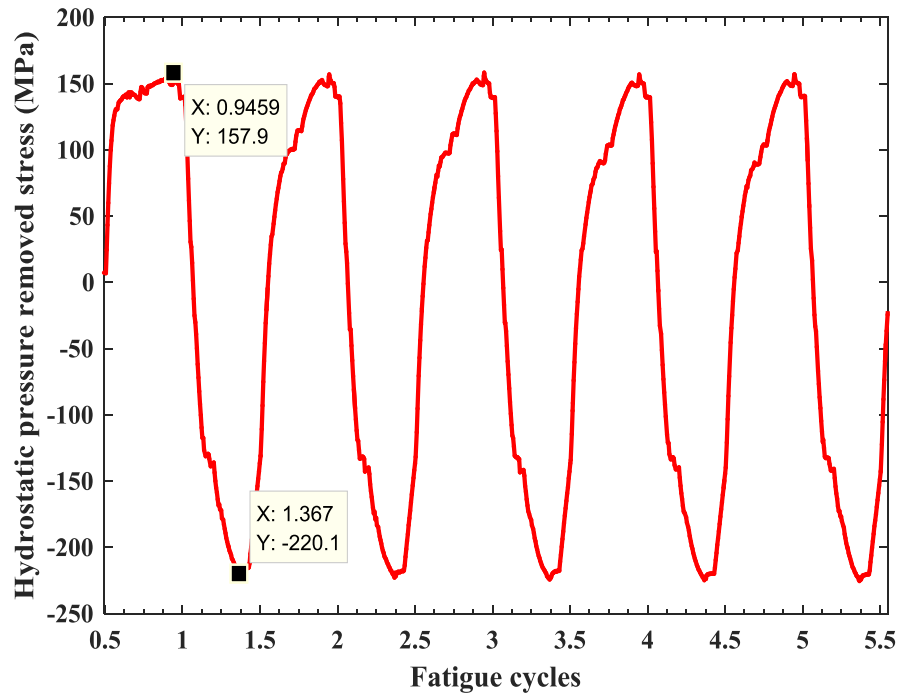


Figure 4. 23 First 5-cycle observed stress for EN-F53 fatigue test.

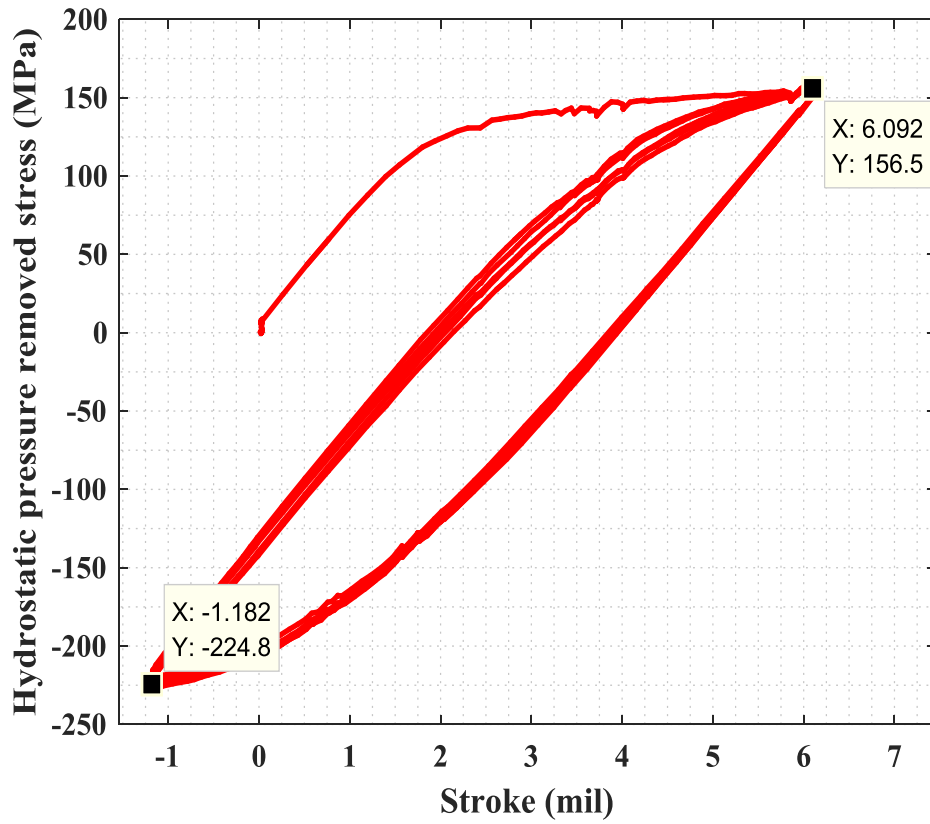


Figure 4. 24 First 5-cycle applied stroke versus observed stress (hysteresis loop) for EN-F53 fatigue test.

5 Deterministic End-of-Life Estimation Using ASME and NURGE-6909 Based Approaches

This section presents the ASME code [24,25] procedure for fatigue life estimation under the in-air condition. In addition, the procedure is discussed for determining the environmental correction factor to estimate the fatigue life under the PWR condition based on NUREG-6909/Rev.1 [26]. On the basis of these procedures, end-of-life was estimated for design-basis and grid-load-following loading cases. The ASME and NUREG-6909 approaches are based on finite element (FE) model results. The FE model results for the design-basis loading case were discussed in our earlier report [1], whereas for the grid-load-following cases, the results are discussed in section 3 of this report. The estimated fatigue lives are compared with the corresponding experimental results either discussed in our earlier report [1] or in section 4 of this report. A summary of the ASME and NUREG-6909 approaches, a discussion of the accompanying test case results, and the way forward follow.

5.1 Article KD-3 of ASME Code Procedure for In-Air Fatigue Evaluation

Article KD-3 of the ASME code (Section VIII-Division 3 of ASME code 2013 version) presents a traditional fatigue evaluation approach for pressure vessels and components under in-air conditions. The procedures relevant to the discussed surge-line fatigue evaluation cases are briefly summarized below:

Step 1: Perform the elastic stress analysis (e.g., using FE computer models) of the component in question.

Step 2: Determine the values of three principal stress components ($\sigma_{i,i=1,2,3}$; σ_1 - maximum, σ_2 - mid, and σ_3 - minimum principal stress components) at the points being investigated (e.g., at a structural stress hotspot) for the complete operating cycles (e.g., for complete reactor fuel cycle consisting of heat-up, power operation, and cool-down loading sequences).

Step 3: Estimate the alternating stress intensities ($S_{alt_{ij}}$) using a combination of principal stress components discussed in step 2. This is done as follows:

$$S_{alt_{ij},i=1,2,3,j=1,2,3} = \frac{1}{2}(S_{ij_{max}} - S_{ij_{min}}) \quad (5.1)$$

where,

$$S_{ij_{max}} = \max \{(\sigma_1 - \sigma_1), (\sigma_2 - \sigma_3), (\sigma_3 - \sigma_1)\} \quad (5.2)$$

$$S_{ij_{min}} = \min \{(\sigma_1 - \sigma_1), (\sigma_2 - \sigma_3), (\sigma_3 - \sigma_1)\} \quad (5.3)$$

The absolute magnitudes of the alternating stress intensities ($S_{alt_{ij}}$), i.e., $|S_{alt_{12}}|$, $|S_{alt_{23}}|$, and $|S_{alt_{31}}|$, are time-dependent (i.e., they depend on the loading history or loading time), and the shear stresses are to be further processed/corrected (if necessary) for fatigue analysis.

Step 4: Estimate the mean stress ($\sigma_{mm_{ij}}$) for mean stress correction (if any) of alternating stress intensities ($S_{alt_{ij}}$). First, the mean stress has to be estimated based on the following criteria:

a) Autofrettaged vessel or non-autofrettaged vessel with compressive mean stress

i) If $S_{ij_{max}} < S_y$ and $S_{ij_{min}} > -S_y$ with S_y is the yield stress, then

$$\sigma_{nm_{ij,i=1,2,3,j=1,2,3}} = \frac{1}{2}(\sigma_{n-ij_{max}} + \sigma_{n-ij_{min}}) \quad (5.4)$$

where $\sigma_{n-ij,i=1,2,3,j=1,2,3}$ are stresses normal to the plane of the maximum shear stress associated with the above-discussed alternating stress intensities ($S_{alt_{ij}}$) and are as given below:

$$\sigma_{n-ij,i=1,2,3,j=1,2,3} = \frac{1}{2}(\sigma_{i,i=1,2,3} + \sigma_{j,j=1,2,3}) \quad (5.5)$$

ii) If alternating stress intensities $S_{alt_{ij}} \geq S_y$ with S_y is the yield stress, then

$$\sigma_{nm_{ij,i=1,2,3,j=1,2,3}} = 0 \quad (5.6)$$

b) Non-autofrettaged vessel with tensile mean stress

iii) If $S_{ij_{max}} < S_y/2$ and $S_{ij_{min}} > -S_y/2$ with S_y is the yield stress, then

$$\sigma_{nm_{ij,i=1,2,3,j=1,2,3}} = \frac{1}{2}(\sigma_{n-ij_{max}} + \sigma_{n-ij_{min}}) \quad (5.7)$$

where

$$\sigma_{n-ij,i=1,2,3,j=1,2,3} = \frac{1}{2}(\sigma_{i,i=1,2,3} + \sigma_{j,j=1,2,3}) \quad (5.8)$$

iv) If alternating stress intensities $S_{alt_{ij}} \geq S_y/2$ with S_y is the yield stress, then

$$\sigma_{nm_{ij,i=1,2,3,j=1,2,3}} = 0 \quad (5.9)$$

If items i-iv do not apply, an appropriate elastic-plastic analysis (based on article KD-3 of code) procedure has to be performed to estimate the mean stress ($\sigma_{nm_{ij}}$).

Step 5: Estimate the mean stress corrected stress, which is called the “equivalent alternating stress intensity” ($S_{eq_{ij}}$) and is expressed as follows:

$$S_{eq_{ij}} = S_{alt_{ij}} \frac{1}{1 - \frac{\beta \sigma_{nm_{ij}}}{S'_a}} \quad (5.10)$$

where S'_a is the allowable amplitude of the alternating stress component when $\sigma_{nm} = 0$ and $N = 10^6$ cycles (beyond that is the regime of high cycle fatigue). The value of β shall be 0.2 for nonwelded construction forged with carbon or low alloy steel. The value of β shall be 0.2 for $\sigma_{nm_{ij}} < 0$ and 0.5 for $\sigma_{nm_{ij}} > 0$ for 17-4 PH or 15-5 PH stainless steel nonwelded construction using forging or bar. However, for nonwelded construction made of carbon or low alloy steels having an ultimate tensile strength (S_u) less than 90 ksi (620 MPa) and for austenitic stainless steel, effects of mean stresses are already incorporated into the ASME design fatigue curve. That means for the 316SS base metal PWR surge line,

$$S_{eq_{ij}} = S_{alt_{ij}} \quad (5.11)$$

Note that Eq. 5.10 is based on or has similar format as the Goodman formula, which is as follows:

$$\frac{S_{altij}}{S_{eqij}} + \frac{\sigma_{nmij}}{S_u} = 1 \quad \text{or} \quad S_{eqij} = S_{altij} \frac{1}{1 - \frac{\sigma_{nmij}}{S_u}} \quad (5.12)$$

Comparing Eqs. 5.10 and 5.12 we can see that the allowable amplitude of the alternating stress component is $S'_a = S_u/\beta$.

Step 6: Estimate the elastic modulus correction factor (E_{corr}). In general, the ASME code fatigue curves (S-N curves) have been derived from fatigue test data. The fatigue tests have been conducted with polished unnotched specimens in dry air and at room temperature under strain-controlled (push-pull) loading with zero mean stress ($\sigma_{nm} = 0$). Hence, to use the ASME code fatigue curve for fatigue life estimation at a different temperature (i.e., other than room temperature), the equivalent stress (S_{eqij}) estimated in step 5 has to be corrected appropriately by multiplying the following factor:

$$E_{corr} = \frac{E_{curve}}{E_{analysis}} \quad (5.13)$$

Step 7: Estimate the fatigue penalty factor (K_e). The ASME code design analysis methodology (NB-3200) provides a method called the “simplified elastic-plastic analysis method,” which allows the correction of elastic analysis based stress for fatigue evaluation without performing full elastic-plastic stress analysis. According to this simplified elastic-plastic analysis procedure (NB-3228.5 of ASME BPVC III.1.NB-2015), the value of stress amplitude used for entering the design fatigue curve has to be multiplied by the fatigue penalty factor (K_e). This factor is calculated as follows:

$$K_e = \begin{cases} 1 & \text{if } S_n \leq 3S_m \\ 1 + \frac{1-n}{n(m-1)} \left(\frac{S_n}{3S_m} - 1 \right) & \text{if } 3S_m < S_n < 3mS_m \\ \frac{1}{n} & \text{if } S_n \geq 3mS_m \end{cases} \quad (5.14)$$

In Eq. 5.14, S_n is range of primary-plus-secondary stress, and the variables m and n are material parameters as given in Table NB-3228.5(b)-1, where n represents the strain hardening exponent of the material. For austenitic stainless steels $m = 1.7$ and $n = 0.3$. This leads to a maximum K_e of $\frac{1}{n} = 3.333$ when $S_n/3S_m \geq (m = 1.7)$. In general, in Eq. 5.14 the parameter S_m has to be estimated from the following expression:

$$S_m = \min \left\{ \begin{array}{l} \frac{1}{3} S_u \\ \frac{2}{3} S_y \end{array} \right\} \quad (5.15)$$

Note that based on the ASME code assumption, when S_n is closed or less than $3S_m$, small plastic zones will be well contained by the surrounding structure, which will be predominantly elastic and is assumed to be shakedown to elastic behavior [28]. According to the ASME code KD-323 (“Alternative Method for Evaluating the Fatigue Penalty Factor”), K_e can also be calculated from the following equation.

$$K_e = \frac{(\Delta \varepsilon_p)_{sp}}{(\Delta \varepsilon_t)_e} \quad (5.16)$$

where $(\Delta\varepsilon_t)_{ep}$ is the equivalent total strain range from elastic-plastic analysis, while $(\Delta\varepsilon_t)_e$ is the equivalent total strain range from elastic analysis. Using the maximum and minimum principal strain histories from elastic-plastic and elastic analyses, we propose to use an equivalent form of Eq. 5.16, which is given as follows:

$$K_\varepsilon = \frac{\max[\varepsilon_1 - \varepsilon_3]_{ep}}{\max[\varepsilon_1 - \varepsilon_3]_e} \quad (5.17)$$

where ε_1 and ε_3 are maximum and minimum principal strains, respectively. Using the data from elastic-plastic and elastic analyses and Eq. 5.17, the value of K_ε can alternatively be found in addition to using Eq. 5.14.

Step 8: Estimate the surface roughness factor (K_r). The ASME code design fatigue curves are, in general, based on test data obtained by conducting fatigue tests of polished specimens. So, for estimating fatigue lives of a component with non-polished surface, a surface roughness factor (K_r) has to be multiplied with the stress intensity. However, for the ASME fatigue curve for stainless steel (KD-320.4), the influence of the surface roughness is already included in the curve, i.e., $K_r = 1$. Therefore, for the fatigue life estimation of the 316SS base metal PWR surge line, a surface roughness factor need not be applied.

Step 9: Estimate the stress amplitude (S_a) using the following expression:

$$S_a = K_r K_\varepsilon E_{corr} \max(S_{sqij}) \quad (5.18)$$

Step 10: Use the stress amplitude (S_a) and the ASME design fatigue curve (e.g., KD-320.4 for stainless steel) to estimate the corresponding in-air fatigue life, N_{air} . The ASME design fatigue curve is shown in Figure 5.1. Note that the design fatigue curve has been derived from fatigue tests (after considering design factors/margins) with polished unnotched specimens in dry air and at room temperature under strain-controlled (push-pull) loading with zero mean stress ($\sigma_{nm} = 0$). The applied strain amplitudes have been multiplied by the elastic modulus and a design margin to arrive at the equivalent stress amplitude magnitudes.

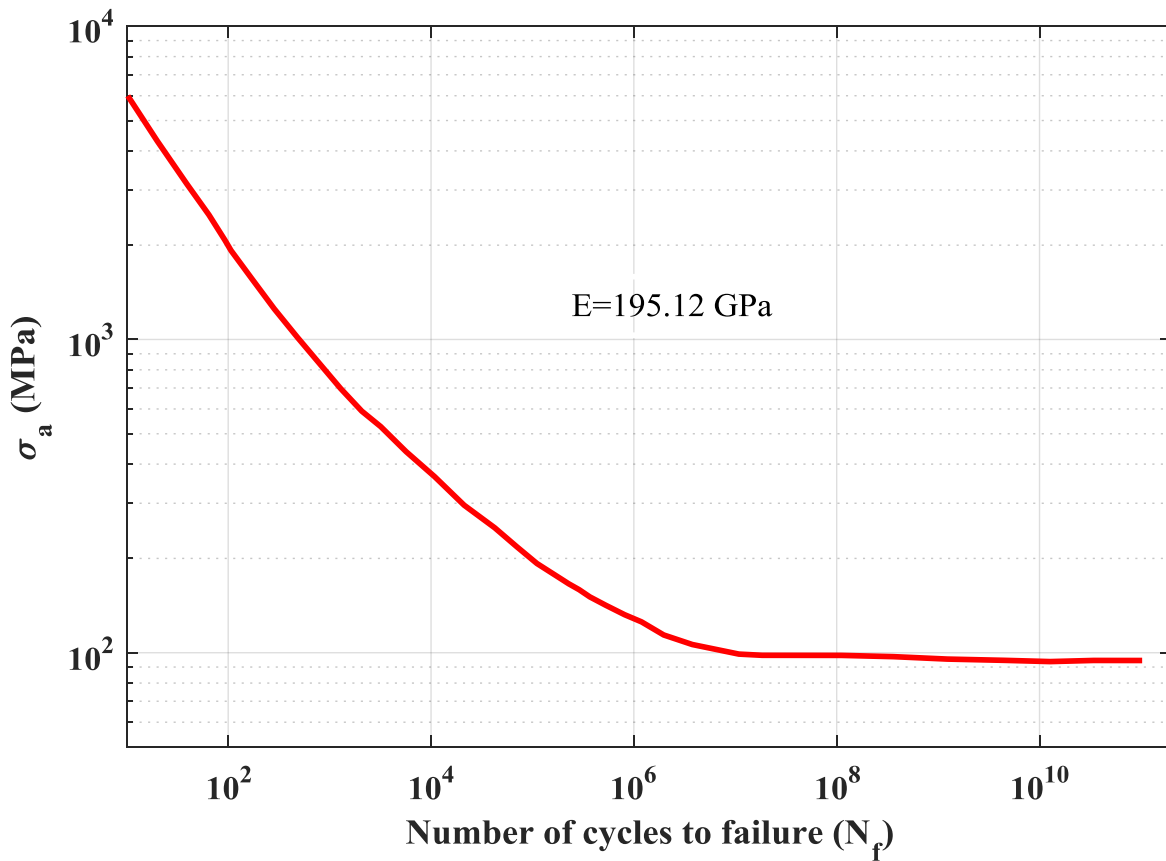


Figure 5. 1 ASME design fatigue curve (2010 code version) for austenitic stainless steel at room temperature [24, 29].

5.2 NUREG-6909 Procedure for PWR-Water Environment Fatigue Evaluation

Once the in-air fatigue life (N_{air}) has been estimated, the PWR water environment life (N_w) can be estimated from the following expression:

$$N_w = \frac{N_{air}}{F_{en}} \tag{5.19}$$

where F_{en} is the environmental fatigue correction factor. According to NUREG-6909, Rev.1 [26], F_{en} for austenitic steel can be determined from:

$$F_{en} = \exp(0.734 - \theta' O' \epsilon') \tag{5.20}$$

where θ' , O' , and ϵ' are transformed temperature, dissolved oxygen (DO), and strain rate, respectively, as follows:

$$\begin{aligned}
 \theta' &= 0 && (\theta < 150 \text{ }^\circ\text{C}) \\
 \theta' &= \frac{(T-150)}{175} && (150 \text{ }^\circ\text{C} \leq \theta < 325 \text{ }^\circ\text{C}) \\
 \theta' &= 1 && (\theta \geq 325 \text{ }^\circ\text{C})
 \end{aligned} \tag{5.21}$$

$$\begin{aligned}
 \dot{\epsilon}' &= 0 && (\dot{\epsilon} > 0.4\%/s) \\
 \dot{\epsilon}' &= \ln\left(\frac{\dot{\epsilon}}{0.4}\right) && (0.0004 \leq \dot{\epsilon} \leq 0.4\%/s) \\
 \dot{\epsilon}' &= \ln\left(\frac{0.0004}{0.4}\right) && (\dot{\epsilon} < 0.0004\%/s)
 \end{aligned} \tag{5.22}$$

$$O' = 0.281 \quad (\text{all DO levels}) \tag{5.23}$$

5.3 Results for Fatigue Lives of PWR Surge Line

The fatigue lives of the PWR surge line under design basis and grid-load-following loading were estimated by using the above discussed ASME code and NUREG-6909 based procedures. The alternating stress intensities ($S_{air,ij}$), which are the basic input for the fatigue evaluation, were estimated based on single-cycle thermal-mechanical stress analysis of a PWR surge line under design-basis and grid-load-following thermal loading cycles. The discussed results demonstrate the overall approach and were checked against the respective results obtained from the corresponding fatigue tests with uniaxial test specimens. The assumed loading and boundary conditions may not be as detailed as those for the actual reactor; however, through this example we would like to discuss the approach (through example case results) and bridge the gaps associated with the fatigue evaluation approach. For the design-basis loading, the details of the FE model and in-air experiment results were discussed in our April 2018 report [1]. The corresponding PWR water environment experiment results are discussed in section 4 of this report. For the grid-load-following loading, the details of the FE model results are discussed in section 3 of this report, whereas the in-air and PWR-water environment experiment results are discussed in section 4 of this report. The material properties used for the FE models and for the discussed fatigue evaluation approaches are given in Table 5.1. The fatigue life estimation for both loading cases is discussed below.

Table 5. 1 Material properties for 316 SS at 300 °C.

Property	Value
$E_{analysis}$: Elastic modulus (GPa) from ANL test	157.92
S_y : 0.2 % offset yield stress (MPa) from ANL test	155.77
S_{el} : Elastic limit (MPa) from ANL test	130.73
C_1 : Chabochee parameter (MPa) from ANL test	10085
γ : Chabochee parameter (MPa) from ANL test	149.97
S_u : Tensile strength (MPa) from ANL test	418.717
$\frac{1}{3}S_u$ (MPa)	139.57
$\frac{2}{3}S_y$ (MPa)	103.85
$S_m = \min\{\frac{1}{3}S_u, \frac{2}{3}S_y\}$ in (MPa)	103.85
m (Eq. 5.14 fatigue penalty factor that holds good for temperature below 425 °C) from Table NB-3228.5(b)-1 of ASME code	1.7
n (Eq. 5.14 fatigue penalty factor that holds good for temperature below 425 °C) from Table NB-3228.5(b)-1 of ASME code	0.3
$3S_m$ (MPa)	311.54
$3mS_m$ (MPa)	529.62

5.3.1 In-air and PWR-water environment fatigue lives under design-basis loading case

The in-air life estimation using the discussed ASME code approach requires the alternating stress intensity ($S_{alt_{ij}}$) histories. This is equivalent to estimating the maximum shear stress ($=\frac{1}{2}(\sigma_1 - \sigma_3)$) histories. Figures 5.2 and 5.3 show the maximum shear stress histories based on elastic and elastic-plastic stress analyses. For the fatigue penalty factor (K_σ) using Eq. 5.17 we also need the maximum shear strain ($=\frac{1}{2}(\epsilon_1 - \epsilon_3)$) histories. Figures 5.4 and 5.5 show the maximum shear strain histories based on the elastic and elastic-plastic stress analyses. In addition, to estimate the transformed strain using Eq. 5.22, we need to have strain rate information. Figures 5.6 and 5.7 show the maximum shear strain rate based on the elastic and elastic-plastic stress analyses. Note that the ASME code approach for in-air fatigue evaluation requires shear stress amplitude based on elastic stress analysis. Figure 5.2 indicates that the maximum shear stress amplitude is 523.7 MPa. The maximum shear stress amplitude based on the elastic-plastic analysis, as determined from Figure 5.3, is 90.56 MPa. This value shows that the stress amplitude based on the elastic analysis is much higher than that based on the elastic-plastic analysis. Nonetheless, following the ASME code approach, the shear stress amplitude based on the elastic analysis was considered further for fatigue evaluation. The fatigue penalty factors were estimated from Eqs. 5.14 and 5.17 and found to be 3.333 and 1.3108, respectively. The estimated in-air fatigue lives are shown in Table 5.2. Note that the elastic FE simulated stress range (S_m in Eq. 5.14) is 1047.4 MPa (which is two times the stress amplitude of 523.7 MPa), which is higher than the $3mS_m$ limit. This leads to a maximum fatigue penalty factor of $1/n = 3.333$. For fatigue life estimation in the PWR-water

environment, the environmental correction factor (F_{sn}) was estimated from the maximum strain rate computed from the elastic analysis, 8.266×10^{-5} %/s (Figure 5.6), and a strain rate of 0.1%/s was considered for actual validation fatigue experiments (EN-F53). The estimated in-air and PWR-water fatigue lives for the design-basis loading case are given in Table 5.2.

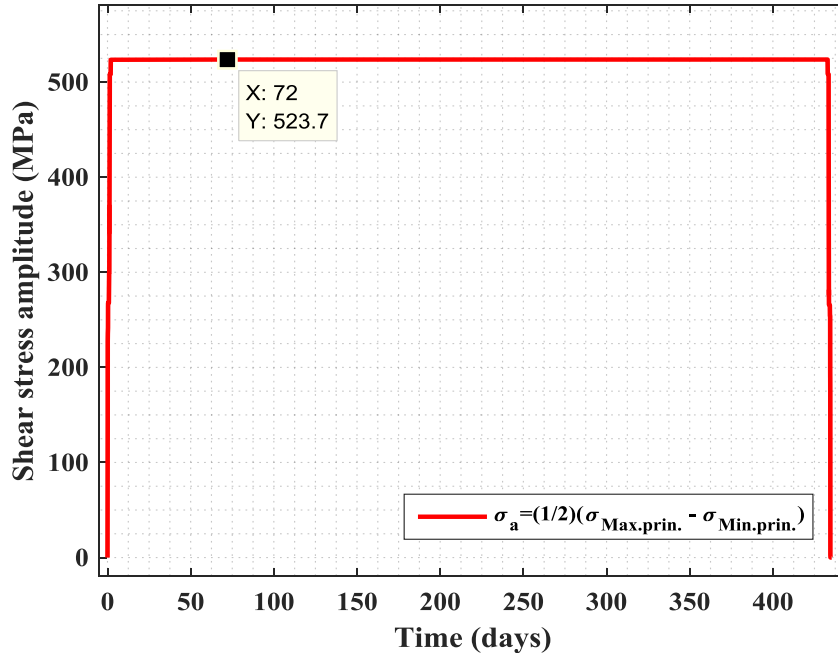


Figure 5. 2 Elastic FE simulated maximum shear stress ($= \frac{1}{2}(\sigma_1 - \sigma_3)$) histories under design-basis loading case.

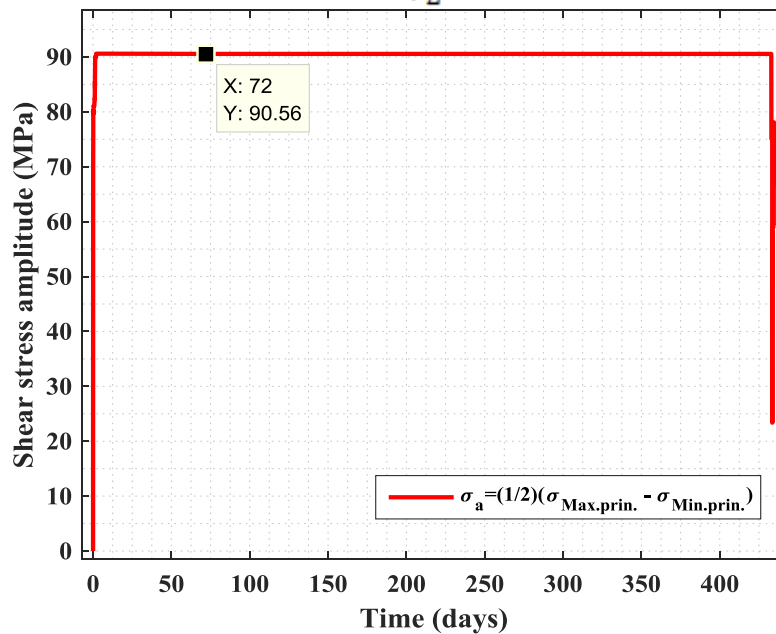


Figure 5. 3 Elastic-plastic FE simulated maximum shear stress ($= \frac{1}{2}(\sigma_1 - \sigma_3)$) histories under design-basis loading case.

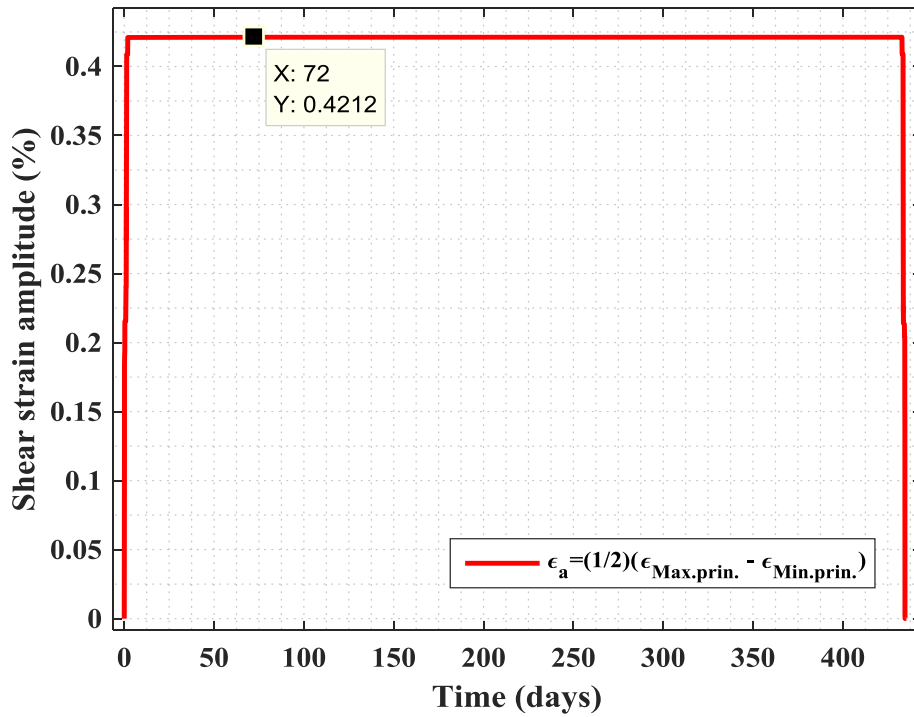


Figure 5. 4 Elastic FE simulated maximum shear strain ($=\frac{1}{2}(\epsilon_1 - \epsilon_3)$) histories under design-basis loading case.

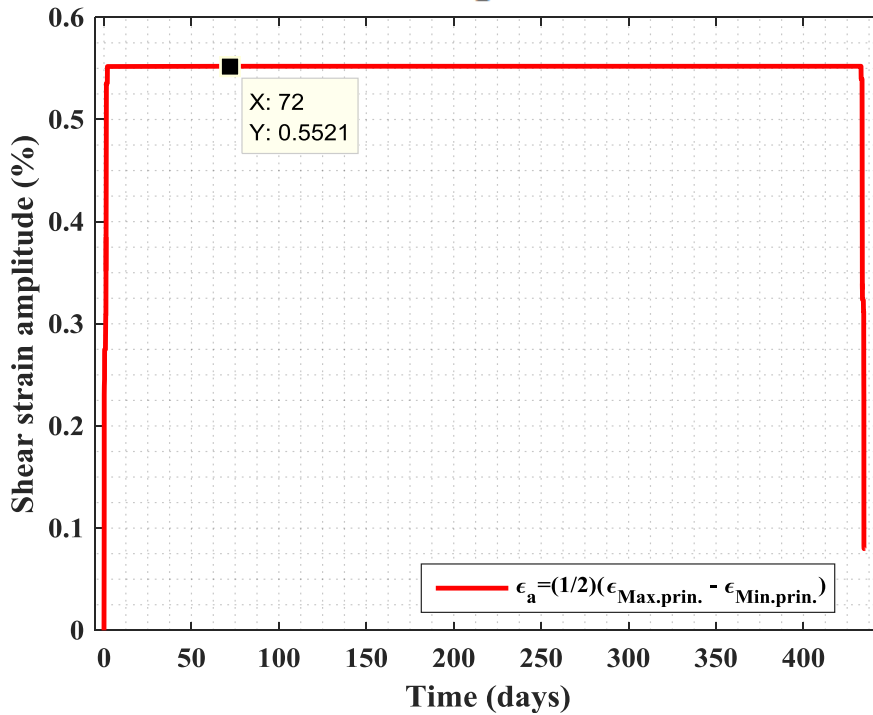


Figure 5. 5 Elastic-plastic FE simulated maximum shear strain ($=\frac{1}{2}(\epsilon_1 - \epsilon_3)$) histories under design-basis loading case.

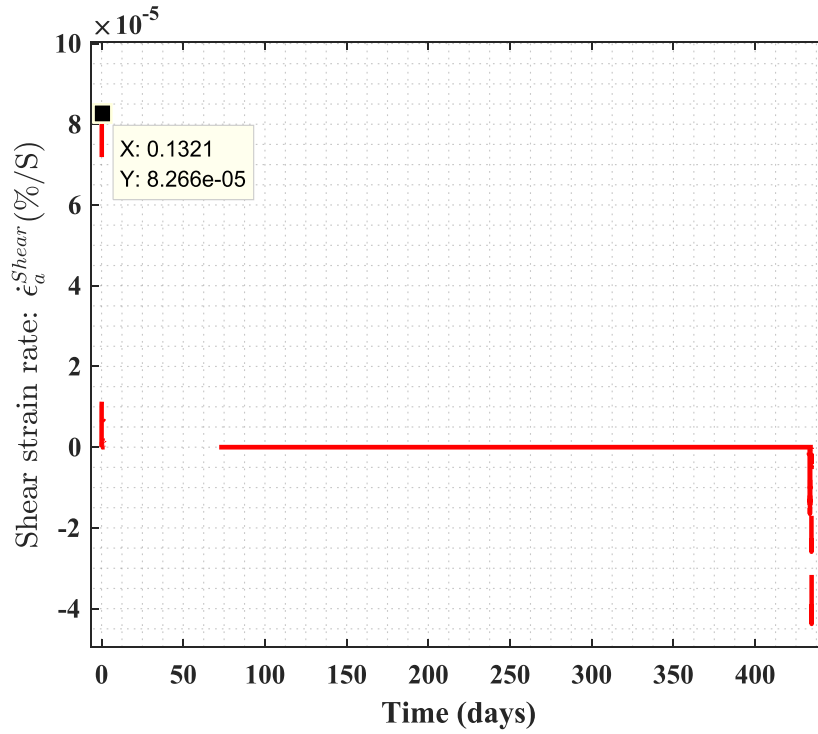


Figure 5.6 Elastic FE simulated maximum shear strain rate ($=\frac{1}{2}(\dot{\epsilon}_1 - \dot{\epsilon}_3)$) histories under design-basis loading case.

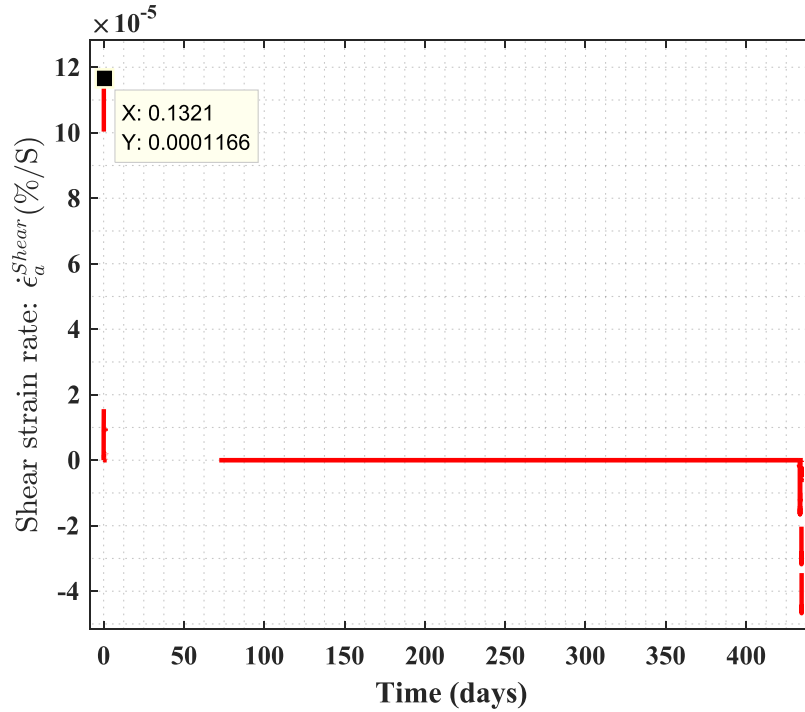


Figure 5.7 Elastic-plastic FE simulated maximum shear strain rate ($=\frac{1}{2}(\dot{\epsilon}_1 - \dot{\epsilon}_3)$) histories under design-basis loading case.

Table 5.2 Fatigue lives under design-basis loading.

Fatigue penalty factor (K_ϵ)	Elastic FE simulated max. shear stress amplitude (MPa)	ASME code (Eq. 5.18) based stress amplitude : S_a (MPa)	ASME code based in-air life	ANL cycle-by-cycle fully mechanistic model life	ANL in-air fatigue experiment (ET-F48) life	NUREG-6909 (Eq. 5.19) based PWR water life	ANL PWR-water fatigue experiment (EN-F53) life
1	523.7	649.98	1634	15,400 [1]	15,966 (ET-F48, refer [1], Strain-controlled test, with polished (up to 0.3 μm) specimen)	149 [#] (562 ^{##})	7,810 (EN-F53, refer section 4, Stroke-controlled test, with machine fabricated as it is form specimen)
3.333 (Based on Eq. 5.14)		2166.6	87			8 [#] (30 ^{##})	
1.3108 (Based on Eq. 5.17)		851.98	765			70 [#] (263 ^{##})	

[#] Considering $F_{en} = 10.999$, with $\dot{\epsilon}_{\epsilon I} = 8.266e-05$ %/s (predicted strain rate the PWR surge line would experience).

^{##} Considering $F_{en} = 2.9093$, with $\dot{\epsilon}_{\epsilon I} = 0.1$ %/s (approximate strain rate during equivalent uniaxial specimen experiment).

5.3.2 In-air and PWR-water environment fatigue lives under grid-load-following loading

Similar to the design-basis loading cycle, the in-air and PWR environment fatigue lives under grid-load-following were also estimated. This is based on model results from both elastic and elastic-plastic stress analysis. The corresponding results, which are required for the fatigue evaluation, are shown in Figures 5.8 to 5.13.

Figures 5.8 and 5.9 show the maximum shear stress histories based on elastic and elastic-plastic stress analyses ($=\frac{1}{2}(\sigma_1 - \sigma_3)$). Figures 5.10 and 5.11 show the maximum shear strain ($=\frac{1}{2}(\epsilon_1 - \epsilon_3)$) histories based on elastic and elastic-plastic stress analyses. Figures 5.12 and 5.13 show the maximum shear strain rate histories based on the elastic and elastic-plastic stress analyses.

From Figure 5.8 the maximum shear stress amplitude is 523.5 MPa, which is very similar to the shear stress amplitude obtained under design-basis loading. The corresponding maximum shear stress amplitude in Figure 5.9 is 90.7 MPa. The maximum shear strain amplitude for elastic (Figure 5.10) and elastic-plastic (Figure 5.11) simulations are 0.4212% and 0.5521%, respectively. These stress and strain amplitude results in the case of grid-load-following loading are similar to those of the design-basis loading and produce identical fatigue life estimations obtained by using ASME and NUREG-6909 based approaches. This is because the ASME and the NUREG-6909 based approach is based on single-cycle stress analysis results. Nevertheless, the estimated in-air and PWR-water fatigue lives for the grid-load-following loading case are given in Table 5.3.

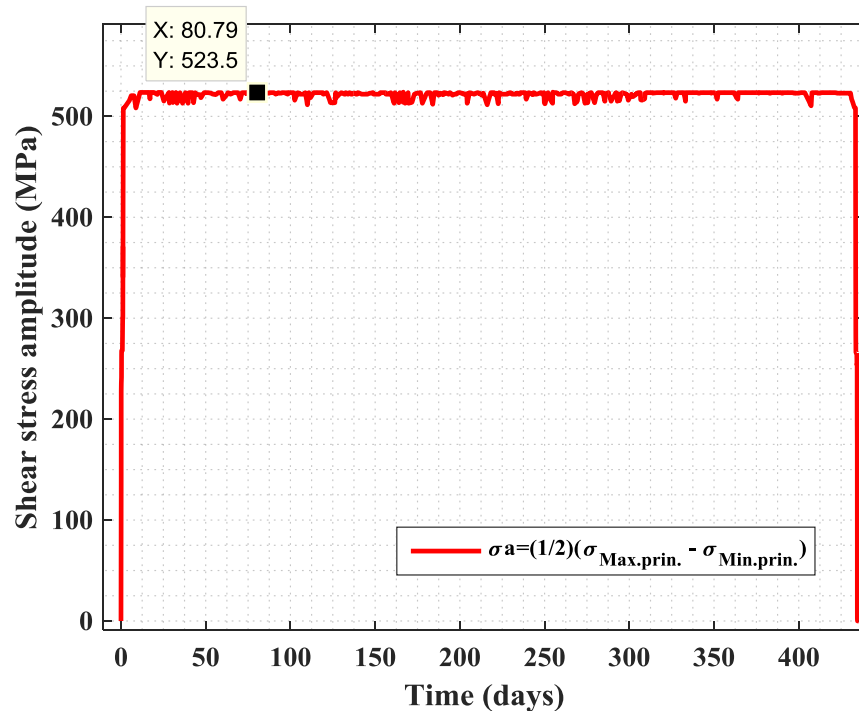


Figure 5. 8 Elastic FE simulated maximum shear stress ($= \frac{1}{2}(\sigma_1 - \sigma_3)$) histories under grid-load-following loading case.

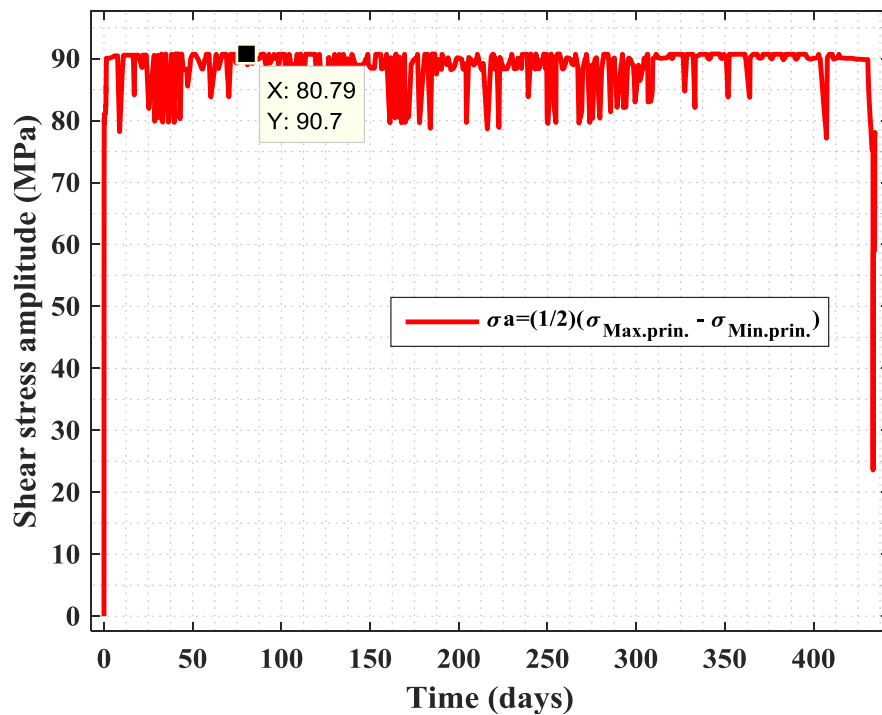


Figure 5. 9 Elastic-plastic FE simulated maximum shear stress ($= \frac{1}{2}(\sigma_1 - \sigma_3)$) histories under grid-load-following loading case.

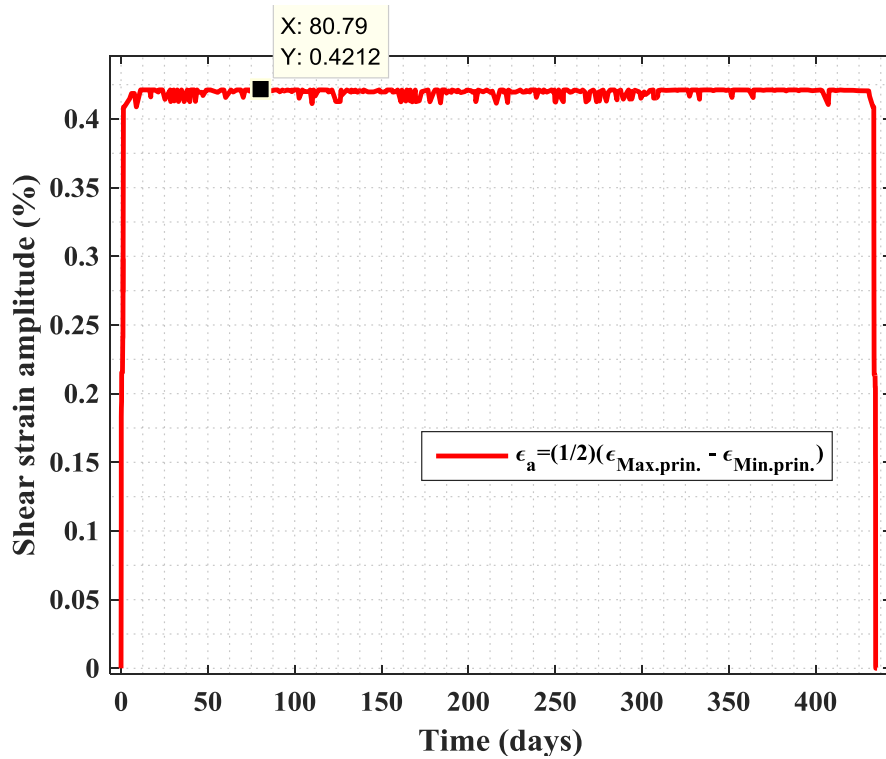


Figure 5.10 Elastic FE simulated maximum shear strain ($= \frac{1}{2}(\epsilon_1 - \epsilon_3)$) histories under grid-load-following loading case.

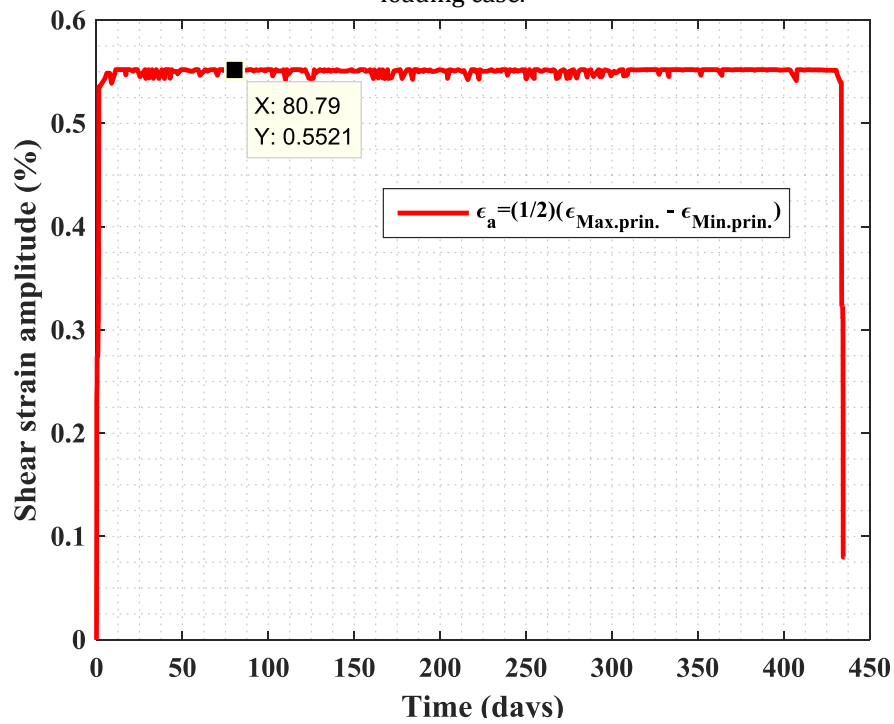


Figure 5.11 Elastic-plastic FE simulated maximum shear strain ($= \frac{1}{2}(\epsilon_1 - \epsilon_3)$) histories under grid-load-following loading case.

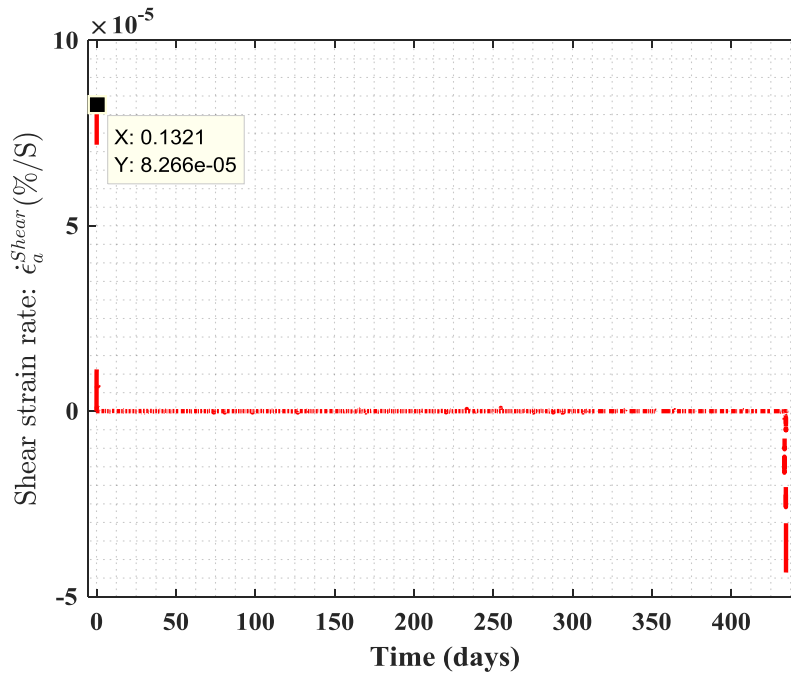


Figure 5.12 Elastic FE simulated maximum shear strain rate ($=\frac{1}{2}(\dot{\epsilon}_1 - \dot{\epsilon}_3)$) histories under grid-load-following loading case.

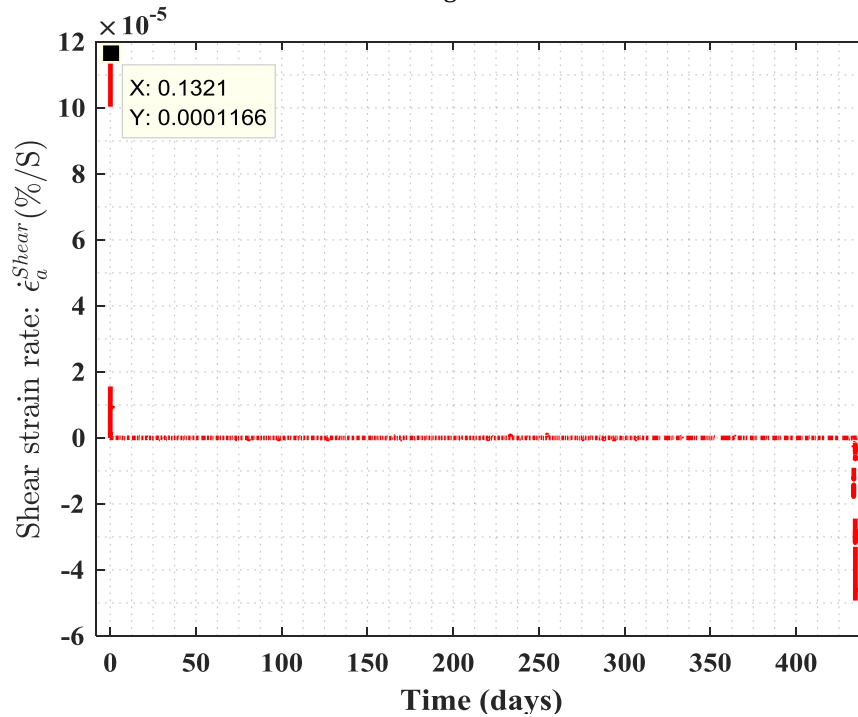


Figure 5.13 Elastic-plastic FE simulated maximum shear strain ($=\frac{1}{2}(\dot{\epsilon}_1 - \dot{\epsilon}_3)$) histories under grid-load-following loading case.

Table 5.3 Fatigue lives under grid-load-following loading

Fatigue penalty factor (K_{ϵ})	Elastic FE simulated max. shear stress amplitude (MPa)	ASME code (Eq. 5.18) based stress amplitude: S_a (MPa)	ASME code based in-air life	ANL cycle-by-cycle fully mechanistic model life	ANL in-air fatigue experiment (ET-F50) life	NUREG-6909 (Eq. 5.19) based PWR water life	ANL PWR-water fatigue experiment (EN-F51) life
1	523.5	649.98	1634	NA [‡]	30,008 [⊗] (ET-F50, refer section 4, Stroke-controlled test, with polished (up to 0.3 μ m) specimen)	149 [#] (562 ^{##})	9,999 (EN-F51, refer section 4, Stroke-controlled test, with polished (up to 0.3 μ m) specimen)
3.333 (Based on Eq. 5.14)		2165.8	90			8 [#] (31 ^{##})	
1.3108 (Based on Eq. 5.17)		851.98	765			70 [#] (263 ^{##})	

[#] Considering $F_{en} = 10.999$, with $\dot{\epsilon}_{\epsilon I} = 8.266e-05$ %/s (predicted strain rate the PWR surge line would experience).

^{##} Considering $F_{en} = 2.9093$, with $\dot{\epsilon}_{\epsilon I} = 0.1$ %/s (approximate strain rate during equivalent uniaxial specimen experiment).

[⊗] Test hadn't finished.

[‡] Currently not available; may be updated in future.

5.4 Issues with ASME Code In-Air Life Estimation Approach and Suggested Way Forward

Table 5.2 shows the fatigue life estimated using ANL's evolutionary cycle-by-cycle stress analysis under the in-air condition. This table also shows the corresponding experimental in-air and PWR-water environment lives. From these results, it can be seen that the in-air estimated life using the ASME code approach is extremely conservative compared to that of experiment. By contrast, ANL's cycle-by-cycle stress analysis approach produces highly comparable results with the experimental in-air life. We believe the major source of the highly conservative results in the ASME code approach is the stress amplitude based on the elastic stress analysis, which is much higher compared to the more realistic stress amplitudes and their cyclic evolution based on elastic-plastic stress analysis. The conservativeness of ASME based in-air fatigue life is further exaggerated due to the use of the fatigue penalty factor (K_{ϵ}). However, the K_{ϵ} based on elastic-plastic stress analysis (i.e., from Eq. 5.17) estimates less conservative results compared to using the K_{ϵ} estimated based on Eq. 5.14. For example, for the design-basis load, the estimated fatigue life based on the ASME code and K_{ϵ} estimated based on Eq. 5.17 results in an in-air life of 765 cycles. Note that ASME design curves (e.g., Figure 5.1) are generally derived by assuming a factor of 20 in life and factor of 2 in stress amplitude to counter the scatter in the base experiment data [30]. If we use a factor of 20 to convert the in-air predicted design life (of 765 fatigue cycles) to equivalent experiment life, it will result in $765 \times 20 = 15,300$ cycles. This predicted equivalent experiment life is comparable to the observed fatigue life of 15,966 cycles. However, if we follow a similar procedure to convert the ASME in-air predicted life of 90 cycles (based on Eq. 5.14) to equivalent experiment life, the result is $90 \times 20 = 1,800$ cycles, much less than the actual experiment life of 15,966 cycles. In summary, the procedure for ASME in-air fatigue life estimation based on Eq. 5.14 is overly conservative and needs to be reviewed by the code committee. In our view, it is always better

to use ANL's fully mechanistic model for fatigue life estimation; however, for simplicity, if the ASME code approach has to be used for in-air fatigue life estimation, we suggest using K_e based on Eq. 5.17 rather than Eq. 5.14.

With respect to the PWR-water environment, the estimated life under design-basis loading and Eq. 5.14 (refer to Table 5.2) is extremely low. But if we use Eq. 5.17, the estimated PWR environment life would be 70 cycles. With time period of 435.4 days for each fuel cycle (for the discussed cases), the reactor component will have a life of 83.5 years. Note that the PWR environment life of 70 cycles is derived based on the actual simulated strain rates. The simulated strain rates are extremely low, and the environmental effect may be aggressive for a lower strain rate compared to strain rate conditions. For experiment purposes, we had chosen an equivalent strain rate of 0.1%/s, which results in the experimental fatigue life of 7,810 cycles. The corresponding simulated PWR-water life (with 0.1 %/s strain rate) is 263 cycles. If we multiply a factor of 20 (to counter the scatter in design fatigue curve) by this estimated PWR water life, the equivalent experiment life would be $263 \times 20 = 5,260$ cycles. Compared to the actual experiment life of 7,810, the predicted equivalent experiment life is 32.6% lower. Note that the EN-F53 specimen (for design-basis and PWR environment test case) was not polished, and the as-machined form was used for testing. However, the use of the design factor of 20 on life is to counter the effect of surface finish and other scatter-related effects. The above discussion shows that despite using a factor of 20 to convert the predicted life to equivalent life, the results show an inaccuracy of 32.6% lower life. These type of results and analysis show the importance of ANL's fully mechanistic approach to life estimation based on cyclic stress/strain evolution as opposed to depending on a single-cycle stress analysis.

By comparing the results in Table 5.2 (design-basis loading case) with the results in Table 5.3 (grid-load-following loading case), we see a large variation in experimental fatigue lives, although the applied stroke (or equivalent strain) cycles are almost identical. This scatter in life could not be (as discussed above) captured by the ASME code design curve factors (for example, use of a factor of 20 for converting the design life to equivalent experiment life). The scatter in fatigue life could be dependent on additional factors such as individual loading types rather than just surface finish, material microstructure scatter, etc. Note that the design factors are, in general, estimated based on the scatter in end-of-life S~N data, which are primarily obtained from R=-1 type push-pull strain-controlled test data. However, the actual loading cycles are not necessarily similar as R=-1 type loading cycles have a different type of load-sequence effect on material microstructure evolution, resulting in different values of scatter bounds. The life scatter and associated probabilistic fatigue lives appear to be loading case dependent rather than dependent on end-of-life data obtained under a particular loading conditions. Some of the related probabilistic life modeling approaches are discussed in this report and follow.

6 End-of-Life Fatigue Data Based Probabilistic Modeling Using Weibull and Bootstrap Techniques

6.1 Introduction

In this section, we discuss the Weibull analysis of the end-of-life fatigue data. The aim is to predict the reliability or probability of failure of stainless steel based on the end-of-life fatigue data given in the literature. In general, the Weibull distribution [31] is one of the most famous equations in the engineering field [32]. Engineers usually use the Weibull distribution to model the failure time (i.e., lifetime) or strength of a given material in a probabilistic way. Although it is well known that the Weibull distribution is appropriate when the given material is brittle [33], we adopted the Weibull distribution for the fatigue life model because the fatigue specimens were relatively large to apply the *extremal value theorem* [34, 35].

After the model estimation with the Weibull distribution is completed, it is also important to quantify the estimate reliability. In this case, Efron suggested a useful approach named the “bootstrapping” method [36, 37]. This bootstrapping is based on random re-sampling from the empirical cumulative distribution function (CDF) of the original data. Because the bootstrap method does not presume any functional form (e.g., Gaussian distribution) for estimation uncertainty, it can be used for most estimation uncertainty problems, even if the data set contains censored information [38].

Symmetric loading life data from Japan Nuclear Energy System Safety Division report [39] were modeled to estimate the Weibull parameters, the associated best-fit curve (of strain amplitude versus life), the confidence bound of best-fit curve estimation, the scatter associated with the mean or best-fit curve, and the associated failure probability for a given strain amplitude. Later (in section 8), the end-of-life data based on the CDF of fatigue life are compared with the CDF fatigue life estimated based on Markov Chain Monte Carlo (MCCS) and time-series damage states. The theoretical background and results from the associated Weibull analysis are discussed below.

6.2 Weibull Modeling of End-of-Life Fatigue Data from the Literature

We obtained fatigue life test data of austenitic stainless steel [39] through digitizing strain versus life graphs. The testing temperature of the data [39] ranged from 100 to 325 °C in air and 100 to 360 °C in PWR water. These high temperature data include austenitic stainless steel grades such as 316 and 304

SS. Figure 6.1 shows the original strain versus life data for the in-air condition [39]. Figure 6.2 shows the original data for the PWR water condition [39].

Figure 6.1 shows a total of 96 obtained fatigue life data points, which consist of 96 exact (i.e., failed at the time) data. Figure 6.2 shows a total of 203 obtained fatigue life data points, which consist of 199 exact data and 4 right censored (i.e., not failed at the time) data. The black solid lines in both Figures 6.1 and 6.2 are the Tsutsumi curve [39] which represents the empirical relationship between ϵ_a and fatigue life in air at room temperature (N_{Air-RT}). This curve is the same in both Figures 6.1 and 6.2 and considered as the reference curve. The equation of the Tsutsumi curve under in-air and room-temperature conditions is as follows:

$$\text{Tsutsumi curve: } \epsilon_a = 23N_{Air-RT}^{-0.457} + 0.11 \tag{6.1}$$

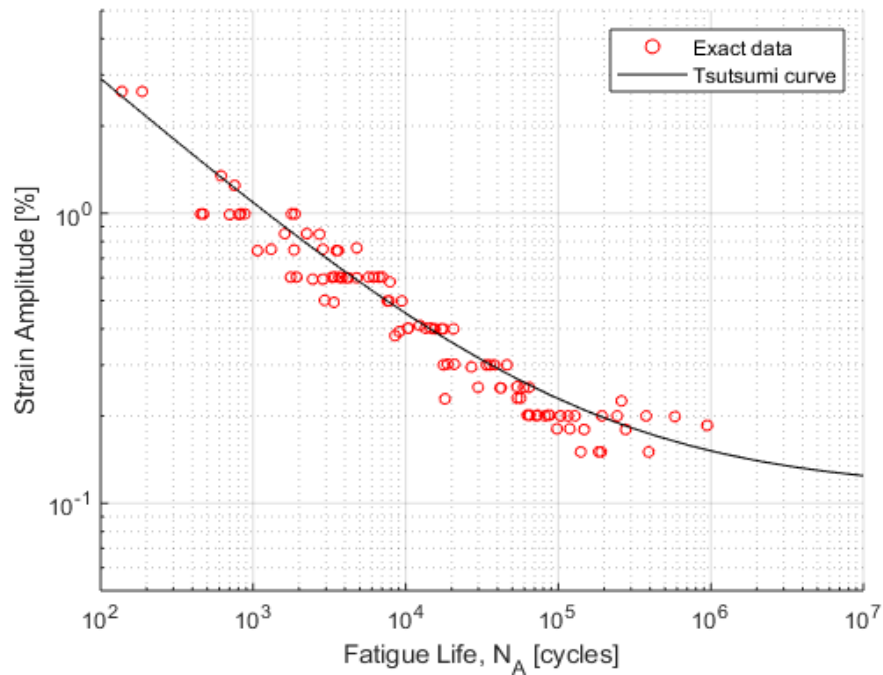


Figure 6. 1 Digitized in-air strain versus life data as obtained from [39]

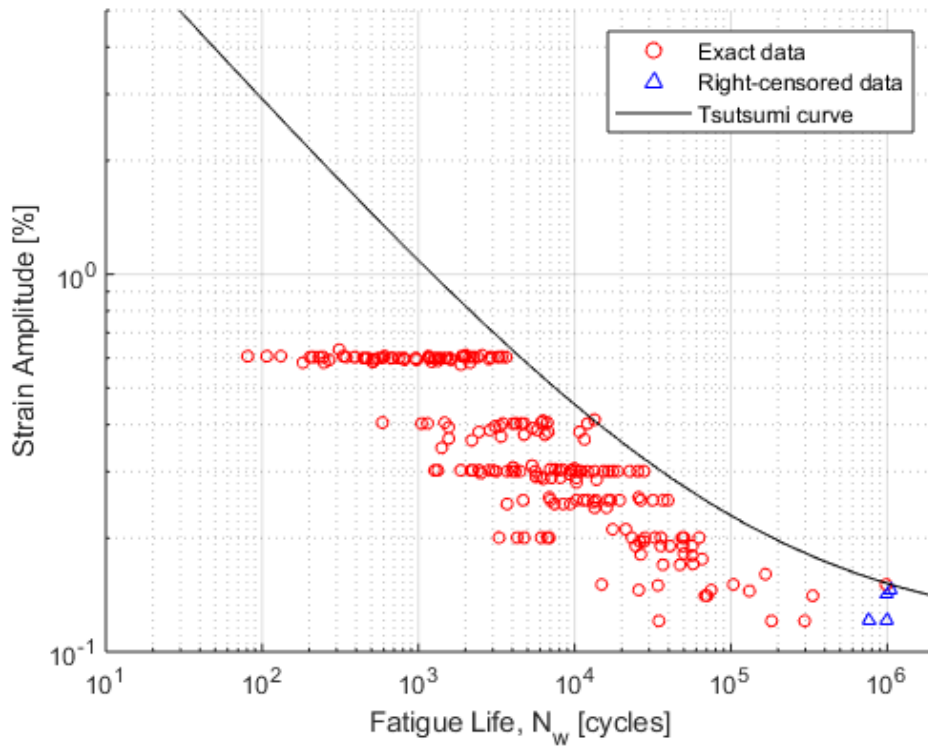


Figure 6.2 Digitized PWR-water strain versus life data as obtained from [39].

6.3 End-of-life Fatigue Modeling Based on Weibull Distribution

The goal of this section is to determine a functional form of the fatigue life model in air and PWR water at high temperature. Figures 6.1 and 6.2 indicate that ε_a (or ε_w) strongly affects N_A (or N_W). Therefore, ε_a (or ε_w) should be an independent variable of N_A (or N_W) functional models. It is reasonable to assume that at high temperature, the relationship between ε_a (or ε_w) and N_A (or N_W) would be similar to that between ε_a and N_{Air-RT} (i.e., Tsutsumi curve). To estimate the best-fit functional form between ε_a and N_A (or N_W), we assumed the following relationship:

$$\varepsilon_a = \theta_{A1} N_A^{\theta_{A2}} + \theta_{A3} \tag{6.2}$$

$$\varepsilon_w = \theta_{W1} N_W^{\theta_{W2}} + \theta_{W3} \tag{6.3}$$

where $\theta_{A1}, \theta_{A2}, \theta_{A3}, \theta_{W1}, \theta_{W2},$ and θ_{W3} are unknown parameters, which should be estimated from the data. In this case, one of the most well-known ways to estimate the above parameters is a functional fitting (i.e., regression). However, when the functional fitting method is used, a critical limitation is that it is very difficult to consider the right-censored data. Note that there are 4 right-censored data points in

the PWR water data (Figure 6.2). Nevertheless, if we neglect the 4 right-censored data in Figure 6.2, the resulting fitting function for the PWR water condition can be represented as in Figure 6.3. The MATLAB (Ver. R2018a) function *fit* was used for the data fitting.

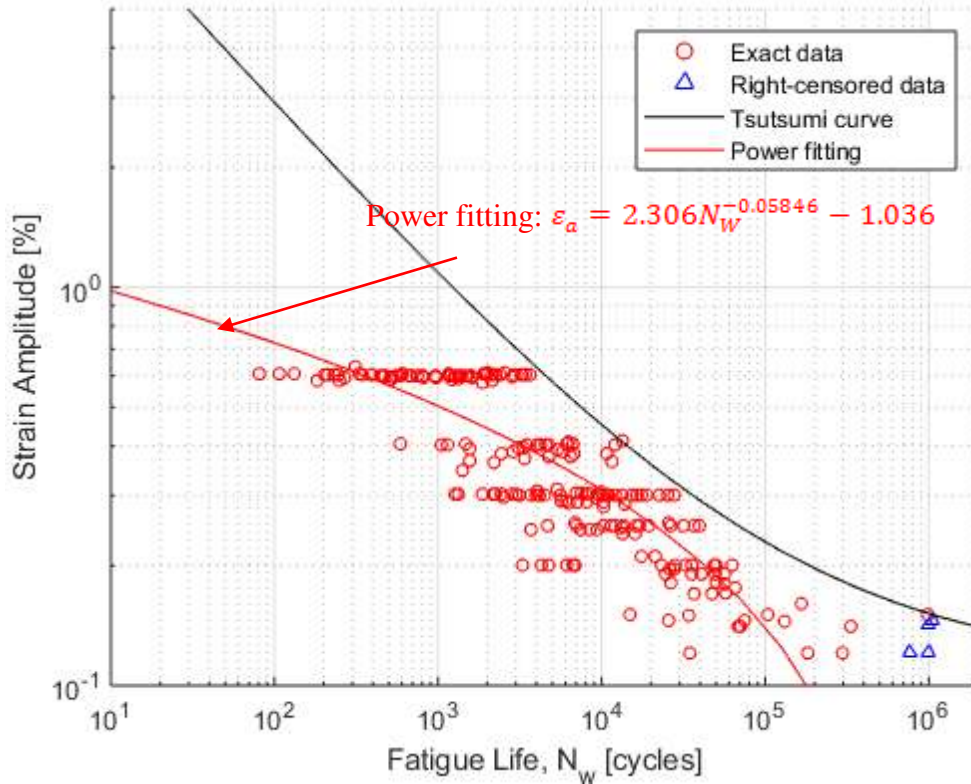


Figure 6.3 Functional fitting result of Eq. 6.3 with only exact data.

As shown in Figure 6.3, the resulting function fits the exact data well, but shows a different behavior in slopes compared to the reference Tsutsumi curve. Additionally, it seems unreasonable that the ϵ_{α} could be negative in the functional fitting model. We suspect that this unreasonable negative value of ϵ_{α} is caused by the neglect of the 4 right-censored data. The above issue can be addressed by using the maximum likelihood estimation (MLE) method, which can include the right-censored data [38]. However, to use the MLE method, the strain~life data sets have to be modeled probabilistically. If the mechanism of failure is governed by the *weakest link behavior*, the Weibull distribution probabilistic technique can be used for modeling the scattered strain~life data. This assumption is reasonable at least for the macroscopic-scale damage creating variable (here the strain amplitude) versus the corresponding life data. [35]. Therefore, let us assume that the fatigue life can be described as a random variable that follows the Weibull distribution as follows:

$$F_A(N_A; \beta_A, \eta_A) = 1 - \exp\left[-\left(\frac{N_A}{\eta_A}\right)^{\beta_A}\right] \quad (6.4)$$

$$F_W(N_W; \beta_W, \eta_W) = 1 - \exp\left[-\left(\frac{N_W}{\eta_W}\right)^{\beta_W}\right] \quad (6.5)$$

where $F_A(\cdot)$ and $F_W(\cdot)$ are the CDFs; β_A and β_W are shape parameters; and η_A , and η_W are the scale parameters of the Weibull distribution for the in-air and PWR-water data. The parameter β determines the aging (i.e., time-dependent degradation) effect of the material. For example, if $\beta < 1$, the failure rate, or hazard function, decreases with time. If $\beta > 1$, the failure rate increases, indicating that the material undergoes time-dependent degradation. If $\beta = 1$, then the failure rate is not influenced by time. The parameter β is usually considered as a material constant. Therefore, we assume that β_A and β_W are not influenced by ε_α .

The parameter η denotes a characteristic fatigue life having a unit of cycles. It is the quantile at which the CDF of the Weibull distribution reaches approximately 0.632 (i.e., $1 - e^{-1}$). When $\beta = 1$, then η is equal to the expected value of the Weibull distribution. Because N_A and N_W are assumed as a random variable, we can choose the characteristic life η_A and η_W as a representative fatigue life. Therefore, Eqs. 6.2 and 6.3 can be rewritten as:

$$\varepsilon_\alpha = \theta_{A1} \eta_A^{\theta_{A2}} + \theta_{A3} \quad \text{or} \quad \eta_A = \left(\frac{\varepsilon_\alpha - \theta_{A3}}{\theta_{A1}}\right)^{\frac{1}{\theta_{A2}}} \quad (6.6)$$

$$\varepsilon_w = \theta_{W1} \eta_W^{\theta_{W2}} + \theta_{W3} \quad \text{or} \quad \eta_W = \left(\frac{\varepsilon_\alpha - \theta_{W3}}{\theta_{W1}}\right)^{\frac{1}{\theta_{W2}}} \quad (6.7)$$

In this case, the likelihood function L can be expressed as follows:

$$L_A(\beta_A, \theta_{A1}, \theta_{A2}, \theta_{A3}) = \prod_{i=1}^{96} [f_A(N_{A,i}, \varepsilon_{\alpha,i}; \beta_A, \theta_{A1}, \theta_{A2}, \theta_{A3})] \quad (6.8)$$

$$L_W(\beta_W, \theta_{W1}, \theta_{W2}, \theta_{W3}) = \prod_{i=1}^{199} [f_W(N_{W,i}, \varepsilon_{a,i}; \beta_W, \theta_{W1}, \theta_{W2}, \theta_{W3})] \cdot \prod_{j=1}^4 [1 - F_W(N_{W,j}, \varepsilon_{a,j}; \beta_W, \theta_{W1}, \theta_{W2}, \theta_{W3})] \quad (6.9)$$

In Eqs. 6.8 and 6.9, the CDFs $F_A(\cdot)$ and $F_W(\cdot)$ can be found by combining Eq. 6.4 with Eq. 6.6 and Eq. 6.5 with Eq.6.7 and are as given below:

$$F_A(N_A, \varepsilon_a; \beta_A, \theta_{A1}, \theta_{A2}, \theta_{A3}) = 1 - \exp \left[- \left(\frac{N_A}{\left(\frac{\varepsilon_a - \theta_{A3}}{\theta_{A1}} \right)^{\frac{1}{\theta_{A2}}}} \right)^{\beta_A} \right] \quad (6.10)$$

$$F_W(N_W, \varepsilon_a; \beta_W, \theta_{W1}, \theta_{W2}, \theta_{W3}) = 1 - \exp \left[- \left(\frac{N_W}{\left(\frac{\varepsilon_a - \theta_{W3}}{\theta_{W1}} \right)^{\frac{1}{\theta_{W2}}}} \right)^{\beta_W} \right] \quad (6.11)$$

In Eqs. 6.10 and 6.11, the $f(\cdot)$ and $f(\cdot)$ are the partial derivatives of the CDFs $F_A(\cdot)$ and $F_W(\cdot)$ and can be expressed as below:

$$f_A(N_A, \varepsilon_a; \beta_A, \theta_{A1}, \theta_{A2}, \theta_{A3}) = \frac{\partial}{\partial N_A} F_A(N_A, \varepsilon_a; \beta_A, \theta_{A1}, \theta_{A2}, \theta_{A3}) \quad (6.12)$$

$$f_W(N_W, \varepsilon_a; \beta_W, \theta_{W1}, \theta_{W2}, \theta_{W3}) = \frac{\partial}{\partial N_W} F_W(N_W, \varepsilon_a; \beta_W, \theta_{W1}, \theta_{W2}, \theta_{W3}) \quad (6.13)$$

The log-likelihood function \mathcal{L} for the likelihood function L (Eqs. 6.8 and 6.9) is as given below:

$$l_A(\beta_A, \theta_{A1}, \theta_{A2}, \theta_{A3}) = \log L_A(\beta_A, \theta_{A1}, \theta_{A2}, \theta_{A3}) \quad (6.14)$$

$$l_W(\beta_W, \theta_{W1}, \theta_{W2}, \theta_{W3}) = \log L_W(\beta_W, \theta_{W1}, \theta_{W2}, \theta_{W3}) \quad (6.15)$$

The estimates of the MLE method can be determined by finding the maximum point of each \mathcal{L} . That is, the estimates should meet the following simultaneous equations:

$$\begin{cases} \frac{\partial}{\partial \beta_A} l_A(\beta_A, \theta_{A1}, \theta_{A2}, \theta_{A3}) = 0 \\ \frac{\partial}{\partial \theta_{A1}} l_A(\beta_A, \theta_{A1}, \theta_{A2}, \theta_{A3}) = 0 \\ \frac{\partial}{\partial \theta_{A2}} l_A(\beta_A, \theta_{A1}, \theta_{A2}, \theta_{A3}) = 0 \\ \frac{\partial}{\partial \theta_{A3}} l_A(\beta_A, \theta_{A1}, \theta_{A2}, \theta_{A3}) = 0 \end{cases} \quad (6.16)$$

$$\begin{cases} \frac{\partial}{\partial \beta_W} l_W(\beta_W, \theta_{W1}, \theta_{W2}, \theta_{W3}) = 0 \\ \frac{\partial}{\partial \theta_{W1}} l_W(\beta_W, \theta_{W1}, \theta_{W2}, \theta_{W3}) = 0 \\ \frac{\partial}{\partial \theta_{W2}} l_W(\beta_W, \theta_{W1}, \theta_{W2}, \theta_{W3}) = 0 \\ \frac{\partial}{\partial \theta_{W3}} l_W(\beta_W, \theta_{W1}, \theta_{W2}, \theta_{W3}) = 0 \end{cases} \quad (6.17)$$

It is truly hard to find an analytical solution of Eqs. 6.16 and 6.17. Thus, we used a numerical *false position* method, because it is known that the Newton-Raphson method does not always converge to the true estimates in MLE [35]. The resulting estimates are as follows:

$$\begin{aligned} \hat{\beta}_A &= 1.6924, & \hat{\theta}_{A1} &= 20.6905, & \hat{\theta}_{A2} &= -0.4397, & \hat{\theta}_{A3} &= 0.0981 \\ \hat{\beta}_W &= 1.2173, & \hat{\theta}_{W1} &= 14.9959, & \hat{\theta}_{W2} &= -0.4747, & \hat{\theta}_{W3} &= 0.1044. \end{aligned}$$

The resulting Weibull estimations for the in-air and PWR-water data are shown in Figures 6.4 and 6.5, respectively. The blue solid lines in these figures are the estimated relationship between ε_a and η (in Eqs. 6.6 and 6.7), and the blue dashed lines are 90% confidence interval bounds of those. It is shown that the MLE model (i.e., blue line) fits all data well and follows a similar trend compared with the Tsutsumi curve, especially for the high-temperature air case. Therefore, we can conclude that the MLE model is plausible.

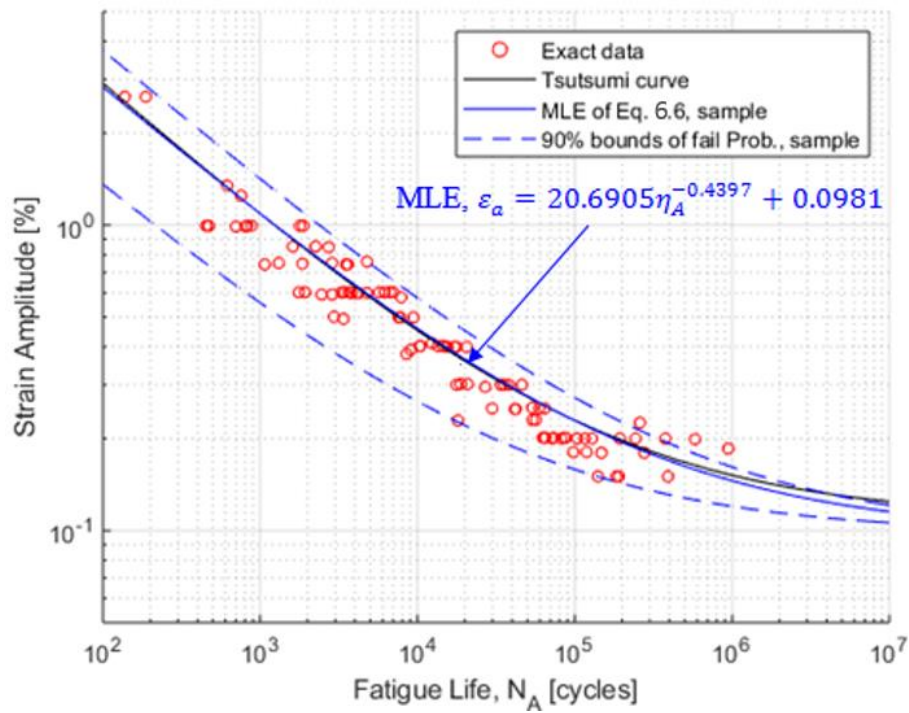


Figure 6.4 MLE result of Eq. 6.6 with sample data of high-temperature air fatigue life.

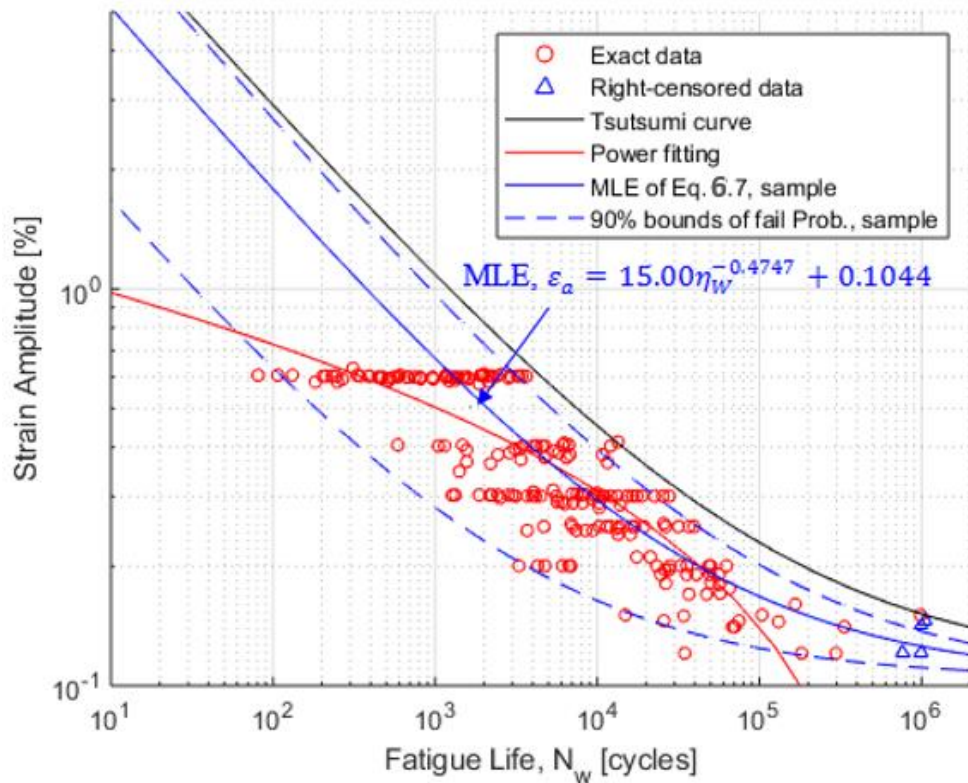


Figure 6.5 MLE result of Eq. 6.7 with sample data of PWR water fatigue life.

6.4 Model Estimation Uncertainty Quantification Using Bootstrapping Method

In the previous subsection, we determined the Weibull model form and estimated the parameters. Next, the estimation (of the model parameters) uncertainty has to be quantified. The bootstrap is a powerful method to quantify the uncertainty in estimated model parameters [37]. Through this method, it is possible to quantify the uncertainty with only experimental data and without any pre-assumption of the distributing function of the estimation uncertainty (e.g., Gaussian distribution). Therefore, this method can be applied even when a parametric interval estimation is impossible or requires a complicated formula [38]. The procedure of the bootstrapping can be simply divided as two parts: 1) *bootstrap sampling* and 2) *bootstrap estimation*. In this case, we performed the bootstrapping as follows:

- 1) A total of 200 *bootstrap sample sets* were generated from the sample set (i.e., the fatigue life data sets for high-temperature air or PWR water).
 - A. Draw a random sample (e.g., a pair of $\varepsilon_a - N_A$ data) from the sample set.
 - B. Iterate Step i as many as the number of the sample set size (e.g., 96 times for high-temperature air case) with replacement. This is a one bootstrap sample set.
 - C. Iterate Steps i and ii 200 times to generate 200 bootstrap sample sets.
- 2) A total of 200 *bootstrap estimates* were made from each bootstrap sample set by the MLE method described in Section 6.3.

Figures 6.6 and 6.7 show the estimates from the original sample set (red lines) and bootstrap sample sets (blue circles) for each case. All of the bootstrap estimates were converged at the numerical estimation step. The above bootstrap estimates distributed well near the sample set estimates without bias. In this case, it seems that the uncertainties of the above eight estimators likely follow a Gaussian distribution. However, the relationships among the estimators are not independent. Therefore, to discuss the uncertainty of each estimator separately is not meaningful.

In Figures 6.8 and 6.9, we draw all of the bootstrap 200 estimation curves for the relationship between ε_a and η (light blue lines imagining as a light blue bands) for each high-temperature air and PWR water case in order to illustrate the estimation uncertainty of Eqs. 6.6 and 6.7. The bootstrap uncertainty can be approximated to its real estimation uncertainty with a large enough sample size [37].

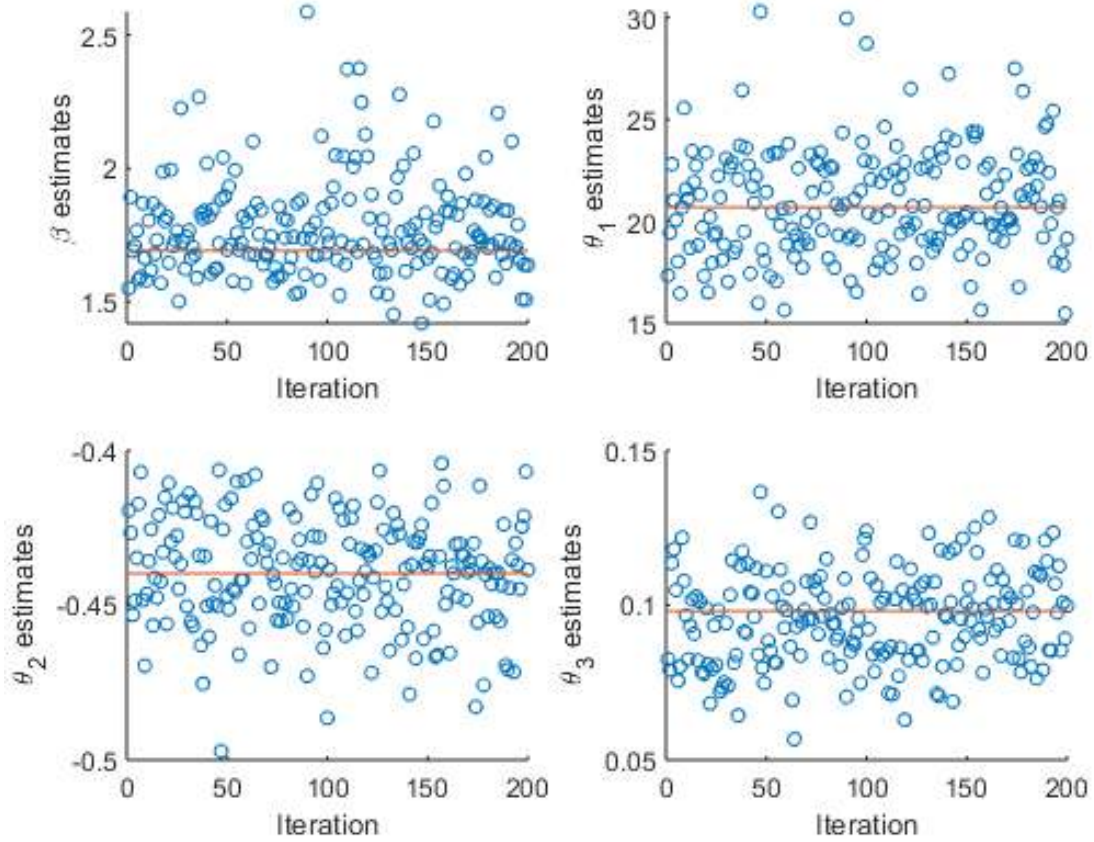


Figure 6. 6 Estimates from sample set (red lines) and bootstrap sample sets (blue circles) for high-temperature air.

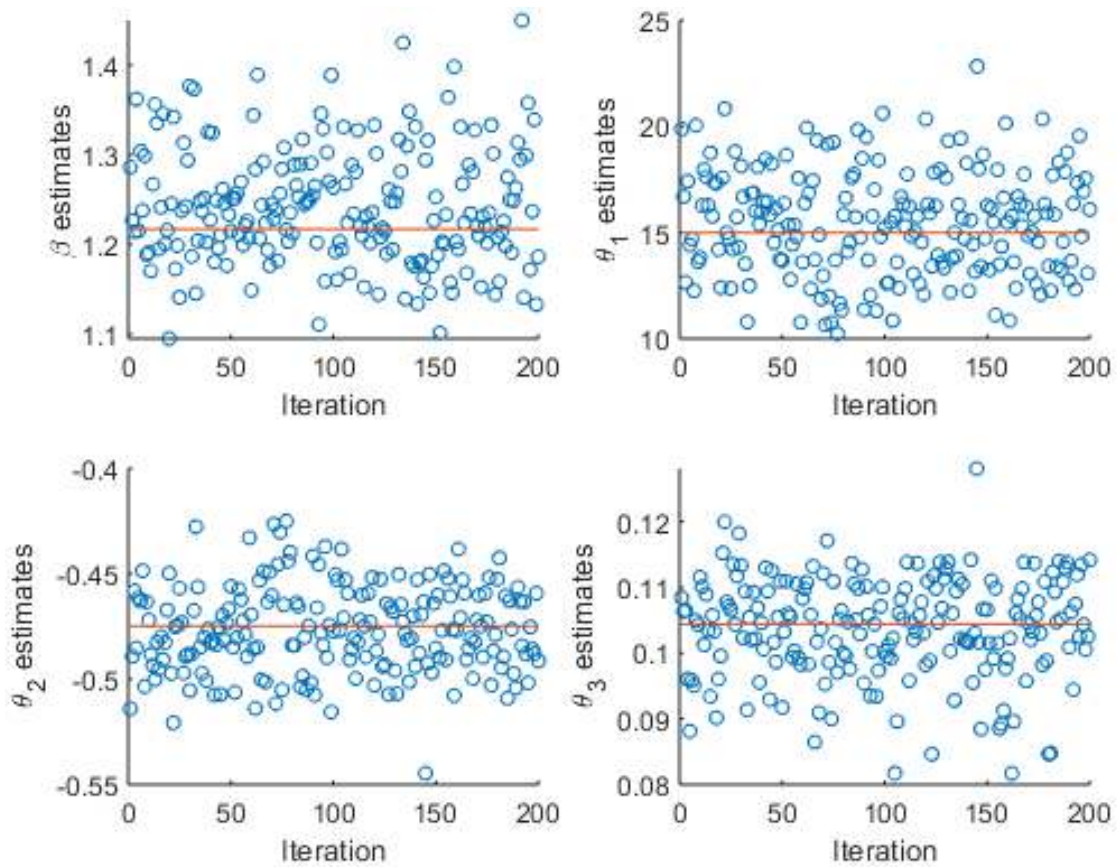


Figure 6. 7 Estimates from sample set (red lines) and bootstrap sample sets (blue circles) for PWR water.

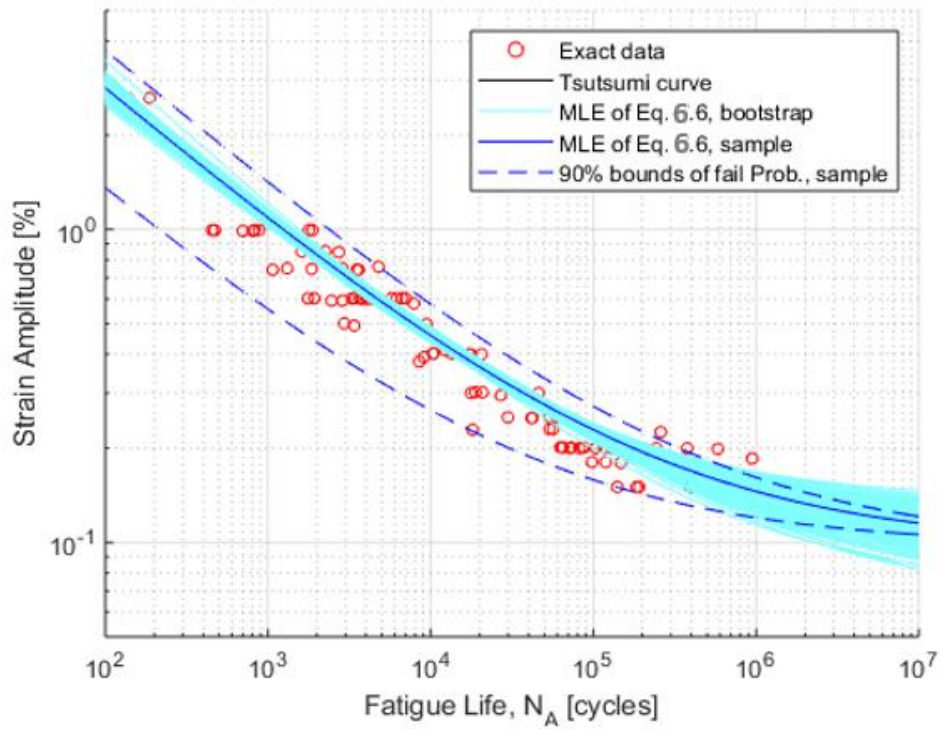


Figure 6.8 Result of bootstrapping for MLE of Eq. 6.6, for high-temperature air.

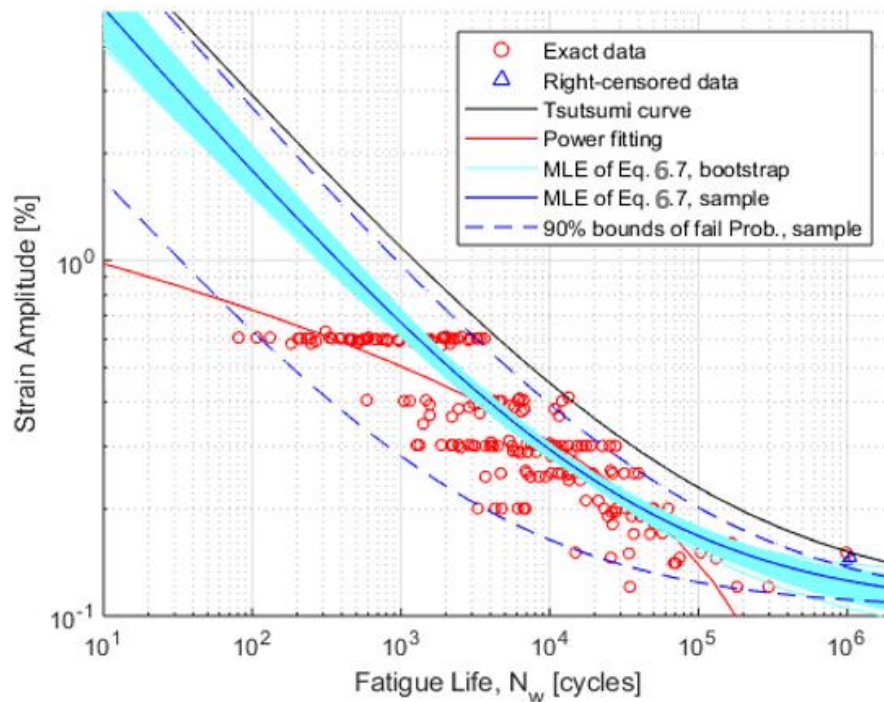


Figure 6.9 Result of bootstrapping for MLE of Eq. 6.7 for PWR water.

6.5 Empirical vs. Weibull CDF for End-of-Life Fatigue Data

There are two variables in the Weibull-based fatigue life model: 1) fatigue life (i.e., N_A or N_W) and 2) strain amplitude (i.e., ϵ_a). Given the Weibull-based fatigue life model, if the two variables are determined, we can calculate the failure probability. Figure 6.10 represents the estimated Weibull CDF for high-temperature air with sample set (i.e., black line) and bootstrap sample sets (i.e., grey lines) when the given ϵ_a is 0.2 or 0.6%. The original or raw data points (Figure 6.1) used for plotting empirical CDFs are the fatigue lives corresponding to strain amplitudes (ϵ_a) of either $(0.2 \pm 0.01\%)$ or $(0.6 \pm 0.01\%)$, respectively. Likewise, Figure 6.11 represents the estimated Weibull CDF for PWR water with sample set (i.e., black line) and bootstrap sample sets (i.e., grey lines) when the given strain amplitude (ϵ_a) is 0.3 or 0.6%. The original or raw data points (in Figure 6.2) used for plotting empirical CDFs are the fatigue lives corresponding to strain amplitudes (ϵ_a) of either $(0.3 \pm 0.01\%)$ or $(0.6 \pm 0.01\%)$, respectively. It is shown that when the given ϵ_a increased, the failure probability also increased (i.e., left shifted). This finding agrees with the actual fatigue behavior. Furthermore, Figures 6.10 and 6.11 show a good correlation between Weibull model estimated CDFs and empirical CDFs (estimated directly based on raw or sample data). This shows that the above Weibull model is well validated and can be used for estimating the CDFs at which the sample data points (ϵ_a versus N_A or ϵ_a versus N_W) are not available. Note that, in the above discussed Weibull model, we haven't considered the effect of strain rate, surface finish, PWR water chemistry, etc. If those additional variables have to be considered, the model estimation techniques would be much more complex and can be considered as a future study.

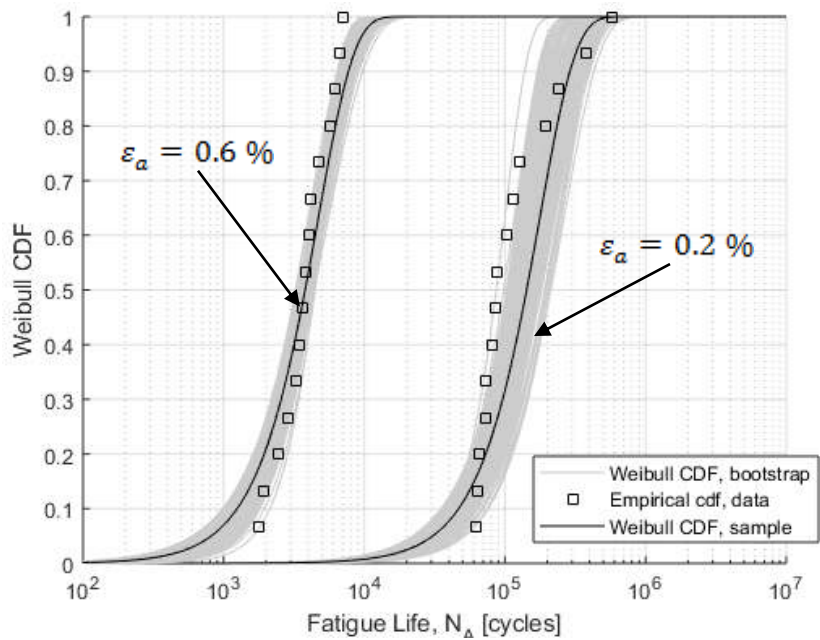


Figure 6.10 Estimated Weibull CDF for high-temperature air with sample set (black lines), bootstrap sample set (grey lines), and empirical CDFs from raw data when the given ϵ_a is 0.2 or 0.6%.

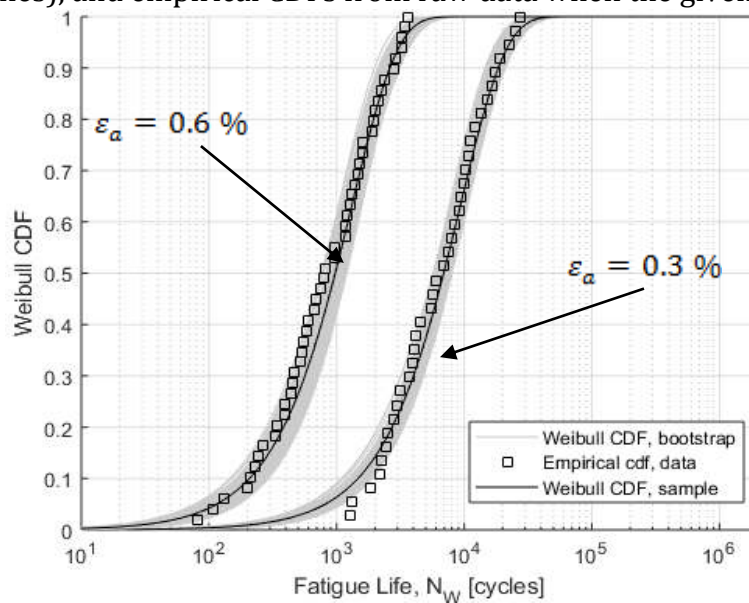


Figure 6.11 Estimated Weibull CDF for PWR water with sample set (black lines), bootstrap sample set (grey lines), and empirical CDFs from raw data when the given ϵ_a is 0.3 or 0.6%.

7 Time-Series Fatigue Damage States and Probabilistic Fatigue Life Prediction Using Markov-Chain-Monte-Carlo (MCMC) Techniques: Symmetric Loading Cases

7.1 Introduction

In the previous section we discussed probabilistic fatigue life estimation using Weibull-bootstrap analysis and end-of-life fatigue data. This is basically using traditional strain/stress ~ life (S~N) data. Although it is always better to estimate the reliability of a component based on probabilistic evaluation of end-of-life data, it may not be always possible to conduct hundreds of costly and time-consuming fatigue experiments for each and every different loading case. The traditional strain/stress ~ life data are mostly related to push-pull type symmetric ($R = -1$) loading cases. The probabilistic model discussed in section 6 was based on the associated end-of-life data. The approach doesn't depend on the time evolution of damage but is just based on end-of-life data. It is our assumption that for a given loading and environment, the time-evolution based probabilistic risk assessment (PRA) and reliability model would produce more accurate results compared to a PRA model simply based on the end-of-life data obtained under a different loading conditions. However, the time-evolution based PRA for a particular loading and environment requires hundreds of fatigue tests, which might not always be possible to perform due to the high cost and time requirements. To overcome these issues, we propose the use of Markov-Chain-Monte-Carlo (MCMC) techniques for time series or time-evolution prediction of damage states under a particular loading condition. Then, the probabilistic fatigue life can be estimated on the basis of the simulated scatter band in damage states for a given failure criteria.

In general, MCMC is a very power method for analyzing time-series data. Even though the Bayesian inference can be applied to a similar task, most Bayesian inference can be done by MCMC, whereas very little can be done without MCMC [40]. Therefore, MCMC-based methods are widely used by many researchers for development of time-series predictive models. For example, in the structural integrity research community, Wu and Ni used the MCMC technique to develop a probabilistic model of fatigue crack propagation [41], and An et al. used MCMC for fatigue failure time prediction [42]. In this section, we discuss the related MCMC theoretical background and numerical results associated with push-pull type symmetric ($R = -1$) fatigue loading test cases under different loading and environmental conditions. In the following section (section 8), we will discuss the MCMC model results related to unsymmetrical fatigue loading cases, such as design-basis and grid-load-following loading.

7.2 The Hypothesis

The use of MCMC method for probabilistic life estimation is based on the following assumption or hypothesis:

“The scatter in end-of-fatigue-life” is the manifestation of material microstructure variability and its interaction with applied loading and environment conditions. Under a given loading and environment condition, the time evolution of damage states and associated end-of-life would be different due to this variability in material microstructure and associated time evolution. The rate of change in time-series damage evolution can be an indirect measure of microstructural variability and its interaction with time-dependent loading sequences and environmental conditions. Using the rate-based MCMC approach, the scatter in time-series damage evolution and associated probabilistic fatigue life can be estimated for any given loading and environment conditions.

7.3 Theoretical Background of MCMC Method

7.3.1 Use of ordinary Monte Carlo method

The Monte Carlo method is a well-known algorithm based on numerous random iterations to obtain numerical convergence [43]. Generally, the Monte Carlo method can be used for modeling any probabilistic problems provided that there is enough computational capability. Therefore, Monte Carlo methods are widely used to solve engineering problems because of their simple algorithm and recent improvements in computational performance. We applied Monte Carlo methods to evaluate uncertainties of time-series fatigue data. For this purpose let us suppose a stochastic process $X_1, X_2, \dots, X_i, \dots, X_n$, where X_i are random variables for integer i in $[1, n]$. In this case, the sequential index i and n can be interpreted as a function of cyclic age for the fatigue modeling cases. Therefore, X_i consists of time-series (or cyclic-series) sequential data, such as observed stress or strain (a form of damage) during a fatigue test.

The *ordinary Monte Carlo* method is also called *independent and identically distributed (i.i.d.) Monte Carlo* [40]. That is, the ordinary Monte Carlo method assumes that the random variable X_i satisfies i.i.d. conditions, and there are no cyclic-dependent effects in the stochastic process. However,

we know this assumption is incorrect for cyclic-series fatigue data such as observed stress or strain due to time-dependent hardening or softening [4]. Therefore, we have to use a more realistic assumption, one that can consider cyclic-dependent or time-dependent effects to evaluate the uncertainty of time-dependent fatigue data or damage states (e.g., time evolution of cyclic strain or stress).

7.3.2 Use of Markov-Chain Method

Ideally, it is realistic to consider a random variable X_i that depends on its entire history. Therefore, the probability of $X_i = x_i$ can be expressed as follows:

$$P(X_i = x_i | X_{i-1} = x_{i-1}, X_{i-2} = x_{i-2}, \dots, X_1 = x_1) \quad (7.1)$$

where x_1, \dots, x_{i-1}, x_i are the deterministic values of observation. In this case, we will name this kind of observation as the *state*. That is, the probability of $X_i = x_i$ is a conditional probability with regard to its entire state history, and thus, we can consider a cyclic-dependent effect. However, it is too complicated to consider its entire state history for fatigue data having at least thousands of cyclic data points.

The *Markov Chain* is a kind of simplification that assumes the probability of $X_i = x_i$ only depends on its previous state, but in a recursive way. In this simplification, the probability of $X_i = x_i$ can be expressed as follows:

$$P(X_i = x_i | X_{i-1} = x_{i-1}) \quad (7.2)$$

This assumption is very effective for Monte Carlo simulation because it reduces a substantial part of the computational burden by ignoring the old history effect. Thus, we performed the Monte Carlo simulation based on the MCMC simulation. In the next section, we describe the detailed procedure and results of MCMC simulations to evaluate the uncertainty of time-dependent fatigue data.

7.4 Prediction of Time-Series Fatigue Damage States and Their Scatter

In this section, we will predict the time-series fatigue data by the MCMC method. For this estimate, we used the scatter in time-series damage states and associated probabilistic fatigue lives data from a

single fatigue test. The fatigue test cases (discussed in this section) and associated loading and environment are summarized in Table 7.1. The details of the test cases are reported in earlier ANL publications [23, 27]. In this subsection we discuss the MCMC results related to symmetric type loading cases (which are the typical loading types used for generating data points in traditional S~N curves). In section 8, we will discuss the MCMC results related to actual reactor loading cases, such as for the design-basis and grid-load-following load cycles.

Table 7.1 Symmetric (R= -1) type fatigue loading cases and associated environment for MCMC method evaluation.

Fatigue Test Case No.	Loading	Environment	Reference
ET-F06	Constant amplitude strain-controlled symmetric (R = -1) fatigue test with a strain amplitude of 0.5%	300 °C, in-air	[27]
ET-F13	Constant amplitude stroke-controlled [¥] symmetric (R = -1) fatigue test, with an equivalent intended strain amplitude of 0.5%	300 °C, in-air	[27]
ET-F43	Initial 12 variable amplitude and then constant amplitude symmetric (R = -1) stress-controlled [¥] fatigue test, with an equivalent intended strain amplitude of 0.5%.	ET-F43	[23]
EN-F14	Constant amplitude stroke-controlled [¥] symmetric (R = -1) fatigue test, with an equivalent intended strain amplitude of 0.5%	300 °C, PWR water	[27]
EN-F44	Initial 12 variable amplitude and then constant amplitude symmetric (R = -1) stress-controlled [¥] fatigue test, with an equivalent intended strain amplitude of 0.5%.	300 °C, PWR water	[23]

[¥] The constant amplitude portion of the stroke-controlled or stress-controlled tests was intended for achieving an equivalent constant strain amplitude of 0.5%, but the observed strain amplitude was not 0.5 % rather was varying due to cyclic strain hardening/softening.

7.4.1 MCMC prediction of time-series ratcheting strain for stress-controlled loading conditions

Two stress-controlled loading cases (in-air and PWR-water environments) were MCMC modeled for predicting the time-series ratcheting strain and their probabilistic scatter bound. The related results are discussed below.

7.4.1.1 Stress-controlled in-air test case (ET-F43)

Figure 7.1 shows the ET-F43 ratcheting strain data obtained from a stress-controlled fatigue test. The input cyclic loading consisted of the initial 12 cycles of variable stress amplitudes followed by constant cycle stress amplitudes. In the first 12 cycles of variable loading, the stress increased from 106 to 216 MPa. In the remaining constant-loading cycles, the stress was controlled at 216 MPa to achieve an intended strain amplitude of 0.5% [23]. The details of the test condition can be found in Table 7.1 and [23]. In general, the probability of a future state of a system may depend on its entire life history (i.e., entire state history). However, the Markov chain process assumes that the future state of the system depends solely on its present state. In this case, we will use the ratcheting strain rate to classify state levels. Figure 7.2 shows a histogram of the ratcheting strain rate for the ET-F43 test data. We defined the state level by corresponding each non-zero histogram bin in ascending order with a state. For example, the histogram bin having smallest ratcheting strain range corresponds to state 1, and that having the largest ratcheting strain range corresponds to the last state. For the ET-F43 data case, the last state number is 40 (see Figure 7.2). The associated time-series state (i.e., the ranking number of strain rates) profile is shown in Figure 7.3. Using the time-series state profile (Figure 7.3), we can calculate the state transition probability P_{ij} . The definition of P_{ij} is a conditional probability of state transitioning from a state i to j (Eq. 7.3). In this case, i and j should not be larger than 40 because there are only 40 states in the ET-F43 data case.

$$P_{ij} = P(\text{next state } j \mid \text{current state } i) \quad (7.3)$$

According to the assumption of the Markov chain process, it is possible to predict the next state probabilistically based on information about the current state level. In this step, we performed 1,000 iterations in a Monte Carlo simulation to evaluate the uncertainty of state transitioning, as shown in Figure 7.4. After then, the Monte Carlo-simulated 1,000 state profiles were used for estimating the corresponding ratcheting strain rate profiles, and then the associated scatter in time-series ratcheting

strain evolutions. Figure 7.5 shows the resulting ratcheting strain histories and their scatters. The estimated uncertainty or scatter band of observed ratcheting strain can be used for estimating the cumulative distribution function (CDF) or life probability. In section 7.5, we will discuss the estimated CDF results and their validity (with respect to the corresponding Weibull-Bootstrap estimated lifetime CDF).

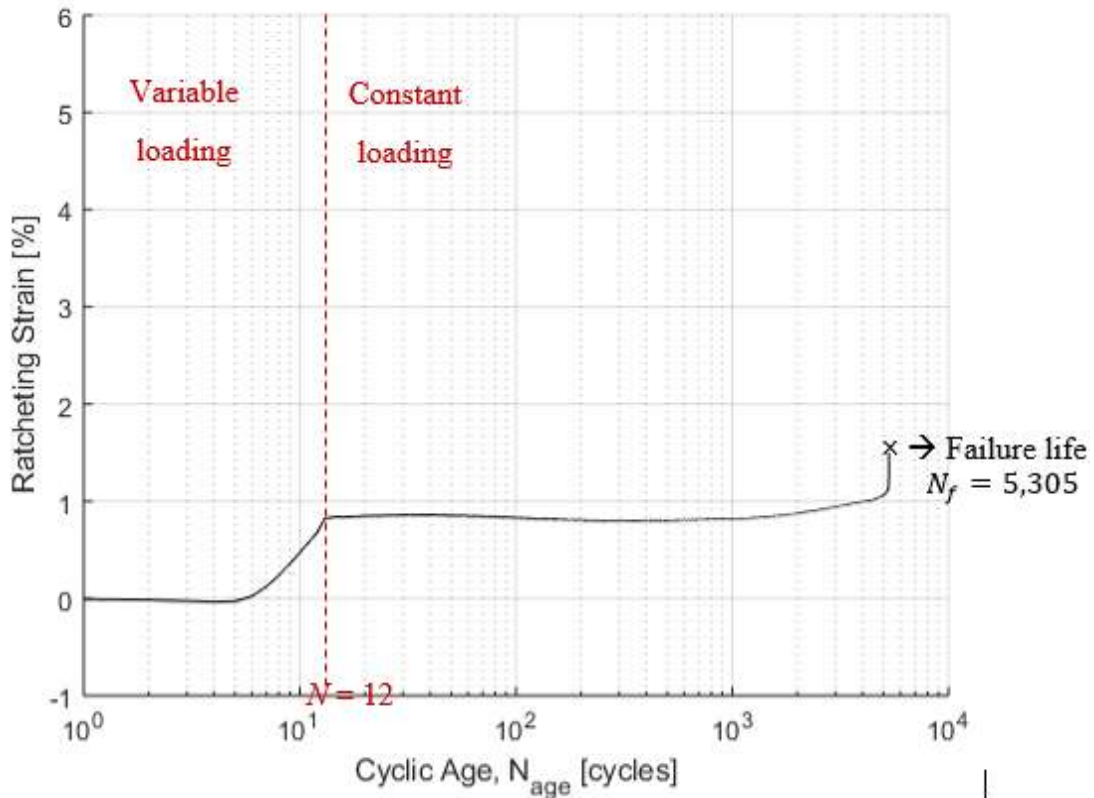


Figure 7. 1 Cyclic age versus ratcheting strain data, which were used as base data for MCMC modeling of ET-F43 test case.

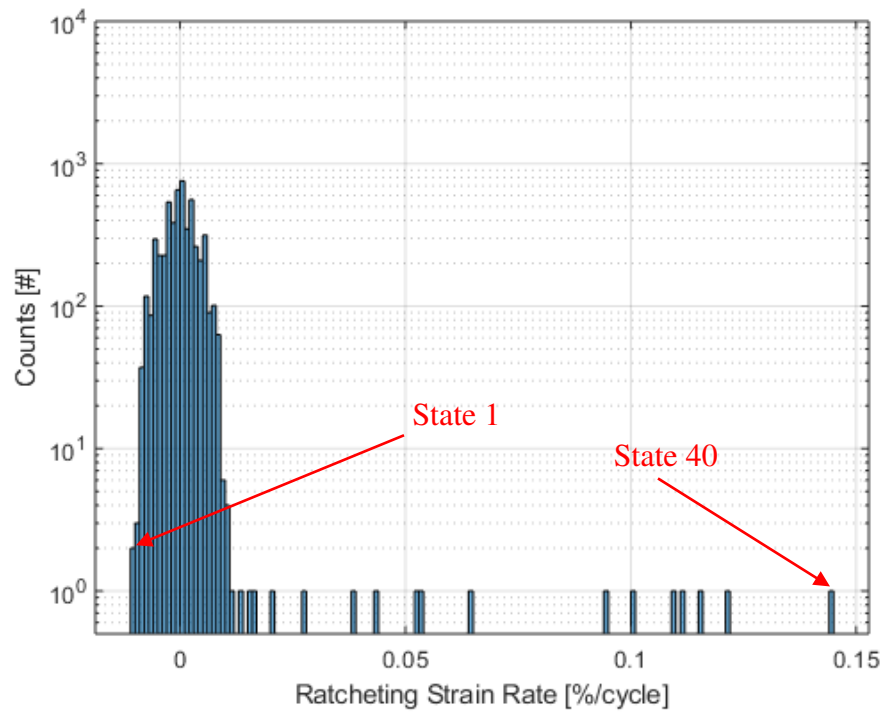


Figure 7.2 Histogram of ratcheting strain rate for ET-F43 data.

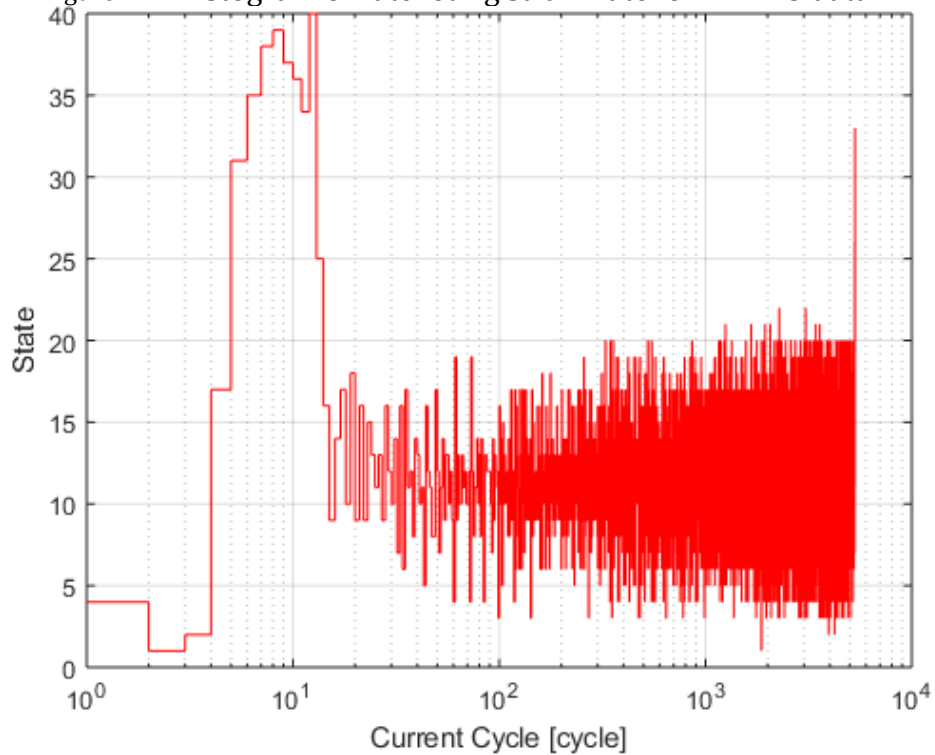


Figure 7.3 Time-series state profile of ET-F43 data.

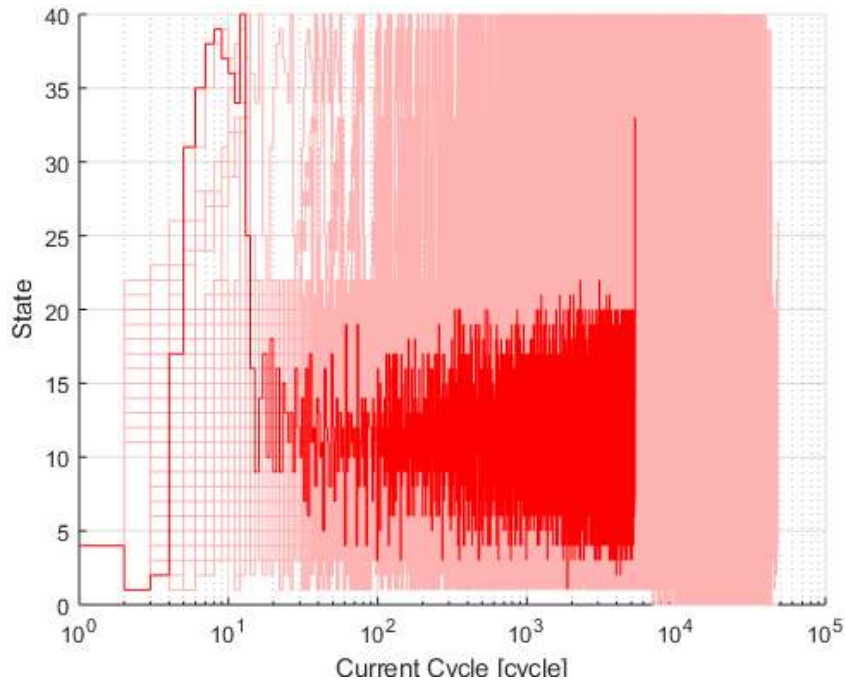


Figure 7. 4 Time-series state profile (red line) and 1,000 MCMC state profiles (light red lines) of ET-F43 data.

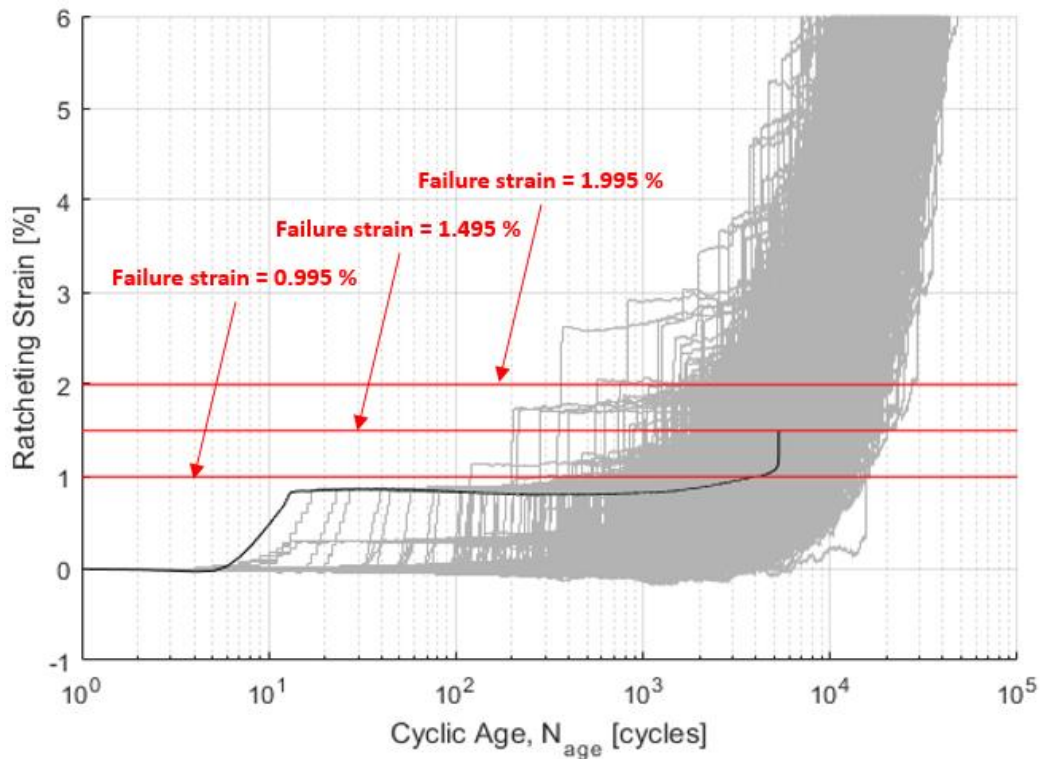


Figure 7. 5 Original ratcheting strain profile (black line), estimated 1,000 MCMC ratcheting strain profiles (grey line), and failure strain limits used for CDF calculation (red line) in ET-F43 test case.

7.4.1.2 Stress-controlled PWR-water test case (EN-F44)

The EN-F44 test was conducted under a similar loading condition as ET-F43 (Table 7.1). However, unlike the ET-F43 test, which was conducted under the in-air condition, the EN-F44 test was conducted under the PWR primary coolant environment. Although the loading condition was the same for both ET-F43 and EN-F44, due to the difference in environment (i.e. in-air versus PWR water), it is expected that the damage progression rate (in this case, the ratcheting strain rate) would be much different for EN-F44 than ET-F43. This different damage progression rate would result in a different scatter band in the ratcheting strain time evolution and associated lifetime probability or CDF. We had performed the MCMC modeling of EN-F44 using EN-F44 cycle versus ratcheting strain data as a base. Figure 7.6 shows the base cycle versus ratcheting strain data. Figure 7.7 shows the corresponding histogram for the ratcheting strain rate. The definition of state for the MCMC process in the EN-F44 case is similar to the case of ET-F43. In ET-F44, the number of state is 42. Figure 7.8 shows both the time-series state profile (red line) and 1,000 Monte-Carlo drawn sample space of time-series state profiles (light red lines). Figure 7.9 shows the resulted ratcheting strain profile and 1,000 MCMC simulation results for EN-F44.

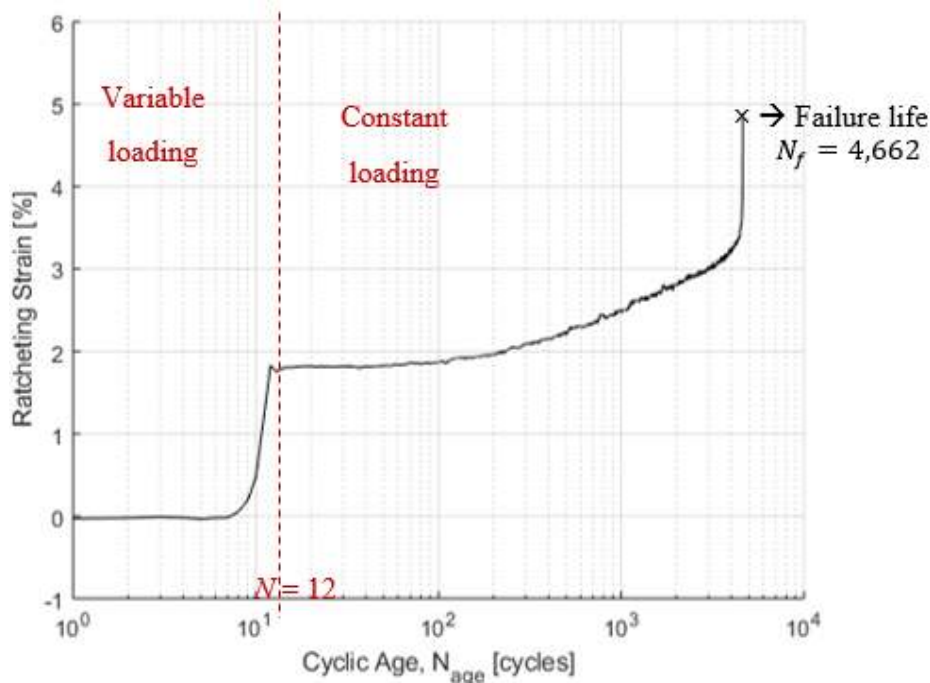


Figure 7.6 Cyclic age versus ratcheting strain data, which were used as base data for MCMC modeling of ET-F44.

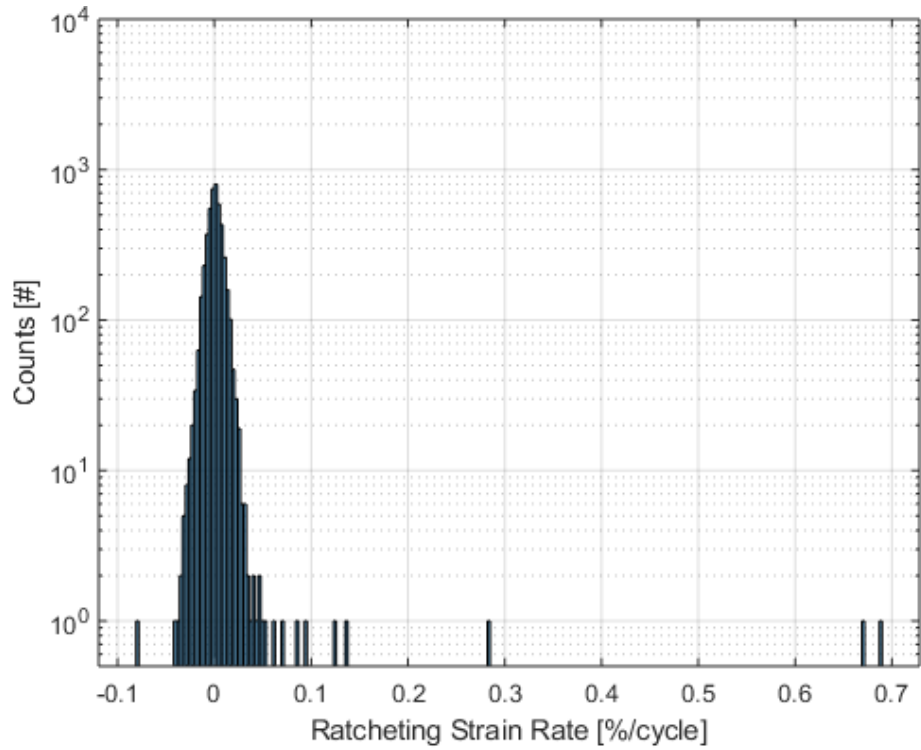


Figure 7.7 Histogram of ratcheting strain rate for EN-F44 data.

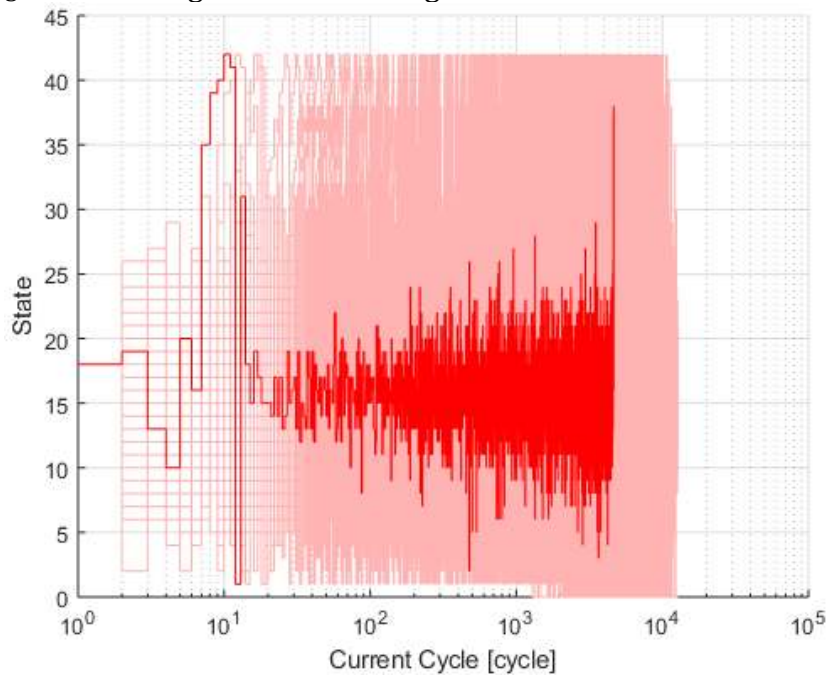


Figure 7.8 Time-series state profile (red line) and 1,000 MCMC state profiles (light red lines) of EN-F44 data.

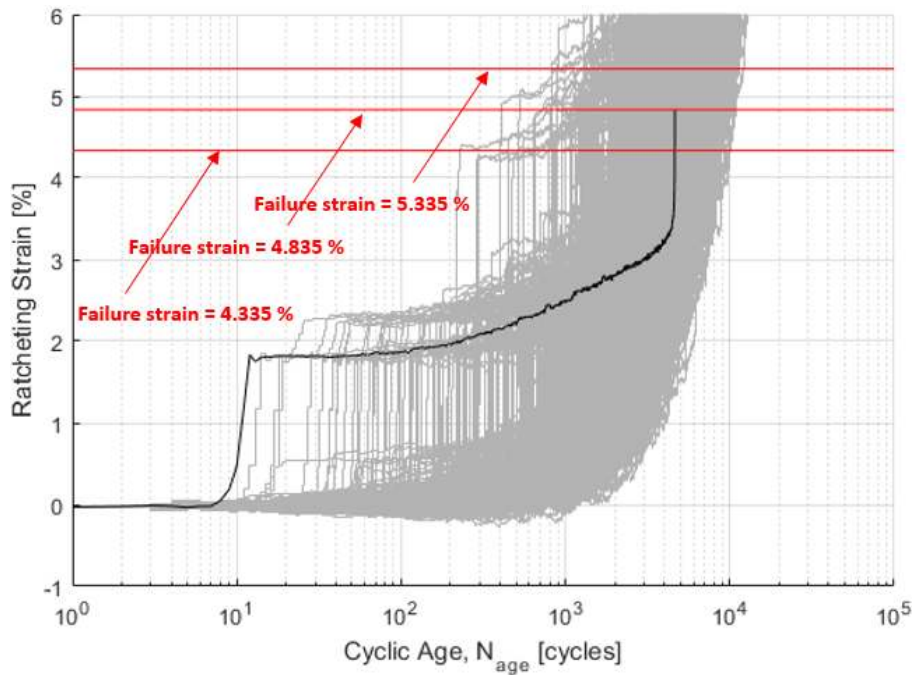


Figure 7.9 Original ratcheting strain profile (black line), estimated 1,000 MCMC ratcheting strain profiles (grey line), and failure strain limits used for CDF calculation (red line) of EN-F44.

7.4.2 MCMC prediction of time-series maximum stress for strain/stroke-controlled loading conditions

In this subsection, we discuss the MCMC results for symmetric ($R = -1$) displacement-controlled (either strain or stroke controlled) test cases. The symmetric ($R = -1$) displacement-controlled loading cases are similar to the loading conditions used for traditional strain versus life ($S \sim N$) data. Unlike the above stress-controlled test cases, where the ratcheting strain histories were used for MCMC modeling, in the present strain/stroke-controlled test cases the maximum stress histories were used for MCMC modeling. Three strain/stroke-controlled loading cases (two under in-air and one under PWR-water environments) were MCMC modeled for predicting the time-series maximum stress and their probabilistic scatter bound. The related results are discussed below.

7.4.2.1 Strain-controlled in-air test case (ET-F06)

Figure 7.10 shows the cyclic age versus maximum stress data for ET-F06. These were used as base data for MCMC modeling of the ET-F06 loading and environment case. It should be noted that ET-F06 strain-controlled test case undergoes initial stress hardening and then stress softening, i.e., the mechanical behaviors of these two stages are quite different. For MCMC modeling, we have considered

separately the hardening and softening portion of the cyclic age versus maximum stress data. Ideally, the result of MCMC simulation would not be accurate when there is a discontinuity such as a transition from hardening to softening stress, as shown in Figure 7.10. Therefore, it is reasonable to consider the two stages separately and combine both the results at the end. For ET-F06, the hardening stage ranged from $N = 1$ to 53 (see Figure 7.10). In this case, we defined the Markov chain stage by using the rate of maximum stress separately for the hardening and softening stages. Figures 7.11 and 7.12 show histograms for the rate of maximum stress at hardening and softening stages for ET-F06. Figures 7.13 and 7.14 show both the time-series state profile (red line) and 1,000 MCMC state profiles (light red lines) for hardening and softening stages, respectively. Based on the Monte Carlo simulated sample space shown in Figures 7.13 and 7.14, the respective time-series evolution of maximum stress is estimated. Figure 7.15 shows the original maximum stress profile (black line) and 1,000 MCMC simulation results (grey lines). As for the MCMC results in the previous subsection (i.e., ratcheting strain in stress-controlled case), we will validate the MCMC results in Section 7.5 by comparing the Weibull-based fatigue life model developed earlier.

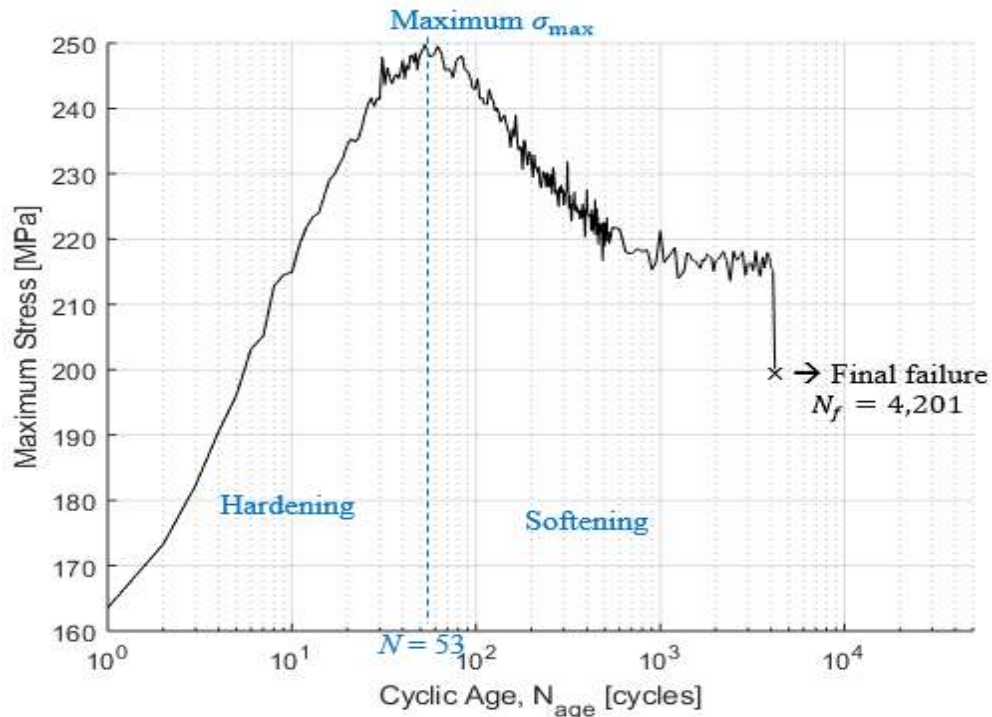


Figure 7. 10 Cyclic age versus maximum stress data, which were used as base data for MCMC modeling of ET-F44 loading and environment case.

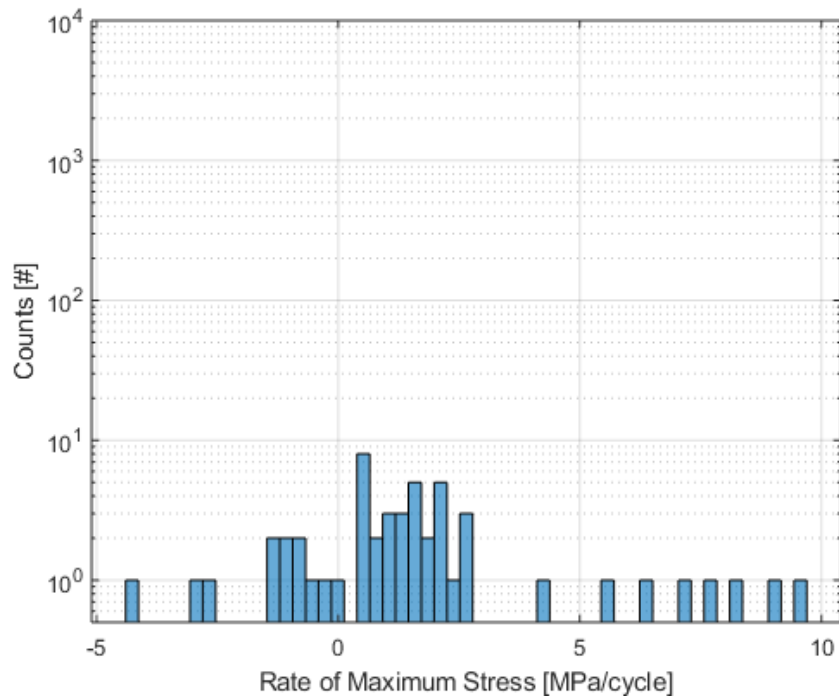


Figure 7.11 Histogram of maximum stress rate for ET-F06 data in hardening stage.

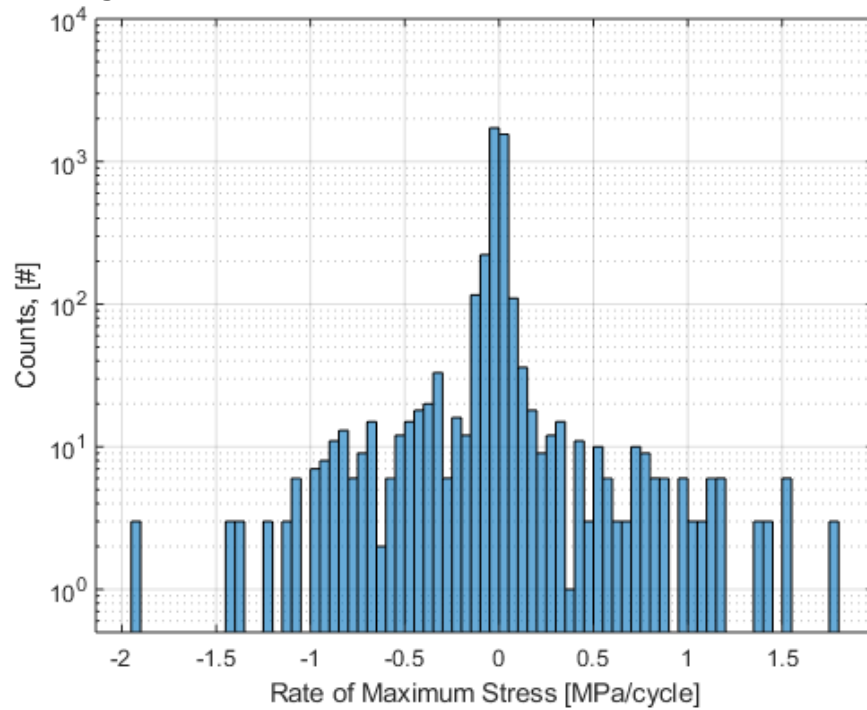


Figure 7.12 Histogram of maximum stress rate for ET-F06 data in softening stage.

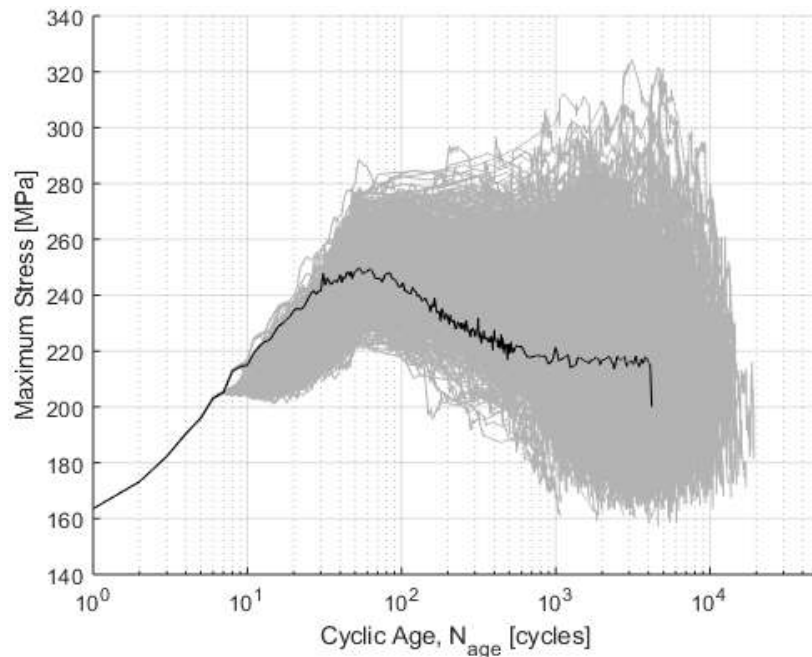


Figure 7.15 Original maximum stress profile (black line) and estimated 1,000 MCMC maximum stress profiles (grey line) for ET-F06 data.

7.4.2.2 Stroke-controlled in-air test case (ET-F13)

The MCMC model was used for time-series and scatter modeling of damage evolution under symmetric cycle ($R = -1$) stroke loading. The fatigue test was conducted under the in-air condition. Figure 7.16 shows the cyclic age versus maximum stress data, which were used as base data for MCMC modeling of the ET-F13 loading and environment case. Similar to the ET-06 case, the cyclic age versus maximum stress data were divided into two stages: hardening and softening. For ET-F13, the hardening stage ranged from $N = 1$ to 52 (see Figure 7.16). Similar to the previously discussed ET-F06 strain-controlled case, in the present stroke-controlled case, we defined the Markov chain states by using maximum stress rates. Figures 7.17 and 7.18 show histograms for the rate of maximum stress at hardening and softening stages for ET-F13. Figures 7.19 and 7.20 show the time-series state profile (red line) and 1,000 MCMC state profiles (light red lines) for the hardening and softening stages, respectively. Based on the Monte Carlo simulated sample space shown in Figures 7.19 and 7.20, the respective time-series evolution of maximum stress was estimated. Figure 7.21 shows the original maximum stress profile (black line) and 1,000 MCMC simulation results (grey lines). The

corresponding predicted lifetime CDF and its comparison with respect to end-of-life test data based on the estimated Weibull CDF will be discussed in section 7.5.

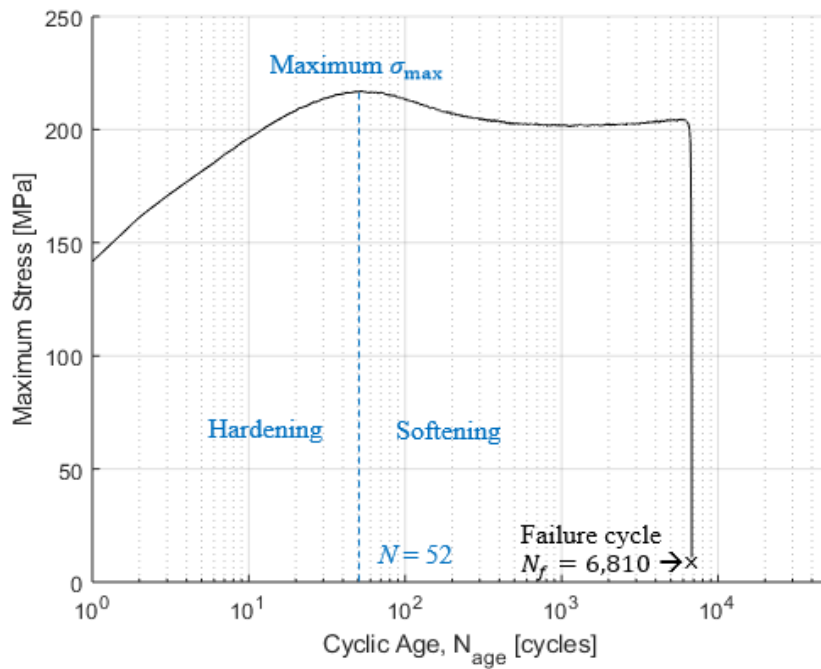


Figure 7.16 Cyclic age versus maximum stress data, which are used as base data for MCMC modeling of ET-F13 loading and environment case.

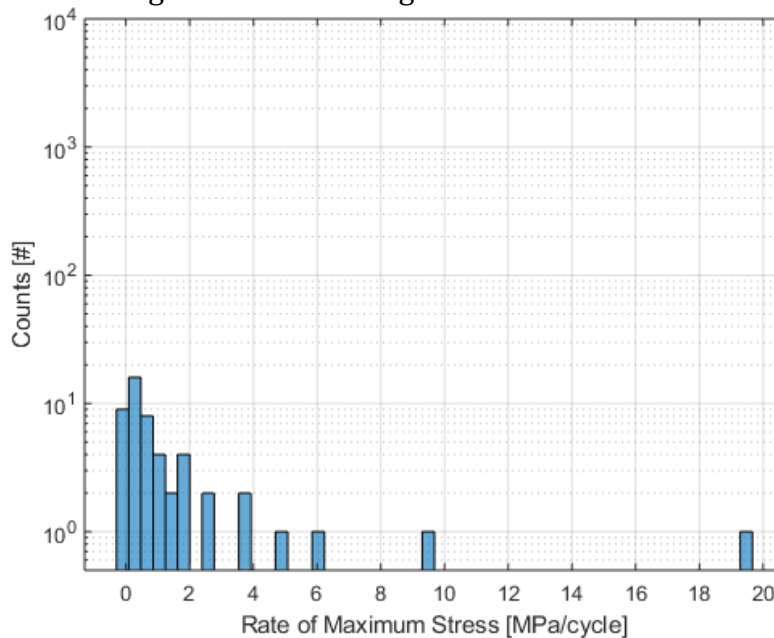


Figure 7.17 Histogram of maximum stress rate for ET-F13 data in hardening stage.

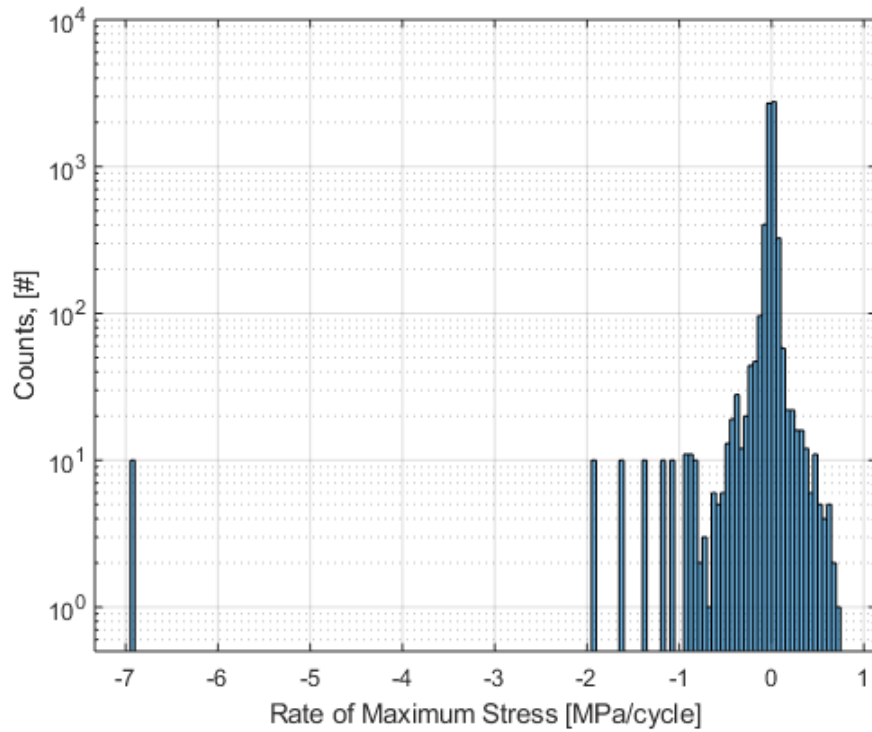


Figure 7.18 Histogram of maximum stress rate for ET-F13 data in softening stage.

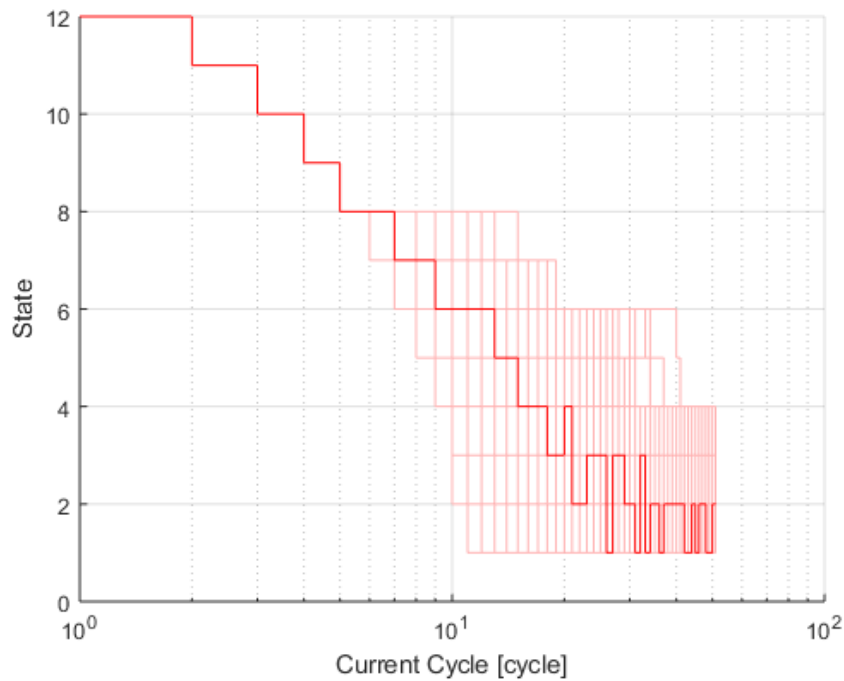


Figure 7.19 Time-series state profile (red line) and 1,000 MCMC state profiles (light red lines) of ET-F13 data in hardening stage.

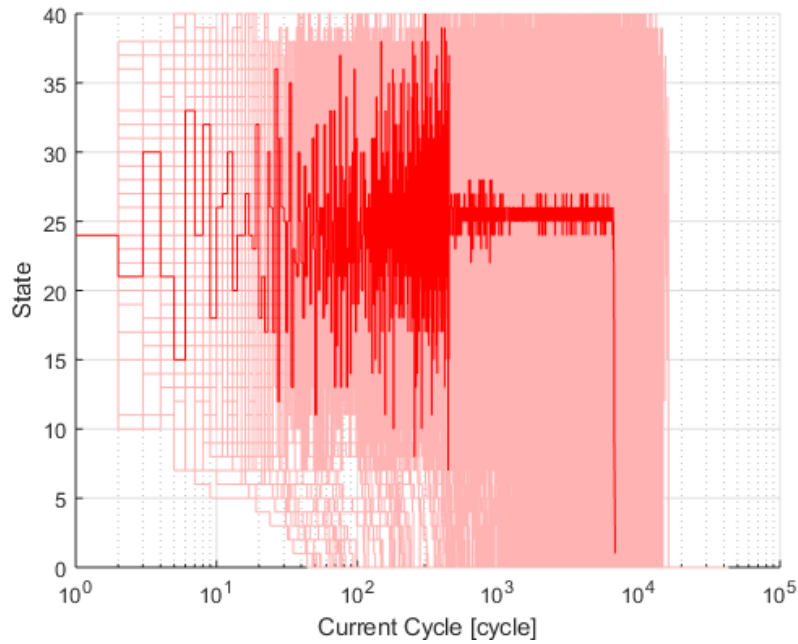


Figure 7.20 Time-series state profile (red line) and 1,000 MCMC state profiles (light red lines) of ET-F13 data in softening stage.

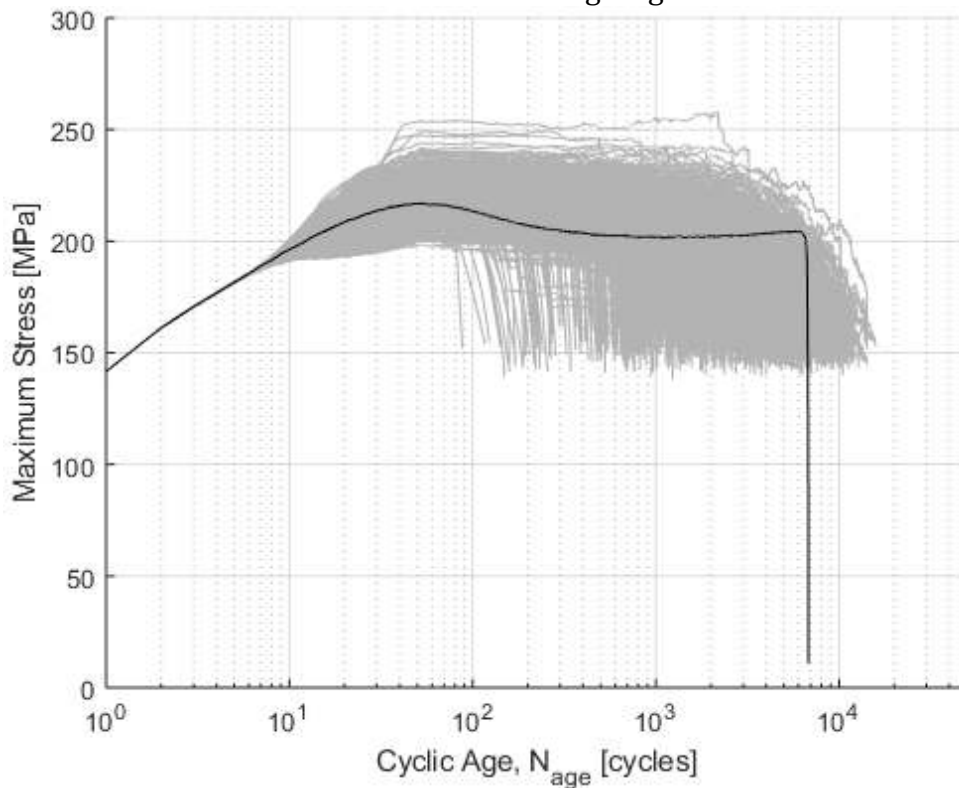


Figure 7.21 Original maximum stress profile (black line) and converted 1,000 MCMC maximum stress profiles (grey line) for ET-F13 data.

7.4.2.3 Stroke-controlled PWR-water test case (EN-F14)

Test EN-F14 was conducted under the same stroke-controlled loading condition as ET-F13. However, unlike ET-F13, which was conducted under the in-air environment, the EN-F14 test was conducted under the PWR primary water environment. The resulting cyclic age versus maximum stress data (Figure 7.22) were used as base data for MCMC modeling of ET-F14 loading and environment case. Like the above discussed displacement-controlled test cases (strain-controlled ET-F06 and stroke-controlled ET-F13 tests), we separated the hardening and softening stages for MCMC modeling. For EN-F14, the hardening stage ranged from $N = 1$ to 45 (see Figure 7.22). Figure 7.23 shows the histograms for the rate of maximum stress during the hardening stage. The softening stage started from $N = 45$ (see Figure 7.22). Figure 7.24 shows the histograms for the rate of maximum stress during the softening stage. Figures 7.25 and 7.26 show the original (directly observed in EN-F14 test) time-series state profile (red line) and 1,000 MCMC state profiles (light red lines) during the hardening and softening stages, respectively. The state information for the hardening and softening stages was combined to predict the time-series damage evolution rates under EN-F14 stroke cycle loading and PWR environmental conditions. Based on these rates, the cyclic ages versus maximum stress curves were estimated. Figure 7.27 shows the original maximum stress profile (black line) and 1,000 MCMC simulation results (grey lines). The predicted lifetime CDF and its comparison with respect to end-of-life test data based on the estimated Weibull CDF will be discussed in section 7.5.

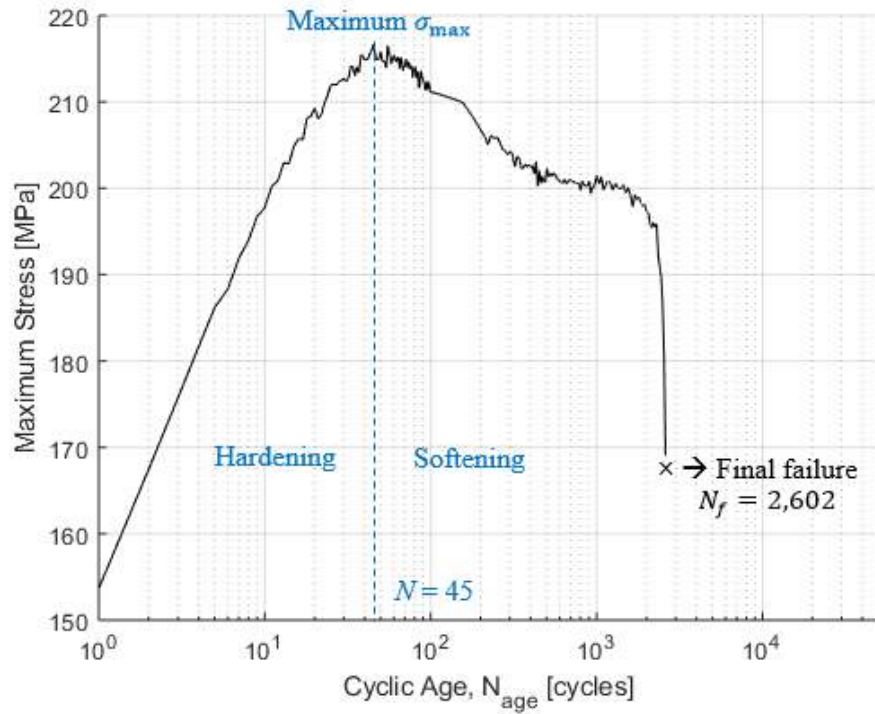


Figure 7.22 Cyclic age versus maximum stress data, which are used as base data for MCMC modeling of EN-F14 loading and environment case.

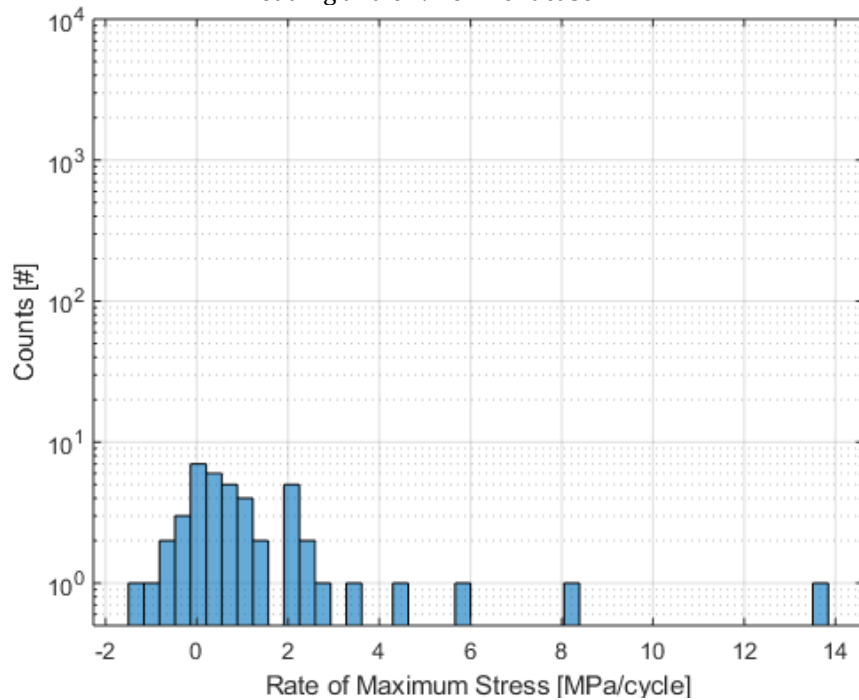


Figure 7.23 Histogram of maximum stress rate for EN-F14 data in hardening stage.

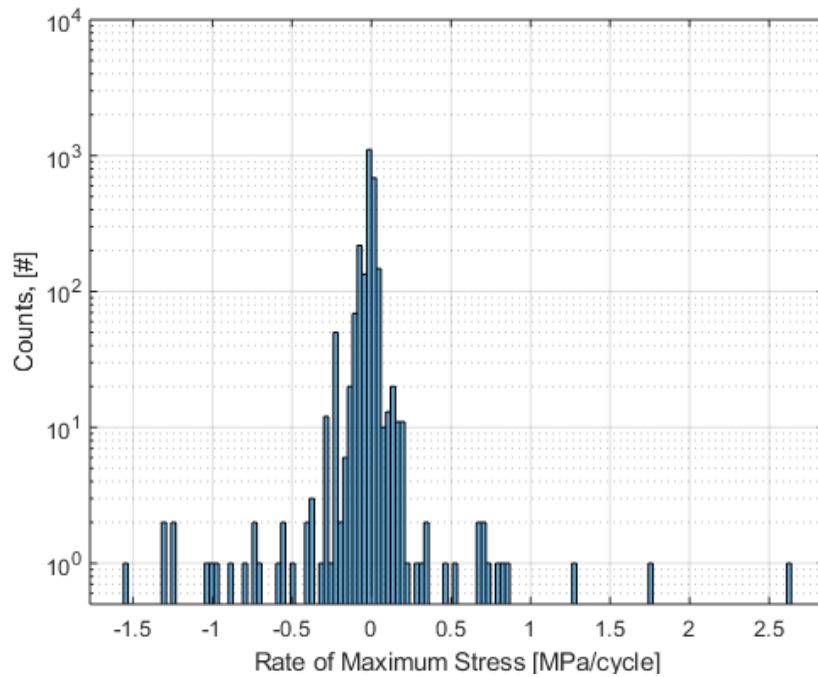


Figure 7.24 Histogram of maximum stress rate for EN-F14 data in softening stage.

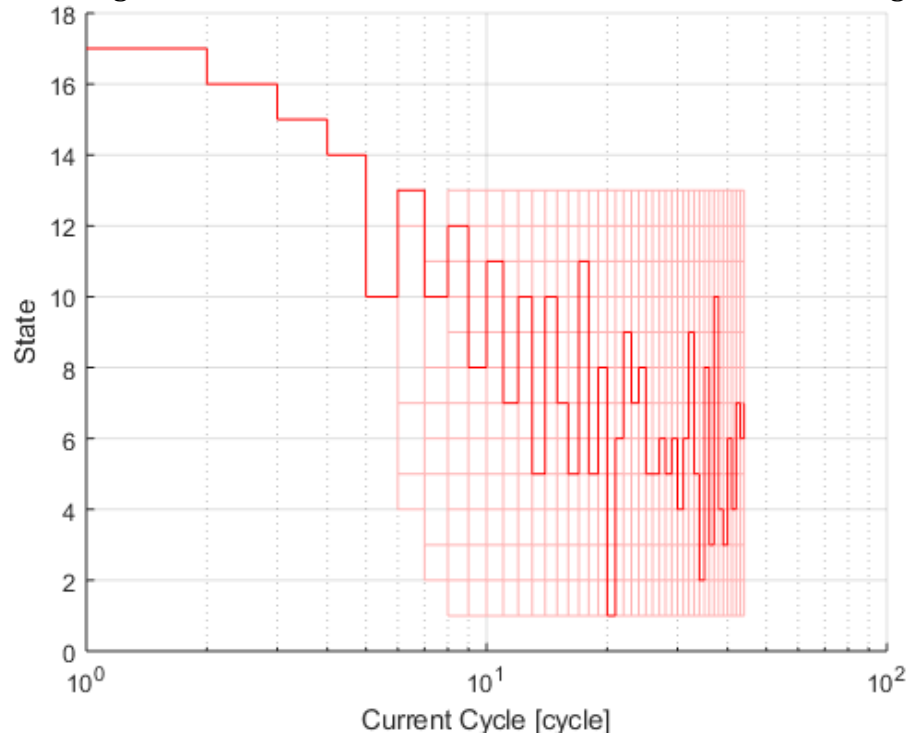


Figure 7.25 Time-series state profile (red line) and 1,000 MCMC state profiles (light red lines) of EN-F14 data in hardening stage.

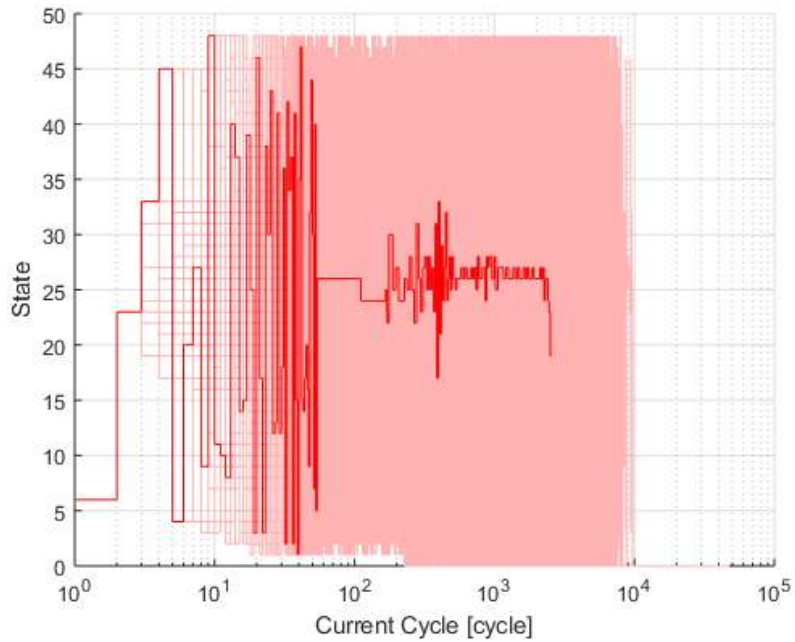


Figure 7.26 Time-series state profile (red line) and 1,000 MCMC state profiles (light red lines) of EN-F14 data during softening stage.

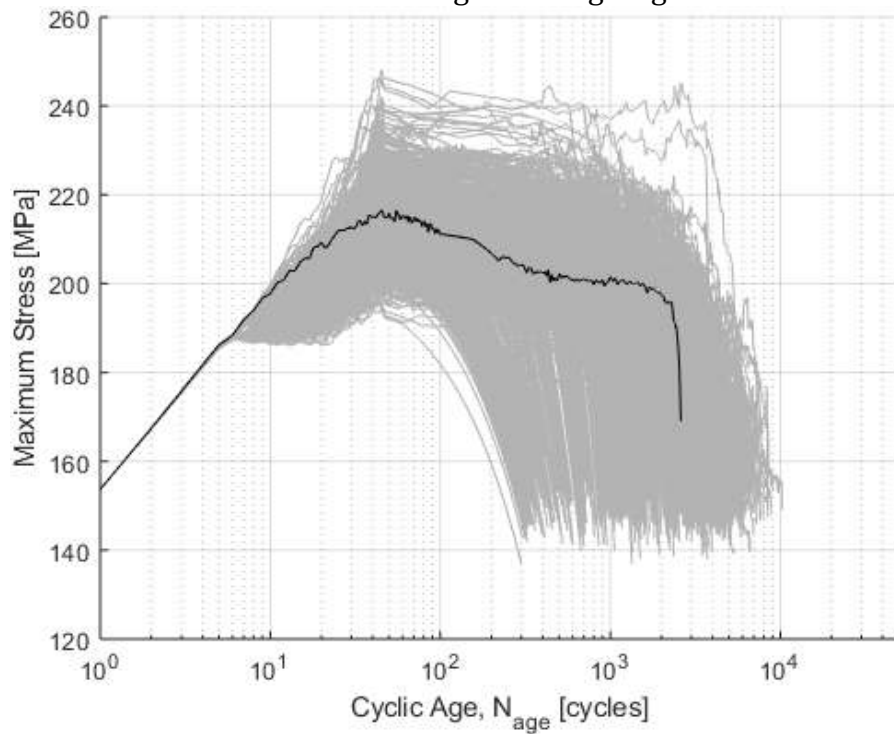


Figure 7.27 Original maximum stress profile (black line) and predicted 1,000 MCMC maximum stress profiles (grey line) for EN-F14 data.

7.5 Prediction of Lifetime CDFs Based on MCMC Predicted Time-Series Damage States

In section 7.4, we discussed the MCMC predicted time-series damage states (either cycle versus ratcheting strain or cycle versus maximum stresses) and their scatter bands. Using these probabilistic time-series data and a given failure criteria, we can estimate the failure probability of the test specimens. The resulting lifetime probability or CDF can be compared with the respective CDF estimated directly based on end-of-life fatigue test data. With the limited availability of time-series test data, this end-of-life CDF comparison will help to judge the accuracy of the overall MCMC method. If the MCMC method is found to produce justifiable results, it can be extended for probabilistic life estimation by just conducting few fatigue tests, prototypical to the actual loading and environment. This method will help to avoid the dependence on traditional stress/strain life data, which might have been obtained under totally different loading and environment conditions compared to the actual loading and environmental conditions of interest. The test cases mentioned in Table 7.1 are grouped into two broad groups, in-air and PWR-water environment conditions, and the associated CDF results are discussed below.

7.5.1 In-air condition probabilistic fatigue life

To compare the CDFs predicted based on MCMC predicted time-series damage states, the lifetime CDFs were estimated directly based on end-of-life fatigue data and the Weibull-Bootstrap model discussed earlier. The intended strain amplitude for which the test cases were modeled was approximately 0.5%. Thus, it is reasonable to set the given strain amplitude of 0.5% for the Weibull-Bootstrap fatigue model. Figure 7.28 shows the Weibull model when the given strain amplitude of 0.5% for the high-temperature air condition. The Weibull model predicted CDF would give the most accurate prediction of lifetime probability since it is directly based on end-of-life test data. Figure 7.28 shows the Weibull model estimated CDF (black line) and the confidence/accuracy bound of the Weibull model prediction (grey line). The estimated MCMC uncertainties or scatter band in time-series damage states (in Section 7.4) were validated by comparison with those from the Weibull-Bootstrap model results. This requires an estimate of the fatigue life distribution (i.e., CDFs) from the MCMC time-series uncertainties and the setting of a failure criterion. For the stress-controlled test cases, where the ratcheting strains are observed data, we assumed a failure ratcheting strain, which is the minimum of the highest observed (experimental) ratcheting strain for the particular test case, and the ASME maximum

ratcheting strain limit of 5%. Note that according to the ASME code the maximum allowable ratcheting strain is 5% for base metal and 2.5% for weld metal. Figure 7.5 shows that the observed maximum ratcheting strain for ET-F43 is well below the ASME code allowable limit of 5% ratcheting strain. Although, ideally, the MCMC method can predict time-series damage states and their scatter bound up to whatever required limit, engineering judgment is required to set the failure criteria. In this work, the MCMC-based CDFs are also predicted by considering a failure criterion in the neighborhood of the selected mean failure criteria. For example, for the mean failure criteria of 1.495% ratcheting strain (refer to Figure 7.5 and Table 7.2), CDFs were estimated not only for the 1.495% mean ratcheting strain failure criterion, but also at its neighborhood of $\pm 0.5\%$ strain, i.e., at 0.995% and 1.995% (Figure 7.5). This is to check the effect of failure criteria variety.

Figure 7.29 shows the empirical CDF from the MCMC ratcheting strain simulation using ET-F43 data (Figure 7.5) for the high-temperature in-air condition. Similar to the stress-controlled test case, a failure criterion is also required for displacement-controlled test cases (e.g., stroke or strain controlled). For the displacement-controlled test cases (strain-controlled case ET-F06 and stroke-controlled case ET-F13), we used the NUREG-6909 load drop criterion [26] of 25%, that is, the failure would occur when the maximum stress drop below 75% of its maximum stress value. In addition, we also used neighborhood failure criteria of 70% and 80% of the MCMC estimated maximum stress to check the effect of failure criteria variety. Figures 7.30 and 7.31 show the estimated empirical CDFs based on MCMC-predicted cyclic age versus maximum stress curves for ET-F06 and ET-F13, respectively.

Table 7.2 summarizes the estimated life distributions for the high-temperature air condition (Figures 7.28-7.31), which includes testing conditions and quartiles of life distribution. Table 7.2 shows that the MCMC-based estimated life distribution quartiles are comparable to the Weibull-Bootstrap predicted CDF. However, some discrepancy appears in the results for the CDFs predicted with the MCMC and Weibull-Bootstrap models. This discrepancy could have several causes. First, the discrepancy could have been caused by the totally different loading types. For example, ET-F43 was tested under stress-controlled conditions, whereas ET-F06 and ET-F13 were tested under displacement (stroke/strain) loading conditions. Second, the discrepancy could also be due to the stainless steel grades used. For example, the end-of-life test data (used for Weibull-Bootstrap CDF prediction) comprise different stainless steel grades such as 316, 304, etc., whereas the MCMC data are only based on 316 SS. Third, the discrepancy could be due to the heat treatment and heat of Weibull data set being different compared to the heat treatment and heat of specimens used for the MCMC test cases. A fourth cause could be the

Weibull data set being generated from fatigue tests conducted at temperatures in a range of 100-360 °C, whereas the MCMC test case specimens were tested at 300 °C. Nevertheless, the highly comparable results of the CDFs based on MCMC and direct end-of-life data show the promise of MCMC-based probabilistic life estimation. The MCMC-based approach can help to estimate the probabilistic life under any loading and environmental condition of practical concern, and at the same time, it requires few test data sets. Note that the in-air Weibull CDF predictions are based on 96 in-air data points, and the PWR-water Weibull CDF (discussed in section 7.5.2) predictions are based on 203 PWR-water data points. It is nearly impossible to conduct this many tests for each and every combination of actual reactor component loading and environmental conditions. The MCMC-based CDF prediction under actual reactor component loading conditions will be discussed in section 8.

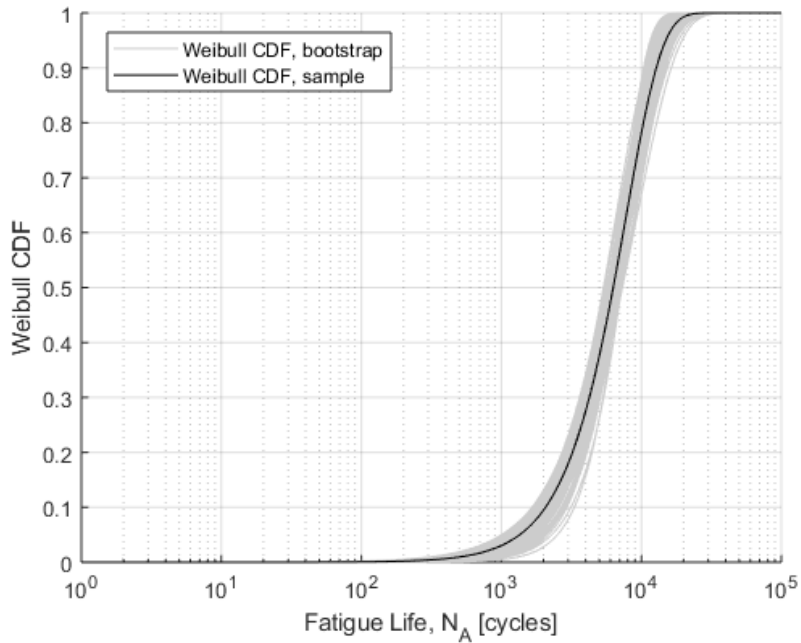


Figure 7.28 CDF of Weibull-based fatigue life model for high-temperature air, strain amplitude of 0.5%, and strain control: best-fit sample set (black lines) and bootstrap confidence bound sample set (grey lines).

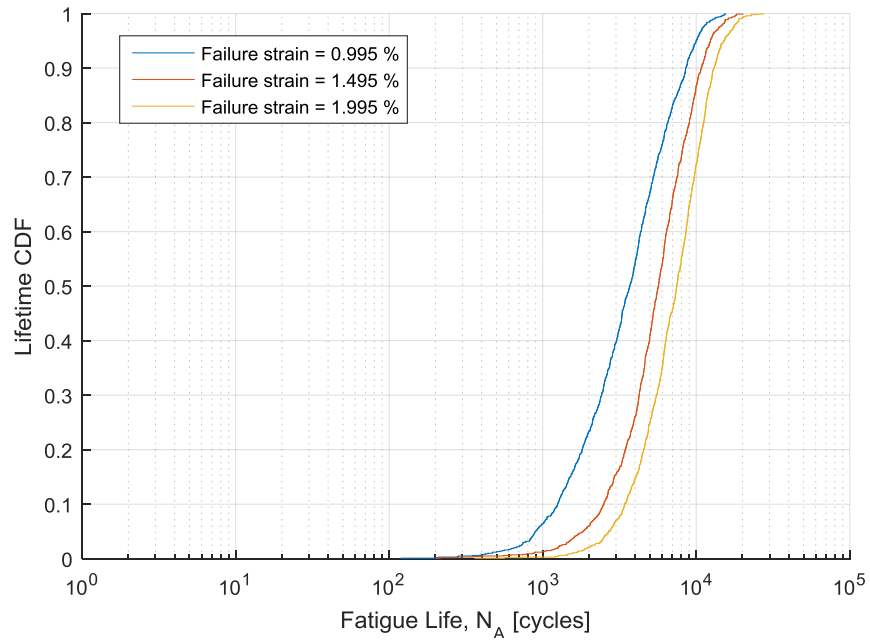


Figure 7.29 Empirical CDF estimated from MCMC time-series ratcheting strain for ET-F43 test case.

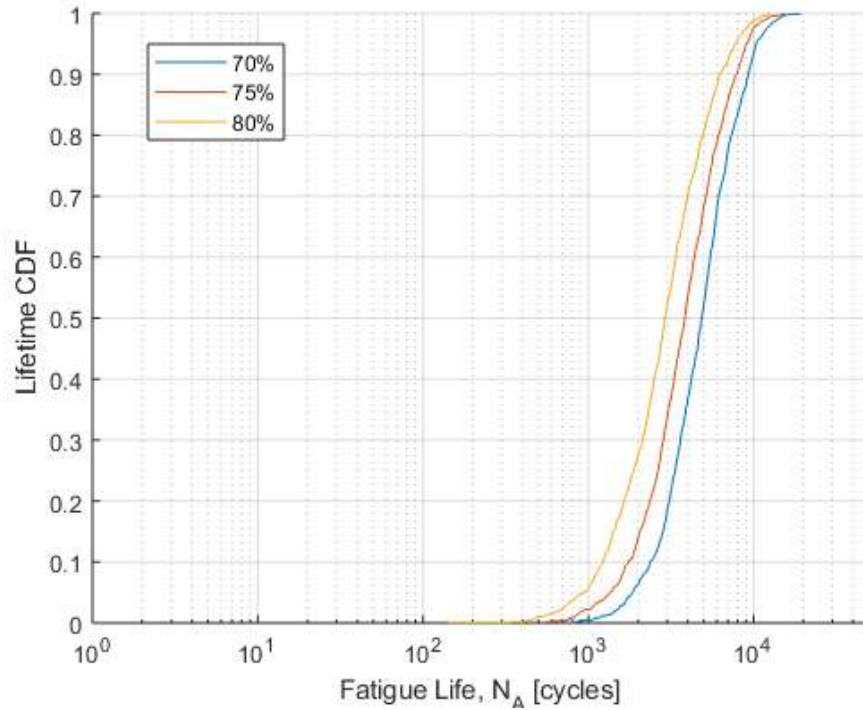


Figure 7.30 Empirical CDF estimated from MCMC estimated time-series ratcheting strain for ET-F06 test case.

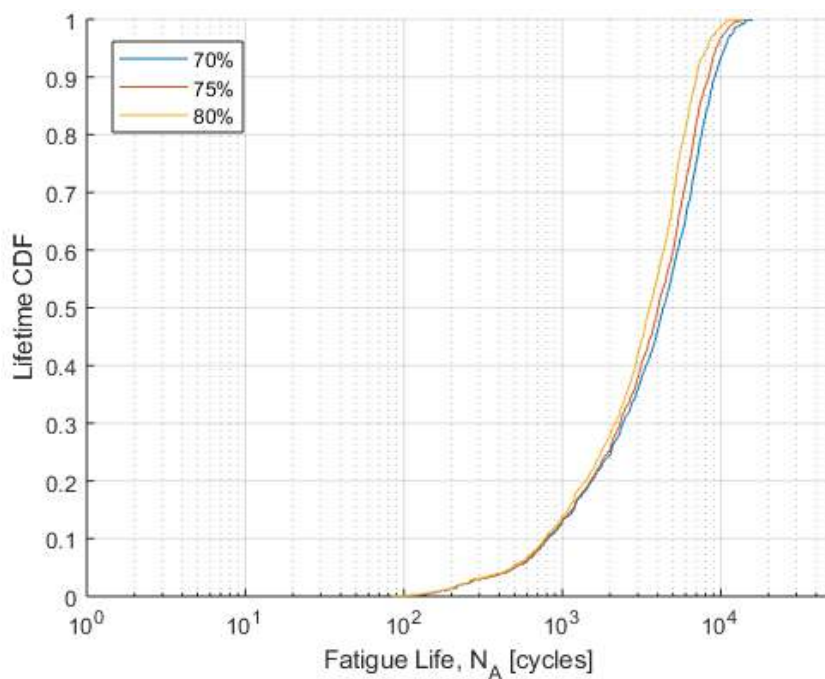


Figure 7.31 Empirical CDF estimated from MCMC estimated time-series ratcheting strain for ET-F13 test case.

Table 7. 2 Summary of estimated life distributions for high temperature in-air condition.

Source data	End-of-life data from literature	ET-F43	ET-F06	ET-F13	
Data type and number of data sets (or test case)	96 $\epsilon_a - N_A$ data sets (from 96 fatigue tests) digitized from JEAEA report	Single time-series data set (obtained from ANL conducted ET-F43 fatigue test) of cycle versus ratcheting strain	Single time-series data set (obtained from ANL conducted ET-F06 fatigue test) of cycle versus maximum stress	Single time-series data set (obtained from ANL conducted ET-F13 fatigue test) of cycle versus maximum stress	
Loading type	Strain-controlled	Stress-controlled	Strain-controlled	Frame crosshead Stroke-controlled	
Material grade	316 SS, 304 SS, etc.	316 SS	316 SS	316 SS	
Strain amplitude	Varying strain amplitude data, but Weibull CDF estimated for a given strain amplitude of 0.5%	Intended strain amplitude of 0.5%, but actual strain amplitude varies over time due to strain hardening/softening	Constant strain amplitude of 0.5%	Intended strain amplitude of 0.5%, but actual strain amplitude varies over time due to strain hardening/softening	
Temperature	100 – 325°C	300 °C	300 °C	300 °C	
Life distribution type	Weibull distribution	Empirical CDF based on MCMC predicted time-series cycle versus ratcheting strain	Empirical CDF based on MCMC predicted time-series cycle versus maximum stress	Empirical CDF based on MCMC predicted time-series cycle versus maximum stress	
Reference line & failure criteria	Weibull CDF, sample	$\epsilon_r \geq$ Min {max. observed ratcheting strain, 5%}	$\sigma_{max} \leq 0.75 \cdot \max(\sigma_{max})$	$\sigma_{max} \leq 0.75 \cdot \max(\sigma_{max})$	
Quartiles [cycles]	25%	3,741	3,910	2,646	1,943
	50%	6,291	5,661	3,832	4,042
	75%	9,475	8,124	5,559	6,362

7.5.2 PWR-water condition probabilistic fatigue life

Similar to the above discussed CDFs estimation for the in-air condition, we have also estimated the CDFs under PWR water conditions. The MCMC-based CDFs were estimated by using the MCMC-predicted time-series cycle versus maximum stress rates and an assumed failure criterion. The MCMC-based CDFs were estimated for two PWR-water test cases (stress-controlled EN-F44 and stroke-controlled EN-F14) and compared with the CDF estimated directly based on end-of-life data and the Weibull model. For the stress-controlled EN-F44 test case, a failure criterion of the lowest value between the highest observed ratcheting strain (for the particular test case) and 5% was selected. For the stroke-controlled ET-F14 test case, a failure criterion of 25% load drop (i.e., 75% of the maximum observed stress) was selected. The earlier developed Weibull-bootstrap model was used for estimating the direct end-of-life CDF for a given strain amplitude of 0.5%. The intended strain amplitude for which the test cases were MCMC modeled was approximately 0.5%.

Figure 7.32 shows the Weibull model for the given strain amplitude of 0.5% and the PWR water condition. To check the effect of failure criteria variety, CDFs are also plotted at the neighborhood above the mean failure criterion. Figure 7.33 shows the empirical CDF data from the MCMC predicted time-series ratcheting strain data for the stress-controlled EN-F44 test case. Similarly, Figure 7.34 shows the same variables plotted for the stroke-controlled EN-F14 test case. Table 7.3 summarizes the estimated life distributions for the PWR water condition (Figures 7.32 to 7.34). This table indicates that for the PWR water condition, neglecting the exception (i.e., EN-F44 stress-controlled case) and considering the differences in testing conditions, the estimated life distribution quartiles for the MCMC-estimated CDF are similar to those of the CDF estimated based on direct end-of-life test data. The exception in the case of EN-F43 could be due to stress-controlled loading that led to substantially different strain loading (associated with cyclic strain hardening/softening) compared to the intended strain amplitude of 0.5%. Also, the PWR water test water chemistry and the strain rates under which the PWR water tests were conducted are not exactly known for the discussed end-of-life test data, which are taken from a Japan Nuclear Energy Safety Organization report [39]. Under a lower strain rate and PWR water condition, the fatigue lives could be substantially lower than those under higher strain rate PWR-water condition. Note that the MCMC models are based on PWR-water tests conducted at ANL, which were performed approximately at an equivalent strain rate of 0.1%/s.

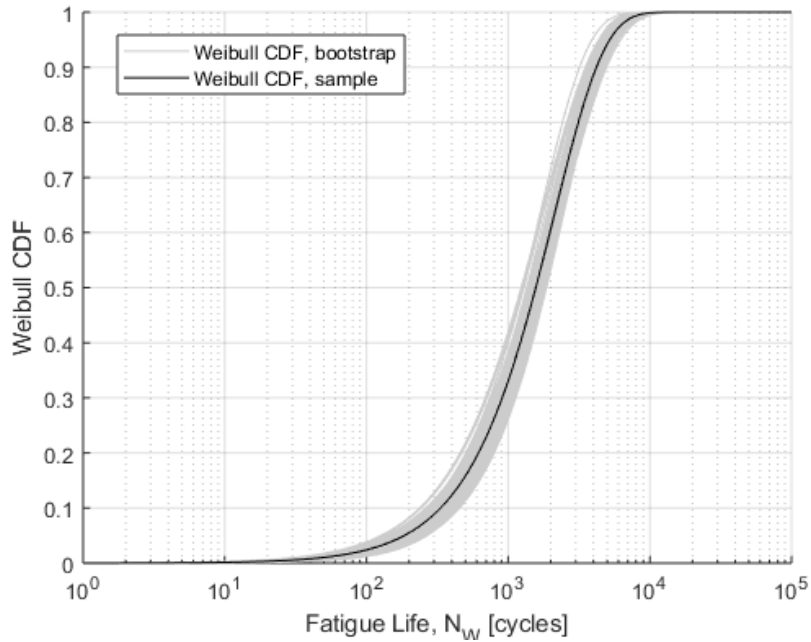


Figure 7.32 CDF of Weibull-based fatigue life model for high-temperature air, strain amplitude of 0.5%, and strain control: best-fit sample set (black lines) and bootstrap confidence bound sample set (grey lines).

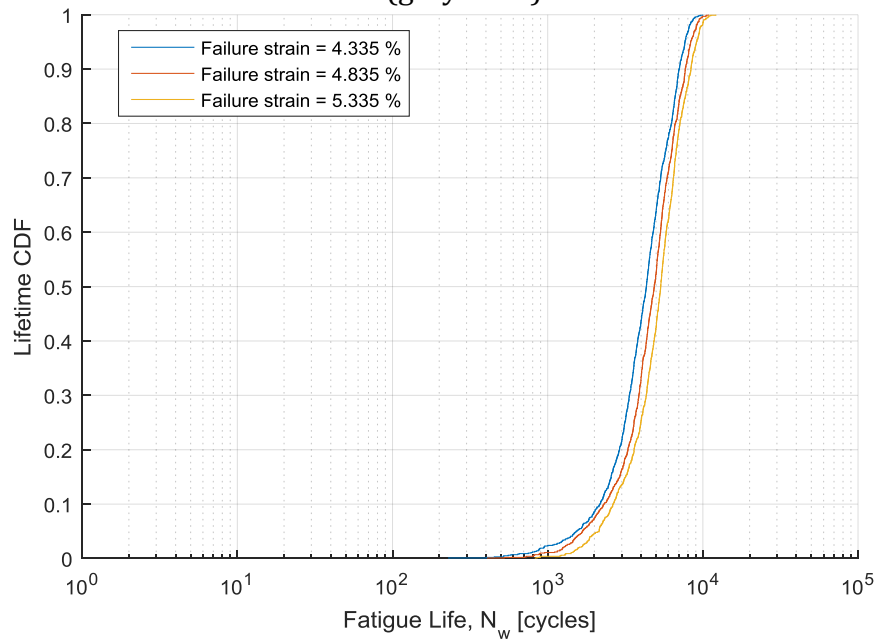


Figure 7.33 Empirical CDF estimated from MCMC-estimated time-series ratcheting strain for EN-F44 test case.

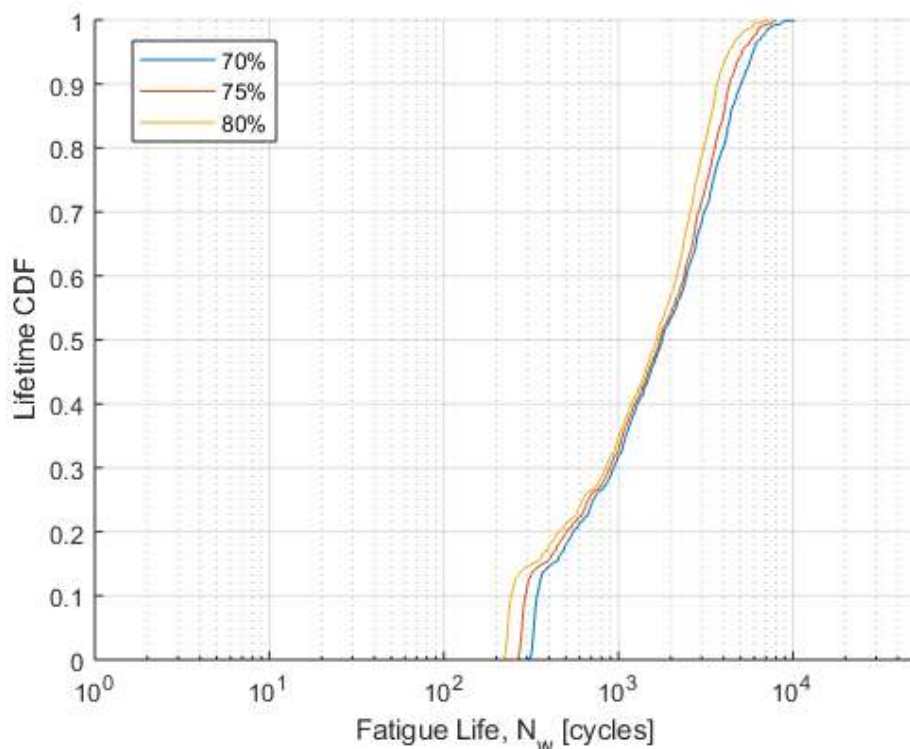


Figure 7.34 Empirical CDF estimated from MCMC-estimated time-series ratcheting strain for EN-F14 test case.

Table 7.3 Summary of estimated life distributions for PWR water condition.

Source data		End-of-life data from literature	EN-F44	ET-F14
Data type and number of data sets (or test case)		199 exact data and 4 right-censored $\epsilon_a - N_A$ data sets (from 203 fatigue tests) digitized from JEA EA report	Single time-series data set (obtained from ANL conducted ET-F44 fatigue test) of cycle versus ratcheting strain	Single time-series data set (obtained from ANL conducted EN-F14 fatigue test) of cycle versus maximum stress
Loading type		Strain/stroke-controlled	Stress-controlled	Frame-crosshead Stroke-controlled
Material grade		316 SS, 304 SS, etc.	316 SS	316 SS
Strain amplitude		Varying strain amplitude data, but Weibull CDF estimated for a given strain amplitude of 0.5%	Intended strain amplitude of 0.5%, but actual strain amplitude varies over time due to strain hardening/softening	Intended strain amplitude of 0.5%, but actual strain amplitude varies over time due to strain hardening/softening
Temperature		100 – 360 °C	300 °C	300 °C
Life distribution type		Weibull distribution	Empirical CDF based on MCMC predicted time-series cycle versus ratcheting strain	Empirical CDF based on MCMC predicted time-series cycle versus maximum stress
Reference line & failure criteria		Weibull CDF, sample	$\epsilon_r \geq$ Min {max. observed ratcheting strain, 5% }	$\sigma_{max} \leq 0.75 \cdot \max(\sigma_{max})$
Quartiles [cycles]	25%	473	3,745	668
	50%	974	4,996	1,727
	75%	1,722	6,460	3,232

8 Time-Series Fatigue Damage States and Probabilistic Fatigue Life Prediction Using Markov-Chain-Monte-Carlo (MCMC) Techniques: Un-Symmetric Loading Cases

In the previous section we discussed MCMC theoretical background and numerical results associated with push-pull type symmetric ($R = -1$) fatigue loading under different loading and environmental conditions. In this section, we discuss the MCMC model results related to unsymmetrical fatigue loading cases, such as design-basis and grid-load-following loading cases. The MCMC modeling procedure for the un-symmetric load case is very similar as the symmetric loading cases discussed in section 7. In the previous section the MCMC modeling results were derived by employing uniaxial test data but unrelated to any actual component. However, in this section we present the MCMC model results for a typical PWR surge line subjected to either design-basis or grid-load-following loading. The discussed results are more relevant for assessment of structural integrity in actual nuclear reactor components. Probabilistic time-series damage states and associated end-of-lives for the mentioned PWR surge line were estimated for the following test cases:

- a) ET-F47: In-air, simplified design-basis type loading (for more detail refer to [1])
- b) ET-F48: In-air, detailed design-basis type loading (for more detail refer to [1])
- c) EN-F51: PWR-water, grid-load-following type loading (for more detail refer to section 5 of this report)
- d) EN-F53: PWR-water detailed design-basis type loading (for more detail refer to section 5 of this report)

Here, we only present summaries of estimated lives (Table 8.1) and a few example figures (Figures 8.1 to 8.8) for the above test cases. The Table 8.1 results show that under the given loading (e.g., with assumed strain rate of 0.1%/s, which is the same as the test specimen strain rate, and with test temperature of 300 °C), material, and environmental conditions, the PWR surge line will survive the following minimum lives, i.e., with zero probability of failure:

- a) PWR surge line subjected to PWR-water environment and design basis loading will have a minimum fatigue life (with zero probability of failure) = 234 cycles = $234 \cdot (435.4/365) = \mathbf{279}$ years
- b) PWR surge line subjected to PWR-water environment and grid-load-following will have a minimum fatigue life (with zero probability of failure) = 273 cycles = $273 \cdot (435.4/365) = \mathbf{326}$ years

Note that we assumed each fuel cycle has a duration of 435.4 days (refer section 3 and [1]). Also note that the design basis test was conducted with an unpolished specimen (as is right after the machine fabrication), whereas the grid-load-following test was conducted with a polished specimen (polished up to 0.3 μm). Because of this difference, the predicted life for the design-basis loading condition is shorter (279 years) than that of the grid-load-following loading condition (326 years). If we consider a maximum surface finish factor of 1.175 (refer to Mandatory Appendix II, Article II-1000, "Experimental Stress Analysis," of ASME BPVC.II.A-2015), the grid-load-following loading case would have a

reduced life of $326/1.175 = 277$ years, which is very similar to the minimum probabilistic life predicted under design-basis loading. We assume the grid-load-following loading case will have a similar stressing effect as to that of the design-basis condition. That means both cases will have similar fatigue lives. Since the resulting stress states will be similar, except for small variation in stress/strain due to grid-load-following temperature fluctuations (assuming no stress concentration and associated large variation due to local defects coupled with grid-load-following loading), the expected lives under both loading cases will be similar for the assumed strain rate of 0.1%/s. Note that the ASME code and NUREG-6909 based approaches also give a predicted identical fatigue life of 263 cycles (refer to Table 8.2 and section 5). The above ASME code also suggests use of a factor to counter the effect of size, i.e., with a maximum value of 1.5. If we consider both the surface finish (assuming the actual industrial component will be much rougher compared to the machined small specimen) and size factors, the minimum expected lives for both the loading cases would be as below:

- a) PWR surge line subjected to PWR-water environment and design basis loading will have a minimum fatigue life (with zero probability of failure) = $234/(1.5*1.175)$ cycles = 133 cycles = $133*(435.4/365) = \mathbf{159}$ years
- b) PWR surge line subjected to PWR-water environment and grid-load-following will have a minimum fatigue life (with zero probability of failure) = $273/(1.5*1.175)$ cycles = 155 cycles = $155*(435.4/365) = \mathbf{185}$ years

If we consider the minimum for both loading cases, the PWR surge line will survive a minimum life of **159 years** under the assumed loading, material, and environmental conditions.

Table 8. 1 Summary of estimated life distributions for high-temperature in-air condition.

	ET-F47	ET-F48	EN-F51	EN-F53	
Material grade	316 SS pure base	316 SS pure base	316 SS base from HAZ of DMW	316 SS base from HAZ of DMW	
Loading type and environment	Strain-controlled, design-basis, 300 °C in-air	Strain-controlled, design-basis, 300 °C in-air	Stroke-controlled, grid-load-following, 300 °C PWR-water	Stroke-controlled, design-basis, 300 °C PWR-water	
Maximum applied/intended strain amplitude (strain rate)	0.575 % (0.1%/s)	0.65 % (0.1%/s)	0.642 % (0.1%/s)	0.642 % (0.1%/s)	
Source data type and number of data sets (or test case)	Single experimental time-series data of cycle versus maximum stress	Single experimental time-series data of cycle versus maximum stress	Single experimental time-series data of cycle versus maximum stress	Single experimental time-series data of cycle versus maximum stress	
Reference line & failure criteria	$\sigma_{\max} \leq 0.75 \cdot \max(\sigma_{\max})$	$\sigma_{\max} \leq 0.75 \cdot \max(\sigma_{\max})$	$\sigma_{\max} \leq 0.75 \cdot \max(\sigma_{\max})$	$\sigma_{\max} \leq 0.75 \cdot \max(\sigma_{\max})$	
Deterministic experimental (25% load drop) life	24,800	15,966	9,999	7,810	
Deterministic ASME code or NUEG-6909 based <u>design</u> life (using Eq. 5.17 K_f factor)	NA	765	263 ^{##}	263 ^{##}	
Deterministic life based on ANL fully mechanistic model	19,700	15,400	NA	NA	
Quartiles or failure probability [cycles]	0%	1,816	157	273	234
	25%	5,391	4,628	4,630	2,183
	50%	7,419	9,512	8,221	4,186
	75%	10,688	14,734	11,724	6,282
	100%	45,684	47,351	29,273	15,582

^{##} Considering $F_{en} = 2.9093$, with $\dot{\epsilon}_{el} = 0.1$ %/s (approximate intended strain rate during actual uniaxial specimen fatigue test).

8.1 MCMC model results for simplified design-basis loading case (ET-F47)

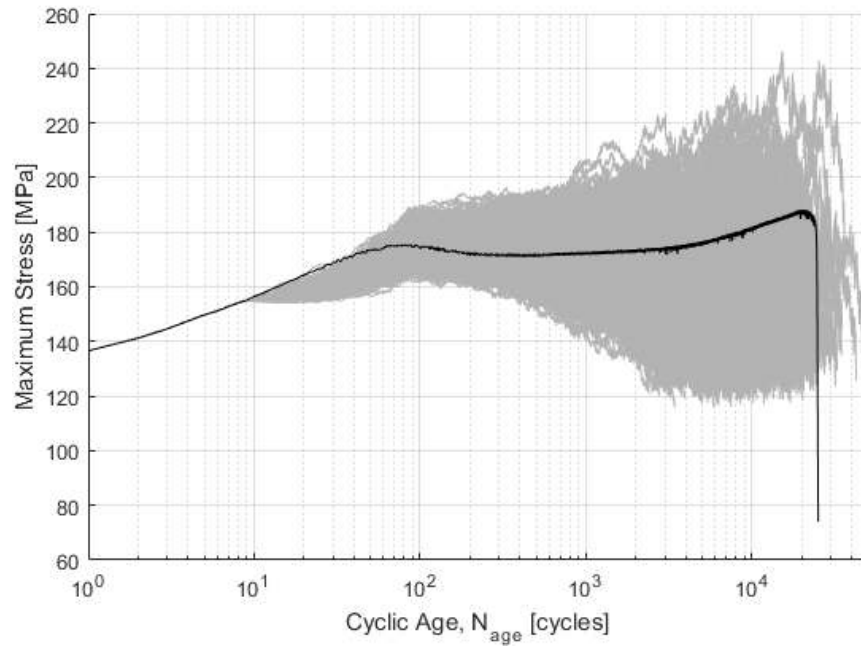


Figure 8. 1 Original maximum stress profile (black line) and estimated 1,000 MCMC maximum stress profiles (grey line) for ET-F47 data.

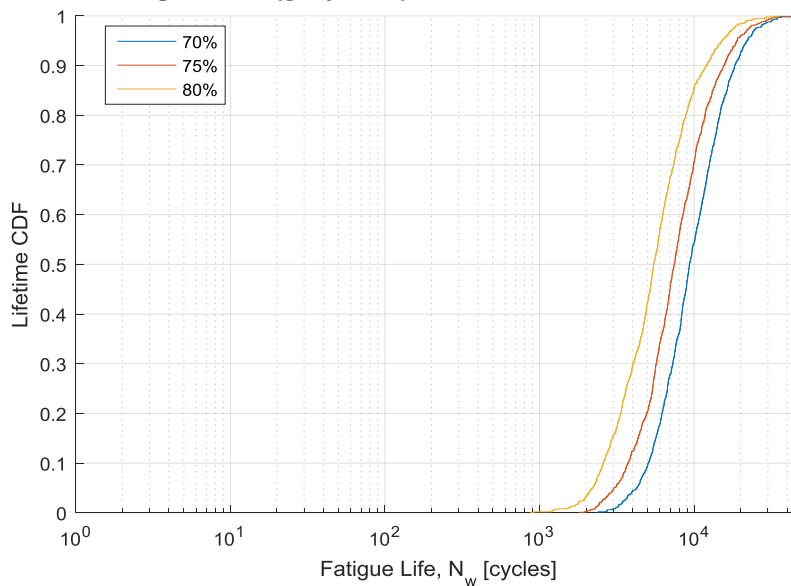


Figure 8. 2 Empirical CDF estimated from MCMC estimated time-series ratcheting strain for ET-47 test case.

8.2 MCMC model results for detailed design-basis loading case (ET-F48)

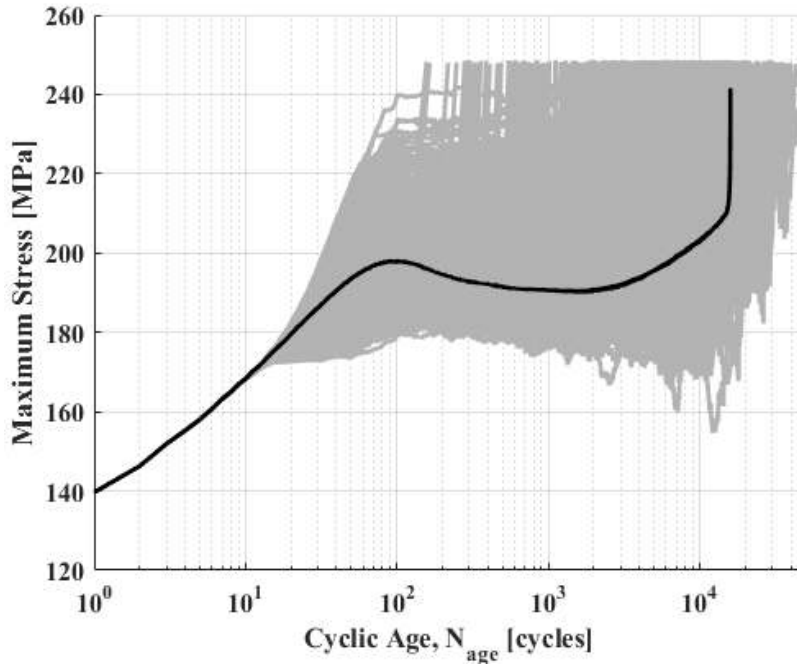


Figure 8. 3 Original maximum stress profile (black line) and estimated 1,000 MCMC maximum stress profiles (grey line) for ET-F48 data.

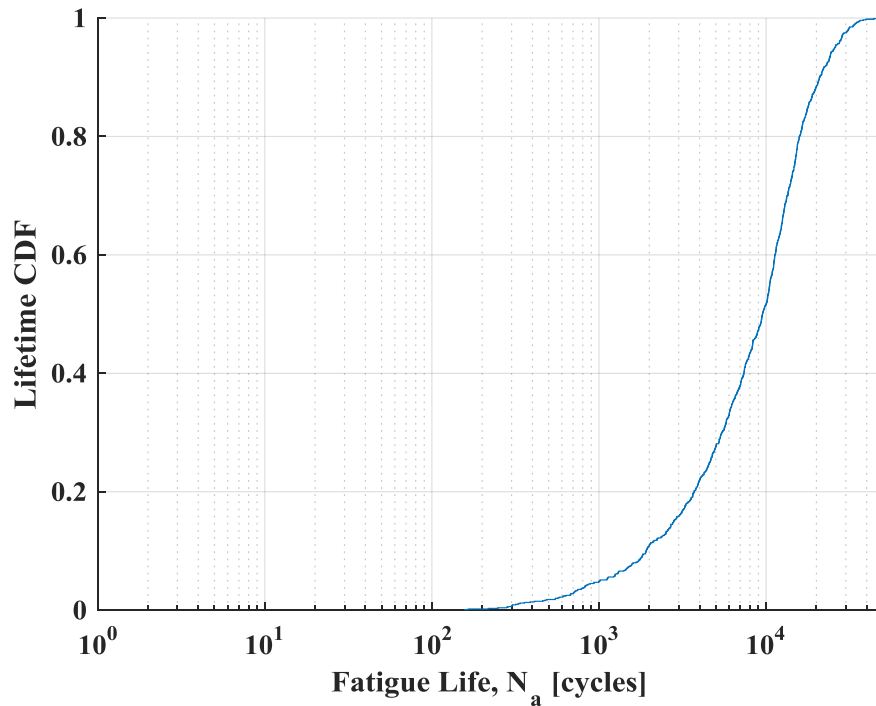


Figure 8. 4 Empirical CDF estimated from MCMC estimated time-series ratcheting strain for ET-48 test case.

8.3 MCMC model results for grid-load-following loading case (EN-F51)

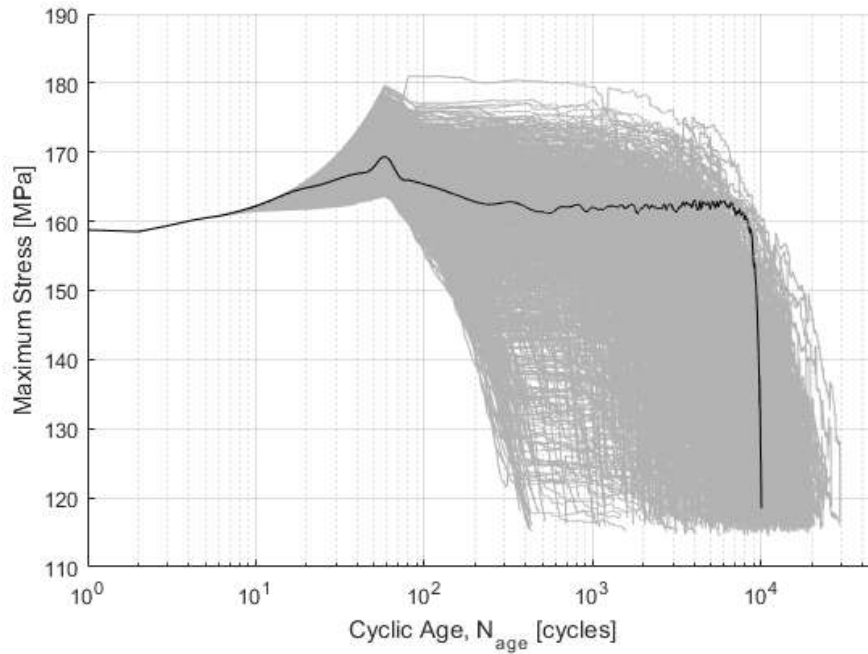


Figure 8.5 Original maximum stress profile (black line) and estimated 1,000 MCMC maximum stress profiles (grey line) for EN-F51 data.

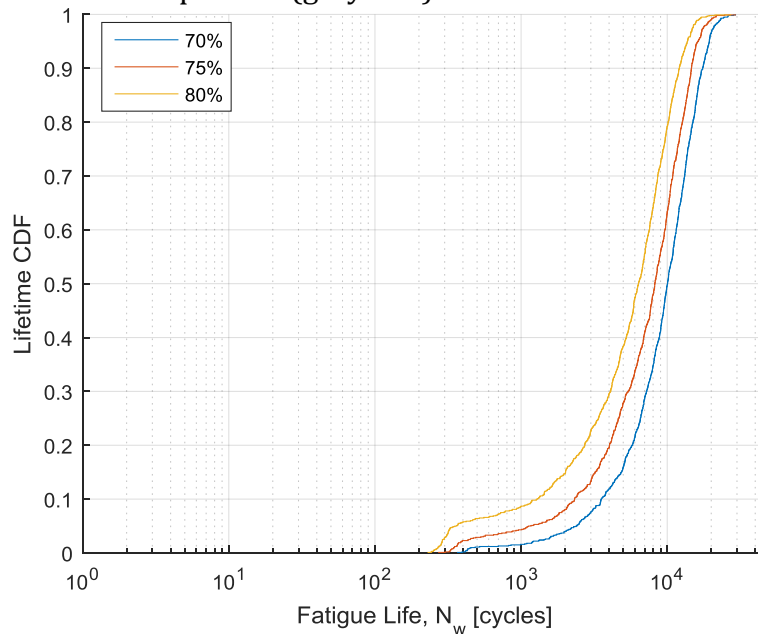


Figure 8.6 Empirical CDF estimated from MCMC estimated time-series ratcheting strain for EN-F51 test case.

8.4 MCMC model results for design-basis loading case (EN-F53)

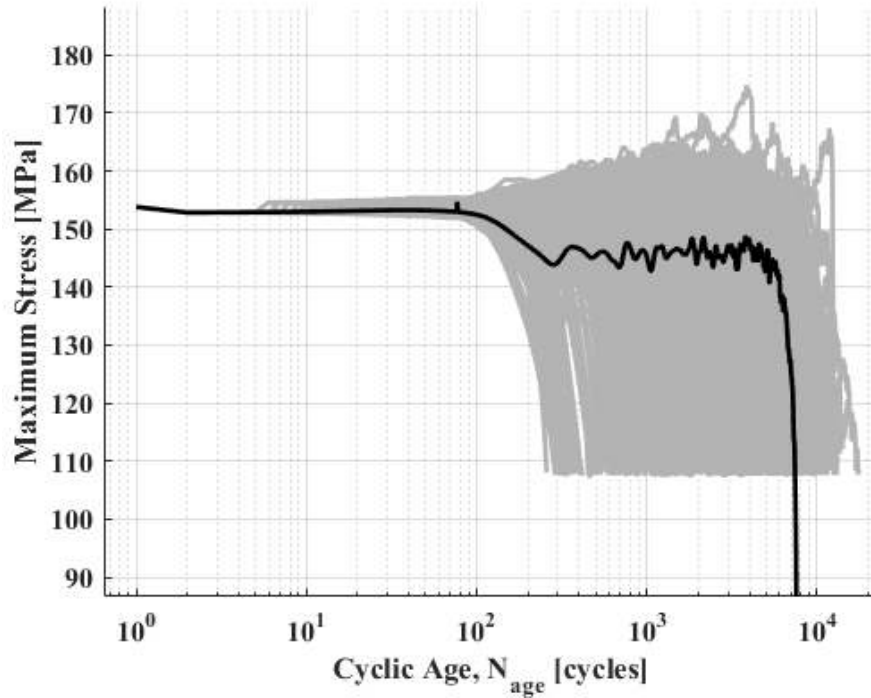


Figure 8.7 Original maximum stress profile (black line) and estimated 1,000 MCMC maximum stress profiles (grey line) for EN-F53 data.

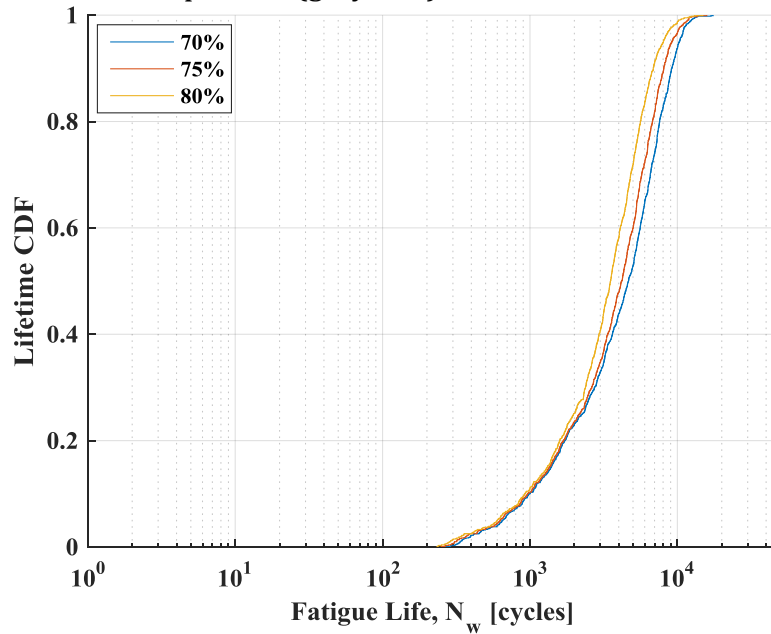


Figure 8.8 Empirical CDF estimated from MCMC estimated time-series ratcheting strain for EN-F53 test case.

9 Summary and Future Study

9.1 Summary

In this report, we have presented a hybrid model-data based framework for deterministic and probabilistic fatigue life estimation of safety-critical nuclear reactor components, such as PWR surge lines under design-basis and grid-load-following loading conditions. In the report period, we studied different computational fluid dynamics modeling tools for thermal stratification modeling in a typical pipe flow condition. We performed ABAQUS FE-based thermal-mechanical stress analysis under grid-load-following loading conditions. We used the associated grid-load-following and design-basis stress analysis results (presented in our earlier report [ANL-LWRS/18-01]) and ASME code and NUREG-6909 based approaches for deterministic fatigue life estimation of a typical PWR surge line under these loading conditions. Based on the FE model results based on thermal-mechanical stress analysis, we selected the test inputs for conducting simulated fatigue tests of a PWR surge line under design-basis and grid-load-following conditions.

We also extensively studied modeling approaches for probabilistic risk assessment or reliability assessment of safety-critical nuclear reactor components such as a PWR surge line under design-basis and grid-load-following loading conditions. We discussed two probabilistic modeling strategies: (1) a Weibull-bootstrap probabilistic technique that is directly based on end-of-life data (traditional S~N data) to estimate the probabilistic lives, and (2) a Markov-Chain-Monte-Carlo (MCMC) based technique for probabilistic forecasting of time-series evolution of damage states, which were then used to estimate the associated probabilistic end-of-life. Using data obtained from our earlier symmetric fatigue tests (stress- or strain-controlled tests under in-air or PWR-water conditions), we extensively tested the MCMC models. We also tested the MCMC models using fatigue test data for un-symmetric loading cases such as the above fatigue tests of a PWR surge line under design-basis and grid-load-following conditions. From the hybrid model-data based framework (under the assumed loading, environment and thermal-mechanical boundary conditions), we have predicted that the 316SS-pure base metal PWR surge line would survive at least 159 years with zero failure probability. The hybrid modeling strategy shows promise of predicting probabilistic life without conducting hundreds of costly fatigue tests relevant to a given loading and environmental condition. However, the discussed probabilistic modeling strategy is in a very incipient stage and requires further improvement and experimental validation.

9.2 Future Work

Future work envisioned is as follows:

1. Further improve the accuracy of the 316 SS SL pipe prediction results by incorporating asymmetric (with non-zero baseline or mean stress/strain effect) fatigue loading material models.
2. Extend the material model of 316 SS to capture the PWR coolant water environment under design-basis and grid-load-following loading cycles.
3. Study the strain rate and hold effect on 316 SS-base metal when the material is subjected to realistic design-basis and grid-load-following loading cycles.
4. Improve the MCMC modeling framework by incorporating more Bayesian and multivariate techniques, such that longer historical information and additional fatigue life affecting variables (e.g., strain rate and water chemistry) can be included.

5. Extend the overall methodology for 316 SS-508 LAS dissimilar metal butter and filler welds and associated reactor components.

References

- [1] Mohanty, S., Barua, B., Listwan, J., Majumdar, S. and Natesan, K., “Implementation of ANL’s mechanics based evolutionary fatigue modeling through ABAQUS-WARP3D based high-performance computing framework,” Report No. ANL/LWRS-18/01. Argonne National Laboratory, April 2018 (<https://www.osti.gov/biblio/1480516>).
- [2] NRC Bulletin No. 88-08: Thermal Stress in Piping Connected to Reactor Coolant Systems.
- [3] NRC Bulletin No. 88-11: Pressurizer Surge Line Thermal Stratification.
- [4] Mohanty, S., Barua, B., Listwan, J., Majumdar, S. and Natesan, K., Final Report on CFD and Thermal-Mechanical Stress Analysis of PWR Surge Line under Transient Condition Thermal Stratification and an Evolutionary Cyclic Plasticity Based Transformative Fatigue Evaluation Approach without Using S-N Curve, No. ANL/LWRS-17/03, Rev-1, August 2018 (<https://www.osti.gov/biblio/1480513>).
- [5] Lu, T., Attinger, D., and Liu, S. M., 2013. “Large-eddy simulations of velocity and temperature fluctuations in hot and cold fluids mixing in a tee junction with an upstream straight or elbow main pipe”. *Nuclear Engineering and Design*, 263, pp. 32–41.
- [6] Jeong, J.-U., Chang, Y.-S., Choi, J.-B., and Kim, Y.-J., 2008. “Parametric CFD Analyses to Simulate Stratified Flows”. pp. 1–6.
- [7] Jo, J. C., Choi, Y. H., and Choi, S. K., 2003. “Numerical Analysis of Unsteady Conjugate Heat Transfer and Thermal Stress for a Curved Piping System Subjected to Thermal Stratification”. *Journal of Pressure Vessel Technology*, 125(4), p. 467.
- [8] Kim, K. C., Lim, J. H., and Yoon, J. K., 2008. “Thermal fatigue estimation due to thermal stratification in the RCS branch line using one-way FSI scheme”. *Journal of Mechanical Science and Technology*, 22(11), pp. 2218–2227.
- [9] Kim, S. H., Choi, J. B., Park, J. S., Choi, Y. H., and Lee, J. H., 2013. “A coupled CFD-FEM analysis on the safety injection piping subjected to thermal stratification”. *Nuclear Engineering and Technology*, 45(2), pp. 237–248.
- [10] Boros, I., Petofi, G., and Aszodi, A. “CFD Analysis of Thermal Stratification in the Primary Circuit”.
- [11] Ensel, C., Colas, A., and Barthez, M., 1995. “Stress analysis of a 900 MW pressurizer surge line including stratification effects”. *Nuclear Engineering and Design*, 153(2-3), pp. 197–203.
- [12] Jo, J. C., Kim, S. J., Choi, Y. H., and Kim, H. J., 2002. “Transient Response of Thermal Stress at a PWR Pressurizer Surge Line Pipe Subjected to Internally Thermal Stratification”. No. October, *Proceedings of the Korean Nuclear Society*, pp. 1–10.
- [13] Jo, J. C., and Kang, D. G., 2010. “CFD Analysis of Thermally Stratified Flow and Conjugate Heat Transfer in a PWR Pressurizer Surgeline”. *Journal of Pressure Vessel Technology*, 132(2), p. 021301.
- [14] Yu, Y., Park, S., Sohn, G., and Bak, W., 1997. “Structural evaluation of thermal stratification for PWR surge line”. *Nuclear Engineering and Design*, 178(2), pp. 211–220.
- [15] Zhang, Y., Lu, T., Jiang, P. X., Zhu, Y. H., Wu, J., and Liu, C. L., 2016. “Investigation on thermal stratification and turbulent penetration in a pressurizer surge line with an overall out-surge flow”. *Annals of Nuclear Energy*, 90, pp. 212–233.
- [16] Rezende, H. C., Santos, A. A. C., Navarro, M. A., and Jordao, E., 2012. “Verification and Validation of a thermal stratification experiment CFD simulation”. *Nuclear Engineering and Design*.
- [17] ABAQUS documentation (2016).

- [18] Gamble, R. "Evaluation of pressure-temperature limits for normal RPV startup and shutdown. EPRI-NRC Public Meeting, Rockville, MD, August 28, 2012 (<http://pbadupws.nrc.gov/docs/ML1224/ML12243A266.pdf>).
- [19] Lokhov, A. "Load-following with nuclear power plants." NEA News 29, no. 2 (2011): 18 (<https://www.oecd-nea.org/nea-news/2011/29-2/nea-news-29-2-load-following-e.pdf>).
- [20] Lokhov, A. Technical and Economic Aspects of Load Following with Nuclear Power Plants: Nuclear Development Division. OECD Nuclear Energy Agency, Paris, France (2011).
- [21] Savolainen, A. (2015). The role of nuclear and other conventional power plants in the flexible energy system, Master's thesis, Lappeenranta University of Technology, (<http://lutpub.lut.fi/handle/10024/118575>).
- [22] Mohanty, Subhasish, Soppet, William, Majumdar, Saurin, & Natesan, Ken. Thermal-Mechanical Stress Analysis of PWR Pressure Vessel and Nozzles under Grid Load-Following Mode: Interim Report on the Effect of Cyclic Hardening Material Properties and Pre-existing Cracks on Stress Analysis Results, Argonne National Laboratory, Lemont, IL, Report No. ANL/LWRS-16/01 United States. doi:10.2172/1249554 (<https://www.osti.gov/biblio/1249554>)
- [23] Barua, B., Mohanty, S., Listwan, J. T., Majumdar, S., & Natesan, K. (2018). Methodology for Stress-Controlled Fatigue Test Under In-Air and Pressurized Water Reactor Coolant Water Condition and to Evaluate the Effect of Pressurized Water Reactor Water and Loading Rate on Ratcheting. *Journal of Pressure Vessel Technology*, 140(3), 031403.
- [24] The American Society of Mechanical Engineers (2010) ASME Boiler and Pressure Vessel Code.
- [25] The American Society of Mechanical Engineers (2013, 2015) ASME Boiler and Pressure Vessel Code, Section VIII, Division 3.
- [26] Chopra, O. K., & Stevens, G. L. (2014). Effect of LWR Coolant Environments on the Fatigue Life of Reactor Materials—NUREG. CR-6909 (Rev. 1), Argon National Laboratory.
- [27] Mohanty, S., Soppet, W. K., Majumdar, S., & Natesan, K. (2015, July). Pressurized Water Reactor Environment Effect on 316 Stainless Steel Stress Hardening/Softening: An Experimental Study. In ASME 2015 Pressure Vessels and Piping Conference, Paper no. PVP2015-45694 (pp. V06AT06A038-V06AT06A038). American Society of Mechanical Engineers.
- [28] Emslie, J., Watson, C., & Wright, K. (2014, July). ASME III Fatigue Assessment Plasticity Correction Factors for Austenitic Stainless Steels. In ASME 2014 Pressure Vessels and Piping Conference, Paper no. PVP2014-28633 (pp. V003T03A062-V003T03A062). American Society of Mechanical Engineers.
- [29] Ranganath, S., & Mehta, H. S. (2015, July). An Examination of the Role of the Assumed Young's Modulus Value at the High Cycle End of ASME Code Fatigue Curve for Stainless Steels. In ASME 2015 Pressure Vessels and Piping Conference, Paper no. PVP2015-45619 (pp. V01AT01A038-V01AT01A038). American Society of Mechanical Engineers.
- [30] Chopra, O. K., & Shack, W. J. (2003). Review of the Margins for ASME Code Fatigue Design Curve: Effects of Surface Roughness and Material Variability, US-NRC Report no. NUREG/CR-6815 (Argonne report no. ANL-02/39), Division of Engineering Technology, Office of Nuclear Regulatory Research, US Nuclear Regulatory Commission.
- [31] Weibull, W. (1951), "A statistical distribution function of wide applicability", *J. Appl. Mech.-Trans. ASME*, 18 (3): 293–297.
- [32] Leemis, L. M. (1995). *Reliability: probabilistic models and statistical methods*. New Jersey: Prentice Hall.
- [33] Bazant, Z. P., & Le, J. L. (2017). *Probabilistic Mechanics of Quasibrittle Structures: Strength, Lifetime, and Size Effect*. Cambridge University Press.
- [34] Fisher, R. A. (1930). *The Genetical Theory of Natural Selection* Oxford University Press, Oxford.
- [35] Park, J. P., Park, C., Cho, J., & Bahn, C. B. (2017). Effects of cracking test conditions on estimation uncertainty for Weibull parameters considering time-dependent censoring interval. *Materials*, 10(1), 3.
- [36] Efron, B. (1979). "Bootstrap methods: Another look at the jackknife". *The Annals of Statistics*. 7 (1): 1–26.
- [37] Chernick, M.R., *Bootstrap Methods: A Guide for Practitioners and Researchers*, second ed., Wiley, 2007.
- [38] Park, J. P., Park, C., Oh, Y. J., Kim, J. H., & Bahn, C. B. (2018). Statistical analysis of parameter estimation of a probabilistic crack initiation model for Alloy 182 weld considering right-censored data and the covariate effect. *Nuclear Engineering and Technology*, 50(1), 107-115.
- [39] JNES-SS Report, "Environmental Fatigue Evaluation Method for Nuclear Power Plants," JNES-SS-1005, Nuclear Energy System Safety Division, Japan Nuclear Energy Safety Organization, March 2011.
- [40] Geyer, C. (2011). Introduction to markov chain monte carlo. *Handbook of markov chain monte carlo*, 20116022, 45 (<http://www.mcmchandbook.net/HandbookChapter1.pdf>)
- [41] Wu, W. F., & Ni, C. C. (2004). Probabilistic models of fatigue crack propagation and their experimental verification. *Probabilistic Engineering Mechanics*, 19(3), 247-257.
- [42] An, D., Choi, J. H., Kim, N. H., & Pattabhiraman, S. (2011). Fatigue life prediction based on Bayesian approach to incorporate field data into probability model. *Structural engineering & mechanics*, 37(4), 427.

[43] Ross, S. M. (2014). Introduction to probability and statistics for engineers and scientists. Academic Press.

This page intentionally left blank



Nuclear Engineering Division

Argonne National Laboratory
9700 South Cass Avenue, Bldg. 208
Argonne, IL 60439

www.anl.gov



Argonne National Laboratory is a U.S. Department of Energy
laboratory managed by UChicago Argonne, LLC